

# Methodologies for City-scale Microgeneration Viability Assessment

James Duncan Gooding

Submitted in accordance with the requirements for the degree of  
Doctor of Philosophy  
as part of the integrated PhD & MSc in Low Carbon Technologies

The University of Leeds  
Energy Research Institute (ERI)  
School of Chemical and Process Engineering

September 2016

## Declaration

The candidate confirms that the work submitted is his own, except where work which has formed part of jointly authored publications has been included. The contribution of the candidate and the other authors to this work has been explicitly indicated below. The candidate confirms that appropriate credit has been given within the thesis where reference has been made to the work of others.

James Duncan Gooding

This copy has been supplied on the understanding that it is copyright material and that no quotation from the Thesis may be published without proper acknowledgement.

© 2016 The University of Leeds and James Duncan Gooding

Over the course of the research project described in this thesis, the following papers have been published or submitted.

### Chapter 3

**Gooding, J., Edwards, H., Giesekam, J., Crook, R. (2013) 'Solar City Indicator: A Methodology to Predict City Level PV Installed Capacity by Combining Physical Capacity and Socio-economic Factors', *Solar Energy*, 95, pages 325-335 DOI: 10.1016/j.solener.2013.06.027**

I devised a methodology to calculate solar insolation for small properties. I was lead author so also coordinated the article submission in the required format. I assisted Jannik Giesekam in developing a methodology for large properties and Holly Edwards investigated social

trends and solar PV investment. I coordinated the research project and led the submission process. Dr. Crook provided general guidance.

**Jacques, D.A., Gooding J., Gieseckam J.J., Tomlin A.S., Crook R. (2014) 'Methodology for the assessment of PV capacity over a city region using low-resolution LiDAR data and application to the City of Leeds (UK)', *Applied Energy*, 124, 28-34.**

I helped to develop the method and the MATLAB code that performs the calculations as well as assisting in writing the article. David Jacques and Dr. Crook were also involved in the method development and MATLAB coding while Professor Tomlin and Jannik Gieseckam provided assistance in writing the article.

**Gooding, J., Tomlin A.S., Crook R. (2015) 'Modelling of roof geometries from low-resolution LiDAR data for city-scale solar energy applications using a neighbouring buildings method', *Applied Energy*, 148, Pages 93–104, DOI: 10.1016/j.apenergy.2015.03.013**

I developed the full methodology and prepared the article for submission with supervision from both Dr. Crook and Professor Tomlin.

## Chapter 4

**Gooding, J., Smith, C.J., Crook, R., Tomlin, A.S. (2015) 'Solar Resource Estimation Using a Radiative Transfer with Shading (RTS) Model', *Proceedings of the 31st European Photovoltaic Solar Energy Conference and Exhibition*, DOI: 10.4229/EUPVSEC20152015-6AV.4.25**

I developed a method to incorporate LiDAR data derived shading analysis into a radiative transfer model for annual solar insolation estimation. I was lead author so also coordinated the article submission in the required format. Chris Smith contributed knowledge of radiative transfer modelling of solar insolation and assisted in the writing of the article. Dr. Crook and Professor Tomlin provided supervision throughout.

## Chapter 5

**Gooding, J. and Tomlin, A.S. (2016) 'Simplified Methods for Estimating Aerodynamic Parameters and Wind Profiles for Height Heterogeneous Surfaces', *submitted to Wind Energy***

I developed the full methodology and prepared the article for submission with supervision from Professor Tomlin.

## Chapter 6

**Adam, K., Hoolohan, V., Gooding, J., Knowland, T., Bale, C.S.E., Tomlin, A.S., (2015)**  
**“Methodologies for city-scale assessment of renewable energy generation potential to**  
**inform strategic energy infrastructure investment.” *Cities*,**  
**DOI:10.1016/j.cities.2015.10.015**

I gave guidance on the capabilities of GIS software which shaped the aims of the paper and its method. I contributed knowledge of existing methodologies to reach the research aims. I assisted in the Python coding that underpins the GIS elements of the method and produced the figures that required GIS software. I extensively edited the article prior to submission.

Katrina Adam was responsible for the solar PV viability method and prepared the article for submission. Victoria Hoolohan developed the wind viability analysis methodology. Both Victoria Hoolohan and Katrina Adam implemented the financial viability method that was developed with input from Dr. Knowland and Dr. Bale. Professor Tomlin supervised the project, providing guidance at each stage.



## Acknowledgements

I would like to thank all of the people who have helped and supported me over the course of this research project which has been compelling, inspiring, challenging and terrifying at different points along the way. Throughout all of it I have been fortunate to have had the love and support of my wife Jane who has helped me to keep going in the toughest times and celebrated with me in the best times. It's fair to say that a lot has happened whilst completing the integrated MSc and PhD over the past five years, including: surgery after crashing my bike, moving house not once, twice but three times; getting married; and both of us have started new jobs. It has definitely been a team effort and I am glad to have this platform to give my thanks to her.

I am indebted to my parents and sister for always putting me into an environment where I could learn and achieve. The times when they have lent a sympathetic ear in recent years have not gone unnoticed and they've helped me to keep things in perspective. So too have Mary and Philip who I am thankful for regularly inviting us away to deepest East Yorkshire to recharge the batteries.

I have to thank my primary supervisor Professor Alison Tomlin who has given up a lot of time to push me to create work that is truly the best I can deliver. I have achieved things that I had never thought I could during the research and have developed not only as a researcher but also as a person under her tutelage.

I have worked closely with my secondary supervisory Dr. Rolf Crook at various points through the project. His constructive and thoughtful feedback on many aspects of my work, particularly with regard to solar photovoltaics, has provided new directions and improved processes to various parts of the methodologies I have developed.

As part of the Doctoral Training Centre in Low Carbon Technologies at The University of Leeds, I have been fortunate to work alongside some very gifted researchers who are passionate about climate change research and the role low carbon technologies could play in a future society. I'm grateful that I can count you all as friends and will enjoy tracking what paths you take through life. I have co-authored a small number of research projects with some of these inspirational colleagues who have enriched my own approach to research. I would therefore like to thank Dr. Holly Edwards, Dr. Jannik Gieseckam, Dr. David Jacques, Dr. Chris Smith, Katrina Adam, Victoria Hoolahan and Dr. Frin Bale for all of their hard work. Although I have not co-authored any research with Dr. Joel Millward-Hopkins, I feel that I

owe him an acknowledgement for the time he has taken to explain how his models work and to give me his thoughts on my work. In addition, James McKay, David Haynes and Emily Bryan-Kinns have worked hard to keep my research project on track so thank you for all you've done for me.

Finally, I would like to thank Professor Paul Williams and the Energy Research Institute for giving me the chance to research city-scale wind and solar microgeneration viability.

## Abstract

Over the last decade, increasing numbers of multi-national corporations, public institutions and individual property owners have become interested in installing solar photovoltaics and small wind turbines. To best inform this broad range of actors, this research aims to assess the financial viability of such investments across broad city regions whilst maintaining accuracy at individual properties. Publicly available digital representations of urban surfaces are central to meeting this aim because they can be used to assess the area, slope and orientation of potential solar photovoltaic (PV) installation sites and to define how vertical wind profiles are altered by urban areas.

A first study utilised digital surface models (DSMs) across seven UK cities to assess the roof spaces available for solar PV and also incorporated socio-economic factors to define the propensity for cities to install the technology. Despite changes to financial incentives that had recently occurred, the technologies remained viable at a very large number of locations and could theoretically meet large percentages (16% to 43%) of the cities' electricity demands.

The accuracy of slope, orientation and available area estimation in roof geometry modelling was then improved through the development of a neighbouring buildings method. In 87% of 536 validated results, the method identified the correct roof shape and roof slope was estimated to a mean absolute error of  $3.76^\circ$  when compared to 182 measured roofs.

Work was then undertaken to improve solar insolation modelling. A radiative transfer model was created that incorporated shading based on DSM data. It estimated the power output of 17 solar PV installations across four UK cities with +2.62% mean percentage error when its 2013 insolation estimates were converted to power outputs using a 0.8 performance ratio. The validation data showed that the RTS model outperformed the market-leading esri ArcMap solar radiation software which incurred a -15.97% mean percentage error. This method was then adapted to be deployable on a city scale and predicted solar insolation with a mean percentage error of -4.39% despite the process being made far more computationally efficient.

A method to estimate long-term average wind speeds for urban areas was then developed that produced results of comparable accuracy to an existing model but with considerably reduced computational demand and complexity in deployment. The mean absolute error in

wind speed estimation was just 1.75% greater using the simplified methodology than the existing model.

Finally, the improved modelling of roof geometries, solar insolation and long-term mean wind speed were brought together to evaluate the city-scale potential for solar PV and small to medium wind microgeneration. The research has shown that wind and solar PV microgeneration at sites that pay back within nine years could theoretically meet 88.5% of annual domestic electricity demand in the city of Leeds, or would be the equivalent of providing electricity to 300,319 homes. Current financial contexts were used to define a baseline scenario from which hypothetical changes to a variety of factors influencing microgeneration viability were investigated. When the costs and revenues were defined from a pessimistic, but still realistic, perspective the percentage of the study area's electricity demand that could theoretically be met by wind and solar PV microgeneration fell to 0.1%. This suggests that government policy will continue to play a key role in the future growth of UK wind and solar PV deployment.

# Contents

Chapter 1	Introduction to City-scale Microgeneration Appraisal.....	1
1.1	Research Overview .....	1
1.2	The Need for Research.....	5
1.3	Research Aims.....	6
1.4	Bibliography of Published Work.....	6
Chapter 2	The Fundamentals of Wind and Solar Electricity and Progress in City-scale Microgeneration Viability Assessment .....	8
2.1	Wind.....	8
2.1.1	Mesoscale Models .....	9
2.1.2	Computational Fluid Dynamics .....	10
2.1.3	Semi-empirical Methods.....	11
2.2	Solar PV .....	20
2.2.1	EU JRC PVGIS Solar Databases .....	23
2.2.2	Esri ArcGIS Solar Radiation Toolset.....	26
2.2.3	Roof Geometry Modelling.....	28
2.3	City-scale Studies of Microgeneration Viability .....	43
2.4	Datasets .....	46
2.5	Summary .....	47
Chapter 3	Solar Resource Appraisal.....	48
3.1	Solar City Indicator.....	48
3.1.1	Methodology.....	49
3.1.2	Results.....	57
3.1.3	Conclusions .....	61
3.1.4	Limitations and Scope for Further Work.....	62
3.2	Neighbouring Buildings Approach .....	63
3.2.1	Method.....	64

3.2.2	Validation and Applications .....	74
3.2.3	Conclusions .....	87
3.3	Summary .....	87
Chapter 4	Improving Solar Insolation Modelling.....	88
4.1	Criticisms of Existing Models .....	88
4.2	Method .....	89
4.2.1	Validation Data.....	91
4.2.2	Implementation of Existing Methodologies.....	92
4.3	Results and Discussion .....	93
4.3.1	Insolation Estimation Sensitivity to Shading.....	94
4.3.2	Suitability to City-Scale Applications.....	95
4.4	Summary of Validation.....	96
4.5	Adaptation for City-Scale Applications .....	96
4.6	Conclusion.....	101
Chapter 5	Wind Speed Prediction Methods for Urban Areas .....	102
5.1	Implementation Issues Related to the Method of Millward-Hopkins et al. ....	102
5.2	Development of a Simplified Wind Speed Estimation Methodology .....	103
5.2.1	Displacement Height.....	103
5.2.2	Surface Roughness .....	109
5.2.3	Effective Mean Building Height.....	116
5.2.4	Effective Parameters.....	117
5.2.5	Windspeed Estimation .....	119
5.3	Results and Analysis.....	120
5.3.1	Comparison of the Simplified and Millward-Hopkins et al. Models .....	120
5.3.2	Comparison of Models to Measured Wind Speeds .....	121
5.4	Conclusions .....	125
Chapter 6	Microgeneration Investment Planning .....	127
6.1	Method .....	127

6.1.1	Resource Estimations.....	127
6.1.2	Viability .....	129
6.1.3	Scenario Testing.....	143
6.2	Results and Analysis.....	147
6.2.1	Baseline Scenario .....	147
6.2.2	Scenarios .....	158
6.3	Conclusions .....	164
Chapter 7	Final Discussion and Conclusions.....	166
7.1	Research Summary .....	166
7.2	Results and Implications .....	166
7.3	Limitations and Further work .....	169
7.4	UK Solar PV and Wind Microgeneration in Perspective .....	172

## List of Tables

Table 2-1 The RANSAC process (adapted from Nguyen et al. (2005)).....	34
Table 2-2 Roof classification by SVM (adapted from Henn et al. (2013)).....	40
Table 2-3 rjMCMC algorithm as applied in Huang et al. (2011) and Huang et al. (2013).....	41
Table 2-4 Summary of data sources.....	47
Table 3-1 Proportion of daylight hours for which there is direct sunlight from Met Office (2012a) Met Office data and the output weather factor for each of the seven selected cities .....	51
Table 3-2 Costs, revenues and their sources as of 09/11/2012 .....	53
Table 3-3 Solar PV panel prices as of 14/12/2012 .....	54
Table 3-4 Approximate solar PV panel and installation costs as of 14/12/2012. Developed by linear interpolation from quotes by Anesco (2012) .....	54
Table 3-5 Total and household electricity consumption 2009 data (DECC, 2009) .....	55
Table 3-6 Feed-in Tariff Rates prior to 03/03/2012 (DECC, 2012).....	55
Table 3-7 Influencing socio-economic factors identified from the literature for the uptake of solar PV. ....	56
Table 3-8 Model output for similarity groups of neighbourhood 364.....	78
Table 3-9 Shape matching success in seven tested neighbourhoods.....	79
Table 3-10 MAE in slope prediction of 169 buildings from a range of test neighbourhoods	81
Table 3-11 Comparison of modelling gabled roof slopes using building footprint defined MATLAB® robustfit regression on individual and combined data (top) against $\beta_{g-MB}$ (bottom).....	82
Table 3-12 Comparison of slope modelling when buildings were considered individually and when combined. * denotes instances where building shape was incorrectly modelled and did not return an angle for the hipped section of the long-hipped roof template .....	83
Table 3-13 Difference in EU JRC annual PV power output estimations with changing slope	85
Table 3-14 Effect of roof shape modelling on annual power output predictions .....	86
Table 4-1 Average performance of all three models and RTS-CS under both the 0.8 and 0.75 PR. ....	97
Table 5-1 Gradients of linear regressions as previously reported by Millward-Hopkins et al. (2013b) and as found in the present study.....	105
Table 5-3 Secondary TTP coefficients to describe trends in the coefficients of TTP polynomial equations for each $\lambda_p + \sigma_n/h_m$ bin $\leq 0.97$ . ....	112



Table 5-4 Validation site characteristics .....	121
Table 5-5 MAPE of each model in comparison to measured wind speeds.....	122
Table 6-1 Costs and revenue streams for the wind viability analysis.....	137
Table 6-2 Quotes for total cost of solar PV systems. <sup>a</sup> (Platt, 2016b) <sup>b</sup> (Roberts, 2016).....	140
Table 6-3 Summary of FiT rates applicable for 1 <sup>st</sup> January 2016 (ofgem, 2015) .....	141
Table 6-4 Three scenario Conditions .....	142
Table 6-5 Variable definitions for scenario testing.....	143
Table 6-6 Production from all financially viable turbines (paying back within 9 years) across the study area .....	156
Table 6-7 Total theoretically viable production from Solar PV sites that pay back within 9 years.....	157
Table 6-8 Total electricity generation under the baseline scenario from wind and solar PV installations that pay back in under 9 years across the study area .....	157

## List of Figures

Figure 1-1 UK Solar PV Installed Capacity December 2009 to August 2015 (DECC, 2015d)....	3
Figure 1-2 Growth of installed PV capacity per capita across Western Europe from 2009 to 2014. Data from IEA-PVPS annual reports (IEA-PVPS, 2015).....	4
Figure 2-1 The development of the UBL and various sublayers (Best et al., 2008).....	12
Figure 2-2 Airborne LiDAR data generation (Bureau of Economic Geology (2009)) .....	14
Figure 2-3 Illustration of the basic geometric measures: $A_p$ , $A_f$ and $A_T$ .....	16
Figure 2-4 Millward-Hopkins et al. (Millward-Hopkins et al., 2011) method of estimating $d$ using height regimes. Adapted from figure 8 of Millward-Hopkins et al. (2011).....	16
Figure 2-5 Summary of the Met Office mean wind speed prediction method (Weekes, 2014) .....	18
Figure 2-6 The p-n junction as described in Crook (2012) .....	21
Figure 2-7 Fluctuation of $G_{0d}$ with Julian day and latitude from Scharmer and Grief (2000) .....	25
Figure 2-8 A: Example viewshed model in which parts of the sky that are obstructed from view are shown in black. B: A sky map. C: A sun map for 53.8° latitude.....	27
Figure 2-9 Plan view of a building with two distinct roof types: hipped (1) and flat (2) .....	36
Figure 2-10 Segmentation of building to primitives using major façades. ....	36
Figure 2-11 Library of roof primitives (Lafarge et al., 2010).....	37
Figure 2-12 A 'jump routine' defined in Huang et al. (2013) for switching between primitive roof templates .....	42
Figure 3-1 Locations of the seven selected cities .....	49
Figure 3-2 Theoretical limit to percentage of electricity demand met by all properties .....	58
Figure 3-3 Percentage of total electricity demand met from all installations to pay back within 15 years under baseline scenario .....	59
Figure 3-4: Individual indicators of potential to install solar PV for each city.....	60
Figure 3-5: Correlation between socio-economic indicator values and installed PV per capita (as of December 2012) for each city.....	60
Figure 3-6 The Solar City Indicator values incorporating physical and socio-economic factors .....	61
Figure 3-7 Segmentation process from concave angles. A: Two concave angles circled. B: Creation of intersection lines from a concave angle and identification of an intersection point (denoted by cross) on the shortest. C: Final segmented shape after intersection process repeated for the second concave angle.....	66

Figure 3-8 A: Original footprint. B: Longest pair of lines to form a right angle (bold line). C: Large rectangle (dotted lines) formed from the longest right-angled lines. Also shows iterative expansion of a new, inner rectangle along width of large rectangle. D: Second expansion along length of large rectangle. E & F: Repetition of expansion process (length first). G: Larger shape created by the two expansions (in grey) accepted as main roof part of original footprint.....	67
Figure 3-9 Polygon (black outline) containing interior angles not approximately 90° or 270° and without right-angled vertices in common with the final desired segmented polygon (grey rectangle).....	68
Figure 3-10 Segmentation of building footprint data (left) across a neighbourhood to extract major roof parts (right) in neighbourhood 690.....	69
Figure 3-11 Similarity thresholds. The small, solid white rectangles have the shortest length and width of the bin to which the building footprint (dotted white line) is a member. The larger, solid white-lined rectangle has the longest length and width of this bin. ....	69
Figure 3-12 Data rotation and combination procedure.....	71
Figure 3-13 A-C: Rotated DSM data for three similar gable buildings prior to combination viewed from the y, z perspective. D: Combined data following height normalisation, outlier identification and ridge repositioning processes.....	72
Figure 3-14 The roof template library.....	73
Figure 3-15 The four regions of a hipped template. 1 and 3: hip sections. 2 and 4: gable sections .....	73
Figure 3-16 Four of the neighbourhoods tested using the methodology where the white lines represent the building footprint data prior to segmentation .....	76
Figure 3-17 Neighbourhood 364 labelled by similarity grouping identification numbers ....	77
Figure 3-18 Modelled and observed orientation for neighbourhood 364. Line denotes a 1:1 relationship .....	79
Figure 3-19 Changes in $\Delta_z$ when data from an increasing number of buildings is combined. The correct template is hipped.....	80
Figure 3-20 Slope accuracy improvement when using combined DSM data from increasing numbers of buildings. Legend items refer to neighbourhood IDs.....	84
Figure 3-21 EU JRC PVGIS estimated annual PV power output for a 2.2kWp installation with optimised azimuth under a range of slope conditions .....	85
Figure 3-22 Effect of modelled roof shape on area available for solar technologies.....	86

Figure 4-1 Orientation (A), slope (B), system size (C) and power output for 2013 (D) attributes of validation sites .....	92
Figure 4-2 Percentage error of annual global radiation estimation for all three methodologies under both PRs.....	93
Figure 4-3 Mean Absolute % Error in annual global radiation estimation with and without shading under both performance ratios.....	95
Figure 4-4 Relationship between RTS and RTS-CS models for all validation sites under the 0.8 PR .....	97
Figure 4-5 Comparison of RTS model with city-scale deployment adaptations to all other models.....	98
Figure 4-6 Annual solar insolation at a large building using RTS-CS .....	98
Figure 4-7 Annual solar insolation at small buildings using RTS-CS.....	99
Figure 4-8 Slope and orientation of small properties across a study area containing Leeds (UK), coloured by insolation ( $\text{kWh m}^{-2} \text{a}^{-1}$ ).....	99
Figure 5-1 $h_m$ (top) and $d$ (bottom) across the Leeds study area. Larger values are observed in more built-up areas for both attributes.....	103
Figure 5-2 Displacement height calculated by Millward-Hopkins et al. (2013a) ( $d_{JMH}/h_m$ ) and Macdonald et al. (1998) ( $d_u/h_m$ ) methodologies from DEM data for three cities.....	104
Figure 5-3 Relationship between Macdonald et al. (1998) displacement height ( $d_u$ ), Millward-Hopkins et al. (2013a) displacement height ( $d_{JMH}$ ) and the normalised standard deviation of heights ( $\sigma_h/h_m$ ) as plan-area density ( $\lambda_p$ ) increases. Solid lines denote a linear regression of the data in the present study whilst dashed lines represent the linear regressions presented in Millward-Hopkins et al. (2013b). .....	104
Figure 5-4 Displacement height under the Millward-Hopkins et al. (2013a) ( $d_{local-JMH}/h_m$ ) and the simplified model ( $d_{local-simplified}/h_m$ ). Line denotes a 1:1 relationship .....	106
Figure 5-5 Comparison of simplified displacement height calculations to reference values from Grimmond and Oke (1999a).....	107
Figure 5-6 Comparison of modelled $d/h_m$ to wind tunnel experimental data from Cheng and Castro (2002b) (red), Zaki et al. (2011a) (purple) and Hagishima et al. (2009) (amber) .....	108
Figure 5-7 Arrangement of obstructions to the flow in Zaki et al. (2011) .....	108
Figure 5-8 $z_{0-JMH}$ across the study area for a southerly wind direction .....	109
Figure 5-9 Surface roughness as per the Millward-Hopkins et al. (2013a) ( $z_{0-JMH}/h_m$ ) and Macdonald et al. (1998) ( $z_{0u}/h_m$ ) models. Line denotes a 1:1 relationship. ....	109

Figure 5-10 Absolute difference between $z_{0-JMH}/h_m$ and $z_{0u}/h_m$ with respect to $\lambda_p$ coloured by $\sigma_h/h_m$ (A). B shows the relationship of $z_{0-JMH}/h_m$ and $z_{0u}/h_m$ coloured by $\sigma_h/h_m + \lambda_p$ where the line denotes a 1:1 relationship. ....	110
Figure 5-11 $z_{0-JMH}/h_m$ and $z_{0u}/h_m$ for $0.33 < \sigma_h/h_m + \lambda_p < 0.37$ . Line denotes the fitted polynomial trend.....	111
Figure 5-12 Coefficients of the TTP fitted curves of each $< \sigma_h/h_m + \lambda_p$ bin (A) and with secondary TTP curves fitted to the data for $\sigma_h/h_m + \lambda_p \leq 0.97$ (B).....	112
Figure 5-13 Normalised predictions of $z_0/h_m$ under the full JMH method ( $z_{0-JMH}/h_m$ ) and the simplified methodology ( $z_{0-simplified}/h_m$ ) for one wind direction (left) and all directions (right). Lines denote 1:1 relationships. ....	114
Figure 5-14 Comparison of predicted $z_{0-simplified}$ to reference values from Grimmond and Oke (1999a).....	114
Figure 5-15 Comparison of modelled $z_0/h_m$ (green) for one wind direction in the city of Leeds to wind tunnel observations by Cheng and Castro (2002b) (red), Zaki et al. (2011a) (purple) and Hagishima et al. (2009) (amber). ....	115
Figure 5-16 $h_{m-eff-JMH}$ across the study area for a northerly wind direction.....	116
Figure 5-17 Relationship between $\sigma_h$ and $h_{m-eff-JMH}$ (A) and the correlation of $h_{m-eff-simplified}$ to $h_{m-eff-JMH}$ (B) in which the line denotes a 1:1 relationship.....	116
Figure 5-18 Wind sectors extending 5 km in North, East, South and West compass directions from the neighbourhood containing the target site (red box) .....	117
Figure 5-19 Effective parameters compared to Millward-Hopkins et al. (2011) values. Lines denote 1:1 relationships .....	118
Figure 5-20 Comparison of simplified and JMH methodology windspeed simulations at 20 m above ground (A and C) and 10 m above $h_m$ (B and D).....	120
Figure 5-21 Performance of all four models at all sites against measured wind speeds ....	122
Figure 5-22 Performance of all four models. The Macdonald model plus sign represents an outlier data point. ....	123
Figure 6-1 Long-term mean wind speed ( $m s^{-1}$ ) at 36 m above ground for every neighbourhood across Leeds .....	127
Figure 6-2 Histogram of long term average wind speeds ( $ms^{-1}$ ) at 36 m (A) and 20 m (B) above ground for each 250 m x 250 m neighbourhood across the study area.....	128
Figure 6-3 Process chart for wind viability assessment .....	129
Figure 6-4 Locations that meet the criteria regarding distance from residences. The Kingspan KW15 is suitable for all locations where a WindEn 45kW turbine is.....	131

Figure 6-5 Weibull distributions from minimum, maximum and median long term average wind speeds modelled for 36 m above ground-level using the method described in section 5.2 and restricted by the criteria presented in section 6.1.2.1.1 .....	132
Figure 6-6 Power curves for the WindEn 45 and Kingspan KW15 turbines (BetterGeneration, 2015) .....	133
Figure 6-7 Histograms of annual power output (MWh a <sup>-1</sup> ) for both turbines in first year of operation at suitable locations in which frequency refers to the number of each turbine	134
Figure 6-8 Power output (MWh a <sup>-1</sup> ) for the Kingspan KW 15 (top) and WindEn 45kW (bottom) turbines in suitable locations in first year of operation.....	135
Figure 6-9 Process chart for solar PV viability assessment using the same key as Figure 6-3 .....	139
Figure 6-10 Interpolated PV array costs from Table 6-2 to 55 kWp .....	140
Figure 6-11 Payback times for selected turbines under the baseline scenario. A: WindEn 45kW, B: Kingspan KW15. C: Kingspan KW15 for all locations where payback is less than 20 years. The dotted line in B denotes 20 years, the lifespan of the FiT.....	147
Figure 6-12 Annual ROI for most and least optimal sites (left) and distribution of ROI across all sites for year 4, 8, 12, 16 and 20 (right). .....	148
Figure 6-13 Annual ROI for Kingspan KW15 at most and least optimal sites (left) and distribution of ROI across all sites for year 4, 8 12, 16 and 20 (right). In the boxplots, the bottom and top whiskers denote the 5 <sup>th</sup> and 95 <sup>th</sup> percentiles, the bottom and top edges of the rectangles represent the 25 <sup>th</sup> and 75 <sup>th</sup> percentiles and the central line is the median. The plus signs are outliers. ....	149
Figure 6-14 Payback times and system sizes for all viable installations .....	149
Figure 6-15 Payback time and system size in the baseline scenario FiT bandings. The boxes, whiskers and outlier dots represent the data in the same way as used in the rest of the thesis .....	150
Figure 6-16 20 year ROI for all sizes of solar PV installation.....	151
Figure 6-17 Sensitivity of payback time to percentage of generated electricity used on site .....	151
Figure 6-18 Past and predicted costs of batteries (Mathiesen, 2015).....	152
Figure 6-19 Annual electricity production (MWh a <sup>-1</sup> ) of both selected turbines at all spatially suitable sites for the first year of operation .....	153
Figure 6-20 Payback Times for Kingspsan KW15 across all time (A) and for less than 20 years only (B) and WindEn 45KW (C) turbines with different usage rates .....	154

Figure 6-21 Geospatial distribution of turbines that meet the 9 year payback criterion and their annual electricity production ( $\text{MWh a}^{-1}$ ) .....	155
Figure 6-22 Payback times for the Kingspan KW15 (A) and the WindEn 45 kW (B) turbines under all scenarios .....	159
Figure 6-23 Payback times under the baseline and scenario conditions.....	160
Figure 6-24 First year production (as a percentage of electricity demand in the study area) from wind turbines (A), solar panels (B) and both technologies (C) in each scenario as “acceptable” payback time increases .....	162
Figure 7-1 Percentage contribution of renewables to annual UK energy generation using data from (DECC, 2016a). Dotted line represents the 15% of energy generation from renewables target by 2020 .....	172
Figure 7-2 LCOE ( $\$/\text{MWh}$ ) of solar PV and onshore wind technologies in developed country markets for 2010 and 2015 (IEA-PVPS, 2015) .....	173
Figure 7-3 LCOE ( $\$/\text{MWh}$ ) for solar PV technology types.....	173

## Glossary of Terms and Symbols

CAPEX	Capital Expenditure
CCC	Committee on Climate Change
CFD	Computational Fluid Dynamics
DECC	Department for Energy and Climate Change
DEM	Digital Elevation Model
DSM	Digital Surface Model
EPC	Environmental Performance Certificate
ESRA	European Solar Radiation Atlas
EU JRC PVGIS	European Union Joint Research Council Photovoltaics Geographical Information System
FiT	Feed-in Tariff
GIS	Geographical Information Systems
IEA	International Energy Agency
LCC	Leeds City Council
LCOE	Levelised Cost of Electricity
LIDAR	Light Detection And Ranging
MAE	Mean Absolute Error
MAPE	Mean Absolute Percentage Error
MCS	Microgeneration Certification Scheme
NCIC	National Climate Information Centre
NOABL	Numerical Objective Analysis of Boundary Layer
NREL	National Renewable Energy Laboratory (US)
OPEX	Operating Expenditure
PR	Performance Ratio
PV	Photovoltaic
RAM	Random Access Memory
RMSPE	Root Mean Square Percentage Error
ROI	Return On Investment
RTS	Radiative Transfer with Shading
RTS-CS	Radiative Transfer with Shading – City-scale
SCI	Solar City Indicator

### Roof Geometry Modelling:

$\hat{\beta}_{g-RB}$	Modelled gable facet slope under robust fit method (°)
$\hat{\beta}_{g-MB}$	Modelled gable facet slope under neighbouring buildings method (°)
$\beta_g$	Observed gable roof facet slope (°)
$\hat{\beta}_{g-IND}$	Modelled roof facet slope under individual buildings method (°)
$\beta_h$	Observed hip section roof facet slope (°)



$\hat{\beta}_{h-MB}$	Modelled hip section facet slope under multiple buildings method (°)
$\hat{\beta}_{h-IND}$	Modelled hip section facet slope under individual buildings method (°)
$\Delta_z$	z-error metric for roof template selection
$K$	Total number of data points in combined data
$Z_m$	Model-derived height above eave-level (m)
$Z_d$	Height above eave-level of combined data (m)

### Solar Insolation Modelling:

#### *All models*

$E$	Global horizontal irradiance (Wh m <sup>-2</sup> )
$E_s$	Global irradiance on a tilted plane (Wh m <sup>-2</sup> )
$I_B$	Direct horizontal irradiance (W m <sup>-2</sup> )
$I_D$	Diffuse horizontal irradiance (W m <sup>-2</sup> )
$I_R$	Ground-reflected irradiance (W m <sup>-2</sup> )
$\hat{I}_T$	Modelled annual global irradiance (Wh m <sup>-2</sup> )
$I_T$	Observed annual global irradiance (Wh m <sup>-2</sup> )
$\phi$	Azimuthal direction (°)
$\theta$	Polar direction angle of incidence (°)
$\rho$	Albedo of surrounding terrain
$R_d$	Diffuse transposition factor
$R_r$	Ground reflection transposition factor
$s$	Tilt of plane (°)

#### *Sharmer and Grief (2000) model*

$B_C$	Direct horizontal irradiance (W m <sup>-2</sup> )
$D_d$	Daily sky diffuse irradiation (Wh m <sup>-2</sup> )
$G_d$	Observed daily global irradiation (Wh m <sup>-2</sup> )
$G_{0d}$	Daily irradiance falling on a horizontal plane outside the atmosphere (Wh m <sup>-2</sup> )
$H_R$	Reference altitude to calculate $(p/p_0)$ . Equal to 8400 m.
$I_C$	Clear sky direct irradiance normal to the beam (W m <sup>-2</sup> )
$KT_d$	Clearness Index
$m$	Relative optical air mass
$(p/p_0)$	Atmospheric pressure correction for altitude
$(\sigma_d)_m$	Monthly mean relative sunshine duration
$T_{LK}$	Linke turbidity factor

$\gamma_S$  Solar altitude angle (°)

*Fu and Rich (2000) model*

$\beta^{m(\theta)}$	Transmittivity of the atmosphere. Where $m(\theta)$ is the optical air mass for the polar direction
$Diff_{\theta,\phi}$	Diffuse radiation ( $W\ m^{-2}$ )
$Dir_{\theta,\alpha}$	Direct (beam) radiation ( $W\ m^{-2}$ )
$Dur$	The duration that diffuse radiation is analysed for (Hours)
$P_{dif}$	Proportion of global normal radiation flux that is diffuse
$R_{glb}$	Global normal radiation ( $W\ m^{-2}$ )
$S_{const}$	Solar constant ( $1367\ W\ m^{-2}$ )
$SkyGap_{\theta,\phi}$	The fraction of the sky diffuse radiation is analysed for
$SunDur_{\theta,\alpha}$	The duration the Sun is in a specific part of the sky
$SunGap_{\theta,\alpha}$	The fraction of the sky sectioned to calculate $SunDur_{\theta,\alpha}$
$Weight_{\theta,\phi}$	The proportion of diffuse radiation originating from a given $SkyGap_{\theta,\phi}$

*Radiative Transfer with Shading Model*

$\alpha_p$	Panel azimuth angle (°)
$\beta$	Panel tilt angle (°)
$F$	Adjusted total downwelling horizontal irradiance due to horizon shading ( $W\ m^{-2}$ )
$f_{ij}$	Sky view fraction
$I_B$	Direct horizontal irradiance ( $W\ m^{-2}$ )
$I_D$	Diffuse horizontal irradiance ( $W\ m^{-2}$ )
$I_R$	Ground-reflected irradiance ( $W\ m^{-2}$ )
$L$	Ground level radiance field
$\theta_z$	Solar zenith angle (°)
$\theta_i$	Solar incidence angle (°)
$W_{ij}$	Spherical geometry weighting

**Long term average wind speed Modelling:**

$A_f^*$	Unsheltered frontal area of obstructions to the wind ( $m^2$ )
$A_T$	Ground area associated with the surface elements contributing to $A_f^*$ ( $m^2$ )

$C_D$	The depth integrated drag coefficient (for bluff bodies)
$d$	Zero-plane displacement height (m)
$d_{eff}$	Zero-plane displacement height in the fetch area (m)
$d_{eff-simplified}$	Zero-plane displacement height in the fetch area under a simplified methodology (m)
$d_{eff-JMH}$	Zero-plane displacement height in the fetch area as per Millward-Hopkins et al. (2013a) (m)
$d_{hi}$	Zero-plane displacement height for an individual height regime (m)
$d_{JMH}$	Zero-plane displacement height as per Millward-Hopkins et al. (2013a) (m)
$d_{local-simplified}$	Zero-plane displacement height using a simplified methodology (m)
$d_u$	Macdonald (2000) expression for zero-plane displacement height of uniform arrays (m)
$h_m$	Mean building height (m)
$h_{m-eff}$	Effective mean building height (m)
$h_{m-eff-eff}$	Effective mean building height in the fetch area (m)
$h_{m-eff-eff-JMH}$	Effective mean building height in the fetch area as per Millward-Hopkins et al. (2013a) (m)
$h_{m-eff-eff-simplified}$	Effective mean building height in the fetch area under a simplified methodology (m)
$h_{m-eff-JMH}$	Effective mean building height as per Millward-Hopkins et al. (2013a) (m)
$h_{m-eff-simplified}$	Effective mean building height under a simplified methodology (m)
$\kappa$	von Kármán constant ( $\approx 0.4$ )
$\lambda_p$	Ratio of building plan area to ground surface area (plan area density)
$\lambda_f$	Ratio of total building frontal areas to $A_T$ (frontal area density)
$\lambda_{p-eff}$	Plan area density without the contribution of sheltered blocks in a neighbourhood
$\sigma_h$	Standard deviation of building heights (m)
$u_*$	Frictional velocity ( $\text{ms}^{-1}$ )
$\bar{U}_z$	Long term average wind speed ( $\text{ms}^{-1}$ )
$Z$	Height above surface (m)
$z_0$	Surface roughness length (m)
$z_{0-eff}$	Surface roughness length in the fetch area (m)
$z_{0-eff-JMH}$	Surface roughness length in the fetch as per Millward-Hopkins et al. (2013a) (m)

$z_{0-eff-simplified}$	Surface roughness length in the fetch area under a simplified methodology (m)
$z_{0-local-simplified}$	Surface roughness length using a simplified methodology (m)
$z_{0-JMH}$	Surface roughness length as per Millward-Hopkins et al. (2013a) (m)
$z_{0u}$	Macdonald (2000) expression for surface roughness length of uniform arrays (m)

#### Wind Turbine Power Output Modelling:

$\beta$	Weibull distribution shape parameter
$f(u)$	Weibull frequency distribution of wind speeds
$\eta$	Weibull distribution scale parameter
$p(u)$	Power output at wind speed $u$

## **Chapter 1 Introduction to City-scale Microgeneration Appraisal**

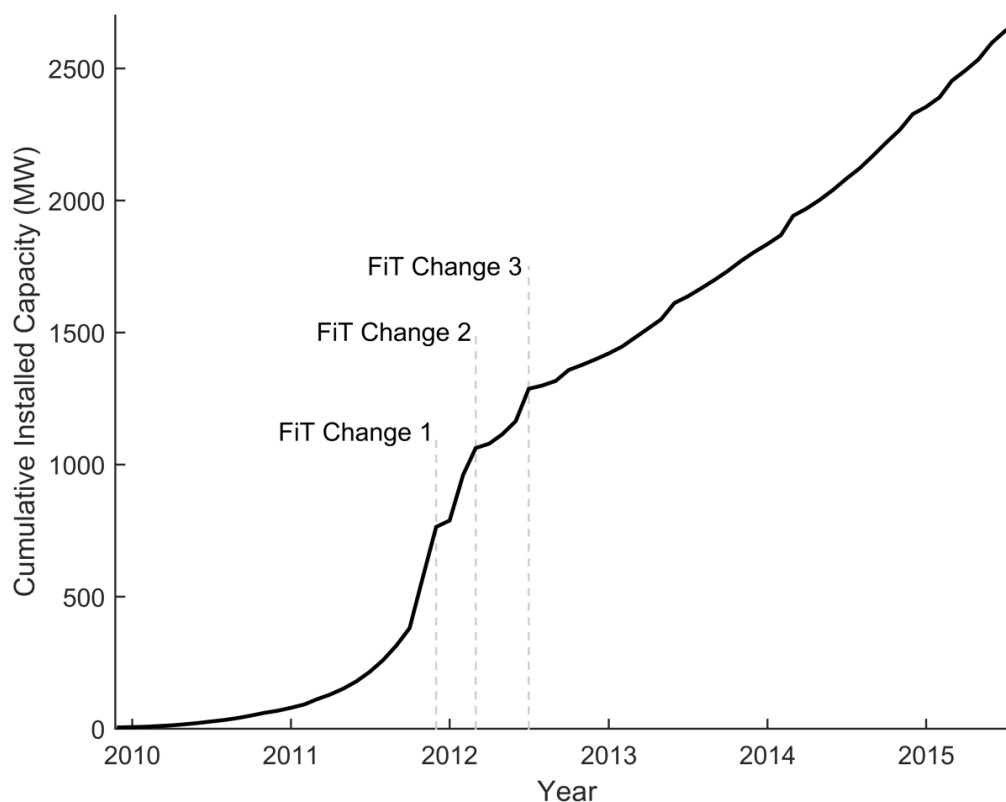
### **1.1 Research Overview**

Almost a decade has passed since the publication of The Stern Review which stated that evidence of climate change was overwhelming and demanded an urgent response (Stern and Treasury, 2007). Lord Stern (2007) stated that attitudes and investment over the coming decades would profoundly influence the future climate and stated that there could be dire consequences from inaction, warning of major disruption to economic and social activity on a scale similar to those associated with the great wars and the 1920's economic depression. The review identified climate change as a cause of market failure due to the environment and environmental services being regarded as an unquantifiable externality to global economies. It led to the 2008 UK Climate Change Act that introduced numerous initiatives that sought to accelerate the growth of renewable energy deployment in the UK. Most importantly, the Act defined a target to reduce UK greenhouse gas emissions by 80% against 1990 baseline data (Climate Change Act, 2008); a binding target that has helped to focus the efforts of policy makers across many sectors of government to reduce emissions. The Act also created a new carbon budgeting system whereby successive four-year strategies assess progress towards meeting emissions reductions targets and layout plans for the following four years (Climate Change Act, 2008). In this way the targets would maintain their prevalence in the policy arena which would be further protected by the Climate Change Act's creation of the Committee on Climate Change (CCC), an independent, statutory body to advise the UK Government on climate change matters (CCC, 2015).

In the same year the Climate Change Act passed to law, the Energy Act received royal assent and brought the Feed in Tariff (FiT) mechanism to the UK (Energy Act, 2008). FiTs had proven successful at encouraging the uptake of small-scale generation of renewable electricity in other European countries such as Germany (Barker, 2013). The FiT mechanism rewards small-scale generators of renewable electricity with payments scaled relative to power output which the government supplements with a flat rate export tariff (DECC, 2013a). Therefore, solar and wind technologies can generate revenue for their owners in addition to providing electricity at substantially lower greenhouse gas emissions than traditionally available from the national grid (Bush et al., 2014; Goe and Gaustad, 2014). However, not all wind and solar systems are eligible for these incentives because the government has also introduced the Microgeneration Certification Scheme (MCS) to protect consumers from

misleading claims about performance from manufacturers. This system ensures that the technologies have been tested to specific standards to guard against bogus claims.

The commitments made in the Energy Act were reaffirmed in 2011 by the then newly elected government's 'Carbon Plan' (DECC, 2011). However, the most recent developments in policy have undermined confidence in the UK government's commitment to reducing greenhouse gases (Harrabin, 2015). The government has announced cuts in subsidies to large onshore wind (Rudd, 2015), commercial solar (Truss, 2014) and industrial biomass burning (DECC, 2015b). In addition, the Green Deal, a scheme to provide housing with improved insulation, has been withdrawn (DECC, 2015c) and no replacement mechanism has been offered. A significant delay on legislation to ensure house builders move towards zero-carbon buildings (Harvey, 2013) and reduced taxation on polluting industries (Harrabin, 2015) have further emphasised a direction in policy that is less supportive of CO<sub>2</sub> reduction. Furthermore, the Climate Change Levy has been extended to the renewables industry (Macalister and Vaughan, 2015), penalising the very companies it was designed to promote. Then, in 2016, the decision was made to close DECC completely and move its responsibilities to the Department of Business, Energy and Industrial Strategy (Harrabin, 2016a). Although too early to assess the consequences to climate related policies, the halving of cabinet ministers with an environmental brief (Huhne, 2016 in Vaughan (2016a)) and the symbolism of removing a department dedicated to tackling climate change has led many environment-focused institutions to conclude that climate change has been significantly de-prioritised (Friends of the Earth, 2016; Clark and Ward, 2016). Set against such a shifting policy context that can be interpreted as increasingly disinterested in the support of renewable energy, it is interesting to note the continued growth of the UK renewable energy industry and its success in delivering renewable capacity. Specifically, solar and wind microgeneration has now demonstrated substantial potential to become a significant contributor to the UK's energy mix and could yet go on to form an important part of meeting the UK's 15% renewable energy by 2020 target set by the European Commission (DECC, 2013b). Of the microgeneration technologies available, solar photovoltaics (PV) has shown the most potential to meet energy demand. At the end of June 2016, UK installed capacity from registered installations (of less than 50 kW) was 4.31 GW from a total of 866,473 sites (DECC, 2016b). To put the present capacity of UK solar PV into a more relatable context, the electricity it generated exceeded that generated by coal for the first time in April 2016 (Vaughan, 2016b).



**Figure 1-1 UK Solar PV Installed Capacity December 2009 to August 2015 (DECC, 2015d)**

The growth of solar PV installed capacity since December 2009 to August 2015, shown in Figure 1-1, features particularly rapid increases prior to government adjustments to the FiT but becomes steadier and more predictable following FiT Change 3. To place the growth of the industry across recent years in an appropriate context, Figure 1-2 presents a map of International Energy Agency (IEA) data to show that PV deployment in the UK is not the most impressive among countries with similar economies despite its promising growth. It is clear that Germany has built a very strong solar PV microgeneration industry and that Ireland has performed especially poorly, achieving only 1-10 W per capita by 2014. When viewed in this context, the UK appears middle-ranking at best, but to have achieved this given the country's northerly latitudes must be regarded as success.

The small and medium wind energy market has not experienced the same growth as domestic solar PV but recent DECC statistics show installed capacity of FiT-supported wind installations contribute 585.8 MW (DECC, 2016b). Beyond the more immediately apparent factors for this, such as the greater visual intrusion of a wind turbine, there have been other obstructions to the development of wind energy microgeneration. Gipe (2013) and Marsh (2004) have made the argument that poor understanding of wind speeds in urban areas has led to the siting of turbines in locations of inadequate wind resource. Confidence in the technology as a whole has then diminished as investor expectations have not been met

(Stankovic et al., 2009). This is despite academic studies that show there are large numbers of sites in specific urban areas that offer a viable wind resource (Millward-Hopkins et al., 2013b; Drew et al., 2013; Sunderland et al., 2013).

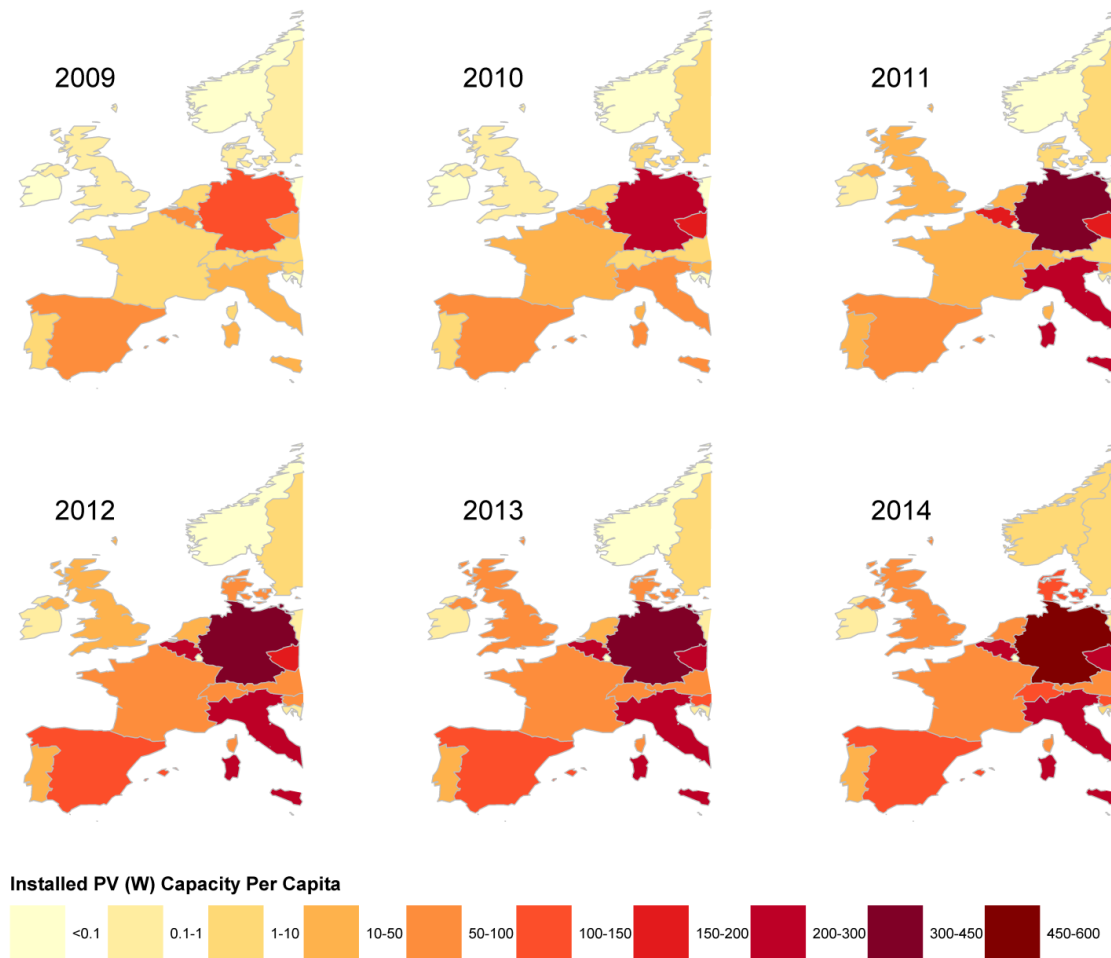


Figure 1-2 Growth of installed PV capacity per capita across Western Europe from 2009 to 2014. Data from IEA-PVPS annual reports (IEA-PVPS, 2015)

The figures for solar PV suggest that microgeneration could be a significant part of the future energy mix but it is important to understand that this would require a very large number of organisations and individuals to make a decision to invest. The US National Renewable Energy Laboratory (NREL) state that the availability of reliable, accurate, and easily accessible solar and wind energy resource data can help tackle this issue and greatly accelerate the deployment of the technologies (NREL, 2012). The methods for the provision of this resource data across broad geographical areas are now briefly discussed.

In support of its region's recent growth in microgeneration investment, Leeds City Council (LCC) commissioned AECOM, an engineering consultancy, to produce a report to establish the potential of the Yorkshire and Humber Region in 2011 (AECOM, 2011). The report identified potential resources LCC could exploit by providing a top-down estimate of the maximum economic potential for each type of renewable energy technology across Leeds.



LCC has also actively engaged with the University of Leeds to produce a report investigating the potential for the development of a low carbon local economy with specific reference to the role that microgeneration could play. 'A Low Carbon Leeds City Region' investigated the most cost effective and efficient methods to decarbonise a city using Leeds as its focus and incorporating microgeneration as one of a plethora of strategies (Gouldson et al., 2012). Further industry-led investigations have been researched on similar regional scales (JBA, 2012) but all are subject to a similar problem. In the studies described above, the physical capacity estimations are based on trends in uptake derived from complex socio-economic factors and result in highly optimistic if not unrealistic capacity estimations. For example, the AECOM study presumed that a 6 kW turbine could be installed at set distances apart regardless of building layout and wind resource. It is more beneficial, therefore, to investigate the potential for solar and wind microgeneration technologies from a bottom-up perspective, evaluating the underlying resource at every individual location across the study area to avoid the sweeping generalisations that top-down methodologies make. This is especially true given the requirement for property owners to make a decision in favour of microgeneration investment. This thesis is dedicated to explaining and enhancing the latest and most accurate methods to estimate city-scale solar and wind resources from a bottom-up perspective.

## **1.2 The Need for Research**

There are many barriers to microgeneration investment that challenge the UK industry's ability to deliver a significant contribution of renewable electricity to the grid. Limited investment capital coupled with a lack of awareness of potentially profitable projects are key barriers that are strengthened by complex and frequently changing government subsidy mechanisms (Allman et al., 2004; Kelly and Pollitt, 2011). These barriers are common to a great many cities around the world and can only be tackled with affordable advice on the technological capabilities of renewable energy systems (Bale et al., 2012) which must be built on accurate estimations of wind and solar resource.

Therefore, the development of rapidly deployable models of wind and solar resource that are accurate at individual properties and also capable of informing city-scale decision making forms the central focus of this thesis. This is made all the more important by the fact that alerting property owners to the potential benefits of microgeneration with an accurate assessment will increase the deployment of the technologies. However, individual property owners are not the only parties that may benefit from such information as large private property owners and local authorities around the world are increasingly conscious of the

need for long-term strategy in the deployment of renewable technologies across their portfolios (Bale et al., 2012). Furthermore, UK national government policy explicitly states a presumption that local authorities lead in the development of local energy generation through support to local communities, investment in local energy schemes and targeted approaches for specific subsets of public buildings, such as schools (DECC, 2014b; DECC, 2014a). With limitations to local government budgets showing no signs of easing, authorities have been, and will continue to be, forced to consider broad ranges of cost cutting and revenue raising projects with solar and wind microgeneration investment one such option.

There are then wider benefits that could be attained from accurate predictions as they could increase investor confidence in the technologies as a whole. An integrated appraisal of both wind and solar options could raise awareness of the potential for small wind amongst those previously only considering PV and protect investors from the potentially turbulent costs and incentives context of an individual technology.

### **1.3 Research Aims**

Given the barriers to the wider deployment of solar and wind microgeneration technologies and the current gaps in the literature, the primary aim of this thesis is to improve the accuracy of solar and wind resource appraisal at the city scale and to demonstrate how such tools could be used to inform investment decision making. This is achieved through the use of a case study based on the city of Leeds, UK. All models must be executable without requiring high power computing to widen the locations where they can be deployed.

### **1.4 Bibliography of Published Work**

Over the course of the research project described in this thesis, the following papers have been published or submitted:

Chapter 3:

Gooding, J., Edwards, H., Giesekam, J., Crook, R. (2013) 'Solar City Indicator: A Methodology to Predict City Level PV Installed Capacity by Combining Physical Capacity and Socio-economic Factors', *Solar Energy*, **95**, pages 325-335 DOI: 10.1016/j.solener.2013.06.027

Jacques, D.A., Gooding J., Giesekam J.J., Tomlin A.S., Crook R. (2014) 'Methodology for the assessment of PV capacity over a city region using low-resolution LiDAR data and application to the City of Leeds (UK)', *Applied Energy*, **124**, 28-34.

Gooding, J., Tomlin A.S., Crook R. (2015) 'Modelling of roof geometries from low-resolution LiDAR data for city-scale solar energy applications using a neighbouring buildings method', *Applied Energy*, **148**, Pages 93–104, DOI: 10.1016/j.apenergy.2015.03.013

Chapter 4:

Gooding, J., Smith, C.J., Crook, R., Tomlin, A.S. (2015) 'Solar Resource Estimation Using a Radiative Transfer with Shading (RTS) Model', *Proceedings of the 31st European Photovoltaic Solar Energy Conference and Exhibition*, DOI: 10.4229/EUPVSEC20152015-6AV.4.25

Chapter 5:

Gooding, J. and Tomlin, A.S. (2016) 'Simplified Methods for Estimating Aerodynamic Parameters and Wind Profiles for Height Heterogeneous Surfaces', *submitted to Wind Energy*

Chapter 6:

Adam, K., Hoolohan, V., Gooding, J., Knowland, T., Bale, C.S.E., Tomlin, A.S., (2015) "Methodologies for city-scale assessment of renewable energy generation potential to inform strategic energy infrastructure investment." *Cities*, DOI:10.1016/j.cities.2015.10.015

## Chapter 2 The Fundamentals of Wind and Solar Electricity and Progress in City-scale Microgeneration Viability Assessment

This chapter presents a discussion of the state-of-the-art in physically derived city-scale microgeneration viability assessment. To better understand the foundations of such methodologies, however, it is important to first appreciate the fundamental properties of how electricity is generated from wind and solar energy. Therefore, this chapter opens with an introduction to the properties of wind and solar energy and how the performance of technologies that convert this energy to electricity is impacted by a variety of factors. There then follows a discussion of how different approaches have been developed to evaluate the environment in which the technologies are placed, leading to the research presented in Chapter 3, Chapter 4 and Chapter 5.

Understanding the physical wind and solar resource is only one step towards predicting microgeneration viability because the financial aspects are complex and have been in fluctuation over recent years but are vitally important. So much so, a significant part of this chapter is dedicated to introducing the relevant cost and revenue streams and how the relative importance of each has changed in recent times. Understanding of the financial considerations can be improved by studying how possible future policies could shape the solar and wind microgeneration industry which is a key aim of Chapter 6. Finally, there is a brief section to summarise the key datasets that are used in the research.

### 2.1 Wind

Electricity from wind energy is generated by the kinetic energy of the wind that passes through the swept area of a rotor that turns in response to the force applied. The blade is connected to a shaft that turns a magnet inside a turbine, generating electricity. The need for accuracy in wind speed estimation for investment appraisal is increased by the cubic relationship between wind speeds ( $U$ ) and the available power in the wind described in equation (2-1) (Gipe, 2004):

$$\text{Wind Power} = 0.5\rho AU^3, \quad (2-1)$$

where  $\rho$  is the density of air and  $A$  is the swept area the wind is passing through. This relationship is caused by the kinetic energy in a particular mass ( $m$ ) of air being  $0.5mU^2$ , while the mass of air passing through a turbine's swept area in one second is  $\rho AU$ . It means that significant errors in wind power estimations can result from minor inaccuracies in predicted wind speeds. This is important because Peacock et al. (2008) stated that although

small wind turbines may offer a possible route for reducing CO<sub>2</sub> emissions, widespread investment is unlikely without an accurate method to calculate energy yield at a specific site. For sites without detailed anemometry, such as all those considered in a typical city-scale viability analysis, an intrinsic part of the energy yield estimation is a prediction of long-term average mean wind speed.

There are physical limits to the power that can be extracted from the wind and there is an absolute limit related to the mass flow rate before and after a turbine. Mass flow must remain constant on both sides of a turbine so it acts to expand the flow of air whilst also slowing the flow. The reduction in velocity is achieved by converting some of the kinetic energy of the flow to mechanical. There is, therefore, a maximum limit where the mass flow rate equilibrium of both sides of the turbine can be maintained regardless of turbine design which is defined by the power coefficient ( $C_p$ ) described in equation (2-2) (Burton, 2001).

$$C_p = \frac{\text{Generated Power}}{0.5\rho AU^3}. \quad (2-2)$$

The coefficient can be calculated using the equation above and momentum theory to define a maximum limit (the Betz limit) to the amount of power that can be extracted from the wind:

$$C_p = \frac{16}{27} = 0.593. \quad (2-3)$$

Hence it will never be possible to extract more than 59.3% of the total power in the wind. There are further physical limits on the power that may be extracted from the wind including the losses as heat or sound energy involved in converting kinetic to electrical energy, the time required for turbines to respond to changes in wind direction and the effects of turbulence in the flow. Due to these physical limits, it is found that turbines typically convert a maximum of 30% of the total energy available in the wind to electrical energy. This further emphasises the importance of accuracy in wind speed prediction. The following section seeks to describe the variety of approaches that have been devised to obtain the greatest accuracy for different scales of interest.

### 2.1.1 Mesoscale Models

Mesoscale meteorology is the study of weather systems of the synoptic scale. This means weather systems generally ranging in horizontal dimension from tens of kilometres to several hundred kilometres and its outputs interest prospective wind farm investors looking to calculate average annual wind speeds for large areas. The UK Met Office offer a product called Virtual Met Mast™ (VMM) that produces long term, site-specific wind predictions

based on their numerical synoptic-scale weather prediction model (Met Office, 2009). The key problem is that mesoscale models of this type tend to fail in urban areas and are not a suitable method for this research. For example, VMM has undergone extensive verification using 58 sites (Met Office, 2012b), however, there were no sites in dense urban settings such as those that will be found in the study areas of this research. Instead, the validation described in the report relates only to open land with different terrains and to offshore locations. In the literature, mesoscale modelling has not been applied in the context of small to medium wind turbines in urban areas. These types of models can be used to define the boundary conditions for models that incorporate a more detailed representation of the complex surfaces that exist in urban areas but are not, by themselves, the most appropriate model for the scales of interest to this research.

### **2.1.2 Computational Fluid Dynamics**

Computational Fluid Dynamics (CFD) is a field of research dedicated to solving the equations of momentum using powerful computer simulations. CFD holds the potential to advance wind energy resource assessments for complex urban areas as it seeks to accurately model wind circulation processes around complex obstacles. The main reason for not selecting mesoscale modelling for this research was that the geometry in urban areas is significantly more complex than in open rural spaces and has a critical influence on wind flow at the scales relevant to small and micro-wind installations in urban areas. Therefore, the possibility that CFD may be able to accurately account for such obstacles marks it out as a field worthy of further investigation. Kalmikov (2010) presents a simulation of the complex wind flows of urban areas using a model called *UrbaWind* to solve Reynolds Averaged Navier-Stokes (RANS) equations with a method which allows for representation of the turbulence and wakes around buildings. The study focused on a campus scale of roughly 1.5km by 3km situated in an urban area and was carried out to optimally site a single small turbine. This demonstrates the different aims and scales of a CFD study to this research as only two sites were investigated in contrast to the many thousands of sites that are to be investigated in this research, even in a small city.

By contrast, a larger section of a city is investigated in a study by the San Francisco Department of the Environment (2007). A combination of two approaches is used in which a simplified 3D reconstructed model of the city-centre is run through the established wind flow analysis software ANSYS Fluent, whilst buildings to the outskirts of the city centre and suburbs are modelled as roughness elements of the surface as they have less individual influence on flow. A big problem in looking to apply this methodology, or any CFD simulation,

is that the city-centre of San Francisco had a high resolution city-centre 3D building model of a quality that may be difficult to source for many cities given presently available data. If the 3D building model on which the CFD calculations are based is of the resolution that is available publicly, the wind speed estimations will be unreliable. However the key reason for not taking a CFD approach to this research is the requirement for considerable computing power and time to complete and validate just one city-scale study; let alone many studies in a rapid manner. Furthermore, in all studies there is still the requirement to develop a wealth of physical wind speed measurements in order to set up the boundary conditions that CFD models are particularly sensitive to and to validate the predicted wind speeds (Rodrigo, 2010; Kalmikov, 2010; San Francisco Department of the Environment, 2007). This represents a considerable increase in the cost and time required to generate the wind speed predictions as well as further increasing the computational demand and is another reason why CFD will not be taken further in this research project. Whilst deployment at the city scale might be impracticable, CFD models have been shown to accurately model flows at the individual building scale (Castro et al., 2006; Lim et al., 2009; Cheng et al., 2007). The findings from these CFD models can be used to develop less computationally intensive methods to estimate the influence of the surface on the flow, such as in the estimation of wake lengths caused by cuboid obstructions, for example.

### **2.1.3 Semi-empirical Methods**

Predicting wind speeds without having to build an extensive database of physical measurements saves considerable costs in a wide variety of instances which would remove one of the barriers to small-scale wind energy investment. In city-scale wind feasibility studies, it is entirely impractical to measure wind speeds at every potential site or run CFD simulations and mesoscale modelling techniques do not accurately reflect the changes to flow caused by urban areas but there is another route to creating a city-scale wind resource map. The following section describes how a wind speed prediction can be made using the logarithmic wind profile equation, a reference wind speed and an understanding of the surface over which the wind has travelled, thus avoiding the need for impractical or costly physical measurements or CFD simulations. Semi-empirical methodologies achieve this through mathematical adaptations to reference wind speed databases such as Numerical Objective Analysis of Boundary Layer (NOABL) (BWEA, 2012) or the Met Office NCIC following the rules of boundary layer physics. The databases consist of mean wind speeds at a height of 10 m above ground level, estimated over 1 km grid squares using geostatistical

interpolation from observations made over a period of years. For NOABL, this collection period is ten years whilst NCIC has a thirty-year collection period (Weekes, 2014).

A boundary layer forms when the surface over which the wind flows changes significantly, such as at the outer periphery of a city (see Figure 2-1). In this region, friction at the surface leads to slower wind speeds downwind of the surface obstructions and an urban boundary layer (UBL) between altered and unaltered flow begins to form on the outskirts of urban areas which commonly reaches heights of 500-1,000 m (Britter and Hanna, 2003). The bottom half of the UBL, approximately 100 to 200 m (Britter and Hanna, 2003), is referred to as the Surface Layer (SL) which has a further two sublayers within it, namely: the inertial sublayer (ISL) and the roughness sublayer (RSL). The unifying feature of the two sublayers is that they are strongly affected by obstructions on the surface with the RSL's highly heterogeneous flow being predominantly controlled by local surface geometry. For this reason, SL wind flows are commonly modelled using simplified geometrical parameters to describe the surface which include the mean building height ( $h_m$ ) and the plan area density of buildings covering the surface ( $\lambda_p$ ).

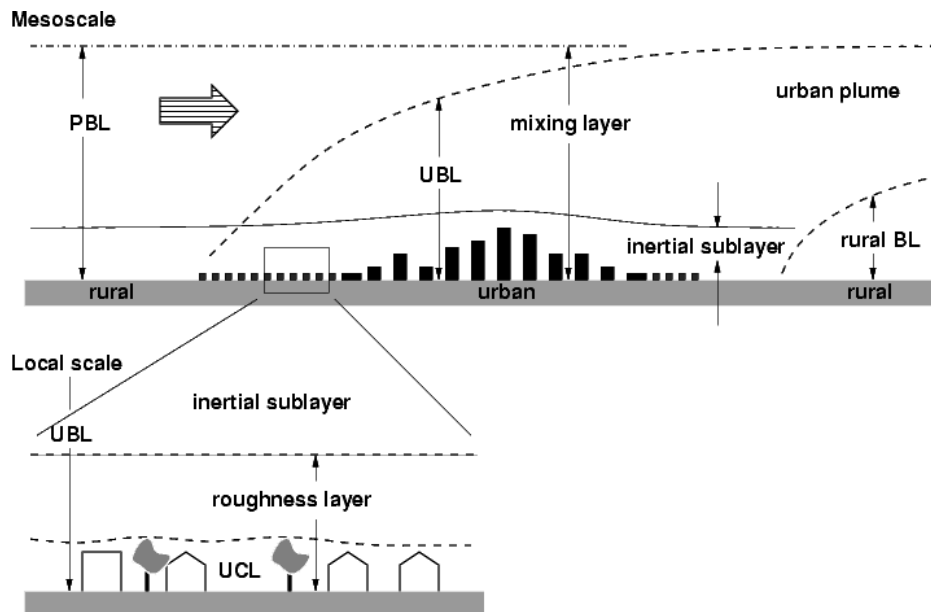


Figure 2-1 The development of the UBL and various sublayers (Best et al., 2008)

Historically, the log profile was only considered to be relevant to wind flows in the ISL which is problematic for this research as small to medium (< 50 kW) turbines occupy the RSL. However, for urban-like surfaces, it has been found that a single logarithmic profile can be applied throughout both the RSL and the ISL to  $h_m$ , provided the profile in the RSL has been spatially averaged (Cheng and Castro, 2002b; Rooney, 2001; Britter and Hanna, 2003).



The geometric parameters can be incorporated into the logarithmic wind profile equations described below to calculate the effect of surface objects on wind speed within the urban boundary layer. The fundamental underpinning of logarithmic wind profile theory stems from a trend in turbulence within the atmospheric boundary layer under the following conditions. When it is assumed that there is a flat, homogenous terrain with a constant wind speed of a constant direction, turbulent diffusion ( $K$ ) in the lowest tens of metres of the atmosphere increases with altitude and eddy intensity in the relationship described in equation (2-4):

$$K = \kappa u_* z, \quad (2-4)$$

where  $\kappa$  (the empirical von Kármán constant)  $\approx 0.4$  (von Kármán, 1930),  $u_*$  is frictional velocity and  $z$  height. The equation shows that the size of turbulent eddies is an influence on  $K$  which is limited by height above ground ( $z$ ).

A more precise definition of  $u_*$  is to consider stresses at the surfaces with which the flow interacts. To do this, the perturbations in the  $u$  and  $w$  directions of flow ( $\overline{u'w'}$ ) can be represented as:

$$u_*^2 = -\overline{u'w'} \quad (2-5)$$

Combining (2-4) and (2-5) gives:

$$u_*^2 = -\overline{u'w'} = K \frac{\partial \bar{u}}{\partial z} = \kappa u_* z \frac{\partial \bar{u}}{\partial z} \quad (2-6)$$

$$\frac{\partial \bar{u}}{\partial z} = \frac{u_*}{\kappa z} \quad (2-7)$$

with the reorganised form of the equation (2-7) showing that mean wind speed is roughly logarithmic. Equation (2-7) can be integrated to give:

$$\bar{u} = \frac{u_*}{\kappa} \log\left(\frac{z}{z_0}\right) \quad (2-8)$$

in which  $z_0$  represents surface roughness which characterises obstructions to the flow on the surface boundary (Garratt, 1990). At a target site,  $z_0$  can be a range of values depending on the type of landscape, be that: open country; land with a low density of development; a semi-rural area with a small number of buildings; a forest or; an urban core. Although there is agreement for  $z_0$  in open country settings to be 0.14 m (Grimmond and Oke, 1999a; Crago et al., 2012), it is not possible to categorize  $z_0$  urban and semi-urban values into groupings and maintain an accurate portrayal of the obstructions to the wind. For example, values for dense urban areas are always  $> 2$  m (Best et al., 2008) but there is significant variation across

an urban area. Given the strong bearing of  $z_0$  in the calculation of  $u(z)$ , recent studies have sought to estimate  $z_0$  values from digital surface models (DSMs) for localised subsections of cities or 'neighbourhoods' (Sunderland et al., 2013; Millward-Hopkins et al., 2013a). DSMs are grids of height above sea-level measurements in metres with coordinate positions where individual height measurements are made using an airborne light detection and ranging (LiDAR) system. A laser is fired to the ground from an aircraft with satellite location tracking at a spatial interval that defines the resolution of the DSM. The distance between the height measurements can be very low but the resolution that is most commonly available for entire cities is currently around 2 m. The great advantage of DSMs over other city-scale data, such as aerial photography, is that there is a relatively accurate ( $\pm 0.15$  m (The GeoInformation Group, 2008)) height measurement at the given spatial interval without the need for any complex processing or interpretation. DSMs give a more accurate representation of the obstructions influencing the flow than generalising the type of surface to a broad category. They provide the height and area of obstructions so they can be used to estimate  $z_0$  through the measurement of frontal area obstructing the wind ( $A_f$ ) for various directions of flow. Equation (2-9) has been adapted from Best et al. (2008) using  $C_D$  (the drag coefficient) and total neighbourhood area ( $A_T$ ) to calculate  $z_0$ .

$$\frac{z_0}{h_m} = \left(1 - \frac{d}{h_m}\right) \exp \left[ - \left(0.5 C_D \kappa^{-2} \frac{A_f}{A_T}\right)^{-0.5} \right]. \quad (2-9)$$

In which  $d$  is a corrective factor to  $z$  that accounts for the rate of fluid flow immediately following an obstacle being equal to zero (Raupach, 1992). Values for this parameter vary between academia and industry standard software with the latter estimating  $d$  as two thirds the maximum building height (Li-COR, 2012) whilst academic models have formulas that incorporate the density of surface roughness elements for grid-square neighbourhoods (of size  $A_T$ ) across a city (Grimmond and Oke, 1999b; Raupach, 1994). Grimmond and Oke (1999b) provide reference tables for  $d$  in four types of urban area, namely: low, medium, high and high-rise density morphometry. These values are built from comparisons of observed building layouts with values obtained from analysis of wind and turbulence observations. The authors carried out a survey of 60 field studies and 14 laboratory studies of real and scale model cities. However, categorising these aerodynamic values to such broad groupings loses a large degree of fidelity so this research seeks to quantify surface elements more precisely.

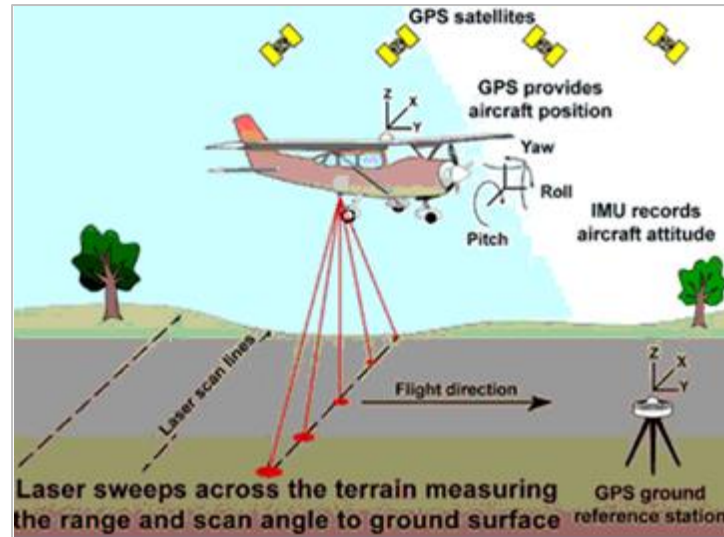


Figure 2-2 Airborne LiDAR data generation (Bureau of Economic Geology (2009))

$A_T$  is a grid-square of a smaller size than the  $1\text{km}^2$  resolution of the reference wind speed database grid and defines the size of neighbourhood that  $z_0$  is being calculated for. Breaking down the study area to neighbourhoods provides a more refined interpretation of the obstructions to the wind flow rather than trying to use a value for the entire area. The most advanced methods have a neighbourhood size that is adaptive to building density (Millward-Hopkins et al., 2013a) which helps to isolate areas that will have a more significant influence on wind speeds.  $\frac{d}{h_m}$  is displacement height ( $d$ ) normalised by the mean building height ( $h_m$ ) for the neighbourhood.

Equation (2-10) adapted from (Jasinski et al., 2005) incorporates  $d$  into the logarithmic downscaling equation shown in (2-8).

$$\bar{U}_z = \frac{u_*}{\kappa} \left[ \ln \left( \frac{z-d}{z_0} \right) \right] \quad (2-10)$$

An early formula to calculate  $d$  is that suggested by Macdonald et al. (1998) in which the subscript 'u' denotes indicates that they are relevant for arrays of uniform height:

$$\frac{d_u}{h_m} = 1 + A^{-\lambda_p} (\lambda_p - 1), \quad (2-11)$$

in which  $h_m$  is mean building height,  $A$  is an empirical constant for which values of 3.59 and 4.43 have been suggested.  $\lambda_p$  is the ratio of building plan area ( $A_p$ ) to ground surface area ( $A_T$ ) which are depicted in Figure 2-3 along with frontal area ( $A_f$ ), therefore:

$$\lambda_p = \frac{A_p}{A_T}. \quad (2-12)$$

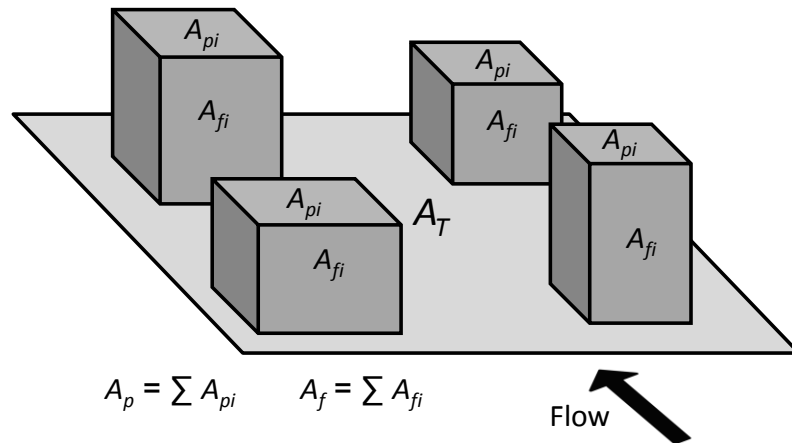


Figure 2-3 Illustration of the basic geometric measures:  $A_p$ ,  $A_f$  and  $A_T$ .

As stated, Macdonald’s model has a fundamental assumption of homogeneous arrays – Macdonald et al. (1998) use  $d_u/h_m$  in place of  $d$  in equation (2-9) to estimate  $z_{0u}$ . This is an inaccurate way to consider the layout of actual urban areas which vary greatly in height. To calculate  $d$  for heterogeneous arrays, where the heights of obstructions vary, Millward-Hopkins et al. (2011) horizontally slice the height data of neighbourhoods into layers at a number of height regimes, calculate  $d$  for each of those layers and then sum the results. The division of the array into height regimes is illustrated in Figure 2-4, where each unique building height defines the start of a new layer.

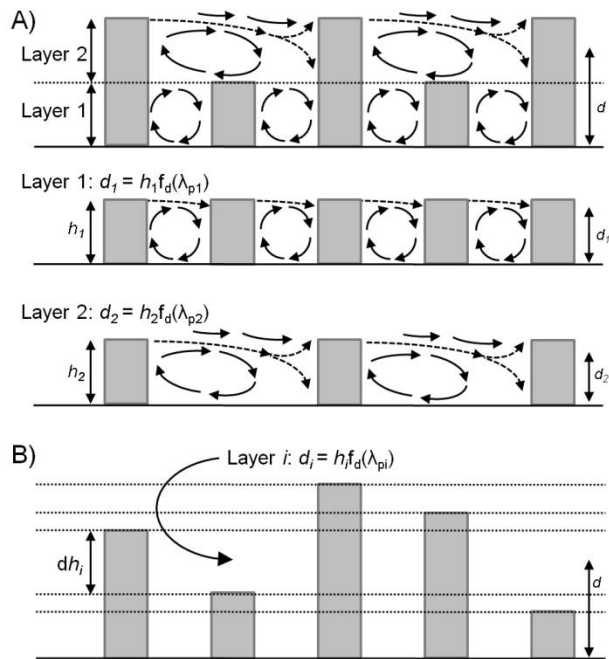


Figure 2-4 Millward-Hopkins et al. (Millward-Hopkins et al., 2011) method of estimating  $d$  using height regimes. Adapted from figure 8 of Millward-Hopkins et al. (2011)

A weighting is applied to each layer which is defined by the density, distancing and heights of obstructions in the neighbourhood. Essentially,  $d$  is defined by wind flow within the canopy layer which can increase or decrease the minimum height at which drag occurs. It is the distinct flow behaviour at different heights that inspires the layer-by-layer approach to estimating  $d$ . An example of two separate flow patterns around a heterogeneous array is provided in Figure 2-4A where there are two clear flow patterns occurring simultaneously. There is a skimming flow amongst layer 1 and a more penetrative flow observed in layer 2. The skimming flow means the flow passes the obstacles largely unhindered and so there is less drag whereas the more penetrative flow of layer 2 interacts more with the obstacles to affect a greater drag force. For each layer,  $d$  can be calculated using equation (2-13) (from Millward-Hopkins et al. (2011)).

$$\frac{d}{h_m} = \begin{cases} \frac{19.2\lambda_p - 1 + \exp(-19.2\lambda_p)}{19.2\lambda_p[1 - \exp(-19.2\lambda_p)]} & (\text{for } \lambda_p \geq 0.19) \\ \frac{117\lambda_p + (187.2\lambda_p^3 - 6.1)[1 - \exp(-19.2\lambda_p)]}{(1 + 114\lambda_p + 187\lambda_p^3)[1 - \exp(-19.2\lambda_p)]} & (\text{for } \lambda_p < 0.19) \end{cases} \quad (2-13)$$

The height of each layer then needs to be taken into account which is achieved by multiplying the values for  $d$  of each layer by that layer's height, i.e.:

$$\begin{aligned} d_1 &= h_1 f_d(\lambda_{p_1}) \\ d_2 &= h_2 f_d(\lambda_{p_2}). \end{aligned} \quad (2-14)$$

It may then be assumed that when the original layout of the obstructions to the flow is reconstituted by stacking the two layers in order,  $d$  of the original configuration is the sum of  $d_1$  and  $d_2$ . The simple example provided in Figure 2-4 can be applied to obstruction layouts of any degree of heterogeneity so long as the canopy is subdivided into a sufficient number of distinct horizontal layers and so,

$$d = \sum_{i=1}^n d h_i f_d(\lambda_{p_i}). \quad (2-15)$$

Once  $d$  has been calculated, equation (2-9) can be completed by estimating the unsheltered frontal area of a building ( $A_f^*$ ) that obstruct wind flows. This is calculated using building wakes defined by Millward-Hopkins et al. (2011) that was informed by detailed CFD models from Castro et al. (2006), Lim et al. (2009) and Cheng et al. (2007).

The definition of  $\frac{A_f^*}{A_T}$  in Macdonald et al. (1998) differs significantly to Millward-Hopkins et al. (2011). Macdonald et al. (1998) assumes that drag below  $d$  is negligible and whilst this may be suitable for arrays of homogeneous height, Bottema (1996; 1997) presents a more appropriate method to estimate  $\frac{A_f^*}{A_T}$  for arrays of heterogeneous heights. It considers the mutual sheltering of all buildings within an array by modelling the wake shapes of the flow caused by the array's form.  $z_0$  can then be estimated by iteratively solving the drag balance equation (2-16) for each wind direction.

$$2A_T\kappa^2 = C_D \left[ \ln \left( \frac{h_{m-eff} - d}{z_0} \right) \right]^2 A_f^*(h < h_{m-eff}) + \int_{h_{m-eff}}^{h_{max}} C'_D \left[ \ln \left( \frac{h - d}{z_0} \right) \right]^2 dA_f^* \quad (2-16)$$

$h_{max}$  in equation (2-16) refers to the maximum height of buildings within a neighbourhood and  $C'_D$  to the drag coefficient for the heights between  $h_{m-eff}$  and  $h_{max}$ .  $h_{m-eff}$  is an approximation of the mean height of only the buildings that have an influence on the flow because small buildings that are sheltered by surrounding tall buildings will have a negligible effect on the flow but a significant influence on  $h_m$ . To estimate  $h_{m-eff}$ ,  $\lambda_{p-eff}$  is introduced which is the plan area density without the contribution of sheltered blocks in an array. For each height regime described in Figure 2-4, the wake shapes of the blocks are calculated, the plan area of sheltered buildings is removed and the remaining area summed across all layers in the same way that  $d$  was calculated.  $\lambda_{p-eff}$  is then applied in equation (2-17) to give  $h_{m-eff}$ .

$$h_{m-eff} = \begin{cases} d \frac{19.2\lambda_{p-eff} [1 - \exp(-19.2\lambda_{p-eff})]}{19.2\lambda_{p-eff} - 1 + \exp(-19.2\lambda_{p-eff})} & (for \lambda_{p-eff} \geq 0.19) \\ d \frac{(1 + 114\lambda_{p-eff} + 187\lambda_{p-eff}^3) [1 - \exp(-19.2\lambda_{p-eff})]}{117\lambda_{p-eff} + (187.2\lambda_{p-eff}^3 - 6.1) [1 - \exp(-19.2\lambda_{p-eff})]} & (for \lambda_{p-eff} < 0.19) \end{cases} \quad (2-17)$$

The entire  $h_{m-eff}$  calculation is repeated for eight wind directions to incorporate the different sheltering that occurs in each direction.

As with  $d$ , Grimmond and Oke (1999b), have developed  $z_0$  reference tables for categories of urban development which are useful for comparing morphometric models to but are too restricted to accurately portray the nuances in urban form that occur from neighbourhood to neighbourhood across a city.

The application of  $z_0$  and  $d$  to estimate wind speeds using the logarithmic equation (2-10) will now be described. The UK Met Office (Best et al., 2008) have presented a methodology which is summarised in Figure 2-5 (from Weekes (2014)).

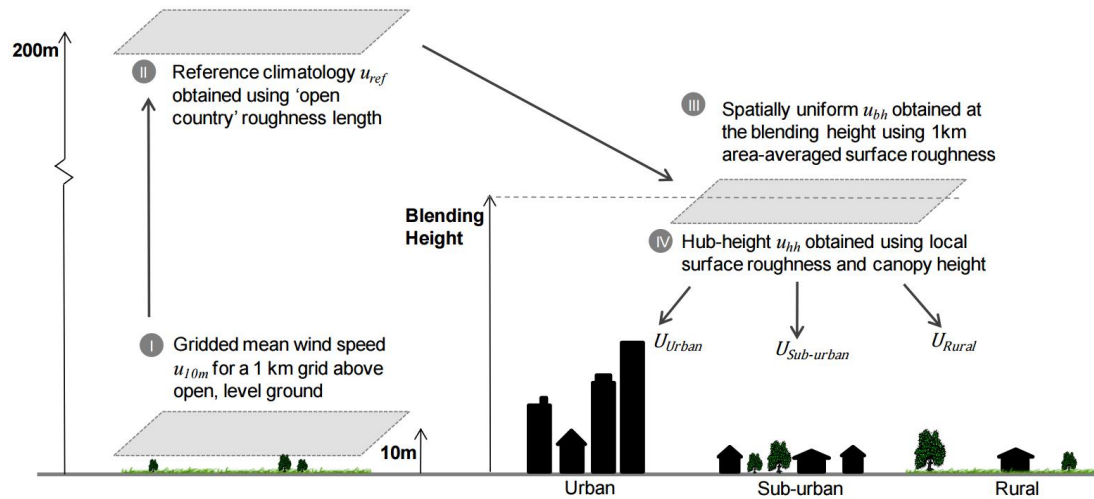


Figure 2-5 Summary of the Met Office mean wind speed prediction method (Weekes, 2014)

In the Met Office method, regional wind climate data such as the Numerical Objective Analysis of Boundary Layer (NOABL) or the National Climate Information Centre (NCIC) database is used that provide wind speeds over the whole of the UK at a resolution of 1 km that are valid at a height of 10 m above a smooth surface. The databases also account for the influence of topographical features on scales greater than 1 km (Best et al., 2008) but not vegetation or buildings. The arrow from I to II in Figure 2-5 shows the scaling of the reference wind speed up to a height that is independent of the friction caused by surface objects at the boundary layer. There are then two downscaling steps to account for surface objects in first the wider fetch area and then a more localised area. In doing so, the parameters in the first downscaling step are suitable for describing the RSL profile and the parameters in the second are suitable for the ISL profile. The first downscale (from II to III in Figure 2-5) is from the UBL to the blending height which is the top of the RSL, both of which were shown in Figure 2-1. To complete the logarithmic equation for this change in height,  $z_0$  and  $d$  are defined for areas 5 km from the target site in eight wind directions and are called  $z_{0-eff}$  and  $d_{eff}$ . The wind directions used are the four compass points and four directions that fall between those compass points, i.e. North-East, South-East, South-West and North-West because reference wind speed data is available in this format.  $d_{eff}$  is calculated by averaging the calculations of  $d$  in each of the wind direction sector areas. In contrast,  $z_{0-eff}$  is estimated using a slightly more complex scaling process that is described in Bou-Zeid et al. (2007) to weight  $z_0$  of neighbourhoods closer to the target site more than those further away.

The second downscale (from III to IV in Figure 2-5) then uses  $z_0$  and  $d$  for a more localised neighbourhood that typically range in size from 250 m x 250 m to 1 km x 1 km. This downscale extends to the hub height of a target site if that site is exposed. However, if the hub height is less than the heights of surrounding objects, and is therefore sheltered, the logarithmic equations can become unreliable.  $h_m$  has been used to define the height to which the final logarithmic downscaling should be applied (Cheng and Castro, 2002a; Rooney, 2001; Britter and Hanna, 2003) and where the power law should then take over as the scaling method for lower sites. However, Millward-Hopkins et al. (2011) use anemometry data to show that it is inaccurate to extend the logarithmic wind profile down to  $h_m$  and so use the effective mean building height

With the height to which the final downscale can be extended defined by  $h_{m-eff}$ , the process of adapting a reference wind speed to an estimate at another location is complete. This approach has been validated by Millward-Hopkins et al. (2013b) by comparison to anemometry data collected at 12 sites across four of UK cities where the mean error was 0.3  $ms^{-1}$ .

A variety of approaches to predicting urban and semi-urban wind speeds at the city scale have been discussed and it is clear that mesoscale models and CFD are not appropriate for this thesis. This section shows where the research described in Chapter 5 builds from. Similarly, the following section introduces solar PV electricity generation and the methodologies used to assess variations in yield caused by the physical setting of the installation, which are the foundations to the research presented in Chapter 3 and Chapter 4.

## **2.2 Solar PV**

Solar energy is a term that describes all the energy that reaches Earth from the Sun as a result of fusion and fission reactions that occur inside the star. However, solar PV technologies only absorb electromagnetic radiation with wavelengths between approximately 400 and 1100 nm (Markvart, 2003) so when the words “solar energy” are used in the context of solar PV, it is usually in reference to a limited part of the total energy that comes from the Sun. The radiation from this smaller section of the electromagnetic spectrum can be received at a PV panel in three ways: as either direct (or beam); diffuse; or reflected which are referred to collectively as global radiation. Diffuse radiation describes radiation that has been deflected by components of the atmosphere to arrive at the solar PV cell whilst direct radiation is that which has not undergone any deviation in its path from the Sun. Reflected radiation is the



radiation that has been reflected by the Earth's surface towards the solar PV panel and is a relatively minor contributor to the total irradiance occurring at a particular surface. The term irradiance is used frequently throughout this thesis and is the rate at which solar energy falls onto a surface, measured in  $\text{W m}^{-2}$ .

The following paragraphs describe the processes that occur if that solar radiation happens to fall on a p-n junction in a mono-crystalline silicon solar PV cell. A p-n junction is the point of contact between an n-doped silicon semi-conductor and a p-doped semiconductor material (Largent et al., 2003). They are usually created in a single crystal of semiconductor with each side receiving a different doping. The n-doped side has excess electrons due to being doped with phosphorus whilst the p-doped side has excess holes for electrons to pass through due to having been doped with boron (Semikron, 2012b). Here, the term doping means a very pure silicon material that has had a very small number of phosphorus or boron atoms added to it in a ratio of approximately one dopant atom to every  $5 \times 10^6$  silicon atoms (Sproul, 2003). When covalently bonded to silicon by four of its five outer orbit electrons, the phosphorus atom in the n-doped silicon has a single electron that is very weakly attracted to the nucleus. At room temperature this electron is unbound from the phosphorus atom altogether and travels freely through the n-doped silicon-phosphorus crystal. By contrast, p-doped silicon contains boron which can only form covalent bonds with three of its outer electrons. A neighbouring electron is pushed into this vacancy creating another vacancy, or hole, in the atom that provided the electron. This pattern reoccurs so that, effectively, the holes move around the p-doped silicon which can be thought of as positive charge moving across the crystal.

When brought together, electrons diffuse from the n-doped to p-doped side with holes diffusing in the opposite direction (Crook, 2012). Positively charged phosphorus ions are left behind in what is called the depletion region when the electrons move to the p-doped side. Negatively charged boron ions are left there when the holes move to the n-doped side. Figure 2-6 shows this and also that a second force pushes the holes and electrons the opposite way which is the "drift" effect caused by the electric fields of the electrons and holes.

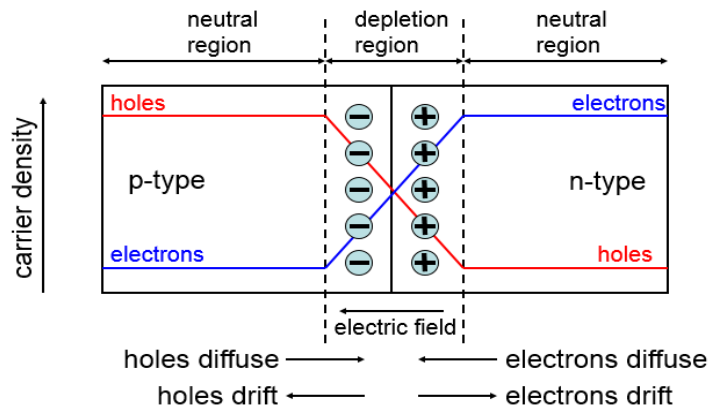


Figure 2-6 The p-n junction as described in Crook (2012)

The two competing forces reach equilibrium in the depletion region meaning that there is no net flow of holes or electrons and only the fixed charges of the dopant atoms are present. This creates a very resistant insulator. However, if an external electrical field is applied to the equilibrium, the depletion region's resistance can be modified. Short-circuit current will flow if: a low resistance wire is connected the two sides of the cell; a negative voltage is applied to the n-doped side; and a positive voltage is applied to the p-doped side (Sproul, 2003). This set-up is called a forward biased configuration. It is important to recognise that despite the flow of current, there is no voltage across the solar cell in this configuration and so no useful power is generated yet. If the wire connecting the two sides externally had a gap in it, however, the current would not have a route to flow out of the solar cell. With the excited electrons and holes continuing to move across the depletion region, a voltage would start to build across the PV cell (Semikron, 2012b). Hence, in order to get useful power from a solar PV cell, a resistor must be added to the circuit that finds an optimum balance between flow of current and voltage (Semikron, 2012a). Once this happens, an illuminated solar PV cell will generate electricity.

When solar radiation illuminates a solar PV cell on Earth, the energy is great enough to break a very small number (1 in  $1 \times 10^8$  atoms) of the bonds holding electrons in place in a silicon crystal, creating excited electrons of a higher energy state (Sproul, 2003). The excited electrons move across the material freely just as the electrons from the phosphorus atoms in the n-doped side of the cell. The holes they leave also move freely across the crystal. However, the electrons are excited for only a short period of time depending on the energy intensity of the solar radiation and when this energy falls they recombine with a neighbouring hole, losing the electrical energy as heat. Therefore, the intensity of sunlight plays a crucial role in the power output of a solar PV cell. There is greater intensity of sunlight when a solar cell is angled toward the sun so modelling roof geometry is fundamental to estimating the potential output of a solar cell.

By multiplying the number of solar cells to make a solar PV panel, then multiplying the number of panels to make an array and then multiplying the number of arrays across a country, solar PV technology provides a renewable source of electricity that can make a significant contribution to meeting national electricity demands. Chapter 1 described how this has started to become reality through the rapid growth of the solar PV industry.

### **2.2.1 EU JRC PVGIS Solar Databases**

As the microgeneration market has grown, so too has interest in the viability of PV at individual properties, leading to an increasing number of academic and industry studies of solar resource. One popular methodology is the European Solar Radiation Atlas (ESRA) model (Scharmer and Grief, 2000) that has been used in many studies (Bergamasco and Asinari, 2011a; Šúri and Hofierka, 2004; Šúri et al., 2007; Wiginton et al., 2010). It was used to create the popular European Union Joint Research Council (EU JRC) PVGIS solar databases by interpolating and correcting near-by solar insolation measurements. It has also been incorporated into the open-source GRASS Geographic Information System (GIS) software by Hofierka (2002) and more recently into the *r.sun* routine (Hofierka, 2007). This model has three major components: the estimation of clear-sky global irradiation for a horizontal surface and a clear-sky index; the calculation of diffuse and direct components of overcast global irradiation; and the conversion of horizontal surface global irradiation estimations for inclined surfaces (EU-JRC, 2012). These components combine to account for the interaction of solar radiation with Earth's geometry, topographical shading and the constitution of the atmosphere. A site's location on Earth alters the calculation of solar irradiance as it defines the declination, latitude and solar hour angle of a particular site. The site's location also impacts the amount of atmosphere that solar radiation encounters before reaching the surface which has an impact on the wavelengths that will reach the site. Each of the three components will now be further described in turn, starting with the estimation of clear-sky global irradiation for a horizontal surface and the estimation of a clear-sky index value. Clouds have a significant impact on the global radiation received at a surface and make it difficult to predict the split between direct and diffuse radiation. Therefore, a clear-sky condition is assumed whereby there are no clouds. This allows a reasonably accurate first approximation of global solar radiation to be made using solar geometry and data about the concentrations of water vapour and particulates in the atmosphere. Prior to considering the constitution of the atmosphere, it is important to consider the amount of atmosphere that the radiation has passed through (the path length) which is defined by the relative optical air mass,  $m$ , described in equation (2-18) from Kasten (1989):

$$m = \frac{(p/p_0)}{\{\sin \gamma_S + 0.50572(\gamma_S + 6.07995^\circ)^{-1.6364}\}}, \quad (2-18)$$

in which  $p$  is the atmospheric pressure at the site and  $(p/p_0)$  is a correction for the site's altitude.  $(p/p_0)$  can be approximated using the site elevation above sea level,  $z$ , and a reference height,  $H_R = 8,400$  m.

$$(p/p_0) = \exp\left(\frac{-z}{H_R}\right). \quad (2-19)$$

$\gamma_S$  in equation (2-18) is the solar altitude angle ( $^\circ$ ) which is the vertical angle between the site's surface and the position of the Sun in the sky.

With  $m$ , the scattering and absorption impacts of the constituents of that atmosphere can be estimated using the Linke turbidity factor ( $T_{LK}$ ) (Remund J., 2003). This approach compares an observed optical depth from a weather station near-by to a theoretical completely clean and dry reference Rayleigh atmosphere,  $\delta_r$  (m) that is a function of air mass. Using  $m$  from equation (2-18), the clear sky direct irradiance normal to the beam,  $I_C$  ( $W\ m^{-2}$ ), at the surface is:

$$I_C = 1367. \varepsilon \exp(-0.8662 T_{LK} m \delta_r(m)), \quad (2-20)$$

where  $\delta_r(m)$  is the Rayleigh optical depth at air mass  $m$  and  $\varepsilon$  is a correction factor to mean solar distance. The clear sky direct irradiance on a horizontal plane,  $B_C$  ( $W\ m^{-2}$ ), can then be calculated by incorporating  $\gamma_S$  to account for the site's position on the Earth.

$$I_C = 1367. \varepsilon \exp(-0.8662 T_{LK} m \delta_r(m)) \sin \gamma_S \quad (2-21)$$

$T_{LK}$  is set to specific values that reflect broad categories of atmospheric conditions. For example, a value of 2 is used for very clear cold air in winter whilst polluted air is given a value greater than 6. Both equations (2-20) and (2-21) require the calculation of  $\delta_r$  which Kasten (1996) defines for two regimes of  $m$  using:

$$\frac{1}{\delta_r(m)} = \begin{cases} 6.630 + 1.751 m - 0.120 m^2 + 0.007 m^3 - 0.0001 m^4 & (m \leq 20) \\ 10.4 + 0.718 m & (m > 20) \end{cases} \quad (2-22)$$

It is worth noting at this point that the academic models discussed later seek to utilise satellite measurements of atmospheric matter such as cloud water vapour, ozone and aerosol particles to move away from such sweeping generalisations of atmospheric conditions caused by  $T_{LK}$ . However, the continued use of EU JRC datasets to project solar

insolation in industry and as a source of validation data in the aforementioned academic models warrants the full description of its methodology presented here.

To estimate a clear-sky diffuse radiation value, the ESRA model uses the measured proportion of beam to diffuse radiation from near-by weather stations which Šúri et al. (2007) explore in greater detail. This proportion is altered for the different  $T_{LK}$  that occurs at the target site in comparison to the weather station sites. The clear sky global irradiation on a horizontal surface is then given by the sum of the clear sky direct and diffuse components.

Once clear sky global irradiance is estimated, the ESRA model considers the effects of cloud cover using an averaged index value of how clear the sky is at the target site (Clearness Index) which is based on satellite and near-by weather station data (Scharmer and Grief, 2000). The Clearness Index ( $G_d/G_{0d}$ ) is the ratio of daily global irradiation observed at a weather station ( $G_d$ ) to the daily irradiance falling on a horizontal plane outside of the atmosphere ( $G_{0d}$ ).  $G_{0d}$  is known to fluctuate with latitude and time of the year as Figure 2-7 shows.

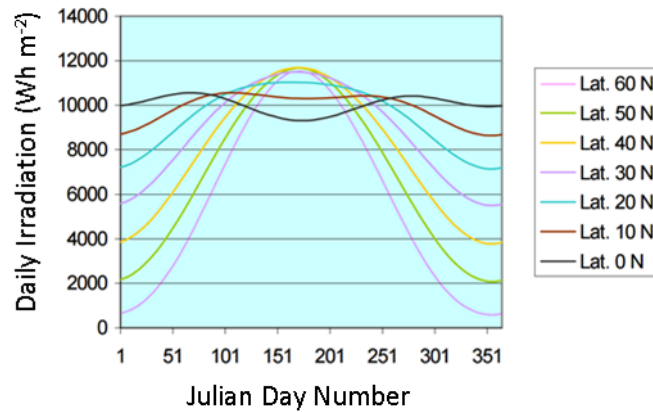


Figure 2-7 Fluctuation of  $G_{0d}$  with Julian day and latitude from Scharmer and Grief (2000)

The clearness index is denoted as  $(KT_d)_m$  and its calculation from weather stations in the vicinity of the site depends on the monitoring of monthly mean sunshine duration  $(\sigma_d)_m$  along with site dependent monthly regression coefficients  $a_m$  and  $b_m$  so:

$$(KT_d)_m = a_m + b_m(\sigma_d)_m \quad (2-23)$$

in which the subscript  $m$  refers to the values being monthly. This means that monthly mean global radiation  $(G_d)_m$  is:

$$(G_d)_m = a_m + b_m(\sigma_d)_m(G_{0d})_m. \quad (2-24)$$

Taking this value and splitting it into direct and diffuse components again uses  $(KT_d)_m$  and coefficients derived from weather station data of measured diffuse radiation to give the polynomial function shown below.

$$(D_d)_m/(G_d)_m = c_0 + c_1(KT_d)_m + c_2((KT_d)_m)^2 + c_3((KT_d)_m)^3 \quad (2-25)$$

$$\text{If } (D_d)_m/(G_d)_m > 1, (D_d)_m/(G_d)_m = 1$$

where  $(D_d)_m$  is the monthly mean daily sky diffuse irradiation ( $\text{Wh m}^{-2}$ ). It has been found that if  $(KT_d)_m$  is as small as 0.2, there is practically no direct radiation. Most commonly, the typical proportion of direct to diffuse irradiance is 40% to 60% which serves to underline the significance of diffuse radiation and the ESRA model's sensitivity to the ratio.

When converting the horizontal surface irradiation to tilted surfaces, the calculations are altered in a number of ways. The orientation of inclined surfaces has a significant impact on solar irradiation and the effects of clouds and shadows from topological features are increased which serves to underline the importance of accuracy in roof geometry modelling. The ESRA model that underlies the EU JRC PVGIS data is highly sensitive to the ratio of direct to diffuse radiation which are impacted by these effects. Hence, the global radiation for an inclined surface differs significantly to a horizontal surface. Classically, the conversion from horizontal to tilted global irradiance ( $E_s$  – in which “s” refers to the tilt angle ( $^\circ$ ) of the sloped plane) estimation takes the form:

$$E_s = I_B + \cos \theta + I_D R_d + \rho E R_r \quad (2-26)$$

where  $I_B$  is direct horizontal irradiance,  $\theta$  is polar direction angle of incidence ( $^\circ$ ),  $I_D$  is diffuse horizontal irradiance,  $R_d$  is a diffuse transposition factor,  $\rho$  is the albedo of the surrounding terrain,  $E$  is global horizontal irradiance and  $R_r$  is a ground reflection transposition factor.

### 2.2.2 Esri ArcGIS Solar Radiation Toolset

Another solar insolation prediction technique that is increasingly being used to estimate global solar insolation is the solar radiation toolset within the market-leading GIS software, Esri ArcGIS (Gooding et al., 2013; Brito et al., 2012a) that is based on the methods of Fu and Rich (Fu, 2000; Fu and Rich, 2000; Rich et al., 1994; Rich and Fu, 2000). In their method a hemispherical viewshed is generated for each point of interest to account for shading effects from surrounding objects and topography. The tallest obstructions across a DSM in 32 directions from the point of interest are determined before the horizon is approximated by interpolating between the returned data points. The horizon line is then converted into a hemispherical coordinate system resulting in a figure showing areas of the sky that are obstructed from view at the point of interest (the black regions of Figure 2-8). This perspective is the same as would be observed if looking up from the point of interest at an angle perpendicular to the ground with  $360^\circ$  vision to sea-level.

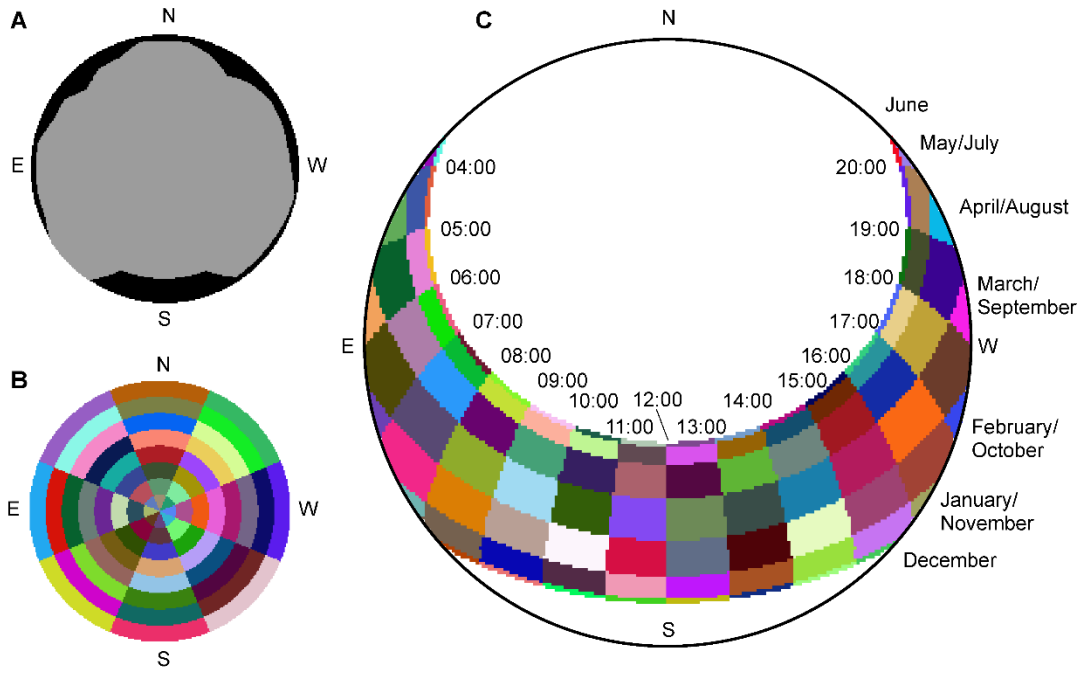


Figure 2-8 A: Example viewshed model in which parts of the sky that are obstructed from view are shown in black. B: A sky map. C: A sun map for 53.8° latitude.

The viewshed model shown in Figure 2-8A can be used to determine if the point of interest is exposed to direct radiation once the position of the Sun is established in the hemispherical coordinate system. Sun position can be calculated using a latitude-defined Sun map (Figure 2-8C) in which each coloured polygon, called a Sun map sector, represents the approximate position of the Sun for a half-hour period of the day in a specific month.

Overlaying the viewshed model onto the Sun map shows the times of a year when the Sun is visible from the point of interest and is exposed to direct radiation. Equation (2-27) from Fu and Rich (2000) is used to estimate direct radiation ( $Dir_{\theta,\alpha}$ ) for each of the sun map sectors that are not completely obscured by the viewshed model:

$$Dir_{\theta,\alpha} = S_{const} \beta^{m(\theta)} SunDur_{\theta,\alpha} SunGap_{\theta,\alpha} \cos AngIn_{\theta,\alpha} \quad (2-27)$$

where  $S_{const}$  is the solar constant ( $1367 \text{ W m}^{-2}$ ),  $SunDur_{\theta,\alpha}$  is the time duration represented by the sunmap sector and  $SunGap_{\theta,\alpha}$  is the gap fraction for the sun map sector. Gap fraction is the proportion of visible sky for each sector.  $AngIn_{\theta,\alpha}$  is the angle of incidence between centroid of sky sector and axis normal to the surface and  $\beta^{m(\theta)}$  is the transmittivity of the atmosphere with respect to the optical path, calculated using:

$$m(\theta) = \frac{\exp(-0.000118 \text{ elev} - 1.638 \times 10^{-9} \text{ height}^2)}{\cos \theta}, \quad (2-28)$$

in which  $height$  is height above sea level in metres. The result is the direct radiation at the sun map sector's centroid zenith angle ( $\theta$ ) and its azimuth angle ( $\phi$ ).

In contrast to direct radiation, diffuse radiation is received from all visible parts of the sky. Fu and Rich (1999) overlay the viewshed model onto a uniformly divided hemispherical perspective of the sky to determine which parts of the sky contribute diffuse radiation to the point of interest.

For each sky map sector that is not completely obscured by the viewshed model, diffuse radiation ( $Dif_{\theta,\phi}$ ) is obtained from:

$$Dif_{\theta,\phi} = R_{glb} P_{dif} Dur SkyGap_{\theta,\phi} Weight_{\theta,\phi} \cos AngIn_{\theta,\phi}, \quad (2-29)$$

where  $R_{glb}$  is the global normal radiation given by:

$$R_{glb} = \frac{(S_{const} \sum \beta^m(\theta))}{(1 - P_{dif})}, \quad (2-30)$$

in which  $P_{dif}$  is the proportion of global normal radiation flux that is diffused,  $Dur$  is the half-hour time interval for analysis and  $SkyGap_{\theta,\phi}$  is the gap fraction for sky sector.

In equation (2-29),  $Weight_{\theta,\phi}$  is the proportion of diffuse radiation originating from a given sky sector which is calculated in one of two ways depending on the selection of the user. The default uniform sky diffuse model has incoming diffuse radiation the same from all sky directions so that:

$$Weight_{\theta,\phi} = \frac{(\cos \theta_2 - \cos \theta_1)}{Div_{azi}}. \quad (2-31)$$

In the standard overcast model, however, the incoming diffuse radiation flux varies with zenith angle so that:

$$Weight_{\theta,\phi} = \frac{(2\cos \theta_2 + \cos 2\theta_2 - 2\cos \theta_1 - \cos 2\theta_1)}{4Div_{azi}} \quad (2-32)$$

in which  $\theta_1$  and  $\theta_2$  are the bounding zenith angles of the sky sector and  $Div_{azi}$  is the number of azimuthal divisions in the sky map.

Diffuse irradiance is calculated by summing the estimations of  $Dif_{\theta,\phi}$  for all sky map sectors that are not completely obscured by the viewshed model. Finally global irradiation is the sum of both the direct and diffuse estimations.

### 2.2.3 Roof Geometry Modelling

The available area, orientation and inclination of surfaces are key inputs to the models described above and have a highly significant impact on global solar irradiance at a site. The most accurate and practicable methods for the assessment of available roof area, orientation



and slope for every property across a city utilise DSMs. However, a major problem in the use of DSMs has been that many properties in urban areas have roof planes that are too small for a large number of LiDAR points to have hit them. This is a result of poor resolution DSMs in which the distance between LiDAR points is too great to register a large number of height measurements on each roof plane. In these instances simplistic interpolations of the few data points of each plane lead to inaccurate estimations of orientation and slope. When the horizontal resolution of the DSM is 2 m, the smallest size of building that can be appraised directly from low resolution DSM data has been found to be roughly 200 m<sup>2</sup> in plan area (Gooding et al., 2013), although the shape of roofs is important as long and narrow buildings may be greater than 200 m<sup>2</sup> in area but have very few LiDAR points across the width of the building, leading to poor estimation of slope. A number of building reconstruction methods have been investigated to find ways to decrease the minimum size of a building that can be modelled which are now described.

The field of building reconstruction from DSM data grew at a considerable rate around the turn of the millennium with a number of authors developing methods to construct 3D city models (Vosselman and Dijkman, 2001; Maas and Vosselman, 1999; Brenner, 2000; Brenner and Haala, 2000). The methodologies, and all that have subsequently followed, generally fall into one of two categories identified by Maas and Vosselman (1999). Where DSM data is used directly or undergoes a small degree of manipulation is known as a data-driven approach but has also been referred to as non-parametric. The second category, model-driven (or parametric) approaches, involve the comparison of raw DSM data to a series of common roof shapes, or 'templates', with the quality of the fit then quantified. Tarsha-Kurdi et al. (2007) provide analysis and comparison of both approaches to further aid distinction between the two, writing that data-driven methods' have a fundamental assumption that buildings are an aggregation of several segmented roof planes. It is the data-driven methodologies that are first described in the following section.

### ***2.2.3.1 Data-driven Approaches***

In broad terms, data-driven approaches generally focus on interpolating values from the DSM directly or apply only minor alterations before extracting slope information with orientation calculated from building footprints. There are a limited number of methodologies that then use additional data sources to provide extra information to improve the accuracy of the modelling. Vosselman and Dijkman (2001) generated a triangulated irregular network (TIN) from the DSM for a roof and then refined the TIN using the original DSM and building footprint information. Other authors have combined entirely separate data sources.

Rottensteiner and Briese (2003) incorporated aerial images to validate a roof plane detection methodology but also discuss the possibilities for integrating aerial images into the reconstruction process itself as a way to increase the quality of the reconstructed models. This idea also formed the central focus of Cheng et al. (2013) who developed a methodology to identify step changes in height from visual imagery. By contrast, Suveg and Vosselman (2004) present a semi-automated method for constructing building models without a DSM using aerial imagery and building footprints. Whilst this is a methodology better suited to individual buildings, connecting building footprint size to likely roof shape is an idea that could potentially increase the efficiency of any roof recognition algorithm. Despite the incorporation of differing additional information, the main underlying similarity is a key first stage to identify and define planes of the roofs. There are essentially three main forms of plane detection in the literature: 3D Hough Transform; RANdom SAmples Consensus (RANSAC) and; region growing which are described in turn below.

#### 2.2.3.1.1 3D Hough Transform

Overby et al. (2004) used Hough Transform to identify planes from DSM data. Hough Transform was originally intended for 2D problems of forming polygons from points (Hough, 1962) and is regarded as the *de facto* standard for line and circle detection in 2D images (Borrmann et al., 2011). Hough Transform for 2D essentially establishes straight lines of the form  $y = mx + c$  between the coordinates of data points. The lines are given an infinite length and the location of the intersection gives the parameters of the line in the original data. Schindler and Bauer (2003) demonstrate how Hough Transform can be extended to 3D in great detail but for the purposes of this research, a brief description adapted from Vosselman and Dijkman (2001) will suffice. Firstly, every coordinate ( $x$ ,  $y$  and  $z$ ) in a single roof segment of a DSM is taken to express a plane of the form

$$z = s_x x + s_y y + d \quad (2-33)$$

in 3D parameter space. The axes of the 3D parameter space are the parameters  $s_x$ ,  $s_y$ , and  $d$ , where  $s_x$  and  $s_y$  are the slopes in  $x$ - and  $y$ -direction and  $d$  is the vertical distance of the plane to the origin. The planes of DSM data points are again given an infinite length with the intersection points in 3D space defining the slopes and dimensions of the planar face.

Two key issues arise from the application of 3D Hough Transform to identify roof shape. Firstly, it is dependent on high resolution datasets with minimal noise to the point where a planar face must, to an extent, be distinct in the data which is often not the case in what are noisy DSM datasets. Secondly, the methodologies in the literature consistently require

additional actions to fine-tune them: single planar faces are often unnecessarily split in two due to a sub-optimal tolerance used to define what a distinct planar face is. This has resulted in studies such as Overby et al. (2004) having to implement post-reconstruction diagnostics to establish the likelihood that the modelled roof-shape suggested is at least logical which is highly inefficient.

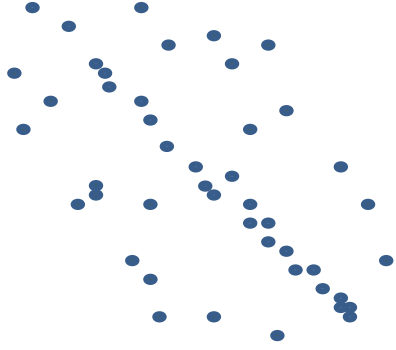
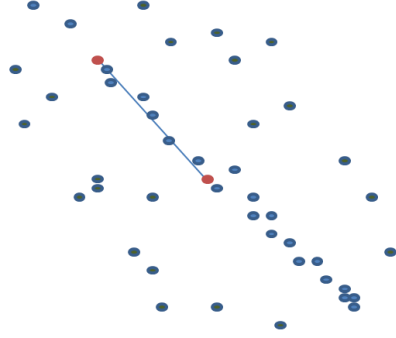
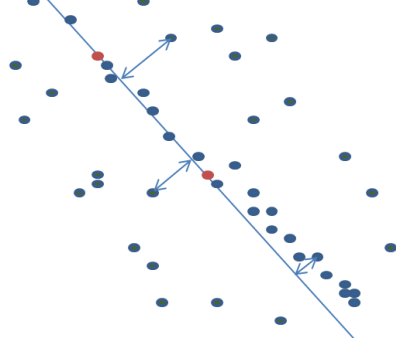
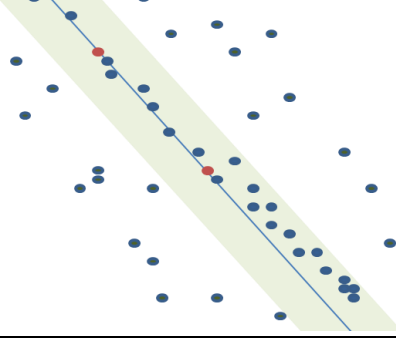
Vosselman and Dijkman (2001) focused on creating 3D city models for the use of town planners and the telecommunications industry which perhaps reflects the state of the PV sector and climate change awareness at the time. In addition to the DSM data, they formed a triangular irregular network (TIN) of the DSM from each building to select points that fell into each plane identified using 3D Hough Transform. In effect, their approach refined a TIN based on data points of close proximity which is only possible using very fine resolution LiDAR as otherwise the TIN would be built from a small number of points with too little discrepancy to permit any refinement. Another problem is that the TIN was built by generating planes by the simplest intersections of data points. The tolerance values for creating the TIN therefore effectively shaped the planes of each roof and it is unlikely that creating a TIN for each of the tens of thousands of structures across a city would be the most computationally efficient method to pursue. It is also important to note that Vosselman and Dijkman (2001) produced results using a resolution of DSM too fine to be generated from current airborne LiDAR systems (five to six points per m<sup>2</sup>). The study also includes a test using a lower resolution DSM which was found to lead to failure of the method, bringing into question its suitability for this research project.

#### **2.2.3.1.2 RANSAC**

Tarsha-Kurdi et al. (2008) state that RANSAC is a better method to establish viable roof planes from DSM data points than 3D Hough Transform. The method stems from image processing studies that sought to detect straight lines amid a dataset with many outliers. Whilst the process has been defined in several sources (McGlone et al., 2004; Fischler and Bolles, 1981), the process is, in the context of spatial interpolation, most suitably described by Nguyen et al. (2005). RANSAC is an algorithm designed to tolerate outliers when fitting models that has a small number of key steps that Table 2-1 describes with figures. The main advantage of RANSAC is that it is a generic segmentation method and can be used on datasets with high noise. A total-least-squares fitting method is used in step 2 (in Table 2-1) of the RANSAC method which is for a two-dimensional line. Application in three dimensions

is achieved by applying the same principles once distinct multiple planes have been identified in the DSM.

The main disadvantages in the RANSAC method are its reliance on user-defined thresholds, namely: the total number of iterations that are permitted for the dataset; the permitted size of the 'inliers' area and; the number of points in an inliers set that is judged sufficient for that line to be refined and stored. These thresholds are most probably specific to types of roof and number of data points and may yet then be misjudged in DSM noise. Identifying sets of thresholds that can be applied to the DSMs in this research project would require substantial time and detailed verification. Also, in the field of roof recognition from low resolution LiDAR, defining distinct planes can be problematic. For these reasons, this technique also performs best on high resolution datasets so it is not likely that it will play a significant role in future work.

Step	Action	Diagram
A	Initial data: A set of $N$ points	 <p>A scatter plot showing a set of approximately 30 blue points distributed in a roughly linear pattern with some noise.</p>
B	Repeat the following:	
1	Choose a sample of 2 points uniformly at random and fit a line through them	 <p>The scatter plot from step A is shown. Two points are highlighted in red. A blue line is drawn through these two points, representing a fit to the sample.</p>
2	Compute the distances of other points to the line	 <p>The scatter plot and the line from step 1 are shown. Blue arrows indicate the perpendicular distances from several points to the line.</p>
3	Construct the inlier set using parameters to define an acceptable distance from the line.	 <p>The scatter plot and the line from step 1 are shown. A light green shaded region is drawn around the line, representing the acceptable distance threshold. Points within this region are considered inliers.</p>

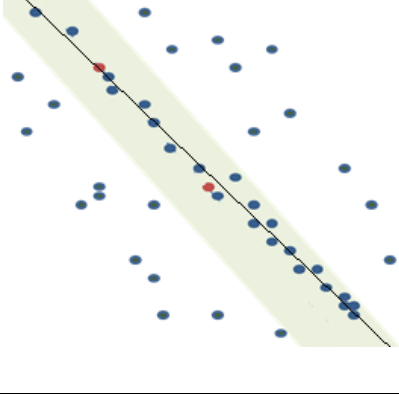
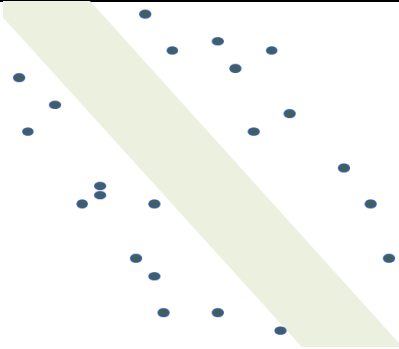
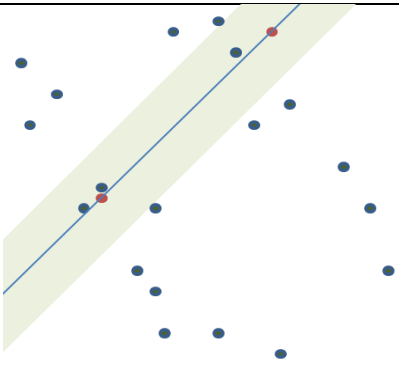
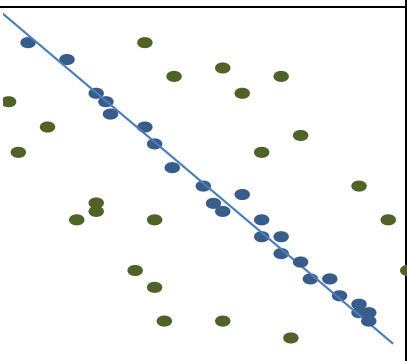
4	If the number of inliers is greater than a pre-determined threshold, refine the line and store its quality of fit, gradient and intercept.	
5	Remove the inliers from the set	
6	Repeat the process with the reduced number of points and reject poorer fitting lines.	
C	Stop repeating when Max.N.Iterations reached or too few points left. Then take the best fitting line.	

Table 2-1 The RANSAC process (adapted from Nguyen et al. (2005))

### 2.2.3.1.3 Region Growing

The final plane detection method is region growing which McGlone et al. (2004) describe as a process that starts with individual points (seed points) that are connected by a line to other neighbouring points according to given criteria such as colour or data value. Whilst McGlone et al. (2004) is a source that discusses region growing as a general concept in photogrammetry, Rottensteiner et al. (2005) applied the technique to plane detection from

LiDAR data. In this context, two points are connected by a line depending on their height values relative to other surrounding data points. This technique quickly identifies steep edges and places a line there. By allowing the construction lines to intersect, roof planes are defined that give the area, orientation and slope of each section of the roof.

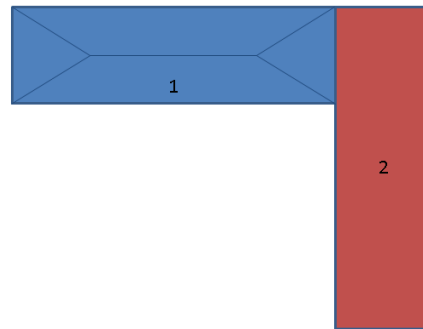
A common problem in region growing occurs when the initial seed points are incorrectly identified which in this context could be points on a chimney or the ground. Allowing these points to join to points to form planes would be an inaccurate representation of a roof. Also, this is a methodology that must have tolerances developed for how much deviation is permitted between points else, in noisy data sets like DSMs, incorrect planes can be identified. A final problem when applying this method to a study with large datasets is that region growing performs far worse than 3D Hough Transform in terms of processing time (Borrmann et al., 2011).

### **2.2.3.2 Model-driven Approaches**

A more viable option for low density and high noise DSM data may be to test the quality of fit of a range of template roof shapes against the raw data. The same conclusion was actually reached by two authors of a study using a data-driven approach. In addition to the DSM resolution issues, Vosselman and Dijkman (2001) stated that DSM data has frequent flaws that mean there would be great benefit to producing "...a more global reasoning strategy that incorporates knowledge on the common shapes of buildings...". Those problems are summarized in Oude Elberink and Vosselman (2011) in that DSMs have: systematic and stochastic errors in the measurement; variable and relatively low densities of height measurements and; data flaws due to occlusion by neighbouring objects (e.g., overhanging trees) or the absorption of LiDAR pulses by water features and window reflections. The following paragraphs describe how common roof shapes are incorporated into efforts to model buildings starting with the disassembly of buildings down to basic shapes.

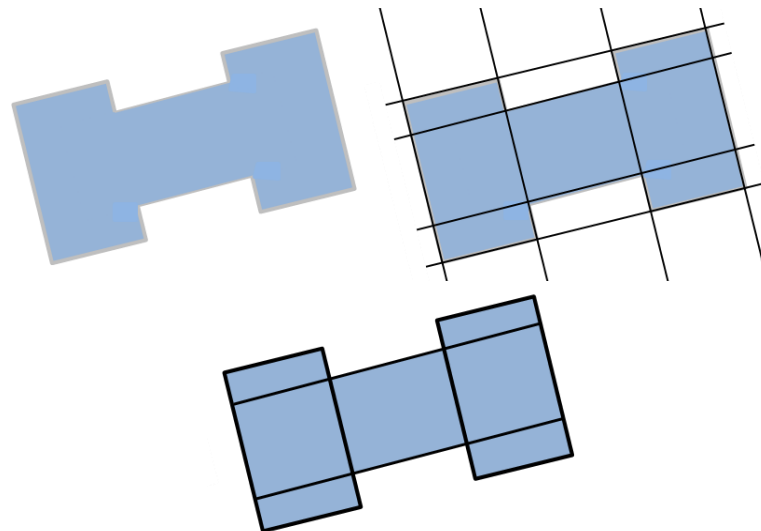
#### **2.2.3.2.1 Segmentation to Roof Primitives**

Building from the assertion that most complex buildings can be broken down into disaggregated 'primitives' (Brenner, 2000), model-driven methodologies seek to find a best fit between an idealised roof template and raw DSM data (Tarsha-Kurdi et al., 2007). A primitive is a rectangular polygon of a single uncomplicated roof type such as flat, gabled or hipped. Figure 2-9 shows a building made up of two distinct roof types: hipped (1) and flat (2).



**Figure 2-9 Plan view of a building with two distinct roof types: hipped (1) and flat (2)**

The first step required to break all properties in a city DSM down to their composite primitives is to detect cases where there are multiple roof types or significant changes in height at a property. Tarsha-Kurdi et al. (2007) use significant changes in building footprint shape as an identifier of where two different roof shapes are adjoined. Once the more complex buildings have been identified, their building footprints must be segmented to rectangular primitives. Various authors have suggested automated or semi-automated methods that could be adopted (Kada and McKinley, 2009; Ortner et al., 2007; Vallet et al., 2011). Kada (2007), however, provides the simplest explanation of the most suitable method. This approach centres on finding substantial sides of buildings from plan view building footprint data to the define primitives from their intersections (see Figure 2-10).



**Figure 2-10 Segmentation of building to primitives using major façades.**

It is recognised that this stage may lose the finer detail of a building footprint, however, given the resolution of the DSM can be as low as one point per 2 m<sup>2</sup> and the approximate size of the lost features (<10 m<sup>2</sup>), it is assumed that such features are not suitable for solar PV anyway. It is acceptable that then matching a roof shape will not produce a perfect fit to the original data but will represent the building in the best detail possible given the data constraints. It is worth noting that in such instances, a data-driven model that would



interpolate from any small amount of data would not accurately represent such small sections of a roof either. With each primitive defined the comparison to a template roof shape can begin. Most studies provide a small library of such templates and a good example has been shown in Figure 2-11 but equally comprehensive and succinct catalogues can be found in Henn et al. (2013) and Huang et al. (2013).

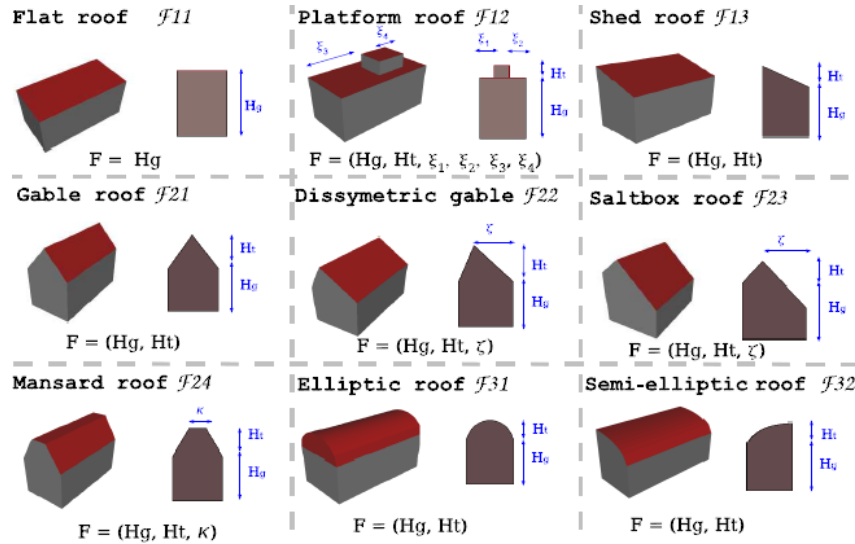


Figure 2-11 Library of roof primitives (Lafarge et al., 2010)

The advantages to using roof primitives instead of attempting to identify and define every plane as the data-driven methods require have been outlined by Huang et al. (2011). The first is that irregular or incomplete roof facets are not permitted as a roof template is forced to fit the data so no slight outlier points can alter the contour of the shape. Secondly, a vast number of buildings will be represented by those templates in the library. Finally, complex roofs can be interpreted more easily through effective combination of multiple simple roof shapes.

#### 2.2.3.2.2 Statistical Testing of Template Fit

The actual assessment of fit is, in the simplest instances, the sum of absolute differences in height between the raw data and the height value prescribed by the overlaid roof template, as used in Brenner and Haala (1999). Huang et al. (2013) have a more nuanced method for calculating the error in that it accounts for the fact that multiple planes are being tested for goodness of fit. They present the equation below in which  $M$  refers to the specific template being compared to the data points,  $D$ , which leads to a 'z-error' value ( $\Delta_z$ ):

$$\Delta_z = \frac{\sum_{f \in \mathcal{F}} \left( \sum_{i \in \Omega_f} |z_M - z_D|_i \right)}{K} \quad (2-34)$$

$f$  is an individual facet from the facet-set ( $\mathcal{F}$ ) of the primitive  $i$ , the data points in the domain of  $f$  are collectively  $\Omega_f$ , and  $K$  is the number of involved data points. Huang et al. (2013) use

absolute deviation instead of square deviation as the desired outcome is not the best fit to all the data points. Instead, finding a ‘consensus fit’ against outliers is preferred in this context as their  $\Delta_z$  calculation is less sensitive to data points caused by clutter objects and local maxima. The likelihood of a particular roof template matching a dataset is proportional to  $\Delta_z$  getting smaller, which can be described using a likelihood function  $L(D)$  as below:

$$\Theta \mapsto L(D) = L(X|\Theta) \propto \exp(-\Delta_z) \quad (2-35)$$

with  $\Theta$  the parameters of the template and  $X$  the observations. Unfortunately, the technique shown above has a tendency to score smaller shapes more favourably than larger ones and would result in smaller roof shapes than observed being taken forward as the best fit. Both Henn et al. (2013) and Huang et al. (2013) seek to compensate for this problem by using an Akaike Information Criterion (AIC). Henn et al. (2013) describe roofs classification using  $AIC_c$  which is an adapted AIC from Hurvich and Tsai (1989). The basic AIC is best described by the following equation from Huang et al. (2013):

$$H_M = -K - 2\ln(L(D|M)) \quad (2-36)$$

In essence, this equation places additional importance on the number of points being considered ( $K$ ) which is equivalent to the size of a proposed roof template. Whilst this is a vital step given the Huang et al. (2013) methodology uses only the DSM, it could easily be avoided by having the position and size of the template controlled by a building footprint segmented to primitives. This would save a large amount of computational time which is vital when looking to appraise individual buildings on a city-scale.

There are methods that significantly differ from this approach to establishing quality of fit. Poullis and You (2009) present a method for roof type identification with a flexible parameterized geometric primitive and in doing so determine the best model concurrently with the estimation of the model’s parameters. The geometric primitive created consists of only two parameters,  $\alpha$  and  $\beta$ , with which several building primitives are then created. The parameters are determined using a non-linear, bound-constraint minimization by means of Gaussian mixture models and an ‘expectation maximization’ algorithm. These complex procedures will not be further explored here because of their requirement for high-resolution data and their processing demands.

Another complex method for assessing the quality of fit and refining the model is through support vector machines (SVM) which have been the subject of many studies into classification, regression, and clustering problems common in building reconstruction from DSMs. Lodha et al. (2006), Haitao et al. (2007) and Römer and Plümer (2010) are amongst

the most significant studies in this area. Given the breadth of studies in this area and the complexity in executing such a technique, it is sensible to consider the approach of Henn et al. (2013) in a step-wise fashion in the same manner that RANSAC was described in section 2.2.3.1.2. The outputs created by the algorithm detailed below are: most likely model  $\tilde{M}$ ; corresponding probability  $P(\tilde{M}|X, R, C)$  and; corresponding standard deviation  $\sigma_{\tilde{M}}$  where  $X$  refers to the DSM data,  $R$  to the specific primitive rectangle being tested and  $C$  to the classifier.

	Action	Description
A	Initialise feature vector: $x_b = (x_{FP}, x_{M1}, \dots, x_{M1})^T$	To start with, this is a blank list of characteristics that will be assigned to the building being tested.
B	Determine model independent features $x_{FP}$	In a similar finding to Suveg and Vosselman (2004), Henn et al. (2013) state that characteristics of a building footprint suggest the building's specific roof type. For example, a rectangular footprint with a small area or low average height is very likely to have a flat roof. For this reason, they split features of the input DSM and footprint data into two groups. The first, $x_{FP}$ contains information on: <ul style="list-style-type: none"> <li>• general shape of footprint</li> <li>• perpendicularity (divergence of polygon angles to 90°)</li> <li>• number of touching buildings</li> <li>• azimuth angle of longest edge in footprint</li> <li>• ratio of length to width of rectangle (slimness)</li> <li>• area of footprint</li> <li>• median height of DSM data points</li> </ul>
C	Repeat the following for each model from the template library ( $M_i \in M$ )	
1	Robust estimation of $M_i$	This involves an adapted version of RANSAC called MSAC (M-estimator Sample Consensus) for the formation and refinement of the model template to test the data against. With each iteration, the model changes to a different shape from the primitive library.
2	Determine model specific features $x_{M_i}$	The second group is made up of features that depend on the roof model $x_{M_i}$ containing: <ul style="list-style-type: none"> <li>• inlier rate for the MSAC tests</li> <li>• complexity of shape</li> <li>• standard deviation of heights</li> </ul>

3	Determine model complexity $x_{C_i}$	Assigns an identification that depends on the roof template model. E.g. $x_{C_{i1}}$ for flat roofs, $x_{C_2}$ for shed roofs etc.
4	Classify $x_b$ with $C$ to derive the best model $\tilde{M}$ , $P(\tilde{M} X, R, C) = P(\tilde{M} x_b)$ and $\sigma_{\tilde{M}}$	These are the key outputs providing model details, probability of model fit and standard deviation of the data point heights to the model template. From this, the best model and its properties can be derived.
	End loop	

**Table 2-2 Roof classification by SVM (adapted from Henn et al. (2013))**

A family of methodologies similar to SVM has been presented by Lafarge et al. (2010), Huang et al. (2011) and Huang et al. (2013) who have implemented a reversible jump Markov Chain Monte Carlo (rjMCMC) algorithm to search for the best fitting geometry and position of a roof template. In this application of rjMCMC, a Markov Chain sampler is able to ‘jump’ from one roof template type from the primitive library to another once the maximum likelihood of a roof template is established from the varying of each template’s geometric properties and location. As such the rjMCMC algorithm applied in the studies can be described as shown in Table 2-3. Note that these methodologies are applied to a DSM without the location of buildings being defined by building footprint data, hence the first step is a global search to establish where a building might be amongst the ‘raw’ DSM.

	Action	Description
1	Global search of the DSM	One template is applied at different positions and with different geometric properties until a most likely fit is found (when the fit reaches a certain threshold)
2	Local search	There are then refinements to the geometric properties of the template
3	Jump to more complicated roof template	More complicated roof template then tested in area of maximum likelihood following the switch routine described in section 2.2.3.2.3
3a	Accept	If there is an improvement to $H_M$ (from (2-36)), accept the new model shape
3b	Reject	If there is no improvement to $H_M$ , reject the change of shape and try a different model following the rules of the switching routine
	Loop part 3	Repeat above until $H_M$ becomes stable or a predefined maximum number of iterations is reached
4	Add another primitive	When there has been a second primitive identified in the segmentation process (see section 2.2.3.2.1) there then follows a testing of a second primitive

		that is allowed to overlap with any preceding templates. This continues until a most likely fit is found
5	Merge the primitives	The two (or more) primitives are combined

**Table 2-3 rjMCMC algorithm as applied in Huang et al. (2011) and Huang et al. (2013)**

Final and most likely z-errors of individual roof reconstructions vary significantly, even when the buildings neighbour one another. With one particular example, Huang et al. (2013) state that the range of error in individual accepted primitives was between 0.05 m and 1.10 m for buildings within 100 m of each other. It is important to remember that this method is founded on an aim to create a plausible model despite a dataset plagued by noise. The values of z-error depend on the complexity of the original building shape and the success in building segmentation which will often omit smaller building parts. The authors argue, therefore, that z-error should be seen as a measurement of consensus, or the most likely fit, and not a directly comparable reconstruction error. This also means that a fixed z-error threshold for the acceptance of a candidate template is not feasible either so acceptance is defined by either  $H_M$  becoming stable or by a predefined maximum number of iterations being reached.

The example provided in the study shows a building made up of two distinct primitives taking 4,900 iterations to become stable. This raises questions about the suitability of the method for entire city-scale studies and suggests that it may only be applicable for problematic buildings either too small or complex for a less intensive method.

#### **2.2.3.2.3 Template Selection**

Model-driven approaches test multiple templates against the raw data to establish the best fit which leads to problems of template selection. Henn et al. (2013) use a sequence to test one template after the other in the most logical progression of simplest to complex roof shapes. In the same vein, Huang et al. (2013) use a series of switches to prevent a very intricate roof type such as a Dutch-gabled roof being tested immediately after the simplest, flat template which is shown in Figure 2-12. The progression through the sequence continues as long as the quality of fit improves. When it fails, a second switch back to the preceding template type occurs. Breaking down roofs to composite primitives permits the modelling of buildings with complex roofs as though they are collections of small simple roofs. Many methodologies attempt to go one stage further than modelling the major roof shapes of a large property and recombine the primitives to give a more detailed roof shape. Whilst this may be important for many fields of research where 3D modelling from DSM has to be highly accurate, it is not of great importance in the city-scale modelling of solar PV viability.

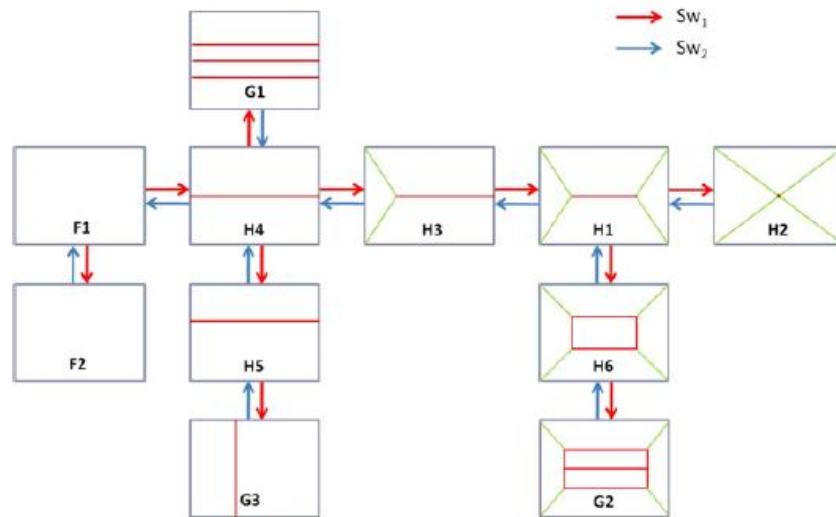


Figure 2-12 A 'jump routine' defined in Huang et al. (2013) for switching between primitive roof templates

### 2.2.3.3 Hybrid Approaches

There have been studies that cannot be described as entirely data- nor entirely model-driven as they combine elements of the two approaches. Oude Elberink (2009) presents a target based graph matching algorithm that relates model information with data features. These features are segments and intersection lines that are matched with 'graphs' (roof models) from a database. So there are stages of simple interpolations (data-driven) and corrections based on idealised roof templates (model-driven). This study presents an interesting combination of the two approaches but it requires very high-density LiDAR of 15 points per m<sup>2</sup> which is very unlikely to be available across the entirety of multiple UK cities in the foreseeable future. Lafarge and Mallet (2012) present another hybrid approach to building reconstruction from a DSM. Buildings are considered to be assemblages of primitives as per the model-driven methods described earlier but then mesh-patches are built from the DSM at points where fitting scores are poor and roofs become irregular which is more of a data-driven approach. The methodology is applied to a city-scale study area and validated in Lafarge and Mallet (2012) but as it has elements of data-driven approaches in the building of the meshes, it requires a large number of data points to accurately represent the irregular buildings. This issue is why the hybrid methods are not described further in this research.

This section has introduced the fundamental workings of solar PV panels and how insolation varies with the positioning of an installation which is defined by roof geometry. Two methodologies for the estimation of solar irradiance have been described as have the two groups of methodologies to assess roof slope, orientation and available area through roof geometry modelling.

### 2.3 City-scale Studies of Microgeneration Viability

There have been a number of studies to investigate the potential for city or regional deployment of renewable energy technologies. This section presents such methodologies and makes a distinction between those that have used DSMs and those that have not. As discussed earlier, the field of building reconstruction from DSM data grew considerably at the turn of the millennium so it follows that there has been somewhat of a lag in the refinement and transferal of the underlying techniques to a specific adaptation such as solar PV viability analysis. Therefore, there have been studies within the last ten years that have utilised other, more established datasets. For example, broad-scale land usage datasets have been combined with regional insolation databases to assess provincial and national potential for solar PV electricity generation in studies by Šúri et al. (2007) and Izquierdo et al. (2008).

Šúri et al. (2007) used the ESRA database which has monthly and annual averages of global irradiation at a resolution of 1 km x 1 km for 1981 to 1990. They carried out a preliminary analysis of regional and national differences in solar energy resource across the 25 EU member states and 5 EU candidate countries that they selected due to their affiliation to the EU JRC. Šúri et al. (2007) then assessed the potential for solar PV by defining a “standard” 1 kWp grid-connected PV system and calculating its annual electricity output in each of the selected locations. From here, the authors investigated both the theoretical maximum potential of solar PV electricity generation for each location and also how much solar PV would need to be installed to meet 1% of national electricity demand. This last aim reflects just how far the solar PV industry has come in the short time since 2007 as the majority of EU countries now meet at least 1 % of national electricity demand from solar PV. The paper goes on to discuss how national and supra-national legal and financial frameworks could be organised to promote the deployment of solar PV which is an interesting discussion but one that is slightly tangential to this research. The use of a “standard” 1 kWp array with optimised slope and aspect is a far less nuanced way to appraise broad-scale solar PV potential than this research is targeting. This research aims to be accurate at individual properties and yet rapidly deployable at the city scale and there are other approaches that offer outputs of a finer resolution than regional and national. Izquierdo et al. (2008) argue the case for this finer level of accuracy, stating that the development of effective energy policy and regulation is dependent upon rigorously founded assessment of the potential for renewable energies at the individual property scale. It is their opinion that the greatest barrier to an accurate and widely deployed model of solar PV potential is in the estimation of available roof area across an area. Their method utilises two groups of data. The first is broad scale land-use,

population and building density data and the second is a set of building footprint data samples for a selection of urban areas. Trends between the two groups of data are calculated and then applied at a national scale. This scale is of interest to national and supra-national bodies but will not aim to accurately estimate the available area of specific properties which is a central objective of this research. It is an interesting study because of its novel use of sampled building footprint data but there have since been studies in which that data is used directly to estimate available roof area across a city, such as Bergamasco and Asinari (2011a). Bergamasco and Asinari (2011a) do not calculate roof shape or slope. Instead, they assume the most popular roof type (gabled) and use average angles for residential or industrial buildings despite acknowledging that typical residential roof slopes in their study area have a range of  $15^\circ$  and that industrial properties have a wide variety of roof geometries. There are also assumptions in the reduction of roof space to account for chimneys, windows and air conditioning units that are defined for residential and industrial buildings separately. The orientation of the roofs is defined by a corrective factor to what would be generated by a south-facing installation which the authors have defined as 0.9. This is a highly inaccurate way to model a specific building and despite improvements made through the incorporation of orthorectified aerial imagery (Bergamasco and Asinari, 2011b), it is not an approach to be taken further in this research. It is the need to model roof slope and orientation at individual properties that means building footprint data cannot be used in isolation and DSMs are essential in order for the research aims to be achieved.

Kodysh et al. (2013) and Brito et al. (2012a) are examples of studies in which DSMs are used in combination with building footprint data. Both methods extract DSM data from the areas that fall within building footprints which are large enough to install a solar PV system. This reduced DSM data is then applied to a roof geometry and solar insolation modelling algorithm that is built in to the market-leading GIS software programme, esri ArcGIS. It is this level of complexity from which the research into city-scale solar PV power output presented in this thesis.

The city-scale study of wind microgeneration viability in urban and semi-urban areas has garnered less interest than solar PV, possibly due to the higher capital expenditure (CAPEX) costs entailed. However, it is also possible that the lack of accuracy that results from attempting to use broad scale datasets, such as land use, have meant that city-scale studies have not been practicable for wind. This conclusion was reached by Peacock et al. (2008) who stated that methods to predict wind energy had not yet been suitable for predicting



power output in an urban environment despite the bountiful resource that is there (Millward-Hopkins et al., 2013c).

Two studies that have sought to address this issue by translating a wind speed measured at a reference across an urban area are Sunderland et al. (2013) and Drew et al. (2013). Sunderland et al. (2013) focus on the city of Dublin, Ireland and use detailed wind speed measurements from the city's airport as reference data, a suburban site and an inner city site to compare a variety of techniques. They conclude that the log profile predicts wind speeds with more accuracy than a range of other techniques but only when the aerodynamic parameters are accurately defined. Similarly, the study of Greater London presented Drew et al. (2013) finds that extending the log profile from the UBL is a sufficiently accurate methodology. Both these studies, however, do not define the aerodynamic parameters from DSMs which provide a relatively accurate ( $\pm 0.5$  m) height-above-sea-level measurement grid with a horizontal and vertical resolution of at most 2 m. However, since Peacock et al. (2008), a small number of studies have sought to increase the accuracy of wind speed modelling using DSMs at their core (Millward-Hopkins et al., 2013a; Weekes and Tomlin, 2013) as discussed in section 2.1.3. From these datasets, the aerodynamic parameters in the logarithmic downscaling equations can be accurately defined for localised areas and the reported error in long-term average wind speed is  $0.3 \text{ ms}^{-1}$  (Millward-Hopkins et al., 2013b) which is sufficient to be used in power output and financial viability estimation.

Besides the estimation of wind or solar resource, various other factors have an influence on whether a site will be financially feasible or not. These include CAPEX and OPEX costs, electricity prices and government incentives (Kelleher and Ringwood, 2009). These factors have been highly variable in recent years which presents a complex problem when trying to best communicate the potential for wind and solar microgeneration. Two studies that have looked in detail at the issue of how to communicate the financial upside in two very different countries are Li et al. (2014) and Sun et al. (2013) which were focused on Ireland and Fujian Province (China) respectively. Unfortunately, the two studies are based on optimised individual installations in different parts of their study. However, that is not to say that their approaches to defining financial viability are any less useful, they just have not been applied on the scale that is of interest to this research. Both methods present clear frameworks of the costs and revenues associated with solar PV microgeneration and make use of payback time (years) and net present value (NPV (£)) viability metrics that are highly useful for this research. It is encouraging that studies of wind and solar microgeneration viability can also

be found in the literature that directly involve communities (Van Hoesen and Letendre, 2010), local authorities (Bristol City Council, 2012) and large private land owners (JBA, 2012).

## 2.4 Datasets

Sections 2.1 and 2.2 have described how wind and solar electricity is generated. Section 2.3 introduced studies that estimate the amount of electricity that could be generated by modelling the physical environment in which the technologies are installed. In order to then assess the financial viability of those installations, a range of costs and revenues have to be applied. All of the datasets that are required by each of these steps are summarised in Table 2-4. It is important to note that the DSM and DTM datasets are now free to the general public but that academic licenses were required in order to use the building footprint data. However, the DSM and DTM datasets that are available through this route are lower in resolution than those that are offered commercially but those privately sold datasets are prohibitively expensive for city-scale studies. This is an important theme that is returned to in later sections of the thesis. One further note is that the export and FIT rates have more than one source due to the changes made to them during the course of the research.

Name	Description	Units	Source(s)
Building footprints	Plan view outlines of buildings with vectorised height data attached	m	Landmap (2014b), MasterMap (2011)
DSM	First returned LiDAR measurement of surface height above sea level	m	Environment Agency (2016)
DTM	DSM data filtered to remove surface objects like vegetation and buildings	m	Environment Agency (2016)
DEM	Subtraction of spatially aligned DSM and DTM data to leave only the height above ground of surface elements	m	N/A
Domestic electricity costs	The average cost of domestic electricity per kWh, as calculated by DECC	£/kWh	DECC (2015a)
Export tariff rates	Payment for every unit of electricity exported to the grid from a renewable energy source	£/kWh	DECC (2013a); ofgem (2015)
FIT rates	Payment for every unit of electricity exported to the grid from a renewable energy source	£/kWh	DECC (2013a); ofgem (2015)
Solar PV & installation costs	The one-off total costs of a solar PV system including the cost of installation	£	Platt (2016b); Roberts (2016); Platt (2016a)

Wind turbine & installation costs	The one-off total costs of a wind turbine including the cost of installation	£	Kerr (2016); Bjerknäs (2016)
-----------------------------------	--	---	------------------------------

**Table 2-4 Summary of data sources**

## 2.5 Summary

This chapter has set the context for the research by explaining the fundamental physics of how electricity is generated from wind and solar energy and the causes of variation in yield caused by an installation's location and positioning. City-scale methodologies to assess the positioning and localised contexts in which the technologies are placed have been introduced and their propensity to generate error has been discussed. Also in this chapter, the financial considerations that determine installation viability have been defined and the sources of key datasets have been summarised. The themes of the literature discussed in this chapter are central to meeting the research aims of the thesis and the chapters that follow aim to improve the accuracy or practicability of the approaches that have been described.

## **Chapter 3 Solar Resource Appraisal**

The preceding chapters have explained how solar PV panels can be installed on the rooftops of individual properties and offer substantial emission savings (Bush et al., 2014; Goe and Gaustad, 2014). The sector has experienced tremendous growth in recent years (Cherrington et al., 2013; Muhammad-Sukki et al., 2013; Chen et al., 2014) but its expansion remains mostly dependent on a very large number of decisions to invest in separate projects (Sauter and Watson, 2007). The absence of reliable performance projections has been identified as a major barrier to the uptake of such low carbon technologies among individuals (Bergman and Eyre, 2011), land owners and local governments (Gouldson, 2011). The roll-out of solar technologies on a city wide scale could be supported by mapping the feasibility of solar installations (Bergman and Eyre, 2011) to influence not only individual property owners but also those responsible for entire portfolios. This process must be supported by accurate installation performance projections (Bull, 2012; Kanters et al., 2014) not on a case-by-case basis, but at the city scale where many thousands of potential investment decisions require information. The city scale approach has further advantages beyond influencing small-scale investment as policy makers would have access to estimations of the regional and national potential of the technologies underpinned by locally accurate appraisals. This could move decision making away from top-down studies based on generalised socio-economic trends that, by their nature, cannot be inspected to the individual property level.

Section 2.2 explained in great detail how electricity is generated from solar radiation and how the incident solar radiation on a surface varies due to its slope and orientation. Therefore, an accurate assessment of a proposed solar PV installation's performance requires detailed knowledge of the property's geometry and positioning (Hong et al., 2014). Height above-sea-level LiDAR data aggregated into a digital surface model (DSM) is a data source that can be used to estimate this information for buildings across an entire city as various sources demonstrate (Lukac et al., 2013; Jakubiec and Reinhart, 2013; Brito et al., 2012b; Kucuksari et al., 2014). This chapter aims to build on those methods and to explore how LiDAR data can be used for the appraisal of roof geometries at the city scale that are sufficiently accurate to underpin solar PV viability calculations.

### **3.1 Solar City Indicator**

In order to meet the research objective of estimating the viability of solar PV installations at the city-scale, research has been undertaken to appraise both physical and socio-economic controls on solar PV uptake across of a number of major UK cities. A 'Solar City Indicator' has

been calculated and used to rank the cities by their capacity to generate electricity from roof-mounted PV. Seven major UK cities were chosen for analysis based on available DSM and building class data; Dundee, Derby, Edinburgh, Glasgow, Leicester, Nottingham and Sheffield which are shown in Figure 3-1 to emphasise the distribution in both northern and central areas.



**Figure 3-1 Locations of the seven selected cities**

The physical capacity of each city was established using a GIS-based methodology to extract data from DSMs with distinct methodologies for large and small properties. To this, a socio-economic model was added using factors including income, education, environmental consciousness, building stock and ownership that were chosen based on existing literature and correlation with current levels of PV installations. The two groups of factors were then combined to produce a value reflective of each city's potential to install PV.

### **3.1.1 Methodology**

#### **3.1.1.1 Physical Capacity**

The physical capacity of each city was established using a GIS-based methodology, employing esri's Solar Radiation Toolset (ESRI, 2014) which exploits digital surface models (DSM)

generated from Light Detection and Ranging (LiDAR) data. With the location and plan area of buildings defined by building footprint data, a DSM can define slope, aspect and annual incident insolation for each rooftop. During this process a series of physical limits were imposed to restrict the evaluated insolation to areas where it would be feasible to install PV. These included:

- limiting the suitable area to the south facing component of roofs (i.e. an aspect between 90° and 270° from North)
- removing areas where insolation is estimated to be less than 850 kWh m<sup>-2</sup>, as such sites are unlikely to prove economic under conceivable tariffs, technology costs or electricity prices
- 10% of rooftop area was removed to allow for chimneys, aerials and other rooftop obstructions that 2 m horizontal resolution LiDAR data is too coarse to consistently capture
- limiting the suitable area of roofs to regions with slopes below 60°.

The restriction on slope was partly included to limit inclusion of crests, areas where transitions between two levels were encountered (which would likely be shaded), and sharp curvatures. The analysis also made an underlying assumption that roofs displaying a low and consistent slope were flat planes and not curved surfaces.

The ArcGIS Area Solar Radiation tool accounts for atmospheric effects, site latitude and elevation, slope and aspect, daily and seasonal shifts of the sun angle, and effects of shadows cast by surrounding topography (ESRI, 2014) and was described in section 2.2.2. However, the toolset does not account for weather and temperature. Fortunately, whilst regional temperature variations across the UK do exist, they are insufficient to cause a significant change in PV cell efficiency and output and can reasonably be ignored. Met Office data for 1981 to 2010 (Met Office, 2016) shows that the smallest annual mean minimum temperature of all the cities in this study is 5.3 °C for Dundee whilst the greatest annual mean minimum temperature is 6.6 °C for Sheffield. There is a similarly minor difference in annual mean maximum temperatures with 12.2 °C in Glasgow and 13.8 °C in Leicester (Met Office, 2016). Solar cell efficiency typically falls by only 0.4% to 0.5% for every 1 °C increase in ambient temperature (Markvart, 2003) so this study does not investigate this minor effect any further.

The influence of weather was accounted for using a corrective factor that was developed using Met Office weather data on the hours of direct sunlight observed in each of the

selected cities. For example, Glasgow receives fewer hours of direct sunlight in comparison to Dundee so its insolation estimations require a reduction that is proportional. The correction factor was derived from Met Office (2012a) data shown in Table 3-1 reflecting the number of hours of direct sunlight at each location. It was assumed that when experiencing periods of direct sunlight the computed insolation was broadly correct, whilst during times without direct sunlight panels would still benefit from a certain amount of diffuse radiation (about 31%). Thus the correcting weather factor,  $\gamma$ , was calculated using the formula shown in equation (3-1):

$$\gamma = \frac{(100 \times \beta) + ((1 - \beta) \times 31)}{100}, \quad (3-1)$$

where  $\beta$  is the recorded proportion of daylight hours featuring direct sunlight. This correction factor was applied to the insolation values derived from the ArcGIS Area Solar Radiation calculations. The weather factors employed are summarised in Table 3-1.

City	Proportion of daylight hours to direct sunlight hours	Weather factor ( $\gamma$ )
Dundee	0.3385	0.5436
Manchester	0.3135	0.5263
Nottingham	0.3139	0.5266
Edinburgh	0.3376	0.5429
Glasgow	0.2815	0.5042
Sheffield	0.3016	0.5181
Leicester	0.314	0.5267
Derby	0.3139	0.5266
Liverpool	0.3135	0.5263

**Table 3-1 Proportion of daylight hours for which there is direct sunlight from Met Office (2012a) data and the output weather factor for each of the seven selected cities**

Whilst this approach is limited in its accuracy when compared to approaches that use minutely weather data to assess if direct radiation is reaching a PV panel, the computational requirements to do so for seven city-scale studies were deemed impracticable. The final output of this part of the method was an estimation of insolation incident on exploitable areas of each large rooftop across each city.

For roofs of less than 200 m<sup>2</sup> an alternative methodology was devised to tackle digital representation inaccuracies that result from the insufficient number of incident DSM data points on smaller roofs. The methodology for smaller properties centred on extrapolating values typical to larger properties of the same building class in the same study area. Building classifications followed National Building Database criteria which categorise buildings based

on age and structure type (The GeoInformation Group, 2008). The potential output from small properties was estimated using the EU-JRC PVGIS model which required three inputs related to the buildings in the study areas, namely: the area of roof space available; the slope angle of the roof space; and the orientation of that roof space (EU-JRC, 2012).

Angles of slope for small property rooftops were estimated by identifying a characteristic slope for each building class from trends observed in large properties. The calculation of small property orientation distribution was again approximated using trends observed amongst different large property building classes. It was assumed that small properties would be arranged with a similar distribution of orientations to large properties, as both would be subject to the effects of defining features such as major rivers, motorways or coastlines. Finally the calculation of small property rooftop area suitable for a PV array was performed using building footprint data. This figure was then corrected for the typical roof being only half south-facing and for the presence of chimneys, skylights and other roof obstacles with 10% of remaining roof space removed following Bergamasco and Asinari (2011a). The EU-JRC PVGIS model tool takes into account insolation, weather patterns, topological shading, and system losses. An estimated correction for non-topography shading based on values suggested in Izquierdo et al. (2008) of 16% was applied to represent the impact of near-by trees and buildings.

The resultant outputs for large and small properties were used to determine the financial viability of available sites. This was achieved by computing the likely payback period based on energy bill savings and income from government incentives. In the UK, the FiT is paid for the total electricity generated, being independent of the amount of electricity used internally or exported at sites with installations except for larger installations. If the generator does not have separate import and export meters then the export tariff is usually calculated under the assumption that half of the electricity generated by PV will be exported to the grid and half used internally. The same assumption was used in these calculations. Electricity bill savings were calculated using DECC data on the average consumption of domestic properties in each city. The cost of installation for each array was then divided by the annual income achieved by the array to provide a payback time in years which is shown in equation (3-2):

$$\text{Payback} = \frac{C_{\text{installation}}}{EBS_{\text{Annual}} + ETI_{\text{Annual}} + FiT_{\text{Annual}}}, \quad (3-2)$$

where  $C_{\text{installation}}$  represents the cost of the installation,  $EBS_{\text{Annual}}$  is the annual electricity bill saving,  $ETI_{\text{Annual}}$  the annual export tariff income and  $FiT_{\text{Annual}}$  the annual FiT income.



A full list of costs and revenues has been provided in the following tables (Table 3-2 to Table 3-6).

<b>Name</b>	<b>Value</b>	<b>Source</b>
$C_{\text{installation}}$	See Table 3-3 and Table 3-4	Various
$EBS_{\text{Annual}}$	See Table 3-5	DECC (2010)
$ETI_{\text{Annual}}$	$4.5 \text{ p kWh}^{-1}$	DECC (2012)
$FiT_{\text{Annual}}$	See Table 3-6	DECC (2012)

**Table 3-2 Costs, revenues and their sources as of 09/11/2012**

<b>Size (kWp)</b>	<b>Panel</b>	<b>Cost (£)</b>	<b>Source</b>
0.69	Panasonic HIT-H250E01	2,923	Solar Essence (2012)
	Sharp NU-R250	2,923	
	Kinve KV250-60M	2,565	
	Komaes KM 240(6)	2,461	
1.25	Panasonic HIT-H250E01	5,295	Solar Essence (2012)
	Sharp NU-R250	5,295	
	Kinve KV250-60M	4,647	
	Komaes KM 240(6)	4,459	
1.5	Panasonic HIT-H250E01	5,618	Solar Essence (2012)
	Sharp NU-R250	5,618	
	Kinve KV250-60M	4,788	
	Komaes KM 240(6)	4,676	
1.75	Panasonic HIT-H250E01	6,033	Solar Essence (2012)
	Sharp NU-R250	6,033	
	Kinve KV250-60M	5,024	
	Komaes KM 240(6)	4,907	
2	Leeds Solar (value)	4,295	Leeds Solar (2012)
	Leeds Solar (high-spec)	4,999	
	Leeds Solar (ultra-efficient)	5,995	
3	Leeds Solar (value)	4,995	Leeds Solar (2012)
	Leeds Solar (high-spec)	5,750	
	Leeds Solar (ultra-efficient)	6,495	
4	Leeds Solar (value)	5,750	Leeds Solar (2012)
	Leeds Solar (high-spec)	7,195	
	Leeds Solar (ultra-efficient)	8,495	
5.5	Panasonic HIT-H250E01	12,584	Solar Essence (2012)
	Sharp NU-R250	12,584	
	Kinve KV250-60M	8,925	
	Komaes KM 240(6)	9,274	
7	Panasonic HIT-H250E01	16,016	

	Sharp NU-R250	16,016	Solar Essence (2012)
	Kinve KV250-60M	11,359	
	Komaes KM 240(6)	11,803	
8.5	Panasonic HIT-H250E01	19,448	Solar Essence (2012)
	Sharp NU-R250	19,448	
	Kinve KV250-60M	13,793	
	Komaes KM 240(6)	14,332	
10	Panasonic HIT-H250E01	22,880	Solar Essence (2012)
	Sharp NU-R250	22,880	
	Kinve KV250-60M	16,227	
	Komaes KM 240(6)	16,861	

**Table 3-3 Solar PV panel prices as of 14/12/2012**

<b>Size (kWp)</b>	<b>Approximate Cost (£ kWp<sup>-1</sup>)</b>
>10 - 50	1650
>50 - 150	1500
>150 - 1000	1200
>1000 - 5000	1200
>5000	1000

**Table 3-4 Approximate solar PV panel and installation costs as of 14/12/2012. Developed by linear interpolation from quotes by Anesco (2012)**

Installation costs were adapted from quotes which were correct as of 09/11/2012. Mid-ranging values were used for the kWp rating categories. Prices for larger installations were based on rough estimates per kWp obtained from communication with Anesco, a prominent UK-based energy services provider. Additional values for intermediary installation sizes were obtained by interpolation.

City	Total Electricity Consumption (kWh)	Average household consumption (kWh)
Dundee	811728506.5	5183.0
Manchester	2609606891.2	4140.4
Nottingham	1364510371.6	3759.5
Edinburgh	2642224648.3	4304.4
Glasgow	2956080911.5	4107.8
Sheffield	2448090110.9	3650.9
Leicester	1454341909.2	3752.0
Derby	1131908499.5	3958.2
Liverpool	1961985581.4	3993.7

Table 3-5 Total and household electricity consumption 2009 data (DECC, 2009)

Installation Size (kWp)	Value (p kWh <sup>-1</sup> )
4	21
>4 - 10	16.8
>10 - 50	15.2
>50 - 250	12.9
> 250	8.5
Stand-alone	8.5

Table 3-6 Feed-in Tariff Rates prior to 03/03/2012 (DECC, 2012)

The results were presented in a format to show total viable generation in kWh for one year increments in payback period up to 25 years, which was the FiT payments lifetime at the time of the study (2012) but has been set to 20 years since late 2013.

### 3.1.1.2 Socio-economic Potential

Research into the socio-economic factors that influence investment in solar PV is, at present, limited. Studies to date have only extended as far as survey and interview based experiments that are limited in scope. The importance of individual socio-economic factors is difficult to infer from the literature due to the wide range of aims amongst the studies. However, consensus has been found among a number of studies for the influencing factors presented in Table 3-7. All of the studies described here state that upfront costs represent a major barrier to the installation of solar PV. Two studies, Willis et al. (2011) and Claudy et al. (2011) found that the mean maximum price that investors would be willing to pay for a residential (2–4 kWp) solar PV system was £2,831 and £3,635 respectively. However, in this time period the actual cost of installation was generally closer to £6,000 for a 3 kWp solar PV unit (Solar Century, 2012). It has also been found that consumers desire payback periods to be around nine years (Claudy et al., 2011), whereas Willis et al. (2011) reported that in 2010, the time required is more likely to be over 10 years. Age and social class are linked closely to

knowledge of the technologies by Ellison (2004) and Caird et al. (2008) which has an obvious impact on the likelihood of investment. An interesting theme emerges in the literature that places great importance on the social acceptance of technologies such as solar PV, specifically in relation to installation on existing properties (Jager, 2006; Faiers and Neame, 2006). Whilst the public may only be interested in the passive consent of large scale deployment of energy technologies, microgeneration requires active acceptance and also then the drive to make the installation a reality (Sauter and Watson, 2007). Therefore, it is necessary to understand the impact that socio-economic factors can have on the uptake of solar PV in order to inform policy in this area, which was the focus of Keirstead (2007) and Candelise et al. (2010).

Socio-economic factor	Reference
Social influences	Claudy et al. (2011); Jager (2006); Faiers and Neame (2006)
Level of education	Claudy et al. (2011); Sauter and Watson (2007)
Level of grant support	Keirstead (2007); Candelise et al. (2010); Faiers and Neame (2006)
Age	Willis et al. (2011); Ellison (2004)
Environmental consciousness	Jager (2006); Sauter and Watson (2007)
Knowledge of the technology	Candelise et al. (2010); Caird et al. (2008); Ellison (2004); Sauter and Watson (2007)
Social class	Ellison (2004); Caird et al. (2008)

**Table 3-7 Influencing socio-economic factors identified from the literature for the uptake of solar PV.**

The first step in assessing the socio-economic potential was to determine which of the factors from the literature (Table 3-7) could be quantified for each city. Education levels of 4 to 5 (degree level), environmental consciousness (represented by recycling rates) and higher social class all showed significant correlations with current solar PV installations per household, across 20 UK cities. However, a strong correlation was found between social class and education level, and therefore, it was decided to remove social class from the analysis to prevent double counting.

Education level and environmental consciousness are considered to be factors that determine the desire of individuals to install solar PV. In addition, three ability factors were also included; mean income, proportion of houses/bungalows to flats and owner occupation. Income did not show a significant correlation with installed PV levels, however, this can be explained by the fact that under the FiT scheme prior to December 2011, a large number of “rent-a-roof schemes” were promoted. With favourable FiT rates it was profitable for

companies to offer free solar panels and installation to customers in return for the majority of subsequent FiT revenues. However, since the FiT rates have decreased these schemes have become less popular, and therefore it was decided that mean income should be included in the analysis. Data for these factors were collected from the following sources:

- Education level, owner occupation, proportion houses/bungalows: Census 2001 (SCROL, 2011; Office for National Statistics, 2010),
- Income: Survey of Personal Incomes 2007–2008 (Office for National Statistics, 2010),
- Environmental consciousness, represented by percentage of household waste recycled, Local authority collection data 08–09 (Defra, 2011) and Waste Data Digest 11: 2009 (SEPA, 2011).

The data for each socio-economic factor was then normalised by assigning a value between 0 and 1 across all cities. Each city was then assigned a socio-economic indicator, being the sum of the normalised socio-economic factors. It is acknowledged that quantifying socio-economic influences brings inherent complexities due to the strong connections between factors. Furthermore, it is simply not possible to assign a value to certain factors that may be important in overall decision making. Therefore the five factors analysed in this study had to be treated as dependent factors, although analysis looks at them separately in order to discover whether there are stand-out influences.

### ***3.1.1.3 Solar City Indicator Calculation***

Once both physical resource and socio-economic factors were quantified, the SCI was calculated by multiplying financially viable output per capita estimations by the corresponding socio-economic indicator for each city. The financially viable output was normalised by the relevant city's population to create a 'per capita' physical output calculation that allowed the comparison of the physical solar resource and final SCI across the different sized cities. This then permitted more detailed analysis of the impact of socio-economic effects on the overall results.

## **3.1.2 Results**

### ***3.1.2.1 Physical Resource***

The theoretical limit in this analysis refers to the cumulative output if all of the suitably sloped and oriented south-facing areas of all the buildings in the study areas were to have solar PV installed on to them. Put simply, it is the generation that is possible when no consideration is given to the costs or payback periods, human behaviours or logistics. In

order to use this information for comparing the selected study areas, Figure 3-2 shows the percentage of each study area's electricity demand that could be met under such an assumption.

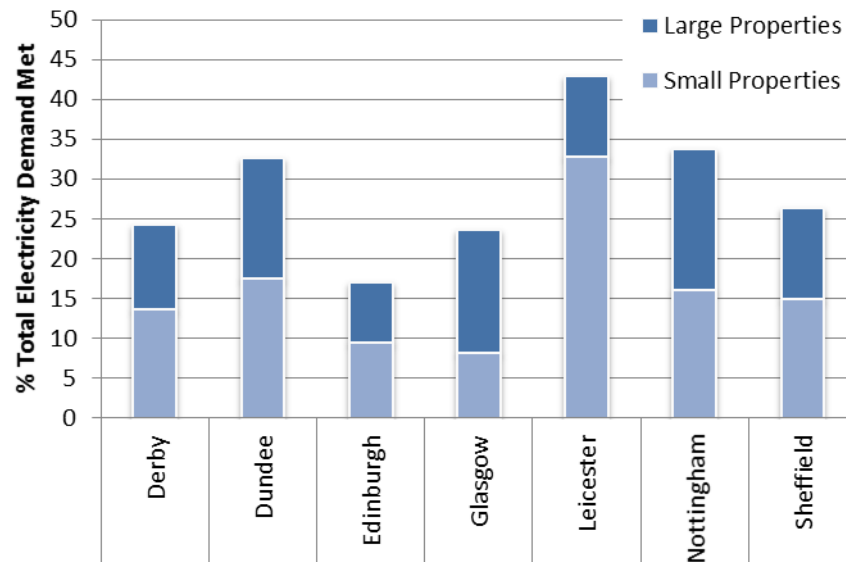


Figure 3-2 Theoretical limit to percentage of electricity demand met by all properties

Clearly, if cost, logistics and human behaviours held no influence, roof-mounted solar PV has the potential to meet a significant proportion of each city's electricity demand, up to 43% in the best case (Leicester). The results show no clear trend for latitude to strongly influence the physical resource when measured against a city's electricity demand and there was no discernible North-South divide as might be expected.

It is important to note that the theoretical limit is of little practical use but has been included to demonstrate the ultimate potential contribution of city-scale roof-mounted solar PV and to show that there are differences between the cities even at this low level of analytical complexity.

Figure 3-3 shows the percentage of each city's total electricity demand could be met from all installations to pay back within 15 years under baseline scenario. It is evident from Figure 3-3 that Dundee has the biggest potential which, whilst performing very well in terms of viable small properties, is primarily due to the high proportion of large buildings that are viable in terms of installation of solar PV. Dundee is characterised by buildings that are aligned to the Firth of Tay and so typically have a roof facet that is close to directly south-facing. The area also has an industrial legacy of large buildings with vast roof spaces. Owing to the economic decline of the area, many of the buildings are empty so their effect is two-fold: not only are the roof-spaces large and south-facing but there is not the increase to the city's total electricity demand that would be expected from a functioning large industrial

building. The worst performer is Edinburgh. The city has large annual electricity consumption for its size which may be related to large numbers of multi-occupancy, multi-level residences. To add context to this suggestion, Edinburgh and Glasgow both contain large numbers of tenement buildings meaning that many contributors to the city's electricity demand will share the same roof. Also, Edinburgh does not have the industrial heritage of the other study areas which provides a possible explanation for its contribution from large properties being the smallest in the analysis.

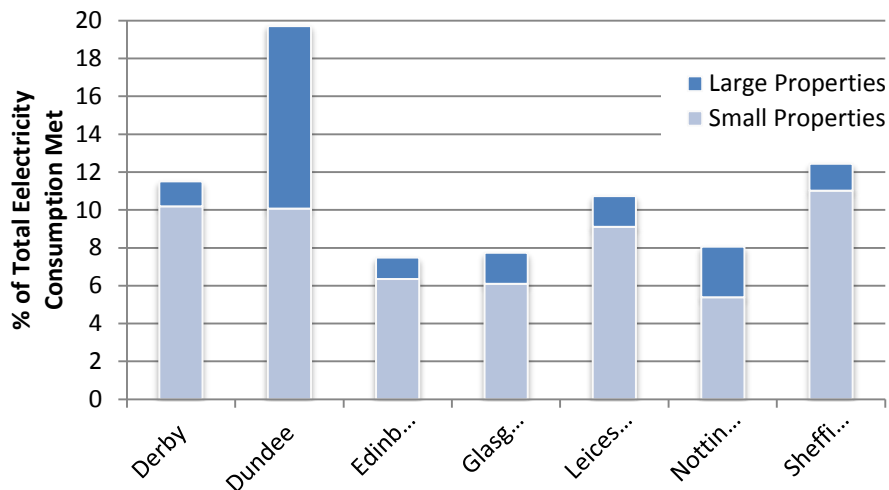


Figure 3-3 Percentage of total electricity demand met from all installations to pay back within 15 years under baseline scenario

### 3.1.2.2 Socio-economic Results

When averaged across all factors, Derby outperformed all other cities in terms of the socio-economic factors that would suggest tendency to invest in solar PV (see Figure 3-4). By contrast, Glasgow showed the least potential in the selected study areas. Manchester and Liverpool were removed from the physical analysis due to a lack of DSM data but have been retained for the socio-economic factor analysis to provide greater context.

The individual factors that contribute to the overall potential of a city to install solar PV show that Derby performs well in all areas. It is also very clear that Edinburgh performs exceptionally well in terms of education and income compared to the other cities, as well as performing very well in terms of ownership of homes. As previously stated, however, the prevalence of tenement flats and high-rise apartment buildings in the city means that many inhabitants will not own the roof-space where they live which greatly reduces the city's overall potential to install. This is also true for Glasgow, although Glasgow performed very poorly in terms of environmental consciousness (recycling) also. The income measure for Nottingham was comparatively poor but was compensated by the city's high levels of home ownership and proportion of houses to flats.

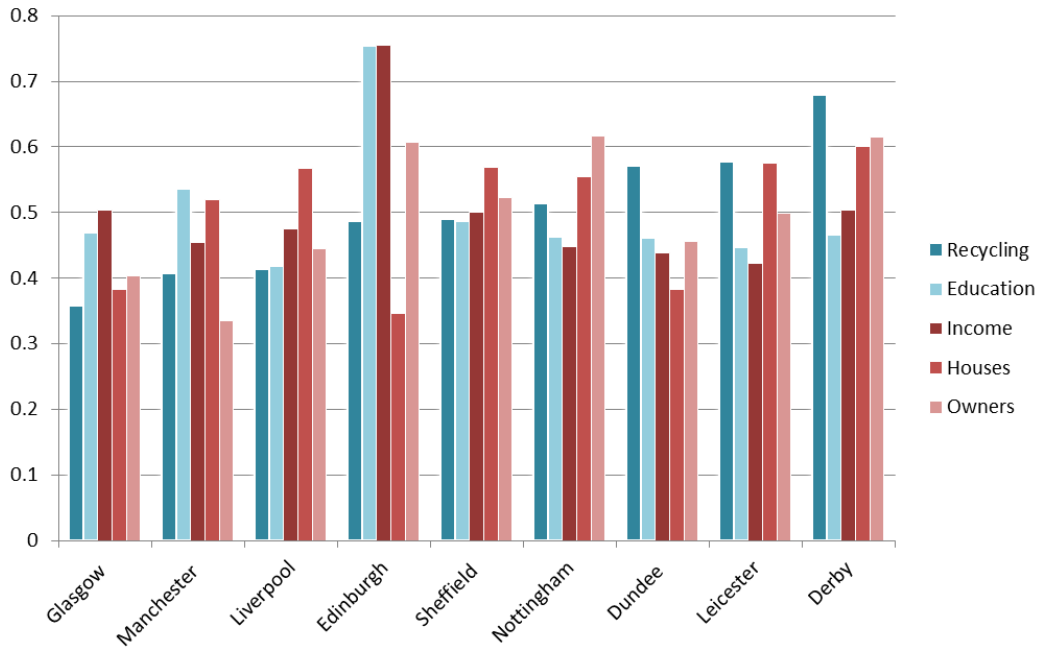


Figure 3-4: Individual indicators of potential to install solar PV for each city

The results of the socio-economic method have been validated by comparison to the actual installed solar PV per capita. Figure 3-5 shows that there is a positive correlation between the two with an  $r^2$  value of 0.5048 although this figure should be treated with caution given that there are only eight data points. Reference table data (Turner, 2014) for this number of observations show that there is a 90% confidence level to support the hypothesis of a correlation between the socio-economic indicator and installed capacity at the time of writing.

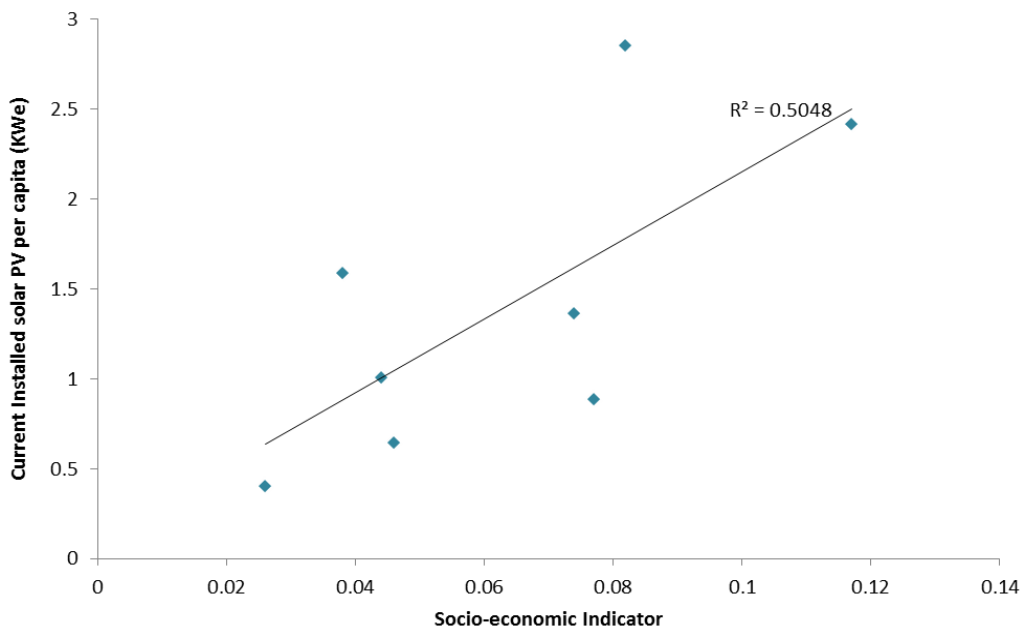
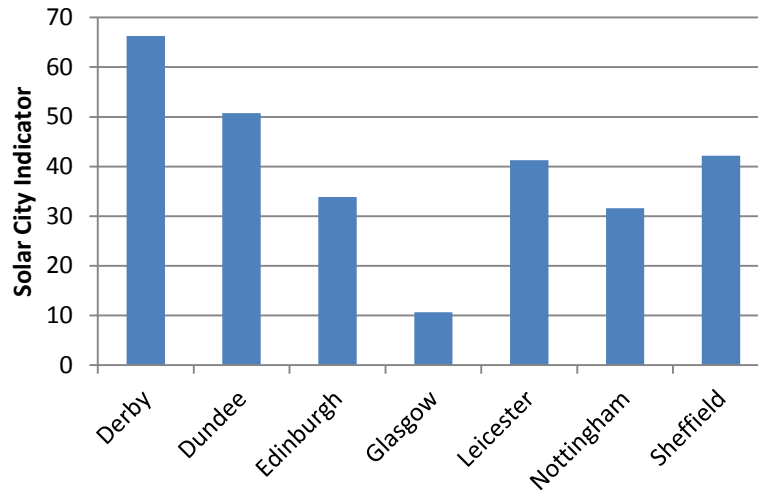


Figure 3-5: Correlation between socio-economic indicator values and installed PV per capita (as of December 2012) for each city



### 3.1.2.3 Solar City Indicator

The combined physical and socio-economic results of the analysis can be seen in Figure 3-6. It is clear that Derby has the greatest overall potential when physical and socio-economic potentials are combined and Glasgow has the lowest SCI.



**Figure 3-6 The Solar City Indicator values incorporating physical and socio-economic factors**

The SCI (Figure 3-6) results are significantly different to both the normalised physical indicator values (Figure 3-3) and the socio-economic indicator values (Figure 3-4). The methodology has been designed so that when the physical and socio-economic results are combined, socio-economic factors have a strong influence on the potential installed PV capacity of each city which has been supported by the correlation of the socio-economic indicator to actual solar PV uptake (Figure 3-5).

### 3.1.3 Conclusions

There is significant potential for solar PV microgeneration in the UK to the extent that a sizeable percentage of all cities' electricity demand could be met by the technology. This is despite the recent changes to the FiT which is shown to still provide incentive to investors at a large number of viable sites. Interestingly, the results did not show a clear north-south divide in physical resource as might have previously been expected based on climate as the most northerly city, Dundee, was found to provide one of the strongest physical resources. Dundee is characterised by a large number (relative to its population) of large industrial properties with roofs that face due South because of building alignment to the North bank of the Firth of Tay.

Differences in FiT rates and array costs between small and large arrays led to small arrays having shorter payback periods than large arrays. This showed the FiT mechanism was

skewed to aid investors in small PV installations rather than large. Whilst this shift could lead toward a more precisely targeted subsidy mechanism for small-scale PV microgeneration, it is also important to note the contribution of large properties in the present study roughly doubled the electricity generated in all cities. Whilst a key reason for the promotion of microgeneration is to affect a shift in behaviour and attitudes to energy, which may be best implemented by increasing the number of small arrays, the actual impact of PV in reducing carbon emissions and increasing energy security would be better served by a mechanism that could promote all scales of PV installations.

Cities with greater proportions of houses and bungalows to flats were found to perform better as ownership of the roofspace is essential to installation. Also, when a greater number of people live under one roof, it reduces the roof area per person for a city whilst the demand per person remains constant.

The study showed that the UK government was fully justified in shortening the time-frame of FiT payments for PV installations because the full cost of installation was repaid at all viable sites within 20 years and the further five years of payments were not necessary.

The study not only examined the potential for PV based on the physical resource but also provided some interesting findings regarding the socio-economic context of different areas of the UK. After all, before people decide whether they can afford solar PV, they must want to install it. Whilst the desire factors that could be quantified in this analysis were limited, they did show that there are potentially large differences in a city's likelihood to install solar PV. For example, if desire factors are studied in isolation, Edinburgh is significantly more likely to install PV than Glasgow. This suggests that the government may benefit from developing schemes to encourage potential investors that are tailored to specific regions' levels of understanding and motivations.

#### **3.1.4 Limitations and Scope for Further Work**

The socio-economic context to microgeneration investment is not explored further in this thesis, instead it is the flaws in the physical resource estimations that form the focus of further work.

A large source of error was the lack of accuracy in the estimation of solar resource for properties of less than 200 m<sup>2</sup> plan area. For such properties, a methodology in the style of Izquierdo et al. (2008) was applied in which trends observed in a city's large buildings were applied to smaller properties. This came about due to an inability to establish roof slope or orientation from the small number of DSM data points that each small property could

provide. This is a key problem as the vast majority of properties in a city are less than 200 m<sup>2</sup> and are unsuitable for the large properties method. Furthermore, it is at these properties where the greatest numbers of potential PV microgeneration investors live and demand an accurate appraisal for. Therefore, an improved methodology must be devised to reduce the minimum size of building that can be accurately appraised for solar PV potential that is less than the plan area of a typical domestic property.

### **3.2 Neighbouring Buildings Approach**

The resolution of DSM is critically important when attempting to model the slope, orientation and available area of roofs as it controls the amount of height data available for each building. As has been discussed, the current availability of DSMs in the UK with horizontal resolutions finer than 2 m is limited to small areas of cities at prohibitively high costs. It has been found that more widely available low-resolution 2 m data is too coarse to provide an accurate reflection of the number of roof planes and their angles when the plan area of a building is less than approximately 200 m<sup>2</sup> (Gooding et al., 2013). This is particularly problematic for city-scale roof shape modelling given that building footprint data for Sheffield, a typical UK city, shows that over 70% of properties fall below this threshold ([*Shape Geospatial Data*], 2011). This is a fundamental problem because it is at these properties where the greatest interest in microgeneration investment lies.

DSM data collection processes detect overhanging trees, chimneys and dormer windows which lead to inaccuracy in the assessment of building height and is exacerbated by the incumbent vertical error of the measurements that can be as great as 0.15 m (The GeoInformation Group, 2008). This is not insignificant as small property roofs are typically less than 3.25 m in height from eave to ridge. In addition, the datasets are also prone to noise and poor geospatial referencing. These issues mean that small property roof shapes and the angles of their facets are inaccurately estimated when using low-resolution DSM data and basic interpolation. Therefore, the most suitable approaches to roof reconstruction from low-resolution DSM data are those defined as model-driven methodologies as opposed to data-driven methodologies. The two types of methodology have been discussed in section 2.2.3 and to briefly recap, data-driven methodologies establish planes directly from the DSM or following a small degree of alteration. By contrast, model-driven approaches compare DSM data to a series of common roof shapes, or 'templates', with the quality of fit quantified, and the best performing template accepted as the modelled roof shape. This means that a model-driven methodology will always return a logical roof shape although it may poorly match the actual roof shape observed. However, this is an improvement on data-driven

methods that have been found to misinterpret low-resolution data and suggest a large number of nonsensical roof facets on each property (Jacques et al., 2014).

The methodology behind the Jacques et al. (2014) model-driven approach focuses on the city of Leeds, UK and uses the same 2 m horizontal resolution DSM as the method described in section 3.1. The smallest roof size for which geometry can be modelled is reduced considerably from the 200 m<sup>2</sup> threshold of section 3.1 as Jacques et al. (2014) outputs a modelled shape for all properties with 10 DSM data points or more. A roof with a plan area of 200 m<sup>2</sup> typically contains 40 to 50 DSM data points so this represents approximately a four-fold increase in the smallest roof shape that it is possible to model from DSM data.

Despite this increase in the number of buildings to which an estimate of roof shape can be derived from DSM data, there are limitations to the Jacques et al. (2014) method. Principally, the number of roof templates is restricted to either gable or hipped with roofs that fail the method being consigned to a “complex” category. This means that roof shapes that occur commonly across buildings smaller than 200 m<sup>2</sup> such as pyramidal and hipped roofs with a long ridge are incorrectly assigned to either the gabled or hipped categories which have significantly different areas available for PV. Alternatively, the method fails to recognise any roof shape and returns the complex result.

Secondly the building footprint data used to identify the location of roofs in the DSM undergoes no segmentation to remove peripheral building components. The DSM data of such areas can then lead to confusion in the goodness-of-fit regression test used to categorise the roof and a greater propensity to model as complex. The following work was undertaken to address these issues and further gaps identified in the wider literature described in section 2.2.3. An approach was devised that identifies similar segmented building footprint outlines that are within the same 250 m x 250 m grid square. The DSM data falling within the similar segmented building footprints are cleaned of outlier data points before being combined to create a dataset of far greater resolution than the original DSM. This higher resolution data is then compared to a series of template roof shapes in a similar fashion to existing model-driven roof recognition methodologies.

### **3.2.1 Method**

Segmentation processes are applied to building footprint data in order to remove peripheral building components, thus disregarding small building protrusions (<20 m<sup>2</sup>) that are unsuitable for solar technologies. The resulting segmented building footprints are assumed to define locations within the DSM containing roof-space potentially suitable for solar

technologies. They are also used to estimate orientation and to provide a basis for identifying similarities in the roof shapes of neighbouring properties. Buildings within the same 250 m x 250 m areas are grouped together if their segmented building footprint dimensions are similar. There is then a process to combine the DSM data from properties of the same group, thus creating a pool of DSM data of a finer resolution than from the original individual properties. The combined data is then compared to a series of common roof shapes in a model-driven approach, with the best fit selected as the modelled roof shape in a similar method to that of Huang et al. (2013), Lafarge et al. (2010) and Henn et al. (2013). Where there are no similar buildings to a particular property, outliers from the segmented individual building's data are removed before the ridge repositioning and template comparison proceed as normal.

The outputs of the methodology are the shape, slope, orientation and plan and sloped area of roofs in a study area. The methodology can, therefore, also better inform three-dimensional city models which have a wide variety of applications including solar resource estimation. The modelled data are validated against measured data from buildings across the study area (containing the city of Leeds, UK). The method has been designed for application on a city-wide scale meaning it can be implemented for a large number of buildings using only moderate computing power. Furthermore, its use of commonly available low-resolution DSM and building footprint data mean its application may be viable in more locations than those requiring finer resolution data.

### ***3.2.1.1 Footprint Segmentation***

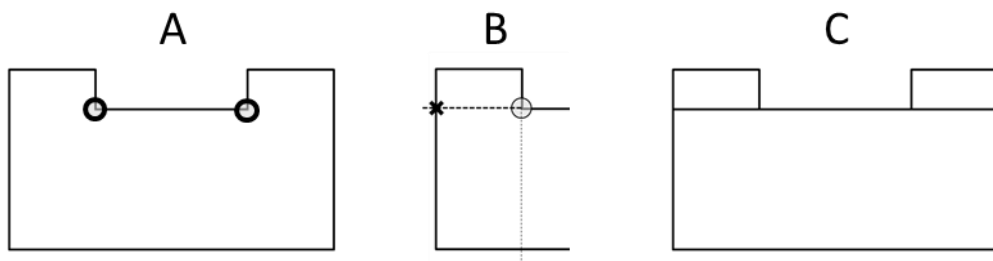
This process aims to establish the largest rectangle that can be inscribed in the original building footprint. Since the DSM only provides height above sea-level information, the boundaries of each property are established using building footprint data sourced from Digimap (MasterMap, 2008). The footprint data is of sufficient detail to include conservatories, porches and other protrusions on small properties which are unlikely to be suitable for solar installations. In addition, such building features can confuse template matching processes as they lead to a wide variety of height measurements across a building which are not representative of the main roof shape.

Segmenting polygons into simple shapes is a non-trivial problem in computational geometry with a body of literature describing potential solutions for specific conditions. A first level of complexity was explored by Fischer and Höffgen (1994) who examined inscribing axis-parallel polygons to convex polygons. Daniels et al. (1997) and Boland and Urrutia (2001)

presented methodologies of greater complexity that consider polygons containing both concave and convex angles but still only accept axis-parallel inscribed rectangles which may not define the largest possible rectangle. Conversely, Knauer et al. (2012) and Molano et al. (2012) have recently explored the problem of computing the largest rectangle of any orientation but only with regard to convex polygons. Hence despite the range of approaches, no single methodology provides a definitive solution to the particular problem faced in this work. However, the building footprint data consists of polygons with characteristics that can be exploited to create a relatively simple and computationally efficient solution. For instance, the small property polygons never feature internal holes, a large (>16) number of vertices or more curved than straight lines which all have the potential to increase computational demand (Molano et al., 2012). There also tends to be a right-angled vertex of the original building footprint that forms part of the largest rectangle that could be inscribed. Utilising these traits, the processes described in the following sections were developed for polygon types of differing complexity.

#### 3.2.1.1.1 Polygon Type 1

Polygons with internal angles that are all approximately  $90^\circ$  or  $270^\circ$  are segmented by proposing locations for a fourth vertex of a protrusion in the original building footprint outline. Concave angles in the footprint outline are identified (Figure 3-7A) as starting points for two intersection lines (Figure 3-7B), the first of which runs from the vertex preceding the concave angle, through the concave angle itself and on to its intersection with the polygon outline (Figure 3-7B grey line). The second line proceeds from the vertex following the concave angle through the concave angle and on to its intersection with the polygon outline (Figure 3-7B black line). The intersection point of the shorter line defines the fourth vertex of a smaller shape within the building footprint (marked with a cross in Figure 3-7B).

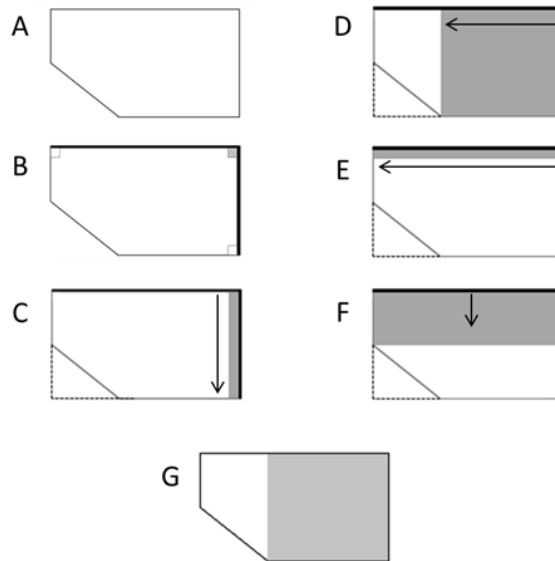


**Figure 3-7 Segmentation process from concave angles. A: Two concave angles circled. B: Creation of intersection lines from a concave angle and identification of an intersection point (denoted by cross) on the shortest. C: Final segmented shape after intersection process repeated for the second concave angle**

The process is repeated for each concave angle. Figure 3-7C shows a polygon with two segmented protrusions and a large rectangle that is assumed to define the location of the building's main roof part in the DSM.

### 3.2.1.1.2 Polygon Type 2

The process described above fails on polygons with internal angles that are not  $90^\circ$  or  $270^\circ$  (Figure 3-8A). For such polygons a second process is presented in which a rectangle is expanded from an internal right-angle of the footprint outline. First, the longest pair of lines to form a right angle in the original building footprint (Figure 3-8B bold line) are identified and used to project a fourth vertex of a new rectangle (Figure 3-8C dotted lines) that will be referred to as the 'large rectangle'.

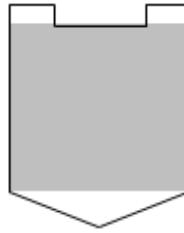


**Figure 3-8 A: Original footprint. B: Longest pair of lines to form a right angle (bold line). C: Large rectangle (dotted lines) formed from the longest right-angled lines. Also shows iterative expansion of a new, inner rectangle along width of large rectangle. D: Second expansion along length of large rectangle. E & F: Repetition of expansion process (length first). G: Larger shape created by the two expansions (in grey) accepted as main roof part of original footprint.**

A 0.5 m by 0.5 m rectangle is constructed at the intersection of the two longest lines to intersect at a right-angle (Figure 3-8B, grey square) that will be referred to hereafter as the 'new rectangle'. The new rectangle is expanded in increments of 0.1 m along the width of the large rectangle until it no longer fits inside the original building footprint (Figure 3-8C). The enlarged new rectangle is then expanded in increments of 0.1 m along the length of the large rectangle again until it no longer fits inside the original building footprint (Figure 3-8D) which defines a first inscribed rectangle. The double expansion process is then repeated but with extension by length preceding the enlargement in width (Figure 3-8E & F) to create a second inscribed rectangle. The larger of the two inscribed rectangles is selected as the best approximation for the location of the property's main roof structure from within the original building footprint (Figure 3-8G, grey rectangle).

### 3.2.1.1.3 Polygon Type 3

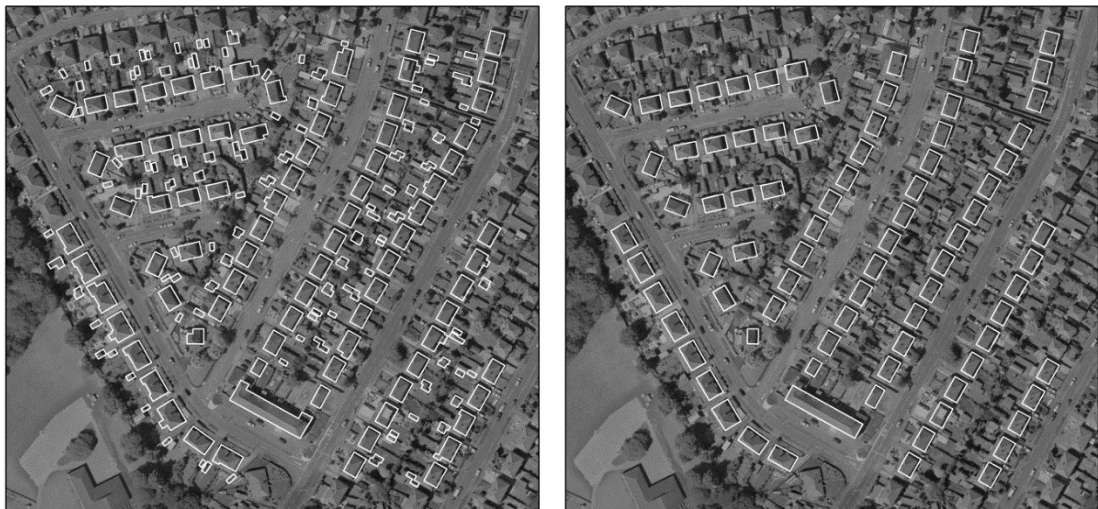
A small proportion of polygons fail the criteria of the processes described above, an example of which has been provided in Figure 3-9.



**Figure 3-9 Polygon (black outline) containing interior angles not approximately  $90^\circ$  or  $270^\circ$  and without right-angled vertices in common with the final desired segmented polygon (grey rectangle)**

Here the interior angles are not all approximately  $90^\circ$  or  $270^\circ$  and do not share right angles in common with the final segmented polygon. A brute force method is implemented for these polygons whereby a small rectangle is expanded and rotated incrementally from the centre of the original building footprint until it occupies the largest space of the original building footprint. There is no prior information to deduce if a building footprint shares any vertices in common with its final segmented building footprint so if the polygon is not type 1, the processes for polygon types 2 and 3 must both be executed. The larger inscribed polygon resulting from the two processes is accepted as the segmented building footprint.

The solutions for polygon types 2 and 3 are iterative procedures that reflect the lack of an elegant mathematical solution for this problem. The resulting modified building footprints are more suitable for identifying the location of roof shapes suitable for solar technologies within the DSM for extraction. Figure 3-10 shows an example of the outcome of the segmentation process when applied across a neighbourhood.



**Figure 3-10 Segmentation of building footprint data (left) across a neighbourhood to extract major roof parts (right) in neighbourhood 690**



The segmented polygons also provide a way to assess the size and orientation of roof structures, saving significant computational time compared to Huang et al. (2013) who use only DSM data and find building locations by ‘blob detection’ and size and orientation by localised iteration.

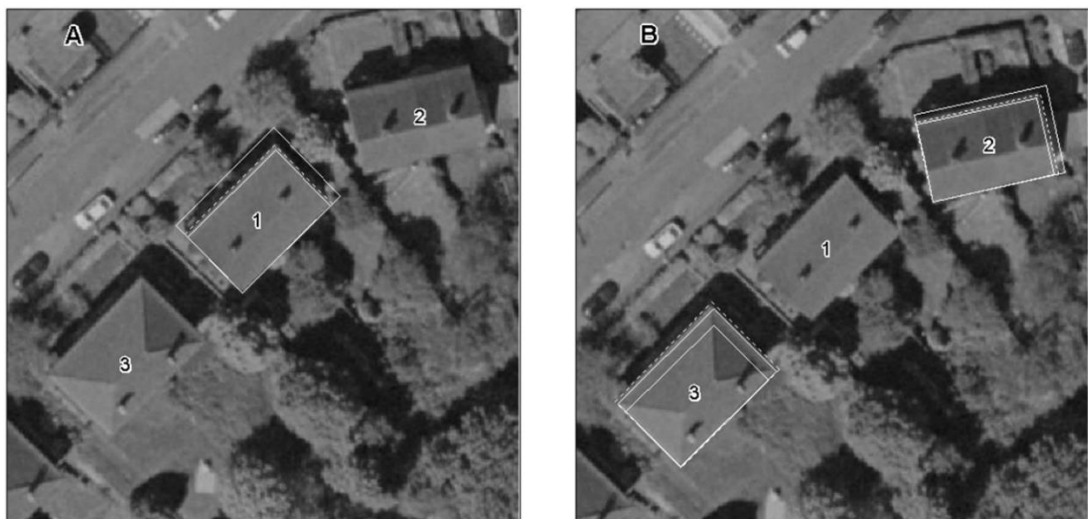
### 3.2.1.2 Data Combination Procedures

It is important here to restate that the combination of data is limited to neighbourhoods where there are similar buildings. The DSM data from buildings that do not share a similar neighbour still undergo the processing steps outlined below and are then compared to a series of roof templates without any combination of data and thus remain at low resolution.

#### 3.2.1.2.1 Similarity Identification

The dimensions of the segmented building footprints are used to identify similar shapes within 62,500 m<sup>2</sup> neighbourhoods. The buildings are categorised using bins of 1.1 m for length and 1.2 m for width which were empirically found to be robust thresholds to group similar buildings together. Buildings within the same bins for both dimensions are assigned to the same similarity group to have their DSM data combined following further processing.

The following paragraphs describe how the tightly constrained plan dimensional thresholds enable the grouping of buildings with identical roof shape. For example buildings 1, 2 and 3 in Figure 5 are within the same 62,500 m<sup>2</sup> neighbourhood and have plan dimensions that are alike, but building 3 has a different roof type (hipped) to 1 and 2 (both gabled).



**Figure 3-11 Similarity thresholds.** The small, solid white rectangles have the shortest length and width of the bin to which the building footprint (dotted white line) is a member. The larger, solid white-lined rectangle has the longest length and width of this bin.

The bin sizes used to assign similarity grouping are based on increments of 1.1 m for width and 1.2 m for length. For example, building 1 has a length of 13.05 m and width of 8.28 m

and falls in to a bin of 12.58 m to 13.78 m for length and a 7.98 m to 9.08 m bin for width. Figure 3-11A shows two rectangles constructed around the segmented footprint of building 1 (dotted outline). The smaller white outline has the dimensions of a rectangle with the smallest width and length of their respective bins creating a rectangle 12.58 m in length and 7.98 m in width. The larger white rectangle has dimensions equal to the longest edges of each bin, meaning a length of 13.78 m and a width of 9.08 m. For buildings 2 or 3 to be considered similar to building 1 they must have a segmented footprint that fits between the solid white lines.

Figure 3-11B shows that the footprint of building 2 fits between the solid white lines meaning it would be considered a similar building. The footprint for building 3 extends out of the two solid lines and so would not be grouped as similar to buildings 1 and 2. The method detects small differences in plan dimensions that reflect differences in building construction and roof shape.

#### **3.2.1.2.2 Outlier Identification and Height Normalisation**

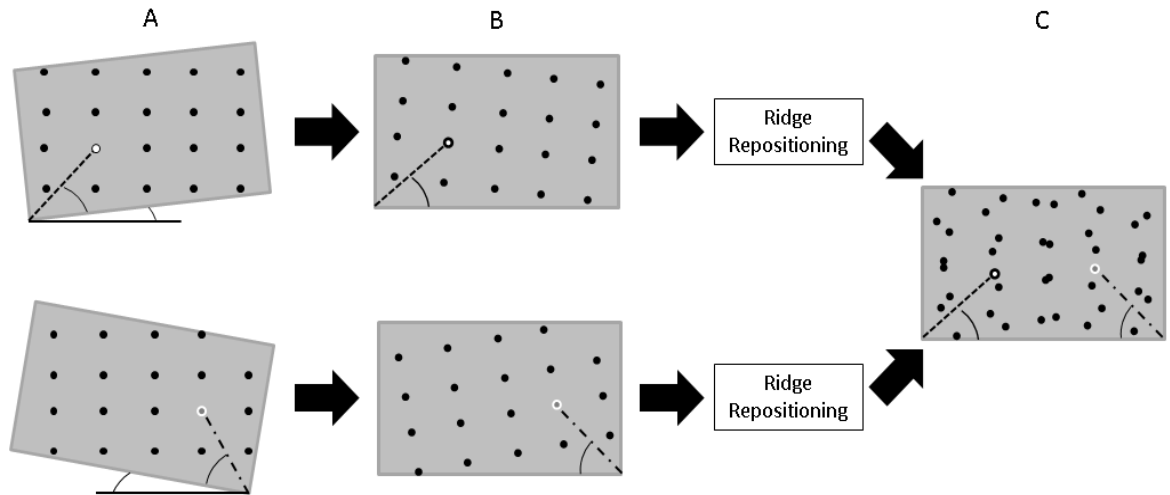
Building footprint and DSM data are often misaligned which can result in ground height data appearing inside a building footprint or conversely, roof data falling outside and being mistakenly disregarded. DSM data also tends to contain many outliers that must be identified and removed. Therefore, data points with an absolute height difference greater than 1.5 m compared to the average of their neighbours were removed.

DSMs provide height above sea-level measurements which means that data from two buildings cannot be directly combined without first normalising the heights such that they are made relative to ground or eave level. Therefore, the lowest height measurement of each property following the removal of outliers is used to define the roof's minimum height. The relative heights of the building's data points are then established by subtracting this minimum height from each DSM data point contained by the relevant segmented building footprint.

#### **3.2.1.2.3 Rotation, Ridge Repositioning and Combination**

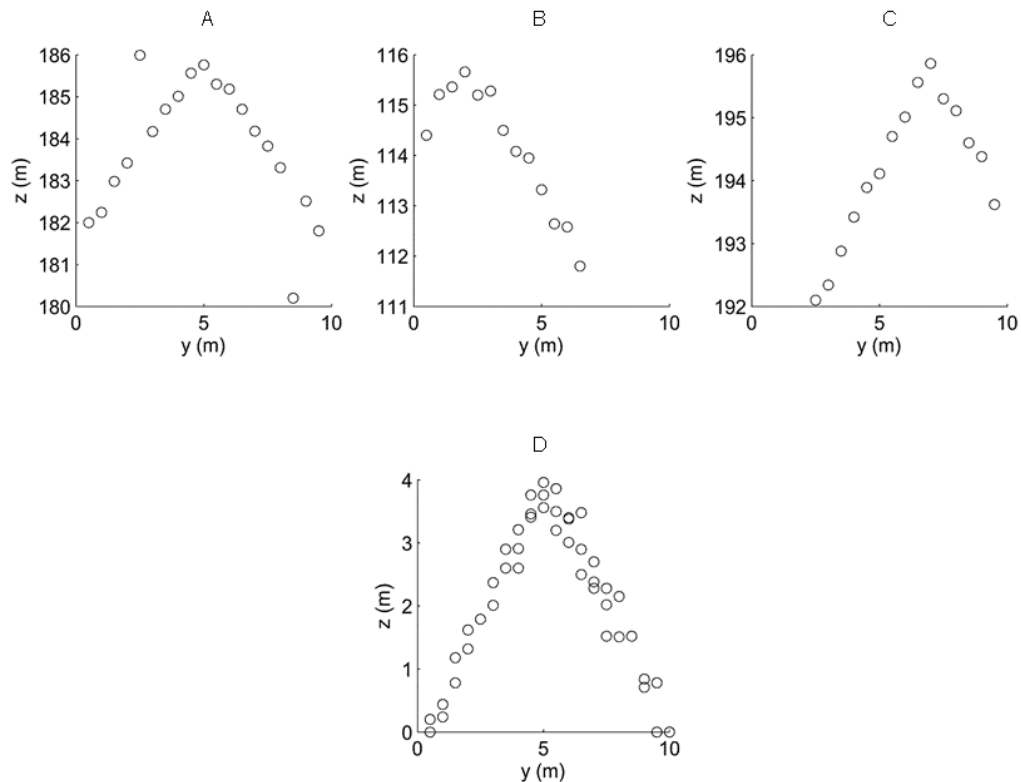
To enable the combination of similar buildings' data, each segmented building footprint and the DSM data it contains are rotated until the lengths of the footprint are made axis-parallel. The processed DSM data of similar buildings from a neighbourhood are then combined and in doing so a dataset of far higher resolution than the original individual buildings is obtained. The following paragraphs explain how this and the outlier identification algorithm are

executed using a gable roof shape template as an example because it is the clearest to visualise. The same approach is applied to the hipped, long hipped and pyramidal templates. The angle between the horizontal and the most southerly line in the building footprint outline is calculated as are the angle and distance of each DSM data point from the most southerly vertex of the building footprint (Figure 3-12A). This information is used to re-project the DSM data points into position when the building footprint is rotated to make its length axis-parallel (Figure 3-12B). This information is used to re-project the DSM data points into position when the building footprint is rotated to make its length axis-parallel (Figure 3-12B).



**Figure 3-12 Data rotation and combination procedure**

The rotated data is used to assess the true position of roof ridges in the data extracted from the DSM using each building footprint. Due to misalignment between the building footprint data and the DSM, the geometric centre of a segmented building footprint is often not the location of the tallest DSM data as would be expected for a symmetrical roof with accurate positioning. This problem is addressed to ensure that data from similar buildings are overlaid correctly. The data is split into 0.7 m bins along the y-axis of rotated data from individual buildings with ridge location identified by the bin containing the highest average DSM data.



**Figure 3-13 A-C: Rotated DSM data for three similar gable buildings prior to combination viewed from the y, z perspective. D: Combined data following height normalisation, outlier identification and ridge repositioning processes**

Figure 3-13A-C show datasets with issues that must be addressed prior to data combination. Figure 3-13A has two outlier data points whilst B and C show the outcome of particularly poor alignments between building footprint and DSM data as two aligned datasets would lead to a peak near 5m on the y-axis. Consequently B contains little data for the left hand side of its roof whilst the data in C has no information regarding its lower right hand side. All three datasets must also have their heights normalised prior to combination. The result of the combination procedures is demonstrated in Figure 3-13D where there is a complete roof profile free of outliers at a far higher resolution than data for individual roofs could provide.

### **3.2.1.3 Template Construction and Selection**

The combined data is then compared to the set of common roof shapes shown in Figure 3-14 with the best fitting selected as the most appropriate model of the similar buildings' roofs.




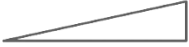


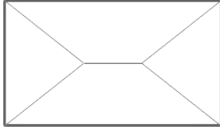





Plan	Width Elevation	Plan	Width Elevation
Flat 	Flat 	Shed 	Shed 
Gabled 	Gabled 	Hipped 	Hipped 
Pyramidal 	Pyramidal 	Long Hipped 	Long Hipped 

Figure 3-14 The roof template library

### 3.2.1.3.1 Construction

For a fair comparison the templates are constructed to achieve the best possible fit whilst maintaining the integrity of their shape. Therefore, templates are constructed using the combined data itself to establish eave and ridge heights from which the rest of the model shape is formed.

The data is first divided between the facets of the particular template depending on its x, y position. Facet dimensions are defined by empirical evidence from aerial photography such that, for example, the ridge length is 35% of the footprint length for the hipped template and 68% for the long hipped template. Figure 3-15 shows a hipped template with four numbered facets.

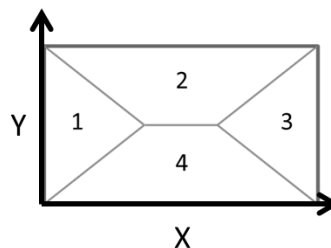


Figure 3-15 The four regions of a hipped template. 1 and 3: hip sections. 2 and 4: gable sections

Owing to the directions of the template's slopes, the y-axis information is disregarded for sections 1 and 3 of Figure 3-15 and regression is applied to the x, z data. By contrast, only the y, z data of sections 2 and 4 is analysed. The MATLAB® robustfit function (MATLAB, 2012) is used to execute an iteratively reweighted least squares fit that reduces the effect of any

remaining outliers that were not identified by the outlier identification criterion described in section 3.2.1.2.3. However, regression lines alone do not constitute a satisfactorily modelled roof shape because they fail to meet at the same ridge height and do not share a common eave height, which are two essential properties of a logical roof shape. Hence the regression lines are used to establish average eave and ridge heights. Returning to the hipped template example, the lowest and highest points of the four regression lines within the facets are averaged by weight of the number of data points in their respective facets, thus calculating the average minimum (eave) and maximum (ridge) heights of the prospective template. The eave and ridge heights are then used to define the template's final shape by constructing facets between them appropriate to the template type. At this stage, if the difference in height from eave to ridge is less than 2 m, all templates except flat and shed are rejected.

### 3.2.1.3.2 Selection

The constructed templates are then compared to the combined data using a z-error ( $\Delta_z$ ) metric similar to Huang et al. (2013) such that,

$$\Delta_z = \frac{\sum |Z_m - Z_d|}{K} \quad (3-3)$$

where  $Z_m$  is height above eave level suggested by the model,  $Z_d$  is the height above eave level of the combined data and  $K$  the total number of data points in the combined data. The template with the smallest  $\Delta_z$  value defines the best fit and provides the modelled angles of facet slopes. The data is compared to each template unless its length is less than 15.9 m, in which case the long hipped template is not tested as in early investigations it was found to bare close similarity to the gable template when scaled for building lengths shorter than this threshold.

## 3.2.2 Validation and Applications

### 3.2.2.1 Data Sources and Test Area

Building footprint data was sourced from EDINA (*[Shape Geospatial Data]*, 2011), a centre that provides spatial data for UK research institutions (EDINA, 2013). It provides the location and two-dimensional plan view shape of buildings which were used in this study to establish areas of the DSM containing roof height information. The 2 m resolution DSM and aerial photography used in the validation were sourced from Landmap (*Small-scale wind energy technical report*, 2008), a service that provided UK academia with spatial data until December 2013 (Landmap, 2014a). The methodology was applied to seven randomly selected 62,500

m<sup>2</sup> suburban neighbourhood zones in North West Leeds, UK containing a total of 536 buildings. Figure 3-16 shows four of the neighbourhoods selected.

The accuracy of roof shape and orientation modelling was validated by comparison to aerial photography. Slope estimation accuracy was appraised from site surveys for which a tripod-mounted laser distance measuring device with an accuracy of  $\pm 20$  mm over 150 m was used.

Across the seven tested neighbourhoods, the number of buildings within each grouping ranged from 2 to 68 and averaged 3.9. Typically 35% of buildings had to be regarded as individual for the tested neighbourhoods. It should be noted that this is highly specific to the test locations and that regional variations are to be expected. However, when the segmentation and similarity identification processes were applied to all neighbourhoods across the city of Leeds, a similar figure of 29.2% of buildings were defined as individual.

The similarity grouping criteria proved to be robust as comparison to geo-referenced aerial photography showed only three buildings (0.6%) erroneously grouped with others that did not share the same roof shape despite having similar plan dimensions.



Figure 3-16 Four of the neighbourhoods tested using the methodology where the white lines represent the building footprint data prior to segmentation

### 3.2.2.2 Model Outputs

An example of the model's outputs is shown for neighbourhood 364 in Figure 3-17 where the buildings are labelled by their similarity grouping before the modelled shape, angle and areas of each group are described in Table 3-8. Facet 1 refers to the modelled slope of the gable section of each roof. Where appropriate, facet 2 refers to the angle modelled for a hip roof section.

For neighbourhood 364, the method successfully modelled roof shape in 39 out of 41 (95.1%) cases. In the two erroneous results, the buildings concerned were regarded as individual buildings and so could only be modelled using the resolution of the input DSM.





**Figure 3-17 Neighbourhood 364 labelled by similarity grouping identification numbers**

The average error in the modelling of plan area for neighbourhood 364 was -6.75% and Table 3-8 shows that there was a slight underestimation in the majority of cases. This is due to both the inherent inaccuracy of building footprint sizes and the adjustments made to polygons that were not completely rectangular during the segmentation process. Slope was modelled with an average error of 2.36% for facet 1 slopes in neighbourhood 364 whilst facet 2 slopes were modelled with an average error of 6.26%. The greater error in the modelling of facet 2 slopes arises from the reduced amount of data available because of the smaller size of facet 2 compared to facet 1 for the long hipped template.

Group	Buildings (no.)	Modelled Shape	Actual Shape	Mean Segmented footprint Plan Area (m <sup>2</sup> )	Mean Measured Plan Area (m <sup>2</sup> )	Difference (% of Measured Area)	Facet 1 Modelled Slope (°)	Facet 1 Measured Slope (°)	Facet 1 Slope % Error	Facet 2 Modelled Slope (°)	Facet 2 Measured Slope (°)	Facet 2 Slope % Error
1	2	Flat	Flat	40.56	41.54	-2.37	n/a	n/a	n/a	n/a	n/a	n/a
2	1	Flat	Flat	68.98	72.17	-4.42	n/a	n/a	n/a	n/a	n/a	n/a
3	8	Hipped	Hipped	78.60	89.74	-12.42	29.12	29.62	-1.69	26.69	29.82	-10.50
4	1	Flat	Hipped	73.34	87.98	-16.64	n/a	32.5	n/a	n/a	31.29	n/a
5	1	Flat	Flat	46.07	43.59	5.69	n/a	n/a	n/a	n/a	n/a	n/a
6	1	Flat	Flat	199.00	186.5	6.70	n/a	n/a	n/a	n/a	n/a	n/a
7	5	Long Hipped	Long Hipped	158.92	183.78	-13.53	27.76	28.90	-3.94	31.97	29.68	7.72
8	1	Gabled	Long Hipped	152.00	184.09	-17.43	33.49	28.90	-15.88	n/a	29.68	n/a
9	18	Long Hipped	Long Hipped	164.31	184.58	-10.98	28.13	28.90	-2.66	33.45	29.68	12.70
10	2	Long Hipped	Long Hipped	176.50	187.67	-5.95	31.15	30.00	3.83	36.84	32.00	15.13
11	1	Gabled	Gabled	440.30	453.44	-2.90	11.71	11.40	2.72	n/a	n/a	n/a

Table 3-8 Model output for similarity groups of neighbourhood 364

Figure 3-18 shows modelled and observed orientation for neighbourhood 364. There was an average absolute error of  $0.82^\circ$  (0.39%) in orientation modelling which may result from slight inaccuracies in the positioning of the input building footprint data or slight changes that result from the segmentation process.

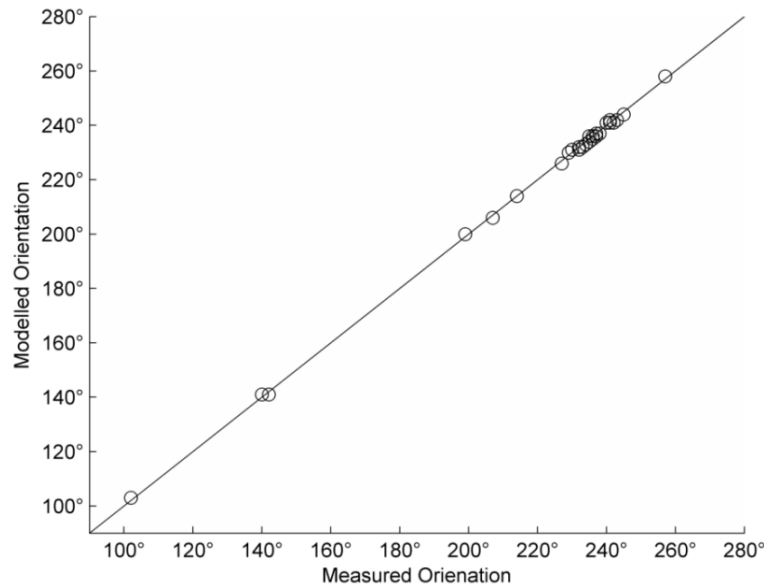


Figure 3-18 Modelled and observed orientation for neighbourhood 364. Line denotes a 1:1 relationship

### 3.2.2.3 Shape Accuracy

Across all seven tested neighbourhoods, the methodology found the correct shape for 87% of roofs, as shown in Table 3-9.

Neighbourhood	Total Buildings	Success (No.)	Success (%)
406	83	76	92
759	64	47	73
209	128	110	86
690	84	82	98
867	49	40	80
364	40	38	95
447	88	75	85
<b>Total</b>	<b>536</b>	<b>468</b>	
<b>Average</b>			<b>87</b>

Table 3-9 Shape matching success in seven tested neighbourhoods

This compares favourably with the one other existing methodology to use low-resolution DSM data by Jacques et al. (2014) who achieved a shape matching success rate of 81% based on a study of 242 buildings using a more limited roof template library.

$\Delta_z$  was found to decrease when the correct template was compared to data from an increasing number of buildings. Figure 3-19 provides  $\Delta_z$  values for five templates as data

from an increasing number of hipped roof buildings of a similarity group with eight buildings were combined and compared.

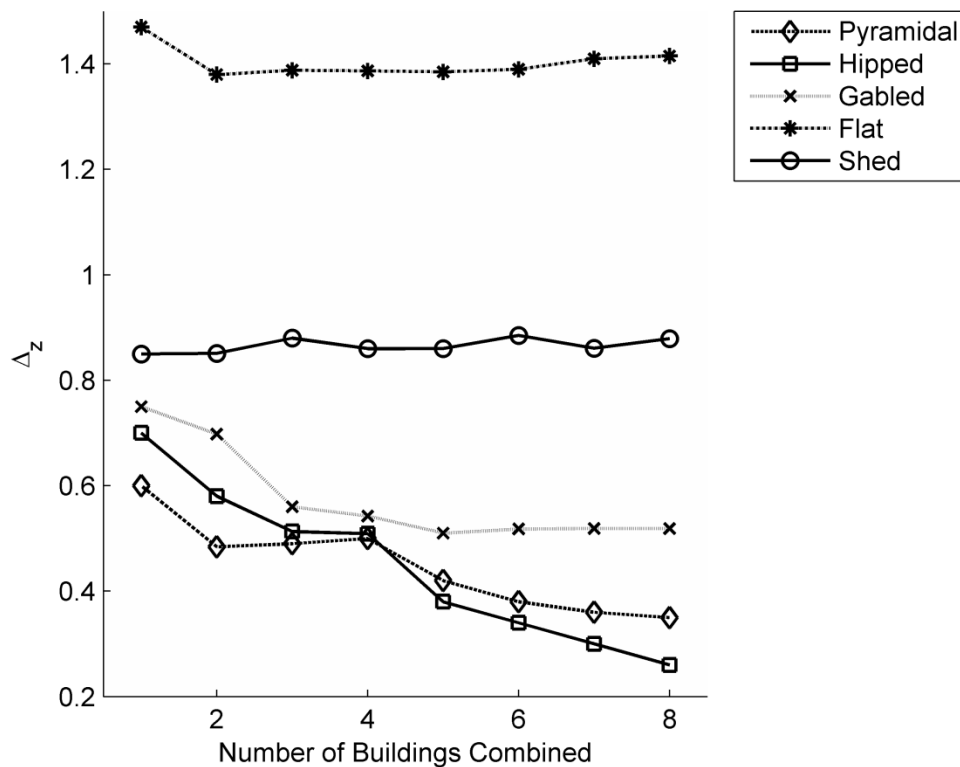


Figure 3-19 Changes in  $\Delta_z$  when data from an increasing number of buildings is combined. The correct template is hipped.

The initial trend for pyramidal, hipped and gabled templates is for  $\Delta_z$  to decrease as data from more buildings are considered in the comparison which signifies an improving fit. It is interesting to note that the correct template (hipped) only scored the lowest  $\Delta_z$  (and therefore best fit) after the DSM data of more than four buildings were combined. With fewer than five buildings' data, a pyramidal roof shape would have been incorrectly modelled, demonstrating the key advantage of using multiple similar buildings.

#### 3.2.2.4 Slope Accuracy

The facet 1 slopes of the modelled buildings were compared to the angles observed when 169 building roofs were surveyed. The mean absolute error (MAE) of each similarity group between the modelled and surveyed roofs has been calculated using the equation:

$$MAE = \frac{1}{n} \sum_{i=1}^n |f_i - y_i| \quad (3-4)$$

where  $n$  represents the number of slope estimations in each neighbourhood,  $f_i$  the modelled slope and  $y_i$  the observed slope. Table 3-10 shows that the MAE when averaged across all of the similarity groups in all of the neighbourhoods was 3.76°.

Neighbourhood	Surveyed Angle (°)	Total Buildings	MAE (°)
406	42.0	19	11.07
209	29.5	49	9.50
690	27.6	68	2.29
867	27.5	5	2.22
364	28.9	18	2.66
364	27.5	5	3.94
364	29.62	8	1.69
364	30.10	2	3.83
447	27.04	5	0.09
447	21.65	3	0.26
<b>Total</b>		<b>182</b>	
<b>Average</b>			<b>3.76</b>

Table 3-10 MAE in slope prediction of 169 buildings from a range of test neighbourhoods

The worst performing group of buildings (neighbourhood 406) had steep roofs of 42°. This could result in an increased probability of outlier identification failure due to the greater difference in height from one data point to the next on a steeper roof. For this reason the outlier identification process may have incorrectly removed data relating to the ridge of the steep roofs leading to a shallower modelled angle than that surveyed.

### 3.2.2.5 Comparison to a Data-driven Model

The simplest method to estimate roof slope would be to fit a regression line to the data points provided by each facet of a single building using, for example, the MATLAB® (MATLAB, 2012) robustfit tool. The expected geometry of the roof would be defined purely from the building footprint such that, for example, the ridge of a gable roof would occur exactly halfway along the width of the building. In this section we compare the slopes predicted for similar individual gabled facets under this more basic method ( $\hat{\beta}_{g-RB}$ , where g refers to gable facets and RB signifies the use of robustfit) and the angle modelled when the multiple buildings methodology described in the present paper was applied ( $\hat{\beta}_{g-MB}$ , where MB denotes the use of multiple buildings). A further comparison is made by applying  $\hat{\beta}_{g-RB}$  to the combined data of the buildings to assess the importance of the features in  $\hat{\beta}_{g-MB}$  other than the combination of DSM data from similar buildings, such as the ridge repositioning process. The buildings below were from a randomly selected similarity group of gable-roofed buildings and had a slope ( $\beta_g$ ) of 37° when surveyed, 3.06° greater than  $\hat{\beta}_{g-MB}$ .

Building ID	$\hat{\beta}_{g-RB}$ (°)	$ \hat{\beta}_{g-RB} - \beta_g $ (°)
2	25.51	11.49
34	8.44	28.56
41	29.07	7.93
44	33.44	3.56
48	35.40	1.60
49	31.03	5.97
Average	27.15	9.85
$\hat{\beta}_{g-RB}$ Combined	28.50	8.50

	$\hat{\beta}_{g-MB}$ (°)	$ \hat{\beta}_{g-MB} - \beta_g $ (°)
$\hat{\beta}_{g-MB}$ Combined	33.94	3.06

Table 3-11 Comparison of modelling gabled roof slopes using building footprint defined MATLAB® robustfit regression on individual and combined data (top) against  $\hat{\beta}_{g-MB}$  (bottom)

In Table 3-11, the average  $|\hat{\beta}_{g-RB} - \beta_g|$  value for individual buildings was 9.85° which is greater than the value for using combined data (8.5°) and substantially larger than the 3.06° value for  $|\hat{\beta}_{g-MB} - \beta_g|$ . This shows that the application of the robustfit MATLAB® tool in evaluating geometry derived from building footprints is a less accurate than the methodology presented here, even when the buildings are combined. Whilst a possible cause of the disparity between the two methods is the approach to identifying outliers, the main reason for the improved performance of  $\hat{\beta}_{g-MB}$  is the correction to the misalignment of the two datasets.  $\hat{\beta}_{g-MB}$  compensates for this misalignment by repositioning individual building DSM data prior to combination, enabling a fairer calculation of template suitability.

### 3.2.2.5.1 Benefits of Considering Multiple Buildings When Modelling Slope

Table 3-12 shows the modelled angles for the gabled ( $\hat{\beta}_{g-IND}$ ) and hipped ( $\hat{\beta}_{h-IND}$ ) facets from a randomly selected group of similar buildings with long hipped roof shapes when processed through the methodology individually (IND denotes the use of individual buildings). This means the segmented buildings' DSM data were each passed through the ridge centring, height normalisation and outlier removal processes, but not the rotation and combination procedures. When surveyed, the buildings were found to have gable ( $\beta_g$ ) and hip ( $\beta_h$ ) section facets of 27.5°. The final row shows the angles modelled when the data for the five similar buildings was combined and the complete methodology presented here ( $\hat{\beta}_{g-MB}$ ) was applied.

Building ID	$\beta_g$ (°)	$ \hat{\beta}_{g-IND} - \beta_g $ (°)	$\beta_h$ (°)	$ \hat{\beta}_{h-IND} - \beta_h $ (°)
6	22.63	4.87	*	*
13	29.5	2.00	21.99	5.51
18	32.24	4.74	42.07	14.57
19	34.85	7.35	41.27	13.77
28	15.46	12.04	*	*
<b>Average</b>		<b>6.20</b>		<b>11.28</b>

	$\hat{\beta}_g$ (°)	$ \hat{\beta}_{g-MB} - \beta_g $ (°)	$\hat{\beta}_h$ (°)	$ \hat{\beta}_{h-MB} - \beta_h $ (°)
$\hat{\beta}_{g-MB}$	29.72	2.22	33.53	6.03

**Table 3-12 Comparison of slope modelling when buildings were considered individually and when combined.**

\* denotes instances where building shape was incorrectly modelled and did not return an angle for the hipped section of the long-hipped roof template

The average  $|\hat{\beta}_g - \beta_g|$  error in slope estimation is 6.2° which is significantly greater than the 2.22° achieved using  $\hat{\beta}_{g-MB}$ . Buildings 6 and 28 of Table 3-12 are instances in which roof shape was incorrectly modelled as gabled when treated as individual buildings, meaning that no  $\hat{\beta}_{h-IND}$  value was returned, re-illustrating the benefit of using multiple buildings to model shape. Due to their size, the hip sections contain less data than gabled so it is unsurprising that the error in slope estimation is greatest for these parts.

As with roof shape modelling, considering an increasing number of buildings' data for the appraisal of roof slope led to more accurate results. In the following example, the roof slope angle predicted by the model was compared to the angles surveyed on 35 buildings from a range of neighbourhoods with a variety of roof shapes. The key result illustrated by Figure 3-20 is the general pattern of decreasing errors in modelled slope as data from an increasing number of buildings are combined.

The largest error shown in Figure 3-20 relates to data from neighbourhood 406 which was characterised by steeper angled roofs. Although requiring further investigation on a larger sample of steep roofs, the results suggest that the method is less accurate on roofs with a slope greater than 40°. Data from such properties have a greater difference in height between neighbouring points and the effect of alterations to the outlier identification criterion should be investigated in future work.

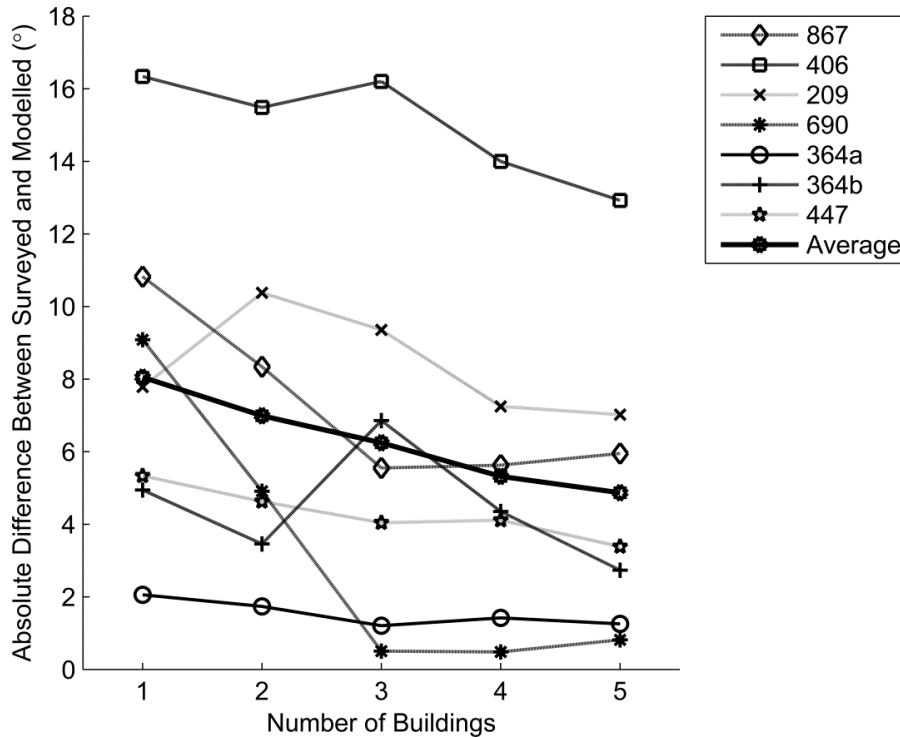


Figure 3-20 Slope accuracy improvement when using combined DSM data from increasing numbers of buildings. Legend items refer to neighbourhood IDs.

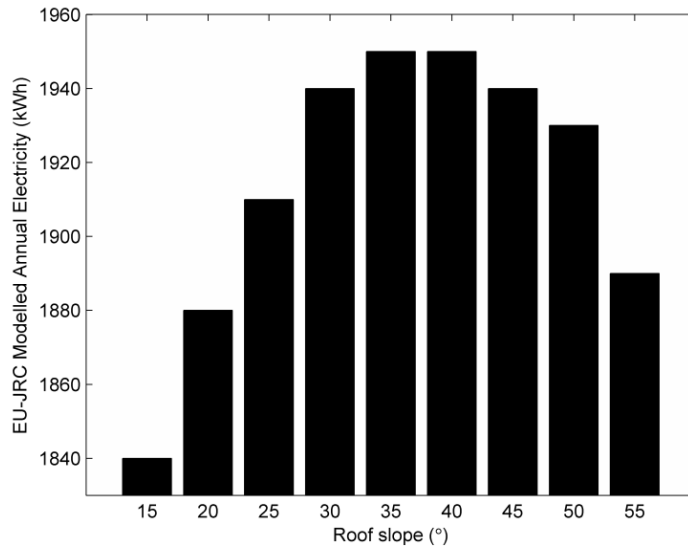
### 3.2.2.6 Suitability to City-Scale Application and Implications for Installation Performance Projections

Using only moderate computing resources, an Intel® Xeon® 3.1GHz processor and 4 GB of RAM, the method executed in under three and a half minutes on each neighbourhood including one particularly dense area containing 128 buildings. This suggests it would be suitable for the estimation of potential PV capacity on a city scale. It would however be important to take account of errors in modelled shape and slope in such estimations and this section discusses the potential impact of such errors on the projection of PV installation performance. It is acknowledged that there will be many other factors that influence the performance of solar technologies including accuracy in radiation estimation and shading from surrounding objects that are beyond the scope of this section which is focused on increasing the accuracy with which area, orientation and slope of roof-spaces are determined from low resolution DSM data. However, these issues are returned to in Chapter 4 of the thesis.

#### 3.2.2.6.1 Slope Errors and Performance Projections

On average over the test areas, the methodology modelled buildings to within 5° of the surveyed slope. Figure 3-21 shows annual electricity predicted by the EU-JRC PVGIS webtool (EU-JRC, 2012) for a 2.2 kWp system with optimised azimuth for increasing slope, demonstrating a non-linear relationship between the two.





**Figure 3-21 EU JRC PVGIS estimated annual PV power output for a 2.2kWp installation with optimised azimuth under a range of slope conditions**

Table 3-13 shows the range of power output predictions at a range of slope angles for a slope error of  $\pm 5^\circ$  and  $\pm 10^\circ$ .

Roof Slope (°)	% change in predicted annual power output for slope error of $\pm 5^\circ$ (%)	% change in predicted annual power output for slope error of $\pm 10^\circ$ (%)
25	3.14	4.71
30	2.06	3.61
35	0.51	2.05
40	0.51	1.03
45	1.03	3.09

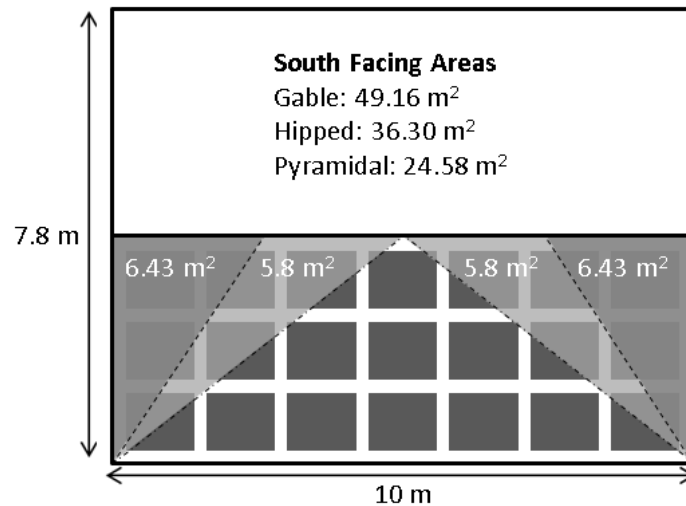
**Table 3-13 Difference in EU JRC annual PV power output estimations with changing slope**

This shows how sensitive annual power predictions are to errors in slope and in particular, how the sensitivity is greater for the extremes of slope compared to slopes close to the optimum value (approximately  $39^\circ$  for Leeds, UK). As discussed above, the MAE for the tested neighbourhoods using the current method is less than  $5^\circ$  and hence is sufficiently accurate to provide predictions of annual power output even for shallow roof slopes.

### 3.2.2.6.2 Shape Errors and Performance Projections

Available roof area is a function of modelled roof shape and orientation as PV panels are deployed on the most southerly facing roof facets of buildings. This emphasises the importance of modelling the correct shape of roofs to estimate the performance of PV installations. Figure 3-22 takes a hypothetical building with a plan area typical of suburban properties ( $78 \text{ m}^2$ ) and roof slope of  $37.5^\circ$  and investigates the impact on available area if it were modelled as gabled, hipped or pyramidal. The figure is a scaled drawing in which the solar panels are 1 m by 1.6 m and rated at 0.25 kWp to reflect a common PV panel on the

market. The darker grey regions on the periphery of the south facing slope represent the area that would be lost if the building were modelled as hipped instead of gabled. The lighter grey regions are the additional south facing area that would be lost if the building was modelled as pyramidal instead of hipped. The inset text states the south facing roof area under each of the templates.



**Figure 3-22** Effect of modelled roof shape on area available for solar technologies

From the available area calculations of Figure 3-22, the impact of roof shape on annual power output predictions could be investigated. The predicted power outputs shown in Table 3-14 were again taken from the EU JRC PVGIS tool (EU-JRC, 2012) for a south-facing, 37.5° sloped crystalline silicon panel type without any shading objects in the vicinity.

Modelled shape	Available area (m <sup>2</sup> )	System size (kWp)	Predicted Output (kWh a <sup>-1</sup> )
Gable	49.16	5.25	4,560
Hipped	36.30	3.25	2,820
Pyramidal	24.58	2.25	1,950

**Table 3-14** Effect of roof shape modelling on annual power output predictions

Table 3-14 shows the importance of finding the correct roof shape as it defines the south-facing area available for a PV installation and therefore system size. Power output is clearly far more sensitive to system size than to slope. In the example provided, the reduction in predicted annual power output from a gabled to a hipped property is 37.35%. The reduction if a hipped property were to be modelled as pyramidal is 50.23%, whilst if a property was gabled but incorrectly modelled as pyramidal, there would be a 68.82% loss in predicted output. Hence, achieving 87% success in shape recognition and 3.76° error in slope estimation has been shown to be especially important when seeking to model the potential for PV at every property in a city or for estimating a maximum yield from PV technologies across an entire region.

### 3.2.3 Conclusions

A methodology is presented to model roof shapes using building footprint and low-resolution DSM data. With moderate computing resources the method executes rapidly and so demonstrates high suitability for application across a whole city region which ties to the research objectives of the thesis.

In 87% of cases tested, the method identified the correct shape of the main roof part of buildings. This was validated using a total of 536 small buildings from different areas of the city of Leeds, UK. The MAE in roof slope was found to be  $\pm 3.76^\circ$  when validated against 182 buildings. Both roof shape and slope were more accurately appraised as greater numbers of similar buildings were incorporated into the combined data set.

Roof slope was defined with greater accuracy than by the application of regression techniques to areas of roofs defined by building footprint data alone. In the example provided, the error of roof slope calculation from the current method was  $3.06^\circ$  whereas using regression on areas of the DSM identified by building footprints led to an average error of  $9.85^\circ$ .

### 3.3 Summary

The importance of increased accuracy in modelling roof slope and shape has been discussed in terms of predicted annual PV installation power output with the caveat that there are additional local factors, such as shading, that may affect the performance of solar installations beyond the factors modelled in this methodology. The discussion shows that outputs from the method could be used to calculate payback periods for PV installations on typical residential properties with greater accuracy than previous methodologies. However, improvements to solar PV viability estimation result not only from greater accuracy in roof geometry modelling but also from improvements to solar insolation models and financial viability tests which form the foci of Chapter 4 and Chapter 6 respectively.

## Chapter 4 Improving Solar Insolation Modelling

This chapter presents literature that challenges the accuracy of the insolation model built in to the market-leading GIS software (esri ArcGIS) and then puts forward a methodology to improve the accuracy of insolation modelling. This is achieved through the integration of a shading model into a recently published method for estimating global radiation on exposed surfaces. The model is then tested against real-world observations of solar PV installation performance from several cities across the UK. To place these results into a suitable context, the accuracy of the esri ArcGIS solar radiation toolset and EU JRC PVGIS web-tool (built from ESRA data) at these locations are also presented. The final section of the chapter explains how the methodology could be adapted for city-scale applications which links to Chapter 6.

### 4.1 Criticisms of Existing Models

Gueymard (2012) provides a detailed comparison of clear-sky irradiance predictions from 18 solar radiation estimation methodologies including Fu and Rich (1999) and Hofierka (2002). Gueymard ranks Hofierka (2002) as the 8<sup>th</sup> most accurate clear-sky irradiance estimation method and Fu and Rich (1999) in last place, concluding that solar radiation routines included in existing GIS software are based on models that are of low or limited performance (Gueymard, 2012). It is important to note that whilst the validation sites used in Gueymard (2012) are renowned for the quality of insolation data captured, they are inconsistent with the urban locations at which solar microgeneration technologies are most commonly installed. For example, they are not subject to the same degree of shading from surrounding objects and topographical features as typical urban and suburban roofs and so it is important to investigate the accuracy of the proposed solar insolation estimation method against other methodologies in the context of urban areas. Of the solar resource estimation methodologies to utilise either the EU JRC PVGIS database or ArcGIS mentioned above, only Šúri et al. (2007) attempts to validate the findings of the solar insolation prediction. However, their validation utilises a meteorological model accurate to a resolution of 1 km<sup>2</sup> and is not compared to physical measurements inside the study area.

This work describes a methodology combining an integrated radiance model with a DSM-derived shading model to create a solar resource appraisal method suitable for urban areas. The outputs of the model are validated against measurements of PV power output converted to insolation estimations using performance ratios. The accuracy of two widely-used solar resource prediction methods are also investigated in this manner, namely the Fu and Rich (1999) method incorporated into esri ArcGIS software and Hofierka (2002) that has been

used in the EU JRC PVGIS webtool and solar radiation databases. The Fu and Rich methodologies will be referred to hereafter as FuRich whilst the methodology behind the EU JRC PVGIS webtool will be referred to as PVGIS and the method presented in this work will be referred to as RTS (Radiative Transfer with Shading).

The use of a DSM to define shading in RTS is a significant development from PVGIS which does not include shading from objects surrounding a site explicitly by default. Furthermore, PVGIS uses cloud reflection derived from satellite data to adjust clear-sky irradiance estimation. By contrast, RTS takes satellite derived cloud properties such as optical depth and cloud fraction and incorporates them directly into the radiative transfer equation. For these reasons, RTS is also far more detailed in its consideration of factors that affect annual global solar radiation than FuRich and PVGIS as will now be explained.

## 4.2 Method

The integrated radiance method (Smith et al., 2016) with a modification for shading was used to calculate the angled insolation at each site. The model uses the DISORT radiative transfer code (Stamnes et al., 2000) with a pseudo-spherical correction to improve accuracy at low Sun angles. The base direct irradiance is altered by atmospheric ozone and water vapour which is provided on an 8-day averaged basis from the MODIS Terra and Aqua satellite data on a  $1^\circ \times 1^\circ$  global grid. Morning conditions are provided by the Terra satellite data that is applicable to approximately 10:30 am each day and the Aqua satellite data that provides the afternoon observations (around 1:30 pm). The use of two satellite datasets allows diurnal effects to be incorporated in to the simulations. Aerosol extinction, single scattering albedo and phase function is introduced through the GLOMAP model, developed by Scott et al. (2014) that includes optical properties in 6 shortwave spectral bands for 4 aerosol species in 4 particle size modes. Cloud fraction, effective droplet radius, and cloud water content for liquid and ice are also provided from the MODIS Terra and Aqua datasets. Finally, surface albedo for 7 shortwave spectral bands is supplied on a  $0.05^\circ \times 0.05^\circ$  grid using combined Terra and Aqua data every 8 days as a 16-day moving average.

From the atmospheric and land inputs the radiative transfer simulation is run for the midpoint of each hour for each 8-day period of 2013 to produce the ground-level radiance field  $L$  along with the direct horizontal irradiance  $I_B$ , diffuse horizontal irradiance  $I_D$  and ground-reflected irradiance  $I_R$ .

Radiances are calculated on a discrete grid of  $3^\circ$  in the polar direction ( $\theta$ ) and  $10^\circ$  in the azimuthal ( $\phi$ ) direction giving a total of  $61 \times 36$  angular bins where the polar angle runs from

0° to 180° to capture both downwelling and upwelling radiances. To calculate tilted irradiance,  $I_T$ , the angular contribution of diffuse radiances  $L$  emanating from each 3°×10° sky bin is summed and added to the direct irradiance contribution, which approximates the integration of radiances as the limit  $\Delta\theta\Delta\phi$  approaches zero:

$$I_T = \sum_{i=0}^{60} \sum_{j=0}^{35} L(\theta_i, \phi_j) W_{ij} \Delta\theta_i \Delta\phi_j + I_B \left( \frac{\cos \theta_i}{\cos \theta_z} \right), \quad (4-1)$$

where:

$$W_{ij} = \max\{0, \cos \beta \cos \theta_i \sin \theta_i + \sin \beta \sin^2 \theta_i \cos(\phi_j - \alpha_p)\} \quad (4-2)$$

is a spherical geometry weighting ensuring that only radiances in the hemisphere of panel view are counted and  $\Delta\theta\Delta\phi$  is the solid angle of summation (3°×10°) in steradians.  $\beta$  is the panel tilt angle,  $\alpha_p$  is the panel azimuth angle,  $\theta_z$  is solar zenith angle and  $\theta_i$  is solar incidence angle. The sum approximates the integration of radiances as the limit  $\Delta\theta\Delta\phi$  approaches zero.

For roof spaces of less than 200 m<sup>2</sup> a single viewshed model is generated for the location of the PV panels. As section 2.2.2 states, viewsheds describe the height of the horizon in all directions from a specified point. Variation in shading across large installations on roofs of more than 200 m<sup>2</sup> is accounted for through the calculation of hemispherical viewshed models for every 25 m<sup>2</sup> that are then combined as follows. The heights of the horizon for each of the 32 search directions from each hemispherical viewshed model across the roof space are averaged to generate a mean hemispherical viewshed model, which is produced on a flat x-y grid of 201×201 pixels. This is then converted into a polar representation and binned into the same 3°×10° resolution as the radiance field. Each pixel in the 201×201 x-y grid is defined as unobstructed, obstructed, or outside of the hemisphere. For each bin the fraction of unobstructed pixels to the total pixels in that bin is used to calculate a skyview fraction  $f_{ij}$  for each of the 61×36 angular bins.

The radiance field is produced assuming a homogeneous flat surface and needs to be adjusted to take into account the obstructed horizon. The direct irradiance is a simple scaling of the skyview fraction for the bin the Sun resides in for the hour in question, becoming  $I_b = f_{ij} I_B$ . The diffuse sky irradiance is more complex as it emanates from all bins of the sky yet is not generally isotropic. Radiances from fully or partially obscured directions are reduced by that sky bin's skyview fraction and then summed over a horizontal plane such that the diffuse horizontal irradiance becomes

$$I_d = \sum_{i=0}^{30} \sum_{j=0}^{35} f_{ij} L(\theta_i, \phi_j) W_{ij} \Delta\theta_i \Delta\phi_j, \quad (4-3)$$

with  $\beta = 0^\circ$  in the definition of  $W_{ij}$  and the sum over  $i$  running to 30 (polar angle  $90^\circ$ ) as no upwelling radiances are required for horizontal downwelling calculations. The adjusted total downwelling horizontal irradiance due to horizon shading is modelled as

$$F = \frac{I_b + I_d}{I_B + I_D}. \quad (4-4)$$

The next stage is then to replace the radiances from fully or partially obstructed bins with a weighting between the ground-albedo radiance value  $I_R/\pi$  and the original diffuse sky radiance value and to multiply all the radiances by the hemispherical shading factor such that

$$l(\theta_i, \phi_j) = F \left( f_{i,j} L(\theta_i, \phi_j) + \frac{(1 - f_{i,j}) I_R}{\pi} \right), \quad (4-5)$$

assuming that the surface albedo of the ground and the obstruction are the same. Finally the shading-adjusted tilted irradiance is derived by substituting the  $l(\theta_i, \phi_j)$  from equation (4-5) back into equation (4-1) and replacing  $I_B$  with  $I_b$  in the same equation, to give

$$I_T = \sum_{i=0}^{60} \sum_{j=0}^{35} l(\theta_i, \phi_j) W_{ij} \Delta\theta_i \Delta\phi_j + I_b \left( \frac{\cos \theta_i}{\cos \theta_z} \right). \quad (4-6)$$

#### 4.2.1 Validation Data

The model has been validated using performance data from 20 PV installation sites across Bristol, Cambridge, Leeds, Middlesbrough and Sheffield in the UK. Figure 4-1 describes the distributions of azimuth (A) and slope (B) which were measured using DSM data of the validation sites and geo-referenced aerial photography. Array size (C) and power generation for 2013 (D) provided by the installation owners are also shown.

The performance of the installations at each validation site has been provided in terms of annual power output for 2013 whilst the models return estimations of annual global insolation. Therefore, a performance ratio (PR) is applied to estimate the annual power delivered by solar modules as a function of their rated power and global insolation. The PR is a measure of the actual power output of a module compared to its performance at standard testing conditions, and takes into account all system losses such as from the inverter and the effects of elevated cell temperature. The literature contains a range of PR values with Pearsall and Gottschalg (2012) suggesting 0.8 to 0.85, PVGIS using 0.75 (EU-JRC, 2012) and Ayompe et al. (2011) using experimental data to show that PR is approximately

0.8 for most of the year but slightly higher in November to January. Owing to the popularity of the EU JRC PVGIS tool, 0.75 has been selected as a lower bound PR value whilst 0.8 is also used as it better reflects the opinion of the scientific community.

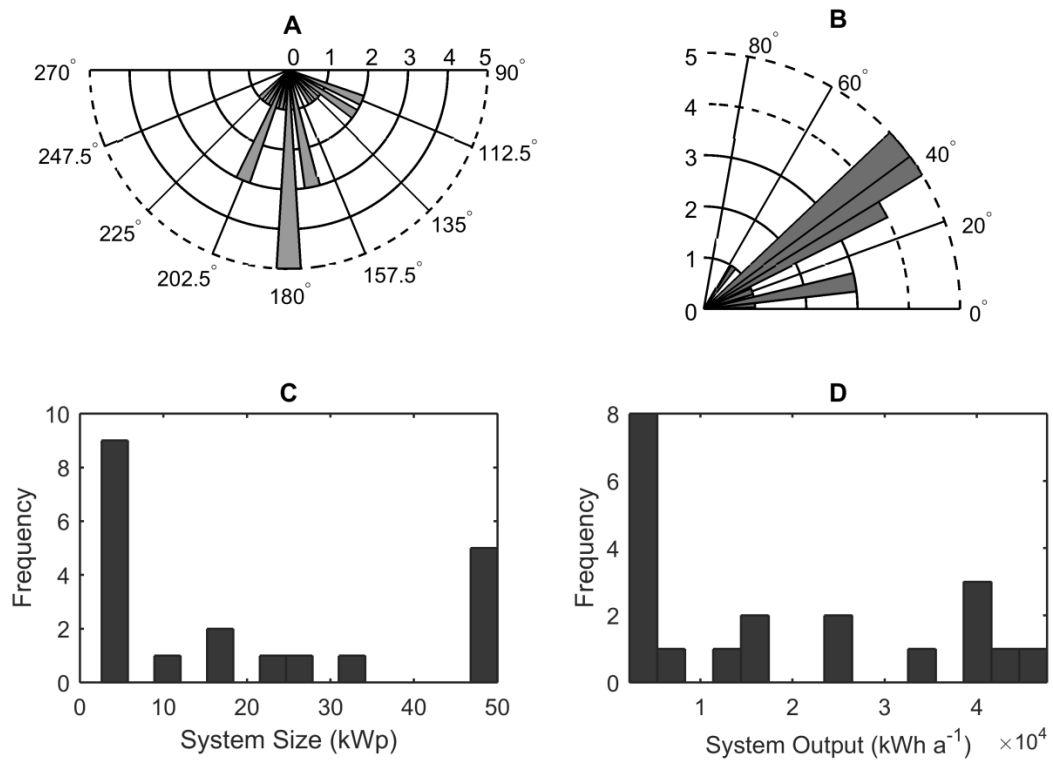


Figure 4-1 Orientation (A), slope (B), system size (C) and power output for 2013 (D) attributes of validation sites

## 4.2.2 Implementation of Existing Methodologies

### 4.2.2.1 *FuRich*

The solar radiation tool within the esri ArcGIS software was run for the validation sites in each city using a DSM of 2 m horizontal resolution. The latitude input was set to match the location of the relevant validation site. The time configuration was set to “whole year with monthly interval” and the year was set to 2013 to match the available validation data. All other options were left as default. The tool outputs an estimation of annual global solar radiation ( $\text{Wh m}^{-2} \text{a}^{-1}$ ) for each validation site.

### 4.2.2.2 *EU JRC PVGIS*

The EU JRC PVGIS webtool was used to estimate annual global solar insolation ( $\text{Wh m}^{-2} \text{a}^{-1}$ ). The locations of the relevant validation sites were found using the webtool map and a marker placed at the location of each installation. The appropriate slope, azimuth and system rating (kWp) were entered and the building mounted option selected. All other options were left as default. The webtool returned a webpage of annual global radiation predictions in  $\text{kWh m}^{-2}$  with a monthly breakdown.



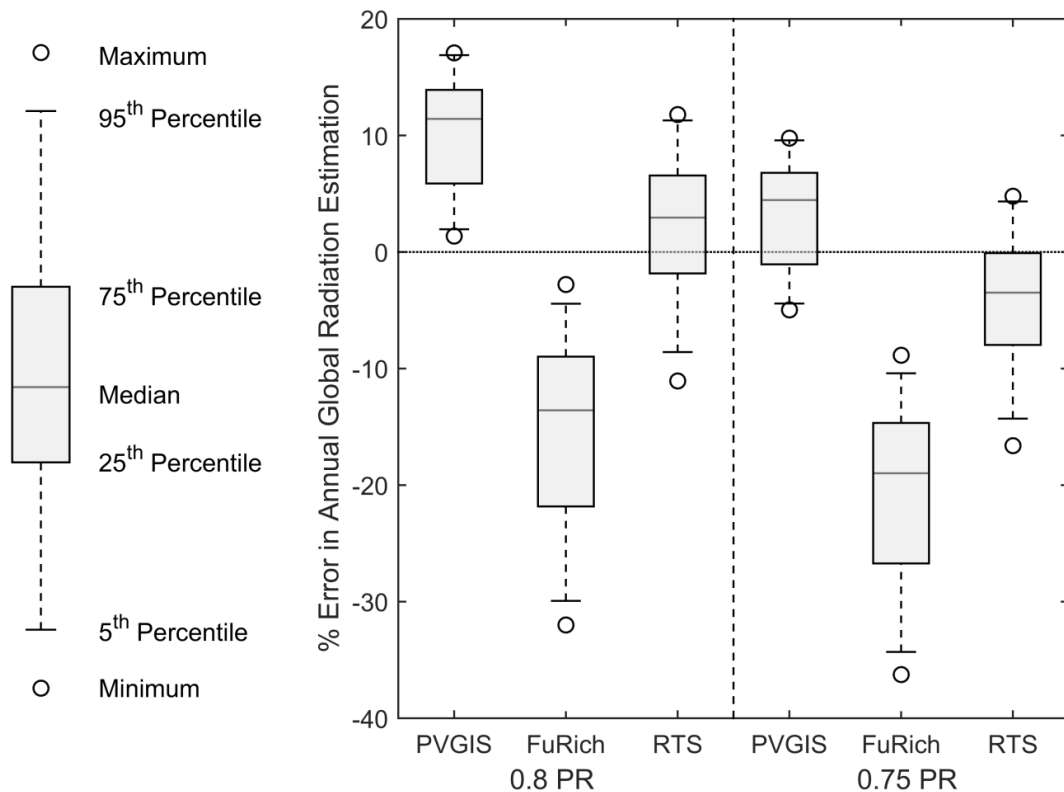
### 4.3 Results and Discussion

The percentage error in annual global radiation was calculated for each site using:

$$\% \text{ Error} = \frac{(\hat{I}_T - I_T)}{I_T} \times 100 \quad (4-7)$$

where  $\hat{I}_T$  is modelled annual global irradiance and  $I_T$  is the estimated irradiance at the site following the PR conversion (subscript  $T$  denotes tilted irradiance).

Figure 4-2 shows the performance of the RTS, PVGIS and FuRich methodologies under both 0.8 and 0.75 PRs. In the boxplots, the bottom and top whiskers denote the 5th and 95th percentiles, the bottom and top edges of the rectangles represent the 25th and 75th percentiles and the central line is the median. This convention is applied to all boxplots presented throughout the thesis. The RTS model showed good agreement to the validation data with a mean percentage error of +2.16% and -4.22% under the 0.8 and 0.75 PRs respectively.



**Figure 4-2 Percentage error of annual global radiation estimation for all three methodologies under both PRs.**

The performance of PVGIS and FuRich are significantly poorer than RTS under the 0.8 PR. FuRich has a -15.48% mean error under the 0.8 PR whilst PVGIS has a +10.18% mean error. Although PVGIS performs better under the 0.75 PR, with +3.3% mean error, FuRich performs worse and incurs -20.76% mean error.

At three sites, FuRich (0.75 PR) generated an error in annual global radiation that was over 25% greater than the measured value. The largest error produced by RTS was -16.62% under the 0.75 PR but the second largest RTS error was more typical of the worst RTS overestimations at 11.8% which is considerably smaller than the three FuRich errors referred to. FuRich produced the largest inter-quartile ranges with the strongest bias toward underestimation of annual global radiation.

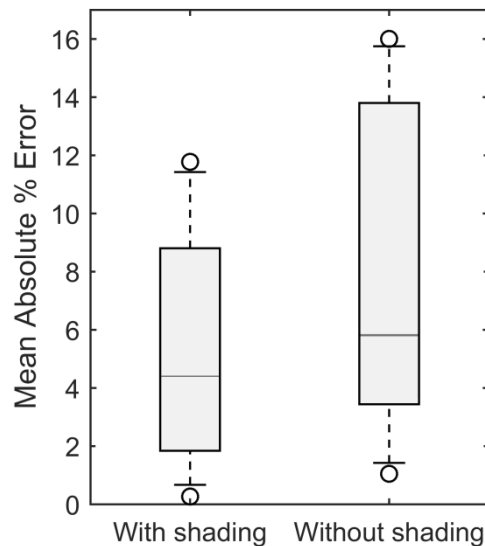
The results show that PVGIS under a 0.75 PR better approximates annual global insolation than when it is used with a PR of 0.8. This may be due to the lack of a shading model in PVGIS that leads to higher estimations of power output before the PR is applied. Despite the good performance of PVGIS under the 0.75 PR, a smaller mean percentage error is achievable when the RTS method is applied with a 0.8 PR and this value of PR is also better supported by the literature (Reich, 2012; Leloux et al., 2012; Taylor, 2015).

#### 4.3.1 Insolation Estimation Sensitivity to Shading

Owing to the gridded 0.05° by 0.05° resolution of the albedo dataset, the baseline radiation calculations are appropriate to approximately 5.6 km latitude by 3.2 km longitude grid squares across a city. This means that the majority of validation sites for each city fell within the same cell. Therefore, the alteration to the baseline radiation estimate in RTS to incorporate slope, azimuth and shading is highly important in solar insolation estimation. Due to the small number of validation sites and constrained combinations of azimuth and slope arrangements, it is not possible to comprehensively examine the role of the two geometrical parameters in the accuracy of solar insolation estimation under RTS. However, the effect of applying the DSM-derived shading model on the accuracy of annual global insolation prediction can be investigated and the mean absolute % error (defined in equation (4-8)) has been calculated for all validation sites under the 0.8 PR both with and without the shading model. The 0.8 PR has been selected for this analysis because it outperformed the 0.75 PR for RTS in section 4.3.

$$\text{Mean Absolute \% Error} = \frac{1}{n} \sum_{i=1}^n \left( \left| \frac{\widehat{I}_{Ti} - I_{Ti}}{I_{Ti}} \right| \times 100 \right) \quad (4-8)$$

$n$  in equation (4-8) is the number of sites (20). Figure 4-3 shows the distribution across all validation sites of mean absolute percentage error. When the shading model is integrated with the radiance model there is a smaller interquartile range, lower median error and smaller outlier errors.



**Figure 4-3 Mean Absolute % Error in annual global radiation estimation with and without shading under both performance ratios**

Under the 0.8 PR, a mean absolute percentage error of 8.16% occurred when shading was not incorporated which is greater than the 5.27% absolute mean percentage error when the shading model was applied. It is important to note that RTS without shading still outperformed the mean absolute percentage error incurred for both FuRich and PVGIS when the 0.8 PR, which is better supported by the literature, was applied.

#### **4.3.2 Suitability to City-Scale Applications**

The large resolution of the baseline radiation output (5.6 km latitude by 3.2 km longitude) means that one of the most computationally intensive parts of the method need only be executed once to cover a considerable area. Whilst the generation of viewshed models for properties within a study area of this size also has considerable processing demands, the estimation of solar resource on a city scale using the RTS model is entirely achievable. This means RTS could be used to achieve greater accuracy in city-scale PV viability analysis than existing methodologies such as that described in section 3.1.

Furthermore, the method would remain efficient if using the multiple hemispherical viewshed models generated for every 2 m<sup>2</sup> across a site for independent solar insolation calculations, rather than the viewsheds being averaged and one solar radiation calculation taking place as presented so far. In doing so the technique could advise potential investors on the siting and optimal sizing of a prospective installation at their property because it could highlight areas of the property that are prone to greater shade that would diminish payback and power generation forecasts.

#### **4.4 Summary of Validation**

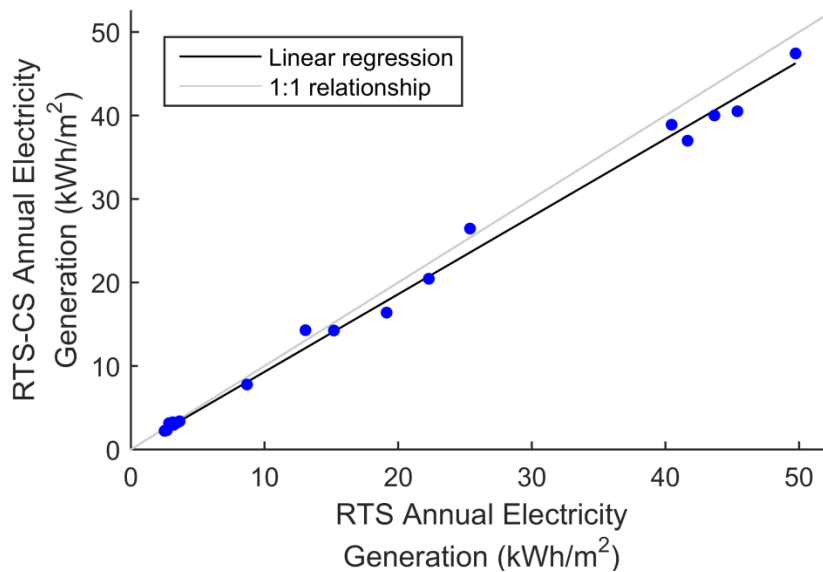
A radiative transfer with shading (RTS) model has been presented that estimates annual global solar radiation with +2.62% and -3.68% mean percentage error under assumed performance ratios of 0.8 and 0.75 respectively. When validated using annual power output data for the year 2013 from 17 sites across four cities, the RTS model outperformed the FuRich methodologies incorporated into the esri ArcMap solar radiation toolset. FuRich incurred -15.97 and -20.78% mean percentage errors under the 0.8 and 0.75 PRs whilst the results for PVGIS were +10.23% and +3.34% mean percentage error for each PR. The 0.8 PR figure for the RTS model were, therefore, the most accurate predictions.

#### **4.5 Adaptation for City-Scale Applications**

Unlike PVGIS, the method could be applied on a city scale after a small degree of adaptation and therefore could be used to inform large numbers of investment decisions with greater accuracy than previously possible using the FuRich methodology. However, the processing time for each site using the RTS method was approximately ten minutes when using a computer with an Intel® Xeon® 3.1 GHz processor and 4 GB of RAM. The study area used throughout this thesis that incorporates the city of Leeds has 178,181 sites and so the RTS model would require approximately 1,237 days to execute. Therefore, despite the increase in accuracy over existing methodologies, the RTS model required changes to make it deployable at the city scale and so meet the central aim of this thesis to develop models for city-scale microgeneration viability appraisal that can be run without the need for high power computing resources. The adapted model is hereafter referred to as the RTS-CS (Radiative Transfer with Shading – City-Scale) model.

The main reason for the lengthy RTS processing times was found to be the integration of the shading model at every time step across the year. In order to address this, a new methodology was devised that first sums the direct and diffuse insolation calculations for each sky sector without the shading model. The hemispherical shading model is then applied to remove all contribution of direct insolation to annual global insolation estimation from shaded sky sectors. Shaded sky sector diffuse insolation values are replaced with the albedo-dependent reflected insolation value. This meant that the use of the shading model occurred only once for each site instead of for each time step at each site which greatly reduced the processing time to approximately 6.5 seconds per site. The completion of a city-scale study required 14 days bringing it to the same approximate running time as the FuRich methodology but with improved accuracy as the accuracy of RTS-CS estimation closely

followed that of RTS. The estimations of annual electricity generation (kWh m<sup>-2</sup>) under the RTS and RTS-CS models with the 0.8 PR adjustment are shown in Figure 4-4 for all validation sites.



**Figure 4-4 Relationship between RTS and RTS-CS models for all validation sites under the 0.8 PR**

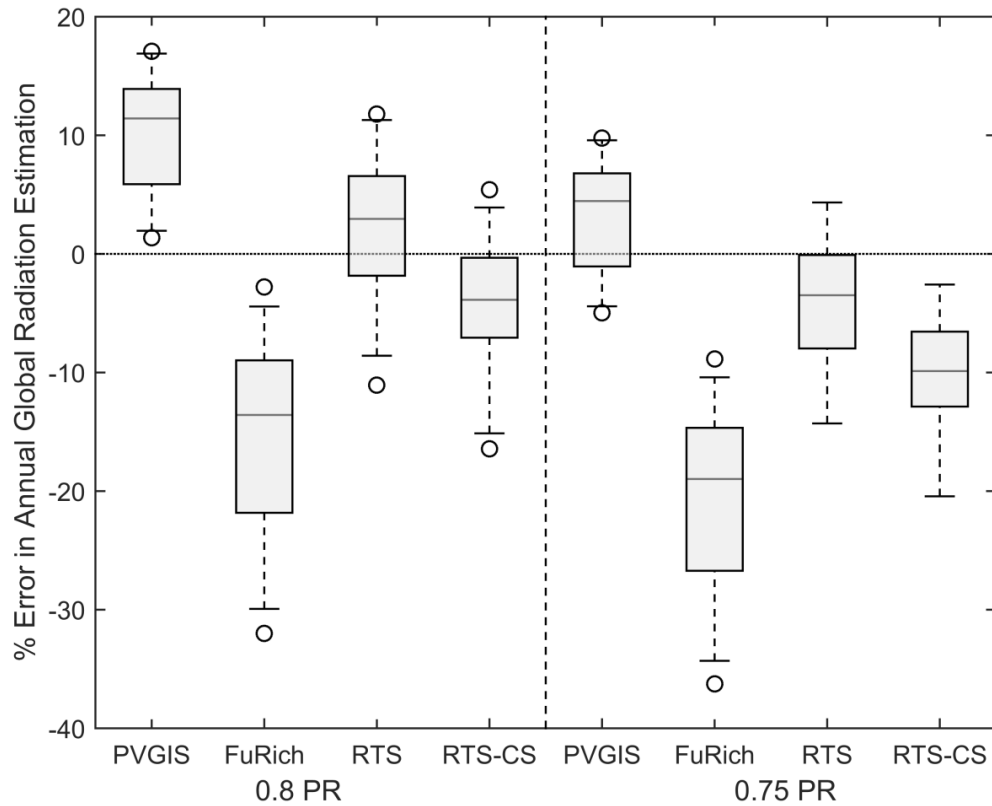
The linear regression in Figure 4-4 has an  $r^2$  value of 0.99 and a gradient of 0.93 showing that there is a strong correlation between RTS and RTS-CS but that RTS-CS tends to predict a slightly smaller annual electricity generation. Therefore, it is clear that the adjustments to adapt RTS for city-scale execution have not led to any systematic failures in the prediction of power output. Moving beyond the relationship of RTS-CS to RTS, Table 4-1 shows how observed electricity generation at all of the validation sites compares to that predicted by each of the models.

	0.8 PR				0.75 PR			
	PVGIS	FuRich	RTS	RTS-CS	PVGIS	FuRich	RTS	RTS-CS
<b>Mean % Error</b>	10.18	-15.48	2.16	-4.39	3.30	-20.76	-4.22	-10.36
<b>Std Dev</b>	4.87	8.13	6.17	5.59	4.57	7.62	5.78	5.24

**Table 4-1 Average performance of all three models and RTS-CS under both the 0.8 and 0.75 PR.**

Table 4-1 shows that RTS-CS estimates annual global insolation with -4.39% average error under the 0.8 PR and -10.36% average error under the 0.75 PR. It is clear from the distributions of each model’s outputs (Figure 4-5) that RTS-CS has the two smallest inter-quartile ranges of the models tested. RTS-CS produces results that fall within a similar range to RTS although it demonstrates a tendency to underestimate solar resource. However, the comparison of greatest importance to RTS-CS is its performance against FuRich because PVGIS and RTS are not methods that can be applied systematically on a city scale. Table 4-1

and Figure 4-5 show that RTS-CS is significantly more accurate and consistent in its estimations.



**Figure 4-5 Comparison of RTS model with city-scale deployment adaptations to all other models**

To demonstrate the outputs of the RTS-CS model when applied for a city, Figure 4-6 and Figure 4-7 show the predicted insolation across a roof for large and small properties respectively. For large properties, an annual global insolation estimate was made for every 10 m<sup>2</sup> across a roof so that roofs with varying geometries would not be inaccurately modelled because only one coordinate had been used.

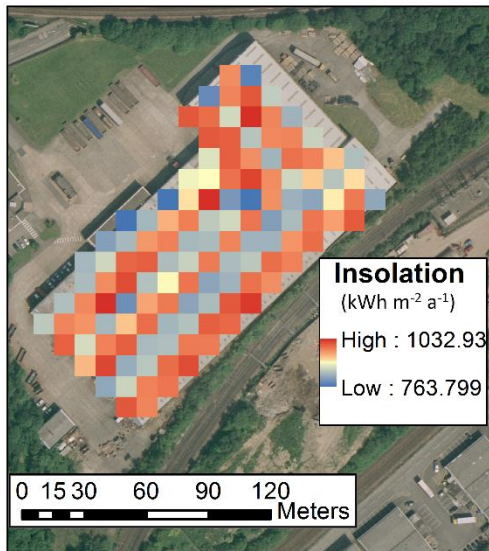


Figure 4-6 Annual solar insolation at a large building using RTS-CS

Figure 4-6 shows annual global solar insolation estimates that follow the shape of the roof with sections that are shaded by taller surrounding features or are North-facing receiving less insolation. The small properties in Figure 4-7 that have the highest insolation estimates are those with the more southerly orientations which is to be expected as the slope of the roofs was very consistent.

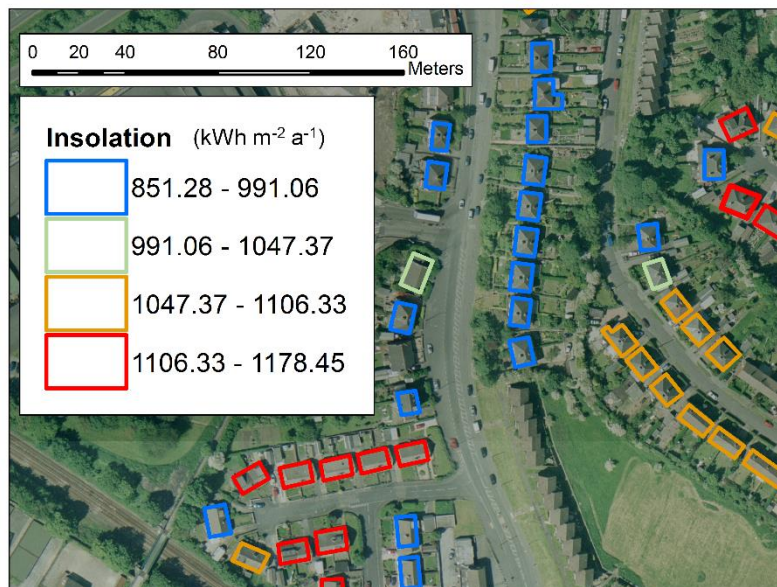
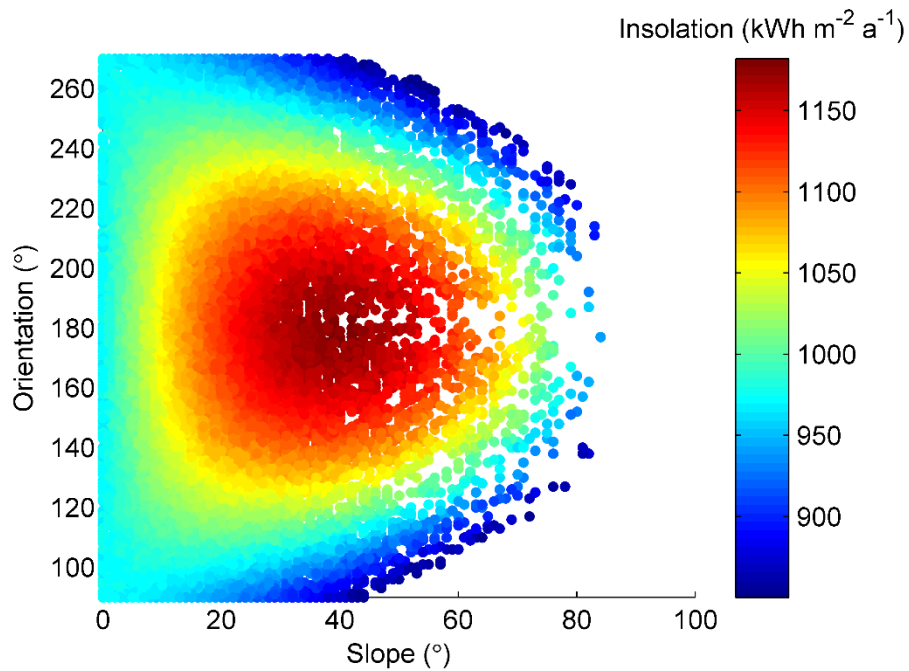


Figure 4-7 Annual solar insolation at small buildings using RTS-CS



**Figure 4-8 Slope and orientation of small properties across a study area containing Leeds (UK), coloured by insolation ( $\text{kWh m}^{-2} \text{a}^{-1}$ )**

A broad breadth of roof geometries were observed across the small properties of the Leeds city region as Figure 4-8 shows. The peak insolation estimations are for roofs with a slope of  $35^\circ$  to  $42^\circ$  and an orientation of approximately  $180^\circ$ . Both optimum slope and orientation are consistent with those in the EU-JRC PVGIS interactive map (JRC European Commission, 2014). As slope increases from zero, modelled insolation starts to diverge which is due to the effect of roof orientation. The optimum South-facing ( $180^\circ$ ) roof spaces in the study area increase in annual insolation with slope more quickly than those that are South-east ( $135^\circ$ ) or South-West ( $225^\circ$ ) whilst annual insolation for East ( $90^\circ$ ) and West ( $270^\circ$ ) facing roofs decreasing as the area faces away from the Sun. For all orientations of roofs the insolation estimation eventually falls when slope has increased beyond a certain point. For the South-east and South-west facing roofs, this occurs sooner than for South-facing roof spaces which only start to decline when slope is past the optimum angle.

It is particularly interesting to note that the difference in colour, and therefore predicted annual insolation, is fairly small at slope angles of  $20^\circ$  to  $55^\circ$  and orientation angles of  $140^\circ$  to  $220^\circ$  which is the area with the highest annual insolation estimates. Therefore, insolation modelling in this area is less sensitive to changes in orientation and slope than other parts of Figure 4-8 such as at slopes of  $30^\circ$  to  $50^\circ$  between orientation angles of  $110^\circ$  and  $130^\circ$ . Here, there is a change from  $1070 \text{ kWh m}^{-2} \text{a}^{-1}$  at  $30^\circ$  slope and  $130^\circ$  orientation to  $960 \text{ kWh m}^{-2} \text{a}^{-1}$  at  $45^\circ$  slope and  $110^\circ$  orientation, which is a decrease of 9.73%. This shows that it is important to model roof geometry accurately as small changes in geometry can lead to



greater differences in annual radiation estimates that are then summed across all years being considered in the viability calculation. Larger errors in solar PV viability at the city-scale, which is the focus of Chapter 6, would occur if such a study were to ignore the increased accuracy of roof geometry modelling techniques described in section 3.2 are neglected in favour of esri's market-leading ArcGIS software and its nearest neighbour approach.

#### **4.6 Conclusion**

The adaptations to the RTS model to create RTS-CS have not caused a significant loss of accuracy and the resulting model far outperforms a widely used city-scale insolation estimation programme incorporated into the market-leading GIS package whilst remaining executable on standard desktop computers. The outputs of the RTS-CS model are suitable for application to city-scale viability analysis and can be combined with the outputs of the roof geometry modelling method described in section 3.2 to estimate annual insolation with greater accuracy and at the city scale. These themes are returned to in Chapter 6.

## Chapter 5 Wind Speed Prediction Methods for Urban Areas

This chapter presents research into the prediction of wind speeds for localised neighbourhoods across a city at all heights above ground. Specifically, a relatively simple and rapidly executable model is presented which addresses issues in the application of the most accurate existing method. Chapter 2 described the importance of surface roughness length ( $z_0$ ) and displacement height ( $d$ ) in the field of annual wind speed prediction with equation (2-10) showing how the two parameters are used. The application of those wind speed predictions to the assessment of wind turbine viability has grown in significance as the UK government's approach to reducing greenhouse gas emissions through financial incentives has led to expansion of the UK wind industry. As of October 2015, wind turbines that qualify for the MCS and ROOFIT subsidies contribute 469.3 MW of installed capacity (DECC, 2016b) and this size of turbine is often installed towards the periphery of urban centres, where there is an influence from the near-by urban and semi-urban areas. Chapter 2 introduced how the Millward-Hopkins et al. (2013c) methodology had achieved highly accurate estimations of long term average wind speeds using DEM data. However, it is not a methodology without problems.

### 5.1 Implementation Issues Related to the Method of Millward-Hopkins et al.

The Millward-Hopkins et al. (2013c) methodology uses 2 m DEM data in full at a number of points through the process. The height data of vegetated areas is reduced by 20% to incorporate the porosity of these areas to the flow. There is then a filtering stage to remove the occasional erroneous height measurements that DEM data is susceptible to. This is fairly computationally intensive as it is executed on a cell-by-cell basis across the large domains. The filtered DEM data is used when calculating building density and adaptive grid sizing before calculating the geometrical parameters such as  $h_m$ ,  $\lambda_p$  and the standard deviation of building heights normalised by mean building height ( $\sigma_h/h_m$ ).

A second cause of the lengthy processing times is the number of iterations that are incurred by the calculation of  $dh_i$  as described in Figure 2-4 for what can be numerous height regimes across a considerable sum of neighbourhoods. The problem is greater for  $h_{m-eff}$  which must be calculated across all height regimes and in eight wind directions for every neighbourhood across a city. While  $z_0$  is not calculated by division into height regimes, it must be calculated iteratively and for each wind direction in every neighbourhood. The combination of manipulation of the high resolution DEM data and this second stage of

calculations leads to execution times for the whole method of the order of days for large cities. These computational requirements, coupled with the complexity of understanding the method may restrict its application for a large number of cities. Therefore, this chapter proposes a methodology that produces a level of accuracy that is comparable to Millward-Hopkins et al. (2013c) but with significant improvements to computational efficiency and simplicity of application so as to remove barriers to its deployment.

## 5.2 Development of a Simplified Wind Speed Estimation Methodology

The chapter will proceed with an explanation of how simplified formulae for the estimation of aerodynamic parameters were developed. For  $z_0$  and  $d$ , the general process centres on adapting the outputs of the Macdonald et al. (1998) model to closely match those of the more accurate but more complex and time-demanding Millward-Hopkins et al. (2013c) model. The latter of the two was selected for model fitting over equations for aerodynamic parameters derived from wind tunnel experiments. This is due to the limited number of wind tunnel studies to investigate surfaces as heterogeneous in obstruction heights as urban surfaces are. It is important to note that the Millward-Hopkins et al. (2013c) model was validated against all wind tunnel validation studies available for heterogeneous arrays at the time it was published. These same wind tunnel studies are used to verify the estimations of  $d$  and  $z_0$  here.

Later in this chapter, the outputs of the Millward-Hopkins et al. (2013c), simplified and Macdonald (2000) models are compared and a further simplified model is introduced and tested. The four models are used to predict annual average wind speeds across four major UK cities which are validated by comparison to physical measurements.

### 5.2.1 Displacement Height

Figure 5-1 shows  $h_m$  and  $d_{JMH}$  across Leeds (UK) which is one of the study areas included in the research. Far greater values of  $d_{JMH}$  are observed in the most developed parts of the city where  $h_m$  peaks whereas the least developed areas towards the periphery of the study area have much smaller values of  $d_{JMH}$ .

Figure 5-2 shows the relationship between  $d_u/h_m$  (as described in equation (2-11) of section 2.1.3) and  $d_{JMH}/h_m$  as calculated in the Millward-Hopkins et al. (2013a) method using DEM data from three cities where each of the 6,490 data points represents an individual neighbourhood. The three cities included in this study were Nottingham, Edinburgh and Leeds. It illustrates the differences caused by the detailed consideration of building height

variability in the estimation of  $d$  under the Millward-Hopkins et al. (2013a) methodology for which values of  $d_{JM}/h_m$  commonly exceed 1 which is not possible using Macdonald's formulae.

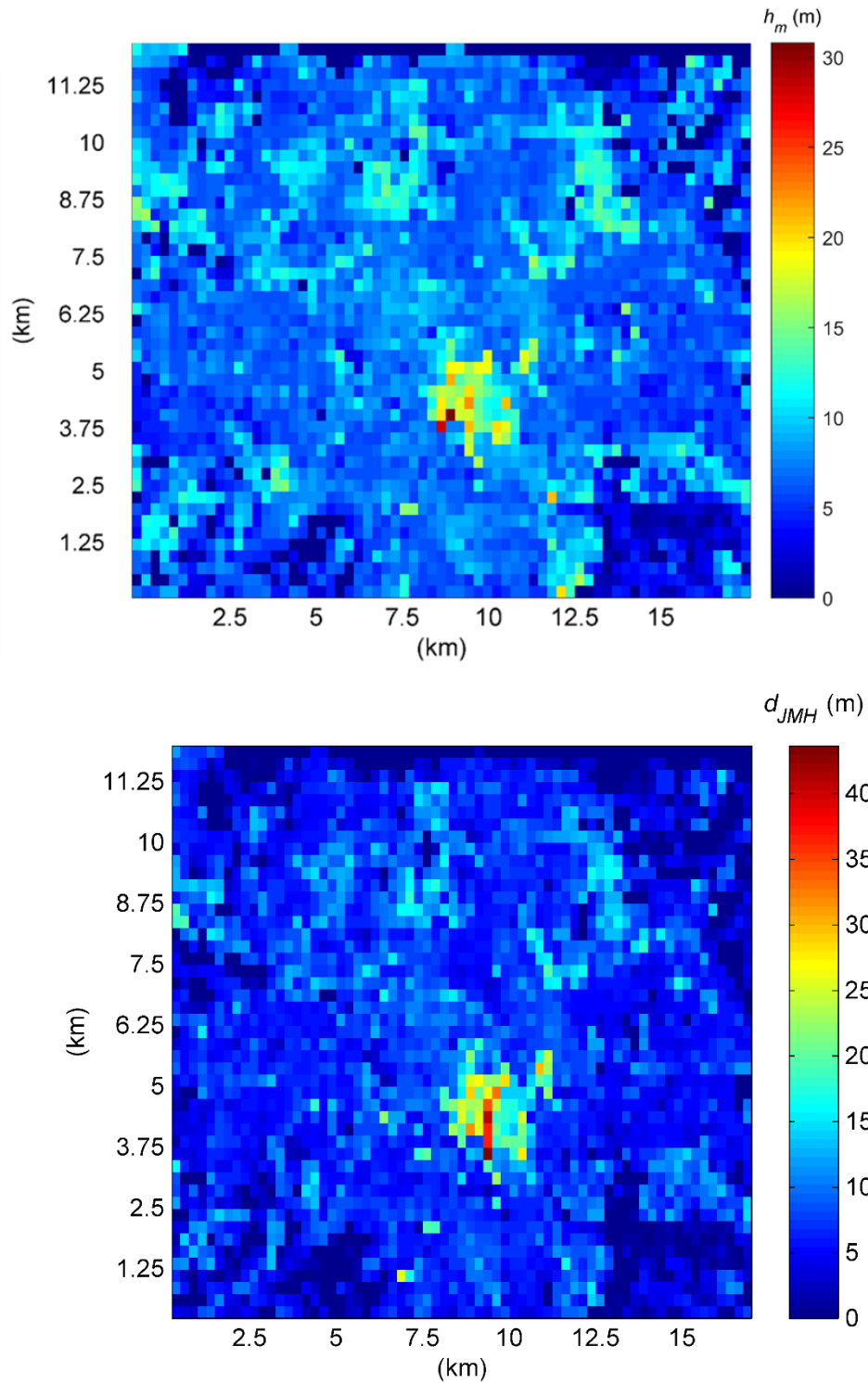


Figure 5-1  $h_m$  (top) and  $d$  (bottom) across the Leeds study area. Larger values are observed in more built-up areas for both attributes

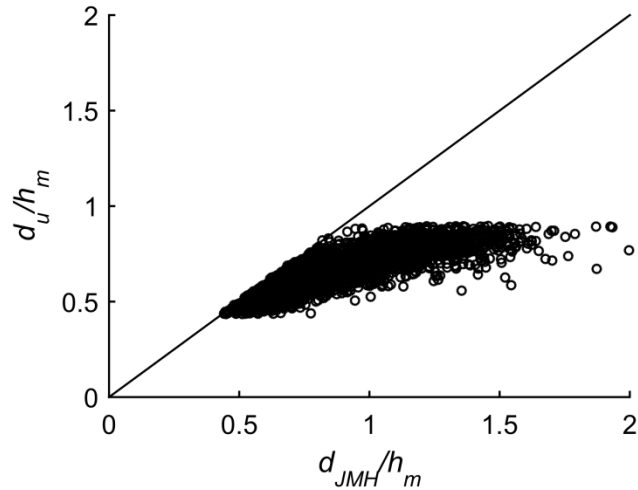


Figure 5-2 Displacement height calculated by Millward-Hopkins et al. (2013a) ( $d_{JM\text{H}}/h_m$ ) and Macdonald et al. (1998) ( $d_u/h_m$ ) methodologies from DEM data for three cities

To evaluate the importance of building density with respect to the  $d_u$  and  $d_{JM\text{H}}$  relationship shown in Figure 5-2, Figure 5-3 shows three regimes of  $\lambda_p$  with regression lines defined using the MATLAB (2014) Robustfit function to minimise the influence of outliers. The normalised differences between the models  $(d_{JM\text{H}} - d_u)/h_m$  are plotted against the standard deviation of building heights in a neighbourhood,  $\sigma_h$ , normalised by  $h_m$  ( $\sigma_h/h_m$ ).

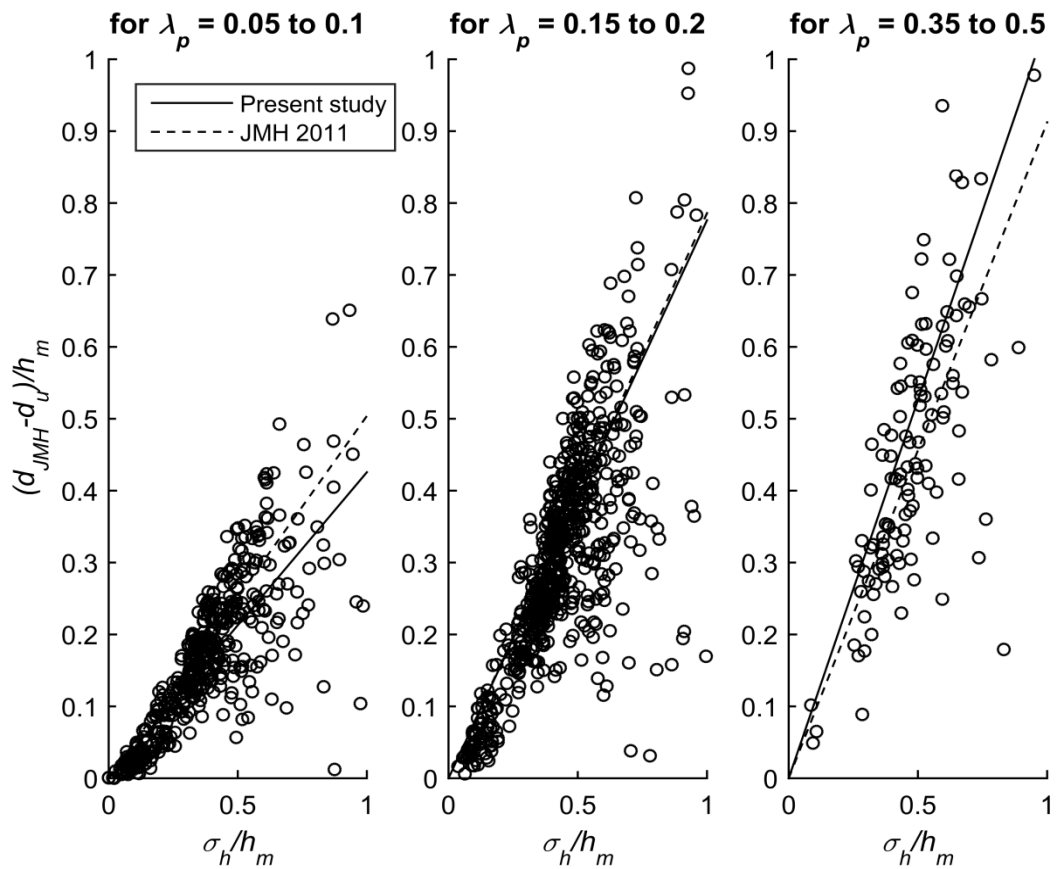


Figure 5-3 Relationship between Macdonald et al. (1998) displacement height ( $d_u$ ), Millward-Hopkins et al. (2013a) displacement height ( $d_{JM\text{H}}$ ) and the normalised standard deviation of heights ( $\sigma_h/h_m$ ) as plan-area density ( $\lambda_p$ ) increases. Solid lines denote a linear regression of the data in the present study whilst dashed lines represent the linear regressions presented in Millward-Hopkins et al. (2013b).

$\lambda_p$ range	Millward-Hopkins et al. (2013a)	Present Study
0.05 to 0.1	0.5038	0.4256
0.15 to 0.2	0.7859	0.7761
0.35 to 0.5	0.9122	1.0520

**Table 5-1 Gradients of linear regressions as previously reported by Millward-Hopkins et al. (2013b) and as found in the present study**

The influence of  $\sigma_h/h_m$  increases with building density which is consistent with Jiang (2008) and Millward-Hopkins et al. (2013b). Therefore an equation to adjust  $d_u$  to match  $d_{JMH}$  should feature a scaling of  $\lambda_p$  with  $\sigma_h/h_m$  as previously suggested by Kanda et al. (2013) in their development of a model specific to morphometric data for Tokyo. This trend is demonstrated more strongly in the present study with DEM derived building heights than in the vectorised height data used in Millward-Hopkins et al. (2013b) as the three gradients for the present study in Table 5-1 have a greater range.

To incorporate a scaling of  $\lambda_p$  and  $\sigma_h/h_m$ , equation (5-2) was developed. The parameters were established using a multistart `fmincon` optimisation routine from the MATLAB (2014) Global Optimisation Toolbox across four processor cores in parallel. The function works by adjusting parameters of the equation within a constrained range and then testing the outcome against a reference dataset which, in this case, was the aerodynamic parameters calculated under the full Millward-Hopkins et al. (2013a) method. The variables were adjusted from 50 starting conditions in order to avoid local minima leading to poorly optimised equations. The error metric used to evaluate the success of each iteration was the root mean squared percentage error (RMSPE) defined in equation (5-1) as:

$$RMSPE = \sqrt{\frac{1}{n} \sum_{i=1}^n \left( \frac{a_i - f_i}{a_i} \right)^2} \times 100 \quad (5-1)$$

where  $n$  is the number of observations,  $a_i$  are the actual values and  $f_i$  are the estimated values. This resulted in equation (5-2):

$$\frac{d_{local-simplified}}{h_m} = \left( 1.074 \frac{d_u}{h_m} \right) + \left( (0.264 \log \lambda_p + 1.068) \frac{\sigma_h}{h_m} \right) + 4.566 \times 10^{-8} \quad (5-2)$$

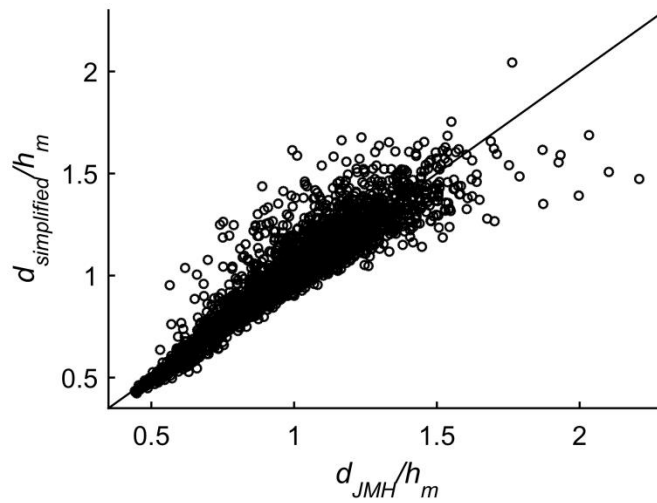
Equation (5-2) produces an agreement between  $\frac{d_{local-simplified}}{h_m}$  and  $\frac{d_{local-JMH}}{h_m}$  of 8.84% RMSPE and 6.63% mean absolute percentage error (MAPE) that in this study is defined as:

$$MAPE = \frac{1}{n} \sum_{i=1}^n \left| \frac{a_i - f_i}{a_i} \right|. \quad (5-3)$$

Differences between the two models became significantly more scattered when  $\sigma_h/h_m$  was greater than approximately 0.76. Therefore, a split equation for neighbourhoods of  $\sigma_h/h_m$  either greater or less than 0.76 was developed using the optimisation techniques outlined earlier so that the simplified methodology estimates  $d_{local}$  using:

$$\frac{d_{local-simplified}}{h_m} = \begin{cases} \left( 1.034 \frac{d_u}{h_m} \right) + \left( (0.149 \log \lambda_p + 0.839) \frac{\sigma_h}{h_m} \right) + 3.575 \times 10^{-6} & \left( \text{for } \frac{\sigma_h}{h_m} \geq 0.76 \right) \\ \left( 0.933 \frac{d_u}{h_m} \right) + \left( (0.383 \log \lambda_p + 1.542) \frac{\sigma_h}{h_m} \right) + 0.008 & \left( \text{for } \frac{\sigma_h}{h_m} < 0.76 \right) \end{cases} \quad (5-4)$$

Equation (5-4) leads to an agreement between the models of 5.543% MAPE and 8.263% RMSPE and the outputs of both models are shown in the scatter plot (Figure 5-4).



**Figure 5-4 Displacement height under the Millward-Hopkins et al. (2013a) ( $d_{local} - JM H/h_m$ ) and the simplified model ( $d_{local} - simplified/h_m$ ). Line denotes a 1:1 relationship**

Figure 5-5 compares  $d_{simplified}$  and  $d_{simplified}/h_m$  to commonly used reference values described in Grimmond and Oke (1999a) for neighbourhoods of specific  $\lambda_p$  and  $h_m$  ranges, which were introduced in section 2.1.3. The  $d_{simplified}/h_m$  estimates shown in Figure 5-5A are significantly greater than the reference table values which do not allow  $d$  to be greater than  $h_m$ . This presumption is invalid when compared to the experimental data of Cheng and Castro (2002b), Jiang et al. (2008) Hagishima et al. (2009) and Zaki et al. (2011b). In physical terms,  $d$  must be allowed to be greater than  $h_m$  to reflect the dominance that atypically tall buildings have over the aerodynamic parameters of an urban surface (Xie et al., 2008).

$d_{simplified}$  in Figure 5-5B is more closely matched to the  $h_m$ -based reference table values although there is a trend of decreasing similarity as density increases which is attributable to the simplified methodology being an approximation of a process that allows  $d$  to be greater than  $h_m$ . There is a more significant difference between  $h_m$  and  $h_{m-eff}$  in more dense neighbourhoods that have greater sheltering and in high rise areas that also contain small buildings leading to substantial deviation in building heights.

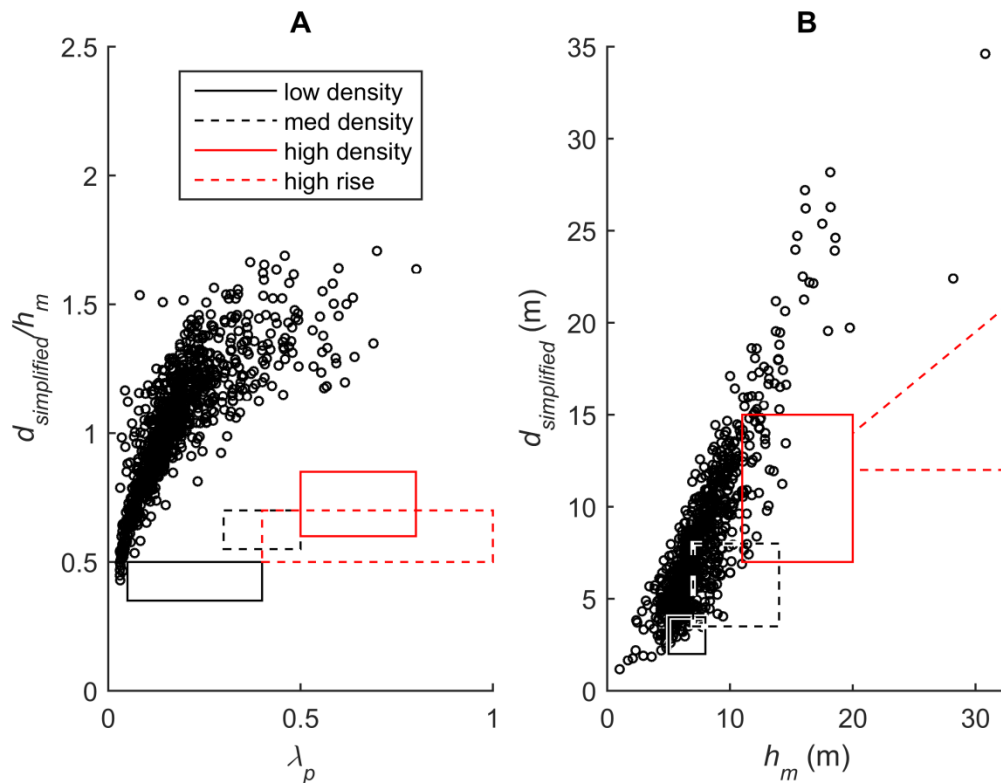


Figure 5-5 Comparison of simplified displacement height calculations to reference values from Grimmond and Oke (1999a)

Figure 5-6 shows  $d/h_m$  as modelled using the simplified methodology for all neighbourhoods across all of the cities and the results of three wind tunnel tests of for specific arrangements of obstructions to the flow with heterogeneous heights. The spread in modelled  $d_{local-simplified}/h_m$  results from the variation in  $\sigma_h/h_m$  across the study area.

The modelled values of  $d/h_m$  show clear agreement with the observations of Hagishima et al. (2009) and Cheng and Castro (2002) although two of the observations from the Zaki et al. (2011) study are not supported.



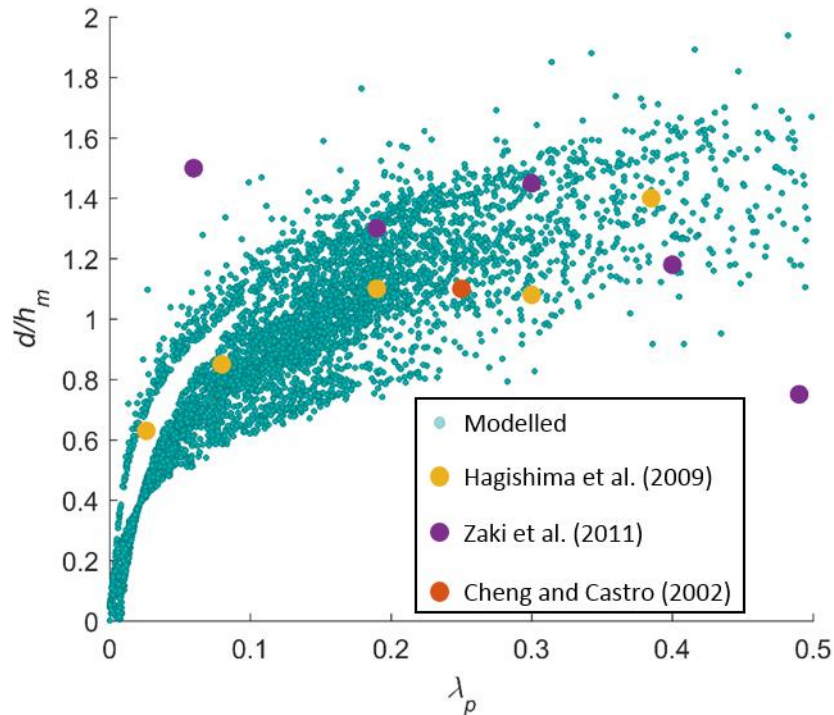


Figure 5-6 Comparison of modelled  $d/h_m$  to wind tunnel experimental data from Cheng and Castro (2002b) (red), Zaki et al. (2011a) (purple) and Hagishima et al. (2009) (amber)

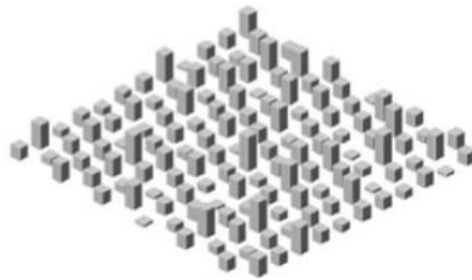


Figure 5-7 Arrangement of obstructions to the flow in Zaki et al. (2011)

The two outlying data points from the Zaki et al. (2011) study were for complex arrangement of obstacles that were not observed in the study areas. Figure 5-7 shows this highly varied layout which was not present in any of the study areas when  $\lambda_p$  was as small as 0.077 or as large as 0.481. It is also important to note that the wind tunnel studies all feature  $d/h_m$  values greater than 1 and show that  $d$  can be significantly greater than  $h_m$  which contradicts a limit Macdonald et al. (1998) found for arrays of homogeneous heights.

### 5.2.2 Surface Roughness

It is useful to first understand how surface roughness varies across the study area which Figure 5-8 shows using  $z_{0-JMH}$  values for a southerly wind direction across the study area. As with  $d_{JMh}$ , the largest  $z_{0-JMH}$  values are in the most developed parts of the study area and the lowest values are in the semi-rural areas towards the periphery.

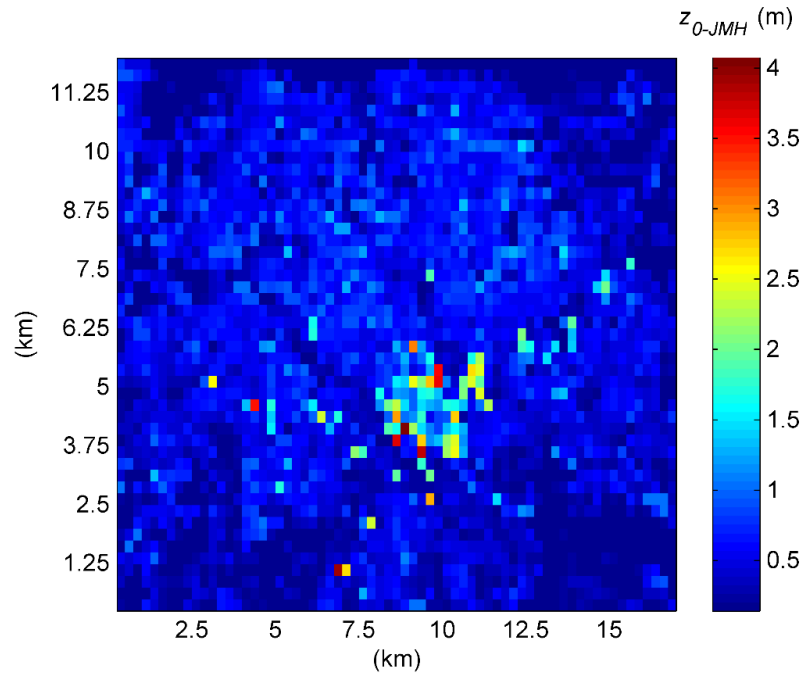


Figure 5-8  $z_{0-JMH}$  across the study area for a southerly wind direction

For the simplified methodology,  $z_{0u}$  is calculated using  $A_f^*/A_\tau$  as defined in equation (2-9) of section 2.1.3 in accordance with Macdonald et al. (1998) approach. This is in contrast to Millward-Hopkins (2013c) which uses the more complicated Bottema (Bottema, 1996; Bottema, 1997) models that consider spacing and aspect ratios of buildings resulting from building shapes. The Millward-Hopkins et al. (2013c) model develops a more refined parameterisation of unsheltered frontal area density but is a significant cause of the greater computational intensity and complexity of that methodology. Therefore, work has focused on developing a correction to the calculation of  $z_{0u}$  to match the Millward-Hopkins et al. (2013c) calculation of  $z_0$  ( $z_{0-JMH}$ ) as closely as possible. As a result, there are significant differences between  $z_{0u}/h_m$  and  $z_{0-JMH}/h_m$ .

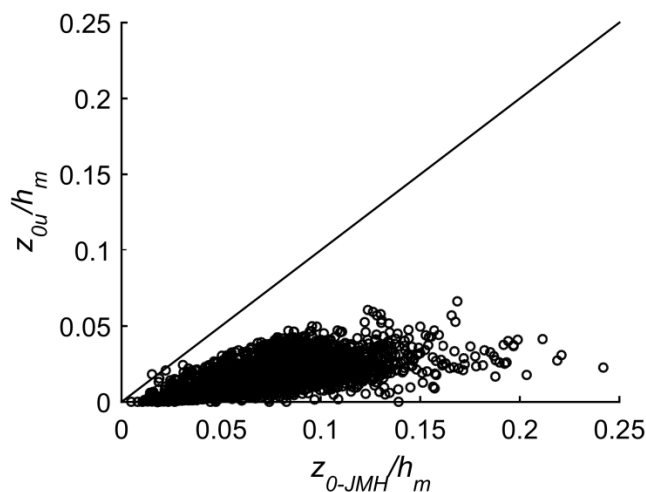
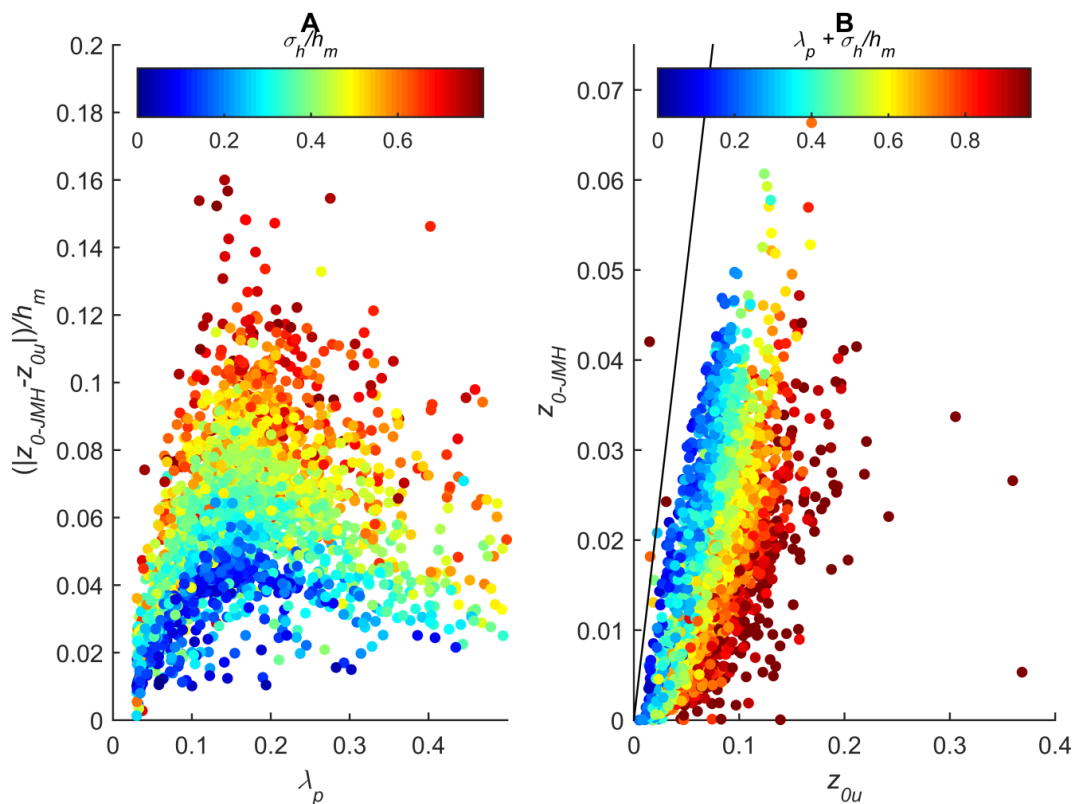


Figure 5-9 Surface roughness as per the Millward-Hopkins et al. (2013a) ( $z_{0-JMH}/h_m$ ) and Macdonald et al. (1998) ( $z_{0u}/h_m$ ) models. Line denotes a 1:1 relationship.

Figure 5-9 shows that  $z_{0u}/h_m$  values are smaller than  $z_{0-JMH}/h_m$  which is expected given that  $d_u/h_m$  is integral to its calculation and Figure 5-2 showed that it is consistently smaller than the  $d_{JMh}/h_m$  that are part of the formulation of the  $z_{0-JMH}/h_m$  estimates. However, there are patterns in the absolute residuals of the two models ( $|z_{0-JMH} - z_{0u}|/h_m$ ),  $\lambda_p$  and  $\sigma_h/h_m$  as illustrated in Figure 5-10A. Figure 5-10A shows that, when treated independently, neither  $\sigma_h/h_m$  nor  $\lambda_p$  are scalable with the differences between  $z_{0-JMH}$  and  $z_{0u}$ . It is also interesting to note that variation in  $\sigma_h/h_m$  is smallest at the extremes of  $\lambda_p$  areas which suggests that the study area was characterised by the most densely packed neighbourhoods having buildings of similar height with few instances of tall isolated buildings.



**Figure 5-10 Absolute difference between  $z_{0-JMH}/h_m$  and  $z_{0u}/h_m$  with respect to  $\lambda_p$  coloured by  $\sigma_h/h_m$  (A). B shows the relationship of  $z_{0-JMH}/h_m$  and  $z_{0u}/h_m$  coloured by  $\sigma_h/h_m + \lambda_p$  where the line denotes a 1:1 relationship.**

A distinct pattern in differences between  $z_{0-JMH}$  and  $z_{0u}$  emerges when  $\sigma_h/h_m$  and  $\lambda_p$  are summed for each neighbourhood (Figure 5-10B). This combination of the two parameters is found to portray a relationship between  $z_{0-JMH}$  and  $z_{0u}$  more clearly than either one individually. The isolation of specific ranges of  $\lambda_p + \sigma_h/h_m$  to bins shows that two-term polynomial (TTP) equations accurately describe the non-linear relationships between  $z_{0u}$  and  $z_{0-JMH}$ . For example, Figure 5-11 shows a bin of  $0.33 < \lambda_p + \sigma_h/h_m \leq 0.37$ . The Polyfit function in the programme MATLAB (2014) was used to calculate each fit by a least-squares method.

When the total range of  $\lambda_p + \sigma_h/h_m$  values is split into bins, a pattern emerges in the coefficients of the TTP equations describing the relationship between  $z_{0-JMH}$  and  $z_{0u}$ . When plotted, Figure 5-12B shows that they can themselves be fitted to a secondary TTP line. However, neighbourhoods with  $\lambda_p + \sigma_h/h_m > 0.97$  fail to produce the same distinct relationships as those with  $\lambda_p + \sigma_h/h_m \leq 0.97$ . When  $\lambda_p + \sigma_h/h_m > 0.97$  the coefficients become less predictable which is most likely caused by a scarcity of data in these bins. The data responsible for the 12 coefficient values to the right of the dotted line in Figure 5-12A make up just 5.63% of the total data.

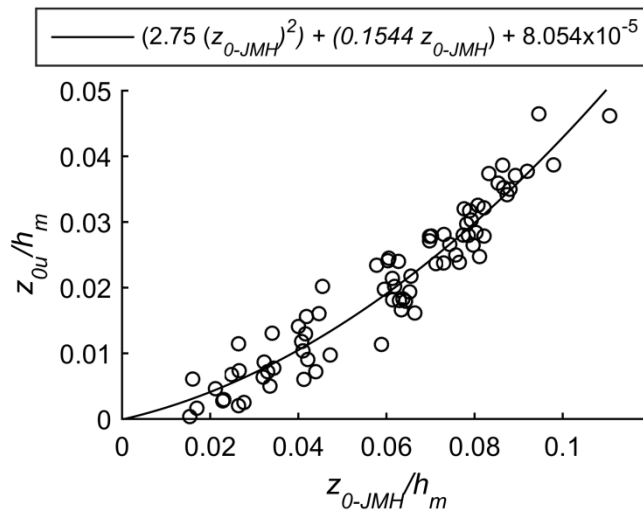


Figure 5-11  $z_{0-JMH}/h_m$  and  $z_{0u}/h_m$  for  $0.33 < \lambda_p + \sigma_h/h_m < 0.37$ . Line denotes the fitted polynomial trend.

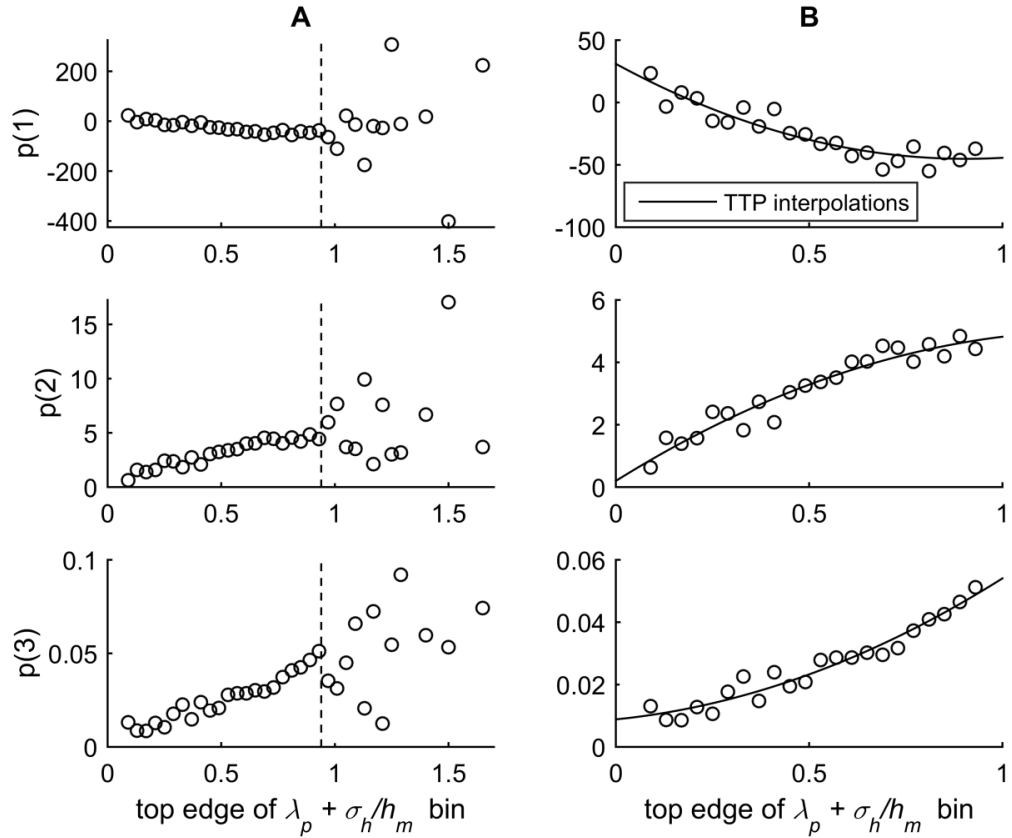


Figure 5-12 Coefficients of the TTP fitted curves of each  $\langle \lambda_p + \sigma_h/h_m \rangle$  bin (A) and with secondary TTP curves fitted to the data for  $\lambda_p + \sigma_h/h_m \leq 0.97$  (B)

Primary TTP Coefficient	Secondary TTP Coefficient 1	Secondary TTP Coefficient 2	Secondary TTP Coefficient 3
p(1)	92.791	-168.12	30.9868
p(2)	-3.101	7.7260	0.1964
p(3)	0.033	0.0125	0.0088

Table 5-2 Secondary TTP coefficients to describe trends in the coefficients of TTP polynomial equations for each  $\lambda_p + \sigma_h/h_m$  bin  $\leq 0.97$ .

The coefficients of the secondary TTP lines shown in Figure 5-12B are described in Table 5-2 and mean the equation for  $z_{0-simplified}/h_m$  takes the form:

$$\frac{z_{0-simplified}}{h_m} = \left( A \frac{z_{0u}}{h_m} \right)^2 + \left( B \frac{z_{0u}}{h_m} \right) + C \text{ for } \lambda_p + \frac{\sigma_h}{h_m} \leq 0.97, \quad (5-5)$$

where:

$$A = \left( 92.7905 \left( \lambda_p + \frac{\sigma_h}{h_m} \right)^2 \right) + \left( -168.1246 \left( \lambda_p + \frac{\sigma_h}{h_m} \right) \right) + 30.9868, \quad (5-6)$$

$$B = \left( -3.013 \left( \lambda_p + \frac{\sigma_h}{h_m} \right)^2 \right) + \left( 7.726 \left( \lambda_p + \frac{\sigma_h}{h_m} \right) \right) + 0.1964, \quad (5-7)$$

$$C = \left( 0.0328 \left( \lambda_p + \frac{\sigma_h}{h_m} \right)^2 \right) + \left( 0.0125 \left( \lambda_p + \frac{\sigma_h}{h_m} \right) \right) + 0.0088. \quad (5-8)$$

This leads to a RMSPE of 18.54% and a MAPE of 11.00% when comparing the values obtained from the simplified method and that of Millward-Hopkins et al. (2011).

Due to the small amount of data available for neighbourhoods of  $\lambda_p + \sigma_h/h_m > 0.97$  that led to unpredictable trends in coefficients shown in Figure 5-12A, an alternative method had to be devised for high  $\lambda_p + \sigma_h/h_m$  neighbourhoods. A linear fit was defined using the MATLAB (2014) Robustfit tool which was found to produce a satisfactory result so that:

$$\frac{z_{0-simplified}}{h_m} = \left(3.4375 \frac{z_{0u}}{h_m}\right) + 0.0631 \left(\text{for } \lambda_p + \frac{\sigma_h}{h_m} > 0.97\right). \quad (5-9)$$

This led to an agreement of 21.20% MAPE and 27.44% RMSPE when compared to the Millward-Hopkins et al. (2011) method. Equations (5-5) and (5-9) create to the  $z_{0-simplified}/h_m$  predictions shown in Figure 5-13 (right). When all wind directions are considered, there is a MAPE of 12.22% and a RMSPE of 18.74% when compared to Millward-Hopkins et al. (2011) values.

As in the comparison of  $d$ , the  $\lambda_p$ -derived Grimmond and Oke (1999a) reference values shown in Figure 5-14A are not observed although there is better agreement to the  $h_m$ -derived values (Figure 5-14B). A strong correlation between  $\sigma_h$  and  $h_m$  has been presented by Ratti et al. (2002) and Kanda et al. (2013) based on building height data from six major cities around the world. The improved agreement to  $h_m$ -derived reference values may be a result of this relationship and suggests that there is a stronger relationship of  $z_0$  to  $\sigma_h$ ,  $h_m$  and  $\lambda_p$  than  $\lambda_p$  alone.

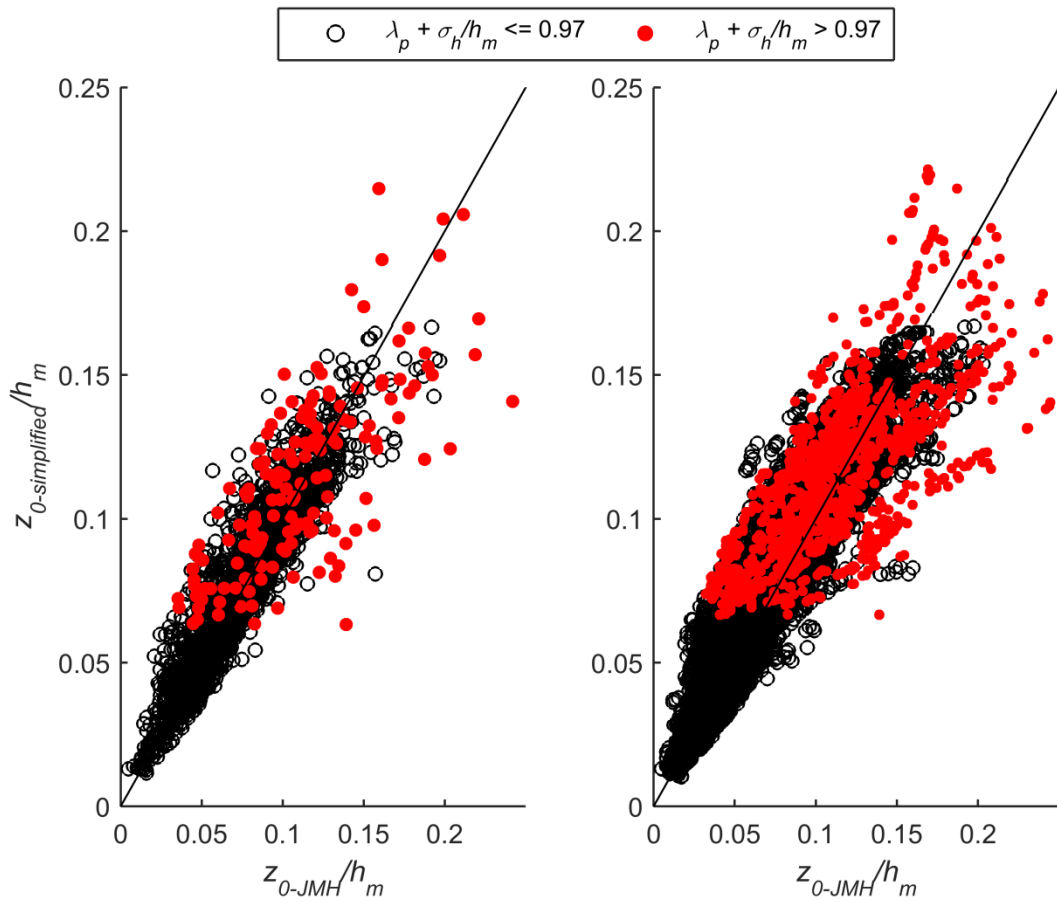


Figure 5-13 Normalised predictions of  $z_0/h_m$  under the full JMH method ( $z_{0-JMH}/h_m$ ) and the simplified methodology ( $z_{0-simplified}/h_m$ ) for one wind direction (left) and all directions (right). Lines denote 1:1 relationships.

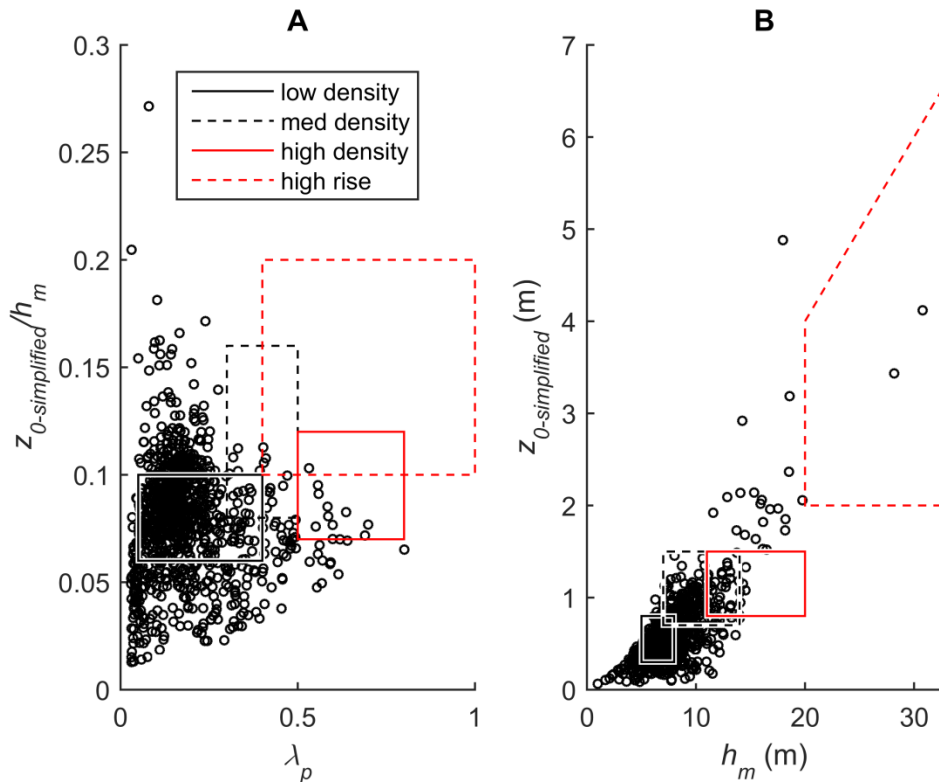


Figure 5-14 Comparison of predicted  $z_{0-simplified}$  to reference values from Grimmond and Oke (1999a).

Figure 5-15 shows that modelled  $z_0/h_m$  for a randomly selected (SE) wind direction in the city of Leeds is in fairly good agreement to the wind tunnel experimental data of Cheng and Castro (2002b), Zaki et al. (2011a) whilst Hagishima et al. (2009) values are slightly greater than modelled in general. The large degree of variation in  $d$  (Figure 5-6) to wind tunnel measurements is a cause of the wide spread observed here and it is important to note again that  $\sigma_h/h_m$  varied significantly across the study areas. Neighbourhoods with  $\lambda_f$  values greater than 0.3 were rare in the study areas and further investigation could be carried out into whether the model is less accurate for these locations.

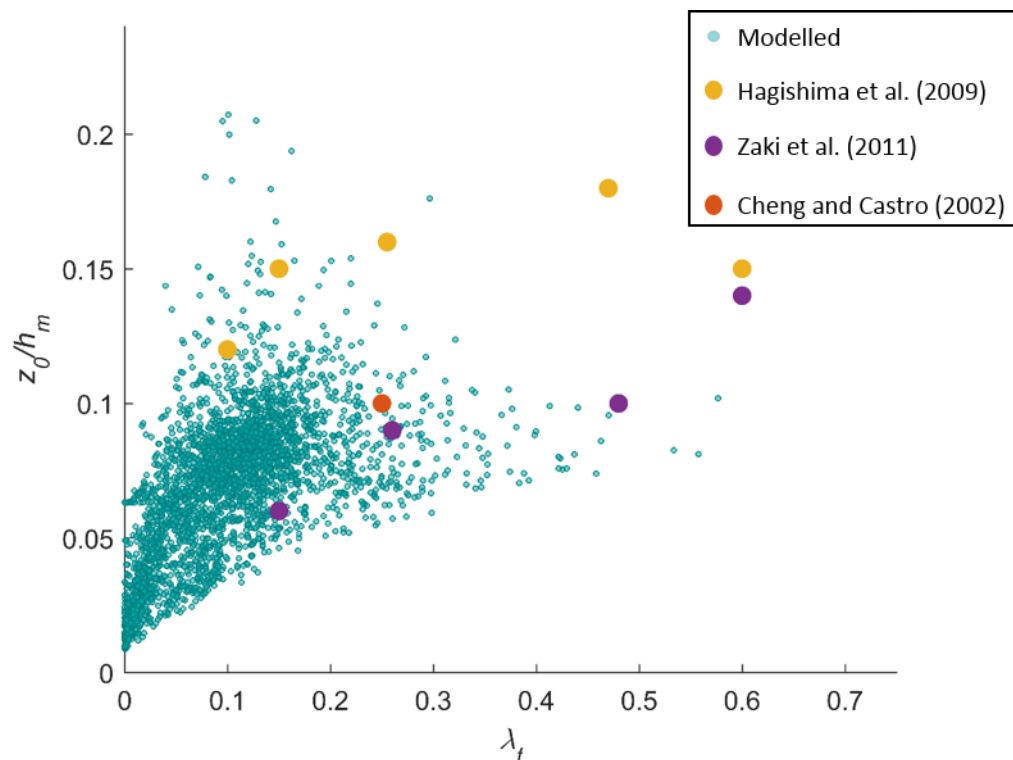


Figure 5-15 Comparison of modelled  $z_0/h_m$  (green) for one wind direction in the city of Leeds to wind tunnel observations by Cheng and Castro (2002b) (red), Zaki et al. (2011a) (purple) and Hagishima et al. (2009) (amber).

### 5.2.3 Effective Mean Building Height

Figure 5-16 shows how  $h_{m-eff-JMH}$  for a southerly wind direction varies across one of the study areas. It is greatest in the most developed parts of the city in a pattern that is strongly linked to  $h_m$ , which is also true for  $d_{JMh}$  and  $z_{0-JMh}$ . The estimation of  $h_{m-eff-JMh}$  under the Millward-Hopkins et al. (2011) requires the summation of calculations made across a number of height regimes for eight wind directions which is being avoided in this study for the sake of computational efficiency and comprehensibility. To simplify its estimation, the relationship shown in Figure 5-17A between  $h_m$ ,  $h_{m-eff-JMh}$  and  $\sigma_h$  is used to approximate  $h_{m-eff-simplified}$ .



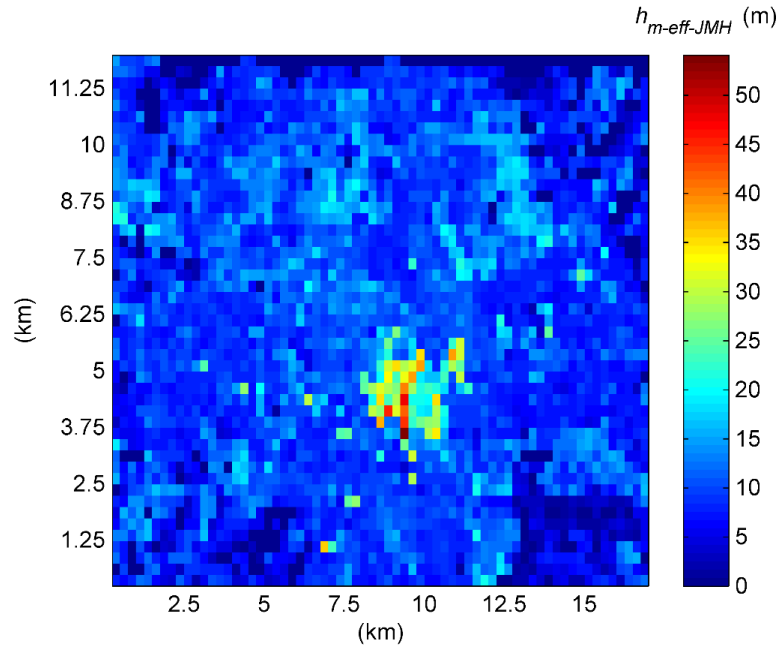


Figure 5-16  $h_{m-eff-JMH}$  across the study area for a northerly wind direction.

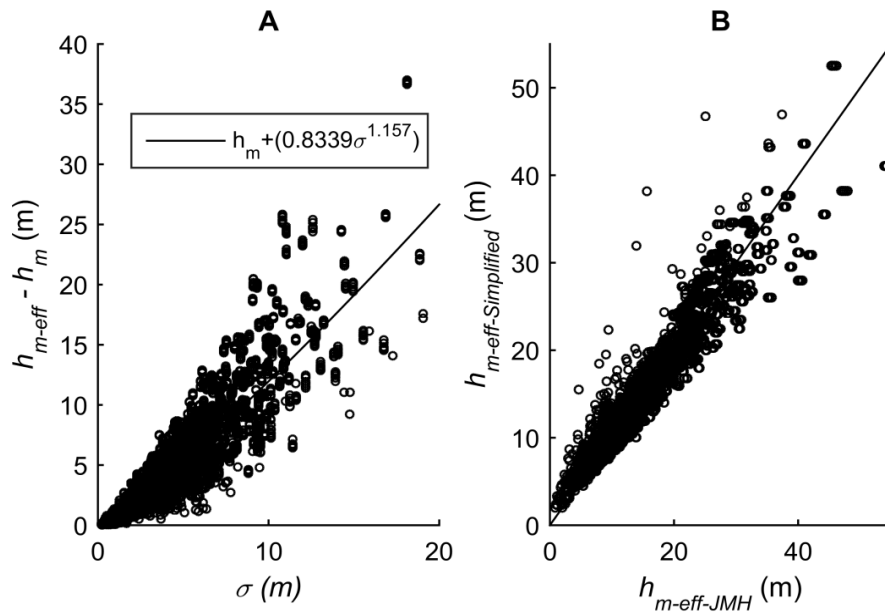


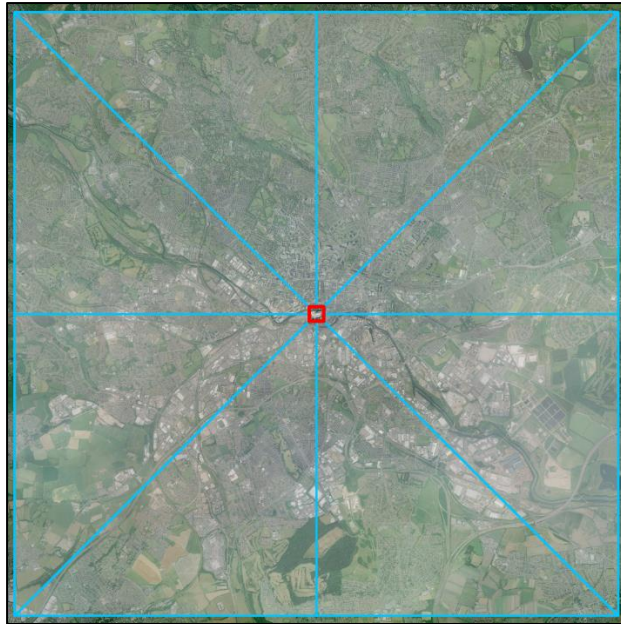
Figure 5-17 Relationship between  $\sigma_h$  and  $h_{m-eff-JMH} - h_m$  (A) and the correlation of  $h_{m-eff-simplified}$  to  $h_{m-eff-JMH}$  (B) in which the line denotes a 1:1 relationship.

$$h_{m-eff-simplified} = h_m + 0.8339\sigma_h^{1.157} \tag{5-10}$$

Using equation (5-10), the models shown in Figure 5-17B agree with 7.36% MAPE and 14.13% RMSPE.

### 5.2.4 Effective Parameters

Effective parameters are created using local parameters to describe the surface of the wider fetch area. Wind direction sectors are equal area triangles extending 5 km from the neighbourhood of interest in four compass directions as shown in Figure 5-18.



**Figure 5-18 Wind sectors extending 5 km in North, East, South and West compass directions from the neighbourhood containing the target site (red box)**

$d_{eff}$  and  $h_{m-eff}$  are means of  $d_{local}$  and  $h_{m-local}$  values in each wind direction sector surrounding the neighbourhood containing the target site while  $z_{0-eff}$  is more complex to calculate as it is scaled by distance from the target site using the blending method presented by Bou-Zeid et al. (2007). It is these parameters that are used in the first downscaling step from the UBL to the ISL, as described in section 2.1.3. Figure 5-19 shows the correlations of  $d_{eff-simplified}$ ,  $z_{0-eff-simplified}$  and  $h_{m-eff-eff-simplified}$  to the Millward-Hopkins et al. (2011) values which had respective RMSPE of 6.4%, 11.3% and 7.43%.

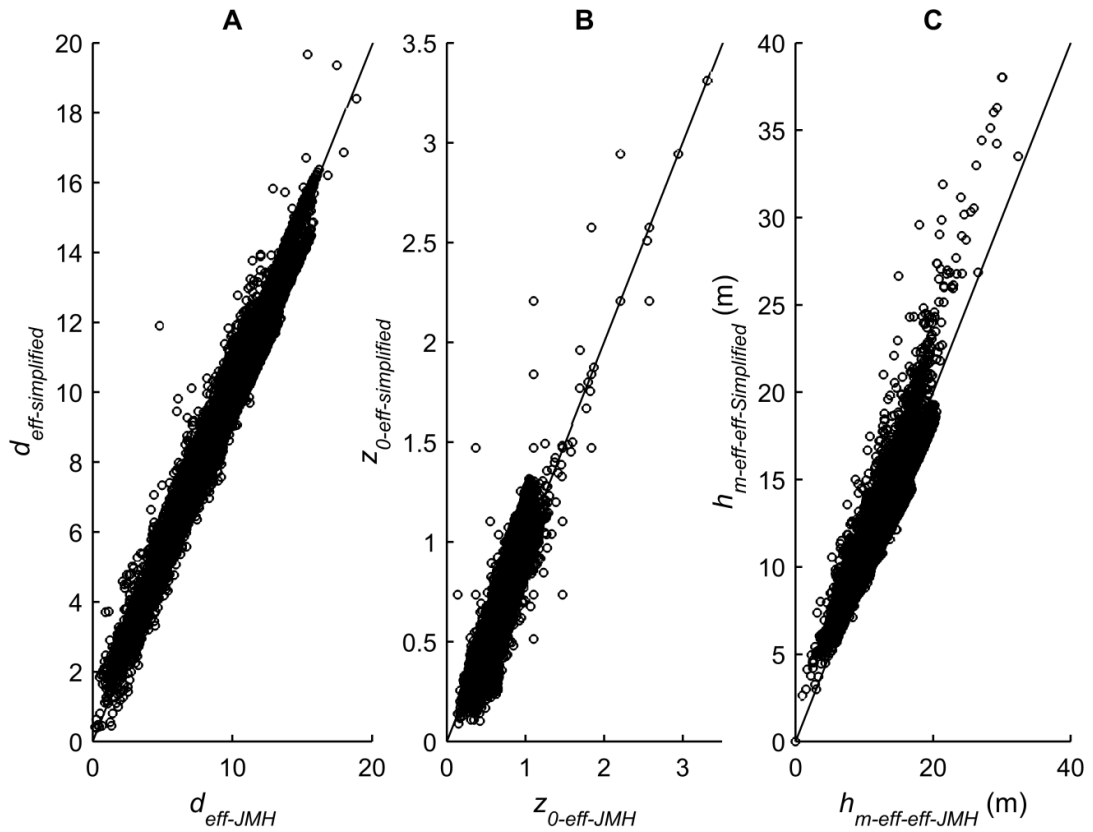


Figure 5-19 Effective parameters compared to Millward-Hopkins et al. (2011) values. Lines denote 1:1 relationships

### 5.2.5 Windspeed Estimation

The aerodynamic parameters calculated using each model are then applied to the three steps of the logarithmic wind profile equation that were described in section 2.1.3. To recap, reference wind speed meteorology, which is for 10 m above ground and independent of the effects of surface obstructions on wind flows, is first scaled up to a height equivalent to the UBL. In this study, NOABL reference wind speed data was used with a correction to match it to the NCIC database. This first upscale process is made using the accepted 0.14 m for “open ground”  $z_0$  without a value for  $d$  in the logarithmic equation (equation (2-10) in section 2.1.3) and is carried out for all wind directions available in the reference climatology (eight in this study). From these windspeed estimations at the height of the UBL, the effective parameters ( $z_{0\text{-eff}}$  and  $d_{\text{eff}}$ ) are used to describe the effects of surface objects in the 5 km fetch areas for each wind direction as the logarithmic profile is again applied to estimate wind speeds at the blending height. The final downscaling equation is from the blending height to the hypothetical turbine hub height and incorporates the local parameters ( $z_{0\text{-local}}$  and  $d_{\text{local}}$ ).  $h_{m\text{-eff}}$  is used to establish is a turbine hub height is exposed or sheltered. Where it is sheltered, the power law is required to convert the wind speed at the height of  $h_{m\text{-eff}}$  to the turbine hub height.

To compare wind speed estimations from the simplified model, the Macdonald model and a further simplified model were also tested which required the following actions to be taken.

#### **5.2.5.1 Macdonald's Model**

Despite the concerns over the validity of its application to heterogeneous arrays raised by Cheng et al. (2007), Macdonald's model for  $z_0$  and  $d$  has since been employed across a range of research fields and specifically in city scale studies of aerodynamic parameters such as Drew et al. (2013) and Heath and Walshe (2007). Due to the continuing popularity of Macdonald's model in the literature, the accuracy of wind speed estimations made using its equations for  $z_0$  and  $d$  were also compared to measured wind speeds in this study. As such, the local aerodynamic parameters were calculated using equations (2-11) (for  $d_u$ ) and equation (2-9) (for  $z_{0u}$ ) based on a fixed neighbourhood grid size of 250 m. Effective parameters were calculated in the same way as the simplified and full Millward-Hopkins et al. (2013a) methodologies. In contrast to the other methodologies, however,  $h_m$  was used in place of  $h_{m-eff}$  to define both the blending height (at  $2h_m$ ) and the height to which the logarithmic downscaling equation was extended down to before the exponential profile was used. This was because  $h_{m-eff}$  has not been used in any other study to employ Macdonald's model for aerodynamic parameters.

#### **5.2.5.2 A further simplified model**

A further simplified model was devised to address additional causes of computational demand in the Millward-Hopkins et al. (2011) method. In this final simplification, the source DEM data was not filtered and the areas of vegetation were not multiplied by 0.8 to reduce the number of times the DEM was processed at its finest resolution. The simplified formulae for  $z_{0-local}$ ,  $h_{m-eff-local}$  and  $d_{local}$  described in sections 5.2.1 to 5.2.3 were used in combination with a fixed grid size of 1 km in length and width. Effective parameters were established from these local parameters in the same way as for the other models tested.

### **5.3 Results and Analysis**

#### **5.3.1 Comparison of the Simplified and Millward-Hopkins et al. Models**

Figure 5-20 shows the differences between the simplified and Millward-Hopkins et al. (2013c) wind speed predictions for Leeds at 20 m above ground (A) and 10 m above  $h_m$  (B) with accompanying scatter plots (C and D). At 20 m above ground, the models agree with

MAPE of 1.89% and RMSPE of 6.4%. When the height is 10 m above  $h_m$  MAPE is 1.61% and RMSPE is 3.99%.

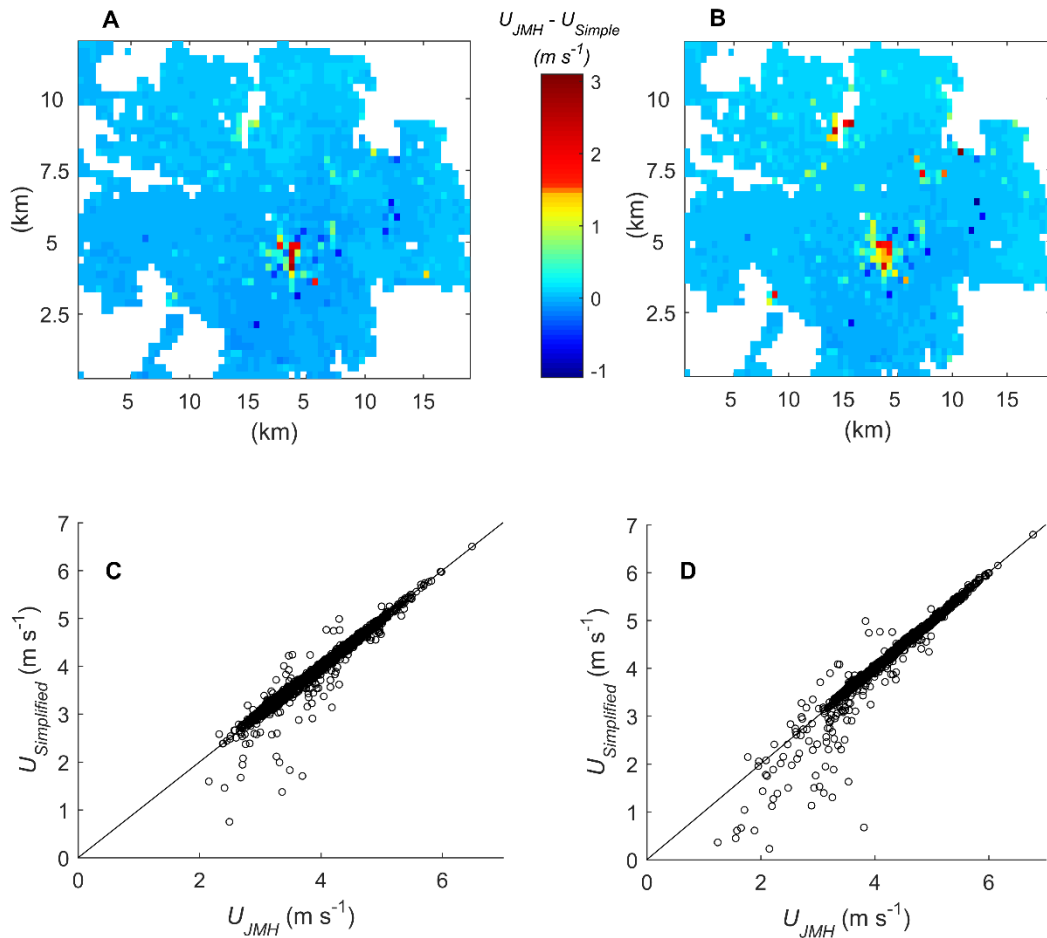


Figure 5-20 Comparison of simplified and JMH methodology windspeed simulations at 20 m above ground (A and C) and 10 m above  $h_m$  (B and D).

The two methods bear similarity although the simplified model predicts slower windspeeds than Millward-Hopkins et al. in the most dense neighbourhoods of the city. The most likely cause for this are the differences in how height variability and density are considered in each model. It is reasonable to suggest that the trends in  $z_{0u}$  against  $z_{0-JMH}$  for neighbourhoods with high  $\lambda_p$  and  $\sigma_h/h_m$  investigated in sections 5.2.1 and 5.2.2 were poorly identified due to the small amount of available data. Furthermore, Figure 5-4 and Figure 5-17B show increased scatter at higher  $d$  and  $h_{m-eff}$  which will also contribute to the differences between the two models in the most dense neighbourhoods.

### 5.3.2 Comparison of Models to Measured Wind Speeds

The accuracy of wind speed estimation under each model in comparison to measured annual average wind speeds is shown in Figure 5-21 for twelve sites from four major UK cities. The Millward-Hopkins et al. (2011) and further simplified models have been abbreviated to JMH and FS in the following figures. Table 5-3 provides more detail regarding each validation site

in which  $h_{m-local}$ ,  $h_{m-eff-local}$  and  $\sigma_h/h_m$  are as calculated with a 250 m grid and  $z$  refers to height above the surface.

Site No.	City	$z$ (m)	$h_{m-local}$ (m)	$h_{m-eff-local}$ (m)	$\sigma_h/h_m$ (m)	Height above roof (m)
1	Leeds	24	11.097	19.576	0.669	6.5
2	Leeds	28	11.097	19.576	0.669	10.5
3	Leeds	17	9.731	13.334	0.364	17.0
4	Leeds	32	9.731	13.334	0.364	32.0
5	Edinburgh	30	17.486	26.774	0.459	5.0
6	Edinburgh	27	17.330	27.071	0.483	5.5
7	Nottingham	10	8.883	9.107	0.036	10.0
8	Nottingham	17	15.582	20.419	0.293	3.0
9	Nottingham	19	9.511	12.725	0.338	3.0
10	Manchester	21	9.110	21.065	1.097	3.1
11	Manchester	42	9.204	15.303	0.607	12.0
12	Manchester	45	17.845	31.053	0.610	2.5

Table 5-3 Validation site characteristics

The greatest overestimations of wind speed occurred under the further simplified and Macdonald methodologies at the two Edinburgh sites (5 and 6) while, under the simplified methodology, site 7 produced the most accurate estimation of annual average wind speed. All methodologies performed most poorly at site 5. Due to the small amount of validation data available it is difficult to identify a specific cause for this however the site has an extent of open ground to the south which continues to the edge of the domain. Whilst in reality there is a large town approximately 6 km to the south, the study area is too small to incorporate this feature. Therefore, in reality a boundary layer has formed long before the validation site whereas the models only develop the boundary layer from 2 km to the south of the site.

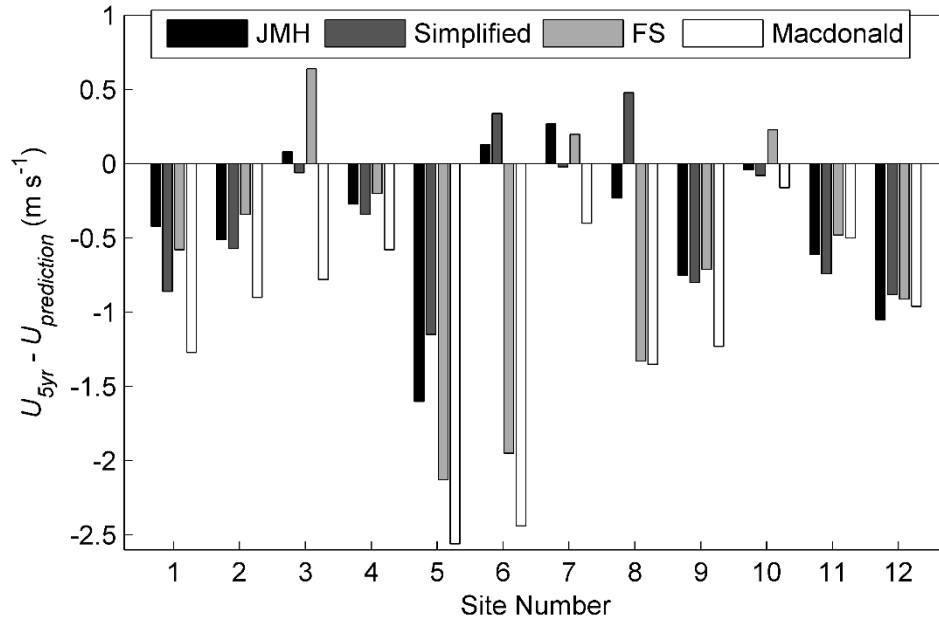


Figure 5-21 Performance of all four models at all sites against measured wind speeds

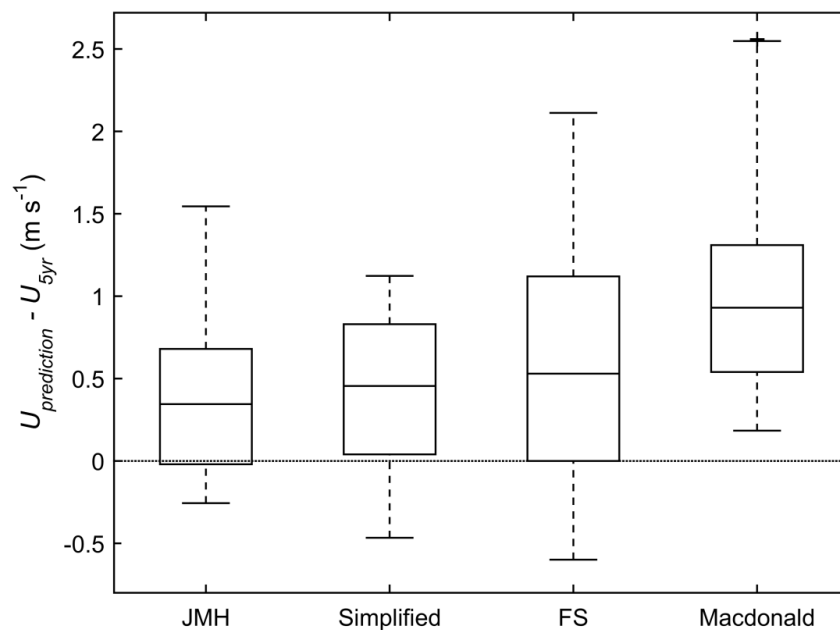
Site 8 produced significant differences in accuracy between the four models. A possible reason for this, as Table 5-3 shows, is that  $z$  is smaller than  $h_{m-eff-local}$  which is unique among the validation sites and means the site is sheltered by surrounding properties under the interpretation of the full Millward-Hopkins et al. methodology. However, in the Macdonald model  $h_m$  is used in place of  $h_{m-eff-local}$  and so it defines the site as exposed. Therefore, the Macdonald model applies the logarithmic profile all the way to  $z$ , whereas the other models use the logarithmic profile to  $h_{m-eff-local}$  and then the exponential profile from  $h_{m-eff-local}$  to  $z$ .

The poor performance of the further simplified model at site 8 is due to the use of the 1 km neighbourhood grid. In contrast to Table 5-3, which displayed 250 m grid geometric properties, the 1 km grid returns substantially different  $h_{m-local}$ ,  $h_{m-eff-local}$  and  $\sigma_h/h_m$  values (37% less, 9% less and 62% greater respectively) which serves to prove that the 1 km grid is too large to use for bulk parameterisation. The larger grid fails to portray the surface with sufficient detail to predict annual average mean wind speeds at an accuracy that is competitive with the JMH and simplified models. The MAPE of all models in comparison to measured wind speeds are shown in Table 5-4.

Model	MAPE (%)
JMH	16.13
Simplified	17.88
Further Simplified	29.66
Macdonald	38.76

Table 5-4 MAPE of each model in comparison to measured wind speeds

JMH was the best performing methodology but there was only a slightly greater error under the simplified methodology with a 1.75% difference between the two. Given that wind power is proportional to wind speed cubed, the additional 11.78% and 20.88% MAPE in wind speed estimation incurred through the use of the further simplified and Macdonald models are significant and suggests they should not be applied in wind resource assessment where there are heterogeneous surfaces, such as urban and semi-urban areas. The large difference in MAPE between the simplified and further simplified models suggests that a neighbourhood grid size of 1 km in length and width is too coarse to adequately model the aerodynamic properties of a surface. It also suggests that the data pre-processing steps to remove outliers and account for vegetation porosity cannot be omitted. This may be particularly important for UK cities which tend to have large areas of tree coverage. This pre-processing requires approximately three hours to execute for the city of Leeds (17 km East to West by 12 km North to South) when using an Intel® Xeon® 3.1 GHz processor and 4GB of RAM. Therefore, the simplified methodology takes approximately half a day to execute for a large UK city and thus could be rapidly applied for a large number of cities where the required input datasets can be obtained.



**Figure 5-22 Performance of all four models. The Macdonald model plus sign represents an outlier data point.**

Figure 5-22 shows that there is a general trend to over-predict annual average wind speeds regardless of the model used but that the JMH model has the median closest to zero and the smallest inter-quartile range. Despite a similar median to the JMH and simplified models, the further simplified model has the largest inter-quartile range. This may be a result of the larger



local neighbourhood size failing to parameterise the most local surface objects to the site as accurately as the smaller local grid sizes used in the other models.

It is important to note that the time required to estimate wind speeds for a large city such as Leeds is considerably shorter under the simplified methodology. From the stages after the DEM data has been filtered, the Millward-Hopkins et al. (2013c) model requires approximately 15 hours to run whilst the simplified approach completes in under one hour when executed using an Intel® Xeon® 3.1 GHz processor and 4GB of RAM. When the time to execute the pre-processing steps is also included, the simplified model estimates wind speeds across a 17 km by 12 km city in approximately four hours. Given the small (1.75%) reduction in accuracy described in Table 5-4 and that the usability of the method is much improved, the simplified model provides a useful tool for wind speed prediction wherever a DEM, building footprint data and reference wind speed data are available.

## 5.4 Conclusions

A rapidly executable and widely deployable city scale wind resource assessment methodology has been demonstrated that estimates wind speeds with only a small increase (1.75%) in MAPE when compared to a more complex and computationally intensive methodology. Height-independent variables ( $\lambda_p$  and  $\sigma_h$ ) have been used in conjunction with empirically determined coefficients to predict the aerodynamic parameters  $d$ ,  $h_{m-eff}$  and  $z_0$  from DEM and building footprint data. The outputs closely match those of the complex methodology with RMSPE between the two of 8.26%, 14.13% and 19.46% for  $d_{local}$ ,  $h_{m-eff-local}$  and  $z_{0-local}$  whilst effective parameters have been modelled with RMSPE of 6.4%, 7.43% and 11.3% respectively.

When applied to the logarithmic wind profile equation and validated against 12 sites from four major UK cities and their surrounding areas, the simplified local and effective  $z_0$  and  $d$  estimations led to an error in wind speed estimation of 17.88% MAPE which compares to 16.13% MAPE under the existing methodology. By contrast, aerodynamic parameters derived under the Macdonald model led to long term average wind speed estimations with 38.76% MAPE showing that it should be used with great caution if applied to wind resource assessment in cities with heterogeneous height profiles.

The outputs of the simplified methodology are sufficiently accurate to inform a first appraisal across a city region of locations that are potentially suitable for a wind turbine and can aid the siting of anemometry for further investigations. Together with the advancements in city-scale solar insolation assessment presented in sections 3.2 and Chapter 4, the simplified

methodology can be incorporated into a city scale wind and solar microgeneration viability analysis which is described in Chapter 6.

## Chapter 6 Microgeneration Investment Planning

This section describes a city-scale study combining the advancements made in the thesis with regard to the appraisal of: roof geometries from DSM data (section 3.2); solar insolation (section Chapter 4); and long-term average wind speeds (section 5.2). It builds from the literature described in section 2.3 to explore the viability of solar and wind microgeneration technologies in a study area containing the city of Leeds (UK) by incorporating the financial context that currently shapes the industry. In addition, a range of scenarios are presented to demonstrate how the methodology can be adapted to examine the impact of changes to policy, technology performance and installation costs.

### 6.1 Method

The method presented here uses modelled solar and wind resource as inputs to a financial model that incorporates a range of cost and revenue streams and produces return on investment (ROI) and payback time estimates. Whilst the solar resource input data is in the form of generated power per m<sup>2</sup>, the wind resource data must undergo a conversion from long term average wind speeds to annual wind turbine power output. The full complement of revenues and costs for each technology can then be defined using installation size and modelled power output which allows for the financial metrics of viability to be calculated. The variables of the model can be adapted as required to investigate a wide range of investment conditions, which are explored as scenarios later in the section.

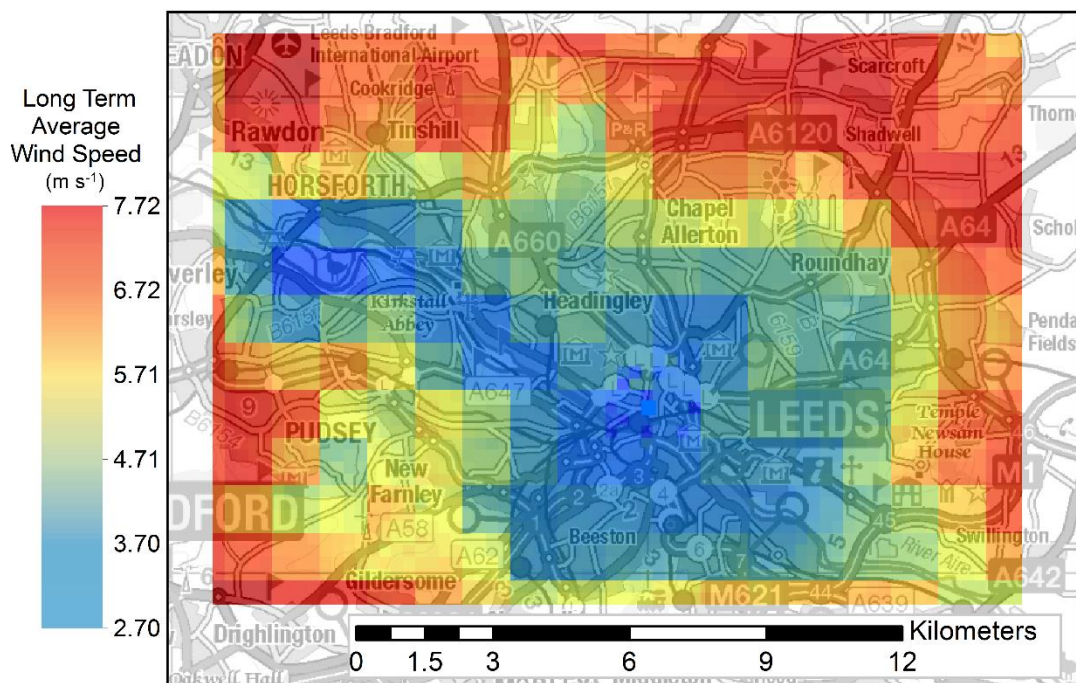
The study area has been defined as the region described earlier in Figure 5-1, namely, a 17 km (East to West) by 12.5 km (North to South) zone incorporating the city of Leeds (UK) at its centre. The reasons for this are that all of the data required for the methodology were available in this area and also that it was also possible to source quotes from local solar PV installation companies and confirm that wind turbine installation costs were applicable to this area.

#### 6.1.1 Resource Estimations

##### 6.1.1.1 Wind

The map of long-term mean wind speeds for every 250 m by 250 m neighbourhood in the study area (Figure 6-1) has been produced using the simplified methodology described in section 5.2 for heights above ground of 20 m and 36 m. As the underlying reference climatology dataset (NOABL with a correction to match the NCIC database) is built from data spanning many years, the wind speeds predicted are long-term averages rather than annual

ones. For example, the NCIC database is built from observational data spanning 30 years from 1981 to 2010 whilst NOABL covers only ten years (Weekes, 2014). 36 m was selected because it is the hub height of the WindEn 45 wind turbine that produced the best return on investment (ROI) in a city-scale study of Leeds by Adam et al. (2015). The Kingspan KW15 turbine, with a hub height of 20 m, did not perform as well but has been included due to its lower CAPEX cost and popularity in the market. Both the Kingspan KW15 and WindEn 45 have achieved MCS approval, meaning they are both eligible for government financial incentives. Roof-mounted micro-turbines, that are typically smaller than 6 kW, are not investigated here due to their lack of penetration into the market, questions regarding robustness in what are turbulent locations and scarcity of turbines with MCS approval which means the devices are rarely eligible for government financial incentives.



**Figure 6-1 Long-term mean wind speed ( $\text{ms}^{-1}$ ) at 36 m above ground for every neighbourhood across Leeds**

At first glance, Figure 6-1 appears to show neighbourhoods of 1 km in width and height. However, the smallest neighbourhood size is actually 250 m in width and height. What has happened is that at 36 m above ground the reference climatology, which has a 1 km resolution, for two neighbourhoods next to one another has a greater influence on long-term mean wind speed than the differences in surface form between those two neighbourhoods. Regardless, when the study area is analysed across the entire city, the patterns that emerge are as one would expect in that there is a very significant difference in long-term mean wind speed for urban areas when compared to more exposed, rural areas. The patterns in long-term mean wind speed are generally inversions of the trends described in section 5.2 for  $d$

(Figure 5-1),  $z_0$  (Figure 5-8) and  $h_{m-eff}$  (Figure 5-16), whereby wind speeds are greater where those aerodynamic parameters are smaller. Figure 6-2 shows the distribution of wind speeds estimated across the city of Leeds for hypothetical hub heights of 36 m (A) and 20 m (B) above ground.

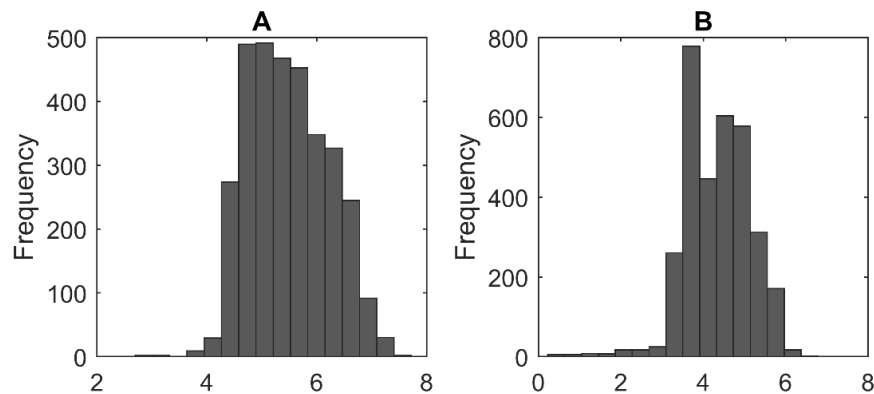


Figure 6-2 Histogram of long term average wind speeds ( $\text{ms}^{-1}$ ) at 36 m (A) and 20 m (B) above ground for each 250 m x 250 m neighbourhood across the study area

### 6.1.1.2 Solar

Roof geometries of buildings with plan areas of less than 200  $\text{m}^2$  were defined as “small” and estimated using the neighbouring buildings method described in section 3.2. For buildings with a plan area of more than 200  $\text{m}^2$  (defined here as “large”) roof slope was estimated directly from DSM data by nearest neighbour interpolation and orientation was estimated from the direction of slope between neighbouring DSM data points. Therefore both orientation and slope calculations for large buildings followed the Gooding et al. (2013) methodology but with an adaptation. To account for the variety of geometries and shading often observed across a single large property, each large property had a grid of points spaced 10 m apart overlaid onto it. Insolation calculations for each of these points were summed to give a total insolation for the building. Whilst a finer grid spacing may have picked up smaller changes across the roof, a grid spacing of 10 m held an advantage in facilitating a method that would not require high power computing which is a key aim of the wider research project. It is also important to note that the aim is to assess where a solar PV installation would be sited and to consider the area it requires. The geometrical information for both large and small properties was then inputted to the RTS-CS method described in section 4.5 which returned an estimation of annual electricity generation in  $\text{kWh m}^{-2}$ .

## 6.1.2 Viability

### 6.1.2.1 Wind

There are three parts to defining wind turbine viability (illustrated in Figure 6-3) which the following sub-sections (6.1.2.1.1 to 6.1.2.1.3) define in turn.

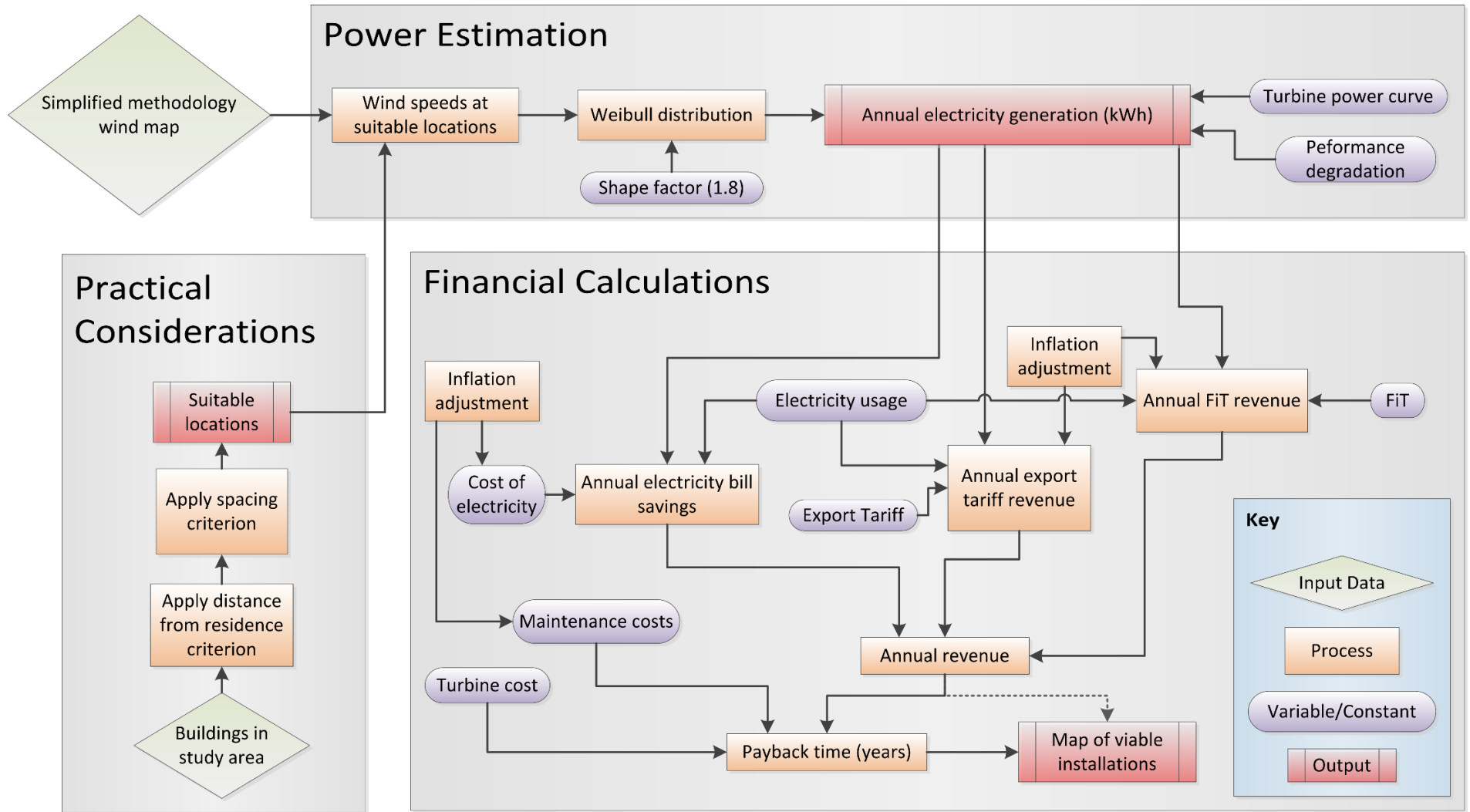


Figure 6-3 Process chart for wind viability assessment

#### **6.1.2.1.1 Practical Wind Turbine Considerations**

Despite the logic of defining them, there are no minimum separation distances between wind turbines and housing defined by the Government and there are no plans to introduce them (Smith, 2015). However, the following criteria were applied in order to estimate a potential for city-scale generation that would reflect likely real-world constraints such as acoustic intrusion, for example. ETSU-R-97 legislation specifies that noise generated by a wind turbine should be no louder than 5 dB above background noise from a residence (Department of Trade and Industry, 1996). Without detailed site-specific acoustic surveys, however, the precise distance from a residence is impossible to accurately model. It is assumed that this distance will be smaller than the distance required to avoid “shadow flicker” which Scottish Government planning guidance defines as ten times the rotor diameter (Scottish Government, 2014). This is 146 m for the WindEn 45 turbine and 98 m for the Kingspan KW15. The distance of ten times rotor diameter is also the largest suggestion for distances between turbines outlined in planning policy statement legislation for Northern Ireland (Department of Environment, 2008).

The locations across the study area that meet the distance from residence criterion are shown in Figure 6-4 and are mostly rural or semi-rural although there are isolated areas within the most urban parts of the study area that remain suitable. The WindEn 45kW is suitable for a large percentage of the areas where a Kingspan KW15 is although there are many highly urban areas where a WindEn 45kW could not be installed. The figure clearly illustrates that a considerable area has been lost and that the investigation of wind turbine viability is significantly restricted before even wind speeds are considered, not to mention financial barriers.



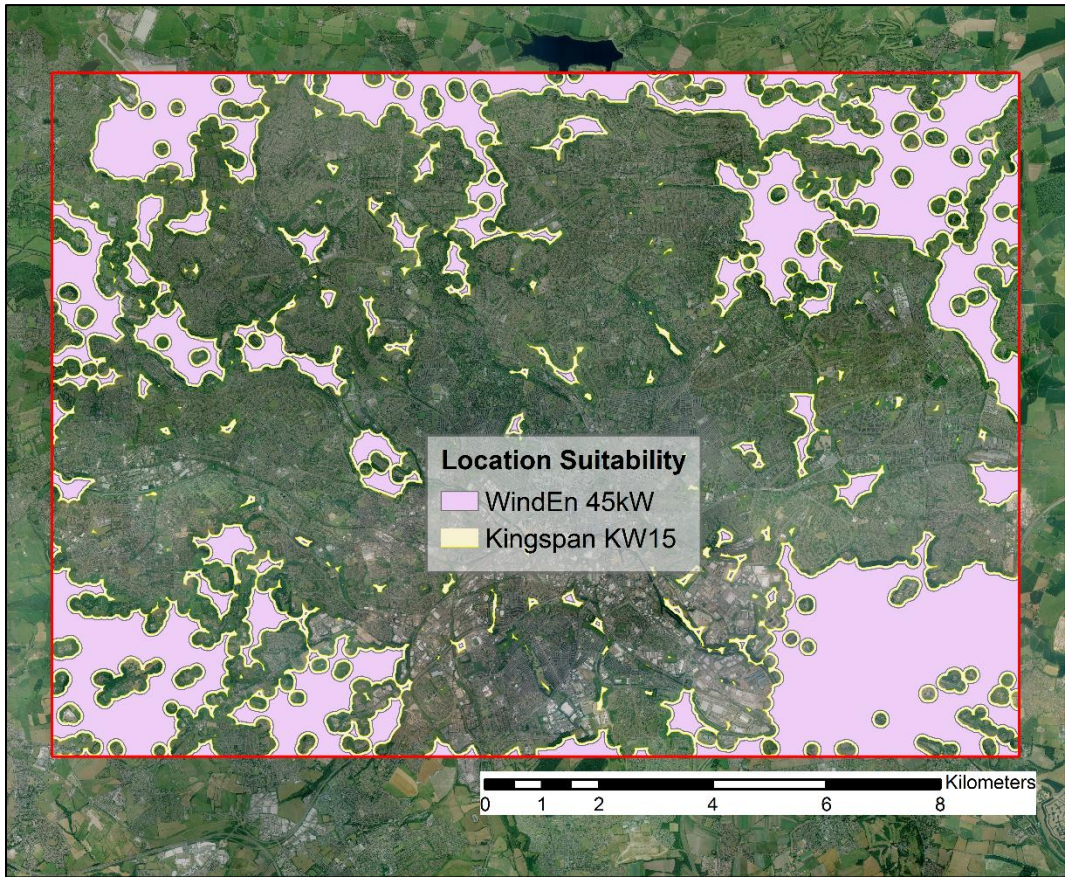


Figure 6-4 Locations that meet the criteria regarding distance from residences. The Kingspan KW15 is suitable for all locations where a WindEn 45kW turbine is.

#### 6.1.2.1.2 Wind Turbine Power Output Estimation

This section describes power output calculations for the locations identified in the preceding section from the long-term average wind speeds estimated using the simplified method (section 5.2). An adjustment has to be made because although the long term average wind speed may be used as a comparative indicator between two sites, wind turbine power output should not be estimated from it. Far greater accuracy can be achieved using the Weibull distribution  $f(u)$  which describes the range and relative frequency of wind speeds. It is a function of a shape parameter ( $\beta$ ) and a scale parameter ( $\eta$ ) and can be calculated using:

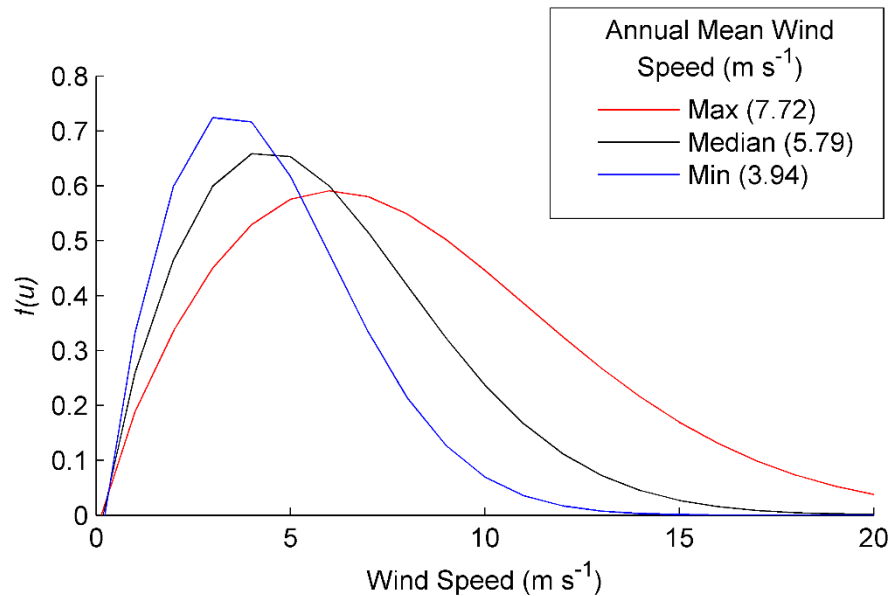
$$f(u) = \frac{\beta}{\eta} \left(\frac{u}{\eta}\right)^{\beta-1} e^{-\left(\frac{u}{\eta}\right)^{\beta}} \quad (6-1)$$

in which  $u$  refers to the particular wind speed and  $\beta$  is 1.8. This value comes from Best et al. (2008) who found that whilst  $\beta$  will vary for any particular site, 1.8 serves as a good approximation for a wide variety of locations across the UK.  $\eta$  in equation (6-1) is given by:

$$\eta = \frac{\bar{u}}{\Gamma\left(1 + \frac{1}{\beta}\right)} \quad (6-2)$$



where  $\bar{u}$  is the long term average wind speed. The Weibull distribution has been found to provide a good fit to measured data (Seguro and Lambert, 2000) and has the shape shown in Figure 6-5 for different annual mean wind speeds with the assumed shape factor of 1.8.

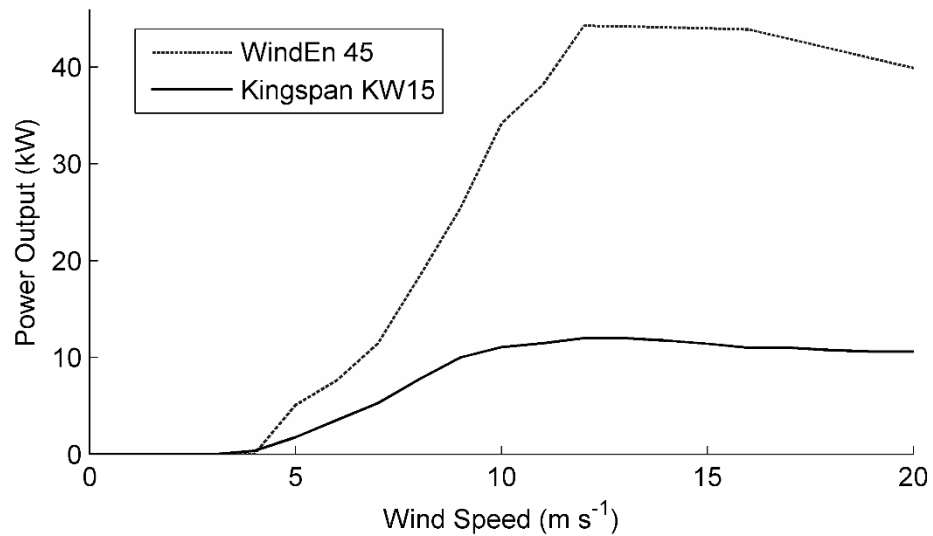


**Figure 6-5 Weibull distributions from minimum, maximum and median long term average wind speeds modelled for 36 m above ground-level using the method described in section 5.2 and restricted by the criteria presented in section 6.1.2.1.1**

Figure 6-5 shows that greater long term average wind speeds lead to Weibull distributions with slightly lower kurtosis and an increased skew to the right which means that greater wind speeds will occur more frequently. The Weibull distribution of wind speeds for a site can then be used to calculate annual energy generation using:

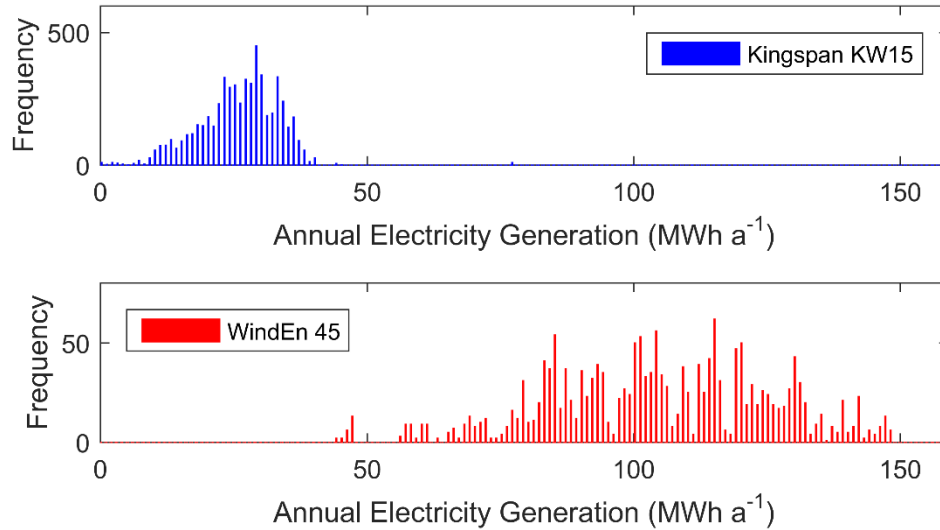
$$\text{Annual Electricity Generation (kWh)} = \frac{\sum_{u=1}^n p(u)f(u) \times (365 \times 24)}{\sum_{u=1}^n f(u)} \quad (6-3)$$

where  $p(u)$  is the expected power output from the turbine at a given wind speed  $u$ , and  $f(u)$  is the frequency with which wind speed  $u$  is expected to occur based on the Weibull distribution. Expected power output for the WindEn 45 and Kingspan KW15 turbines are shown in Figure 6-6 using data from the manufacturer (BetterGeneration, 2015). Unfortunately no data is available for wind speeds greater than  $20 \text{ ms}^{-1}$  despite the Kingspan KW15 having continuous operation in all wind speeds (Kingspan, 2015) and the WindEn 45 being operational to  $52.5 \text{ ms}^{-1}$  (WindEn, 2015). Figure 6-5 shows that for the maximum long term average wind speed of the locations suitable for a turbine, the frequency of wind speeds faster than  $20 \text{ ms}^{-1}$  is greater than zero though relatively small. Therefore, the decision to ignore power output for this portion of observed wind speeds will not have a significant impact on the accuracy of the viability assessment.



**Figure 6-6 Power curves for the WindEn 45 and Kingspan KW15 turbines (BetterGeneration, 2015)**

The power curve outputs shown in Figure 6-6 do not account for inverter losses that occur after a wind turbine's generator. For the WindEn 45 turbine, two suitable inverters have been found that operate with 93% (NewEnCo, 2004) and 96.1% efficiency (CCL Components, 2009) so as a conservative estimate, inverter losses of 7% have been incorporated into estimated annual electricity generation. The Kingspan KW15 is compatible with variants of the two inverters previously mentioned so the 7% loss is applied again. Approximate costs of inverters were supplied as part of the quotes for the turbines' total costs from the turbine manufacturers (Bjerknäs, 2016; Kerr, 2016). Applying the power curves in Figure 6-6 to equation (6-3) for the suitable sites identified in Figure 6-4 with the 93% inverter efficiency produced the distributions of annual electricity generation estimates shown in Figure 6-7 in which a<sup>-1</sup> is used to denote that the figures are per annum (used throughout the thesis). The same x-axis scale has been applied to both top and bottom histograms to highlight the difference in annual power output.

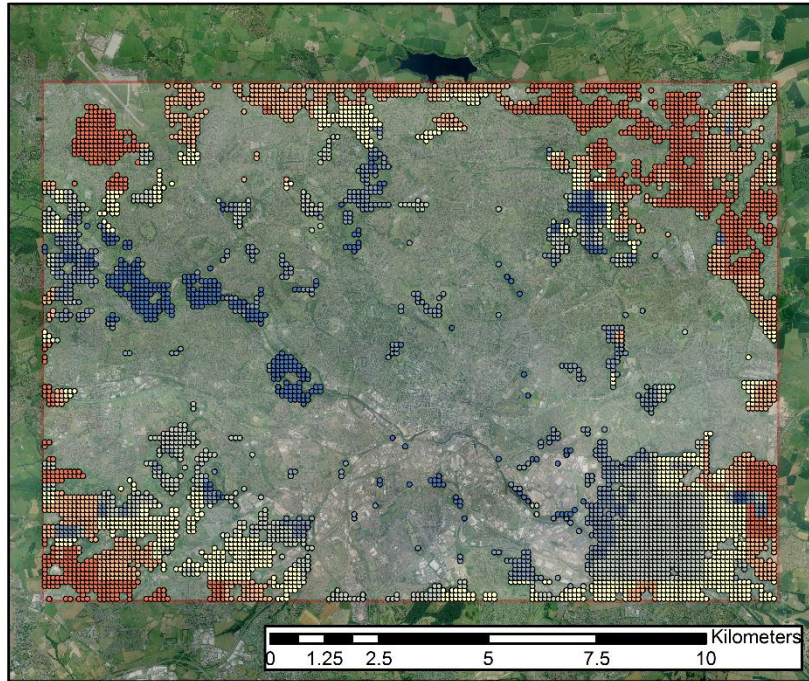


**Figure 6-7 Histograms of annual power output (MWh a<sup>-1</sup>) for both turbines in first year of operation at suitable locations in which frequency refers to the number of each turbine**

The histograms in Figure 6-7 show that although the number of suitable locations are far smaller for the larger WindEn 45 turbine given the spacing it requires, the annual power output will be considerably larger. The maps in Figure 6-8 show the distribution of the sites around the study area. When viewed this way, the geospatial patterns exhibit a strong similarity to the map of long term average wind speed at 36 m (Figure 6-1) as should be expected but this has the unfortunate result that the large area of suitable and exposed land in the South-East of the study area has relatively small long term average wind speeds and accordingly low annual power output.

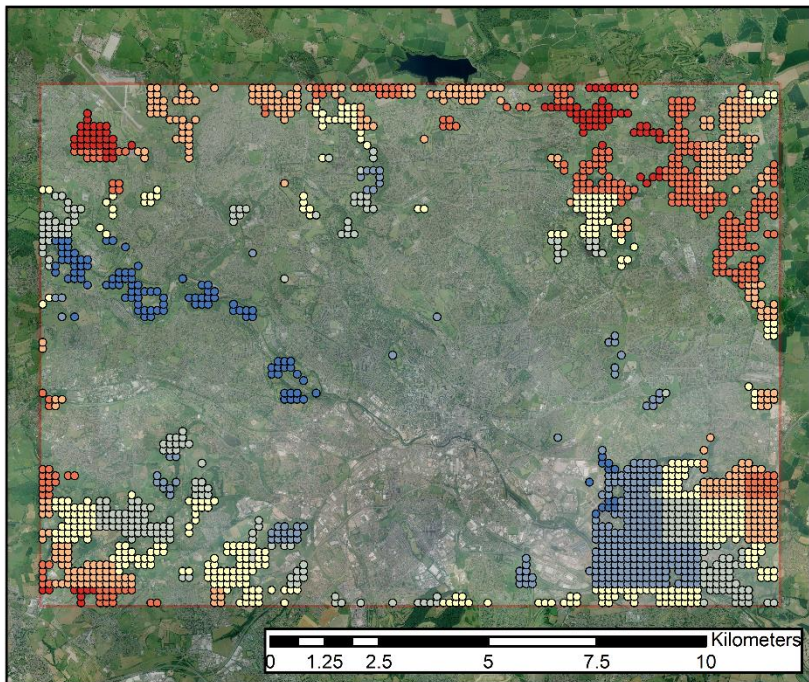
**Annual Power Output MWh a<sup>-1</sup>**

- 2 - 14.38
- 14.38 - 20.18
- 20.18 - 24.56
- 24.56 - 28.30
- 28.30 - 32.44
- 32.44 - 45.17
- 45.17 - 77.76



**Annual Power Output MWh a<sup>-1</sup>**

- 44.45 - 70.74
- 70.74 - 86.11
- 86.11 - 96.74
- 96.74 - 108.60
- 108.60 - 121.55
- 121.55 - 134.87
- 134.87 - 159.54



**Figure 6-8 Power output (MWh a<sup>-1</sup>) for the Kingspan KW 15 (top) and WindEn 45kW (bottom) turbines in suitable locations in first year of operation**

A further problem with the power curves shown in Figure 6-6 is that they are applicable to the wind turbine operating in its optimum condition when the performance of the turbine is known to decline with time. Detailed data relating to the degradation of the performance of the selected WindEn and Kingspan turbines over time is not available but Staffell and Green (2014) have reported a trend in the output of wind farms falling by 12% over a twenty-year

lifetime. In this model therefore, wind turbine power output is reduced by 0.6% for every year of operation (which is rounded from the compound 0.6371% rate).

The results will present the potential for both wind turbine technologies to contribute cost effective renewable electricity generation in the study area. Therefore, if a site is suitable to accommodate either turbine, it follows that the turbine capable of generating the most electricity must be selected. The area required for each turbine must also be incorporated into this calculation as it is possible that numerous Kingspan KW15 turbines could be installed in the area required for only one WindEn 45kW.

#### 6.1.2.1.3 Financial Viability

The annual power output of a wind turbine is a starting point from which financial viability can be calculated. The metric selected to describe both wind and solar installation viability is annual return on investment (ROI) which is described in equation (6-4) as the ratio of total annual revenue (from electricity bill savings and government incentives minus operating expenditure (OPEX)) to capital expenditure (CAPEX). OPEX has been defined by the European Wind Energy Association as £0.02 / kWh of electricity generated The European Wind Energy Association (2013).

$$\text{Annual ROI} = \left( \frac{\text{Annual Revenue} - \text{Annual OPEX}}{\text{Outstanding CAPEX}} \right) \quad (6-4)$$

The FiT, export tariff, electricity bill savings and OPEX undergo a correction for inflation that has been incorporated into the model using the average Retail Prices Index (RPI) rate from 2009 to 2013 (3.38%) as published by the Office for National Statistics (ONS, 2015).

In addition to ROI, a second measure of viability presented is payback time, which is the number of years required for the CAPEX and OPEX costs to be exceeded by the cumulative annual revenue. Both metrics of financial viability are used for the wind and solar analyses to enable a clear comparison. Table 6-1 summarises the costs and revenues for the wind technologies used in this study to complete equation (6-4) along with their sources.

Description	Source	Value	Applicable Dates
Average cost of domestic electricity for Yorkshire	DECC (2015a)	£0.1501 / kWh	From 2015 data
FiT for < 50 kW wind turbine	Energy Saving Trust (2015a)	£0.1373 / kWh	Prior to 15 January 2016
Export tariff	Energy Saving Trust (2015a)	£0.0485 / kWh	No forthcoming changes proposed at the time of writing

Maintenance costs	The European Wind Energy Association (2013)	£0.02 / kWh	2013 - No more current source available
WindEn 45 turbine, inverter and installation and groundworks costs	Bjerknäs (2016)	£180,000	As per personal communications in 2016
Kingspan KW15 turbine, inverter, installation and groundworks costs	Kerr (2016)	£78,400	As per personal communications in 2016

**Table 6-1 Costs and revenue streams for the wind viability analysis**

The first entry is related to the estimation of electricity bill savings using DECC statistics of typical electricity costs (£/kWh) by region (DECC, 2015a). The average cost of electricity for Yorkshire is marginally below the national average (£0.1538 / kWh) reported by DECC (2015a) so this can be regarded as a slightly conservative baseline condition. The cost of electricity is multiplied by an assumed proportion of the electricity generated that is used on site to give electricity bill savings. Adam et al. (2015) assumed that 50% of electricity generated by a wind or solar PV system would be used on site but that is felt to be too large and inconsiderate of the differences between the two technologies. For example at night, when electricity usage is very low, a wind turbine can generate electricity and Energy Saving Trust (2015b) estimate that a lower figure of 30% of domestic supply coincides with the wind generation profile so this is the figure selected for the Kingspan KW15 baseline scenario. Owing to the considerable size difference between the Kingspan KW15 and the WindEn 45, a lower baseline usage of 20% of electricity generated has been used for the latter turbine. Electricity bill savings are then calculated by multiplying the cost of electricity by the proportional amount of electricity used on site. The electricity bill savings are adjusted for inflation based on the 5-year average RPI described earlier in this section. The final column in Table 6-1 describes the dates that the costs and revenues are applicable to. This is made necessary by the frequently shifting policy context surrounding incentives to install microgeneration technologies. For example, the FiT rate for an MCS registered wind turbine is set to fall by 38% to 8.53 p/kWh from 08/02/2016. This incoming FiT rate is incorporated into the scenario testing section. In line with legislation quoted in Energy Saving Trust (2015a), the export tariff is applied to 50% of electricity generated regardless of the technology used to generate it so the same rate applies to both wind and solar in this study. There are plans to link this tariff to smart meter measurements of the actual electricity exported to the grid, though these had not come to fruition at the time of writing.

### **6.1.2.2 Solar**

Figure 6-9 describes the order of processes required to define solar PV installation viability which are discussed in the paragraphs that follow. Unlike the estimation of wind resource, the RTS-CS method described in section 4.5 provides a power output estimation in kWh m<sup>-2</sup> a<sup>-1</sup> using a PR adjustment and so there is no requirement for conversion from solar insolation to generated electricity. The roof geometries of small buildings (smaller than 200 m<sup>2</sup> in plan area) fed into the RTS-CS method were found using the neighbouring buildings methodology described in section 3.2. The slope and orientation of larger properties were defined by nearest neighbour regression of DSM data as in Gooding et al. (2013) before being inputted to the RTS-CS method to calculate annual insolation.

#### **6.1.2.2.1 Power Estimation**

For wind, two types of installation were used at every site whereas for solar the capacity of a solar PV installation varies with available roof area. Using the modelled South-facing area and the area required for each panel, the size and cost of installation can be scaled for each building. In this study, the total area required for a single PV panel in an array was 1.8 m in length and 1 m in width which is based on the dimensions of a popular LG 285 W mono-crystalline PV panel (1.6 m<sup>2</sup>) with a small addition for the surrounding space required. The typical power output of a solar PV cell declines with time and although no data for the degradation of the selected LG 285 W was available, NREL (US) research found a median percentage degradation rate of 0.23% per year for mono-crystalline PV panels (Jordan and Kurtz, 2013) which is the rate applied here. In addition to the fall in the efficiency of the solar cells, there are also losses at the inverter. SMA solar is a market leader (Ali-Oettinger, 2013) that offers a range of inverters to cover all sizes of PV installation that typically perform at 98% maximum efficiency (SMA, 2015a; SMA, 2015c; SMA, 2015d; SMA, 2015e; SMA, 2015b). Maximum inverter efficiencies should be treated with caution as inverter efficiency varies with the power generated by the PV panel. To capture this effect, the inverter efficiency applied in the study was reduced by 1.75% to 96.25%.



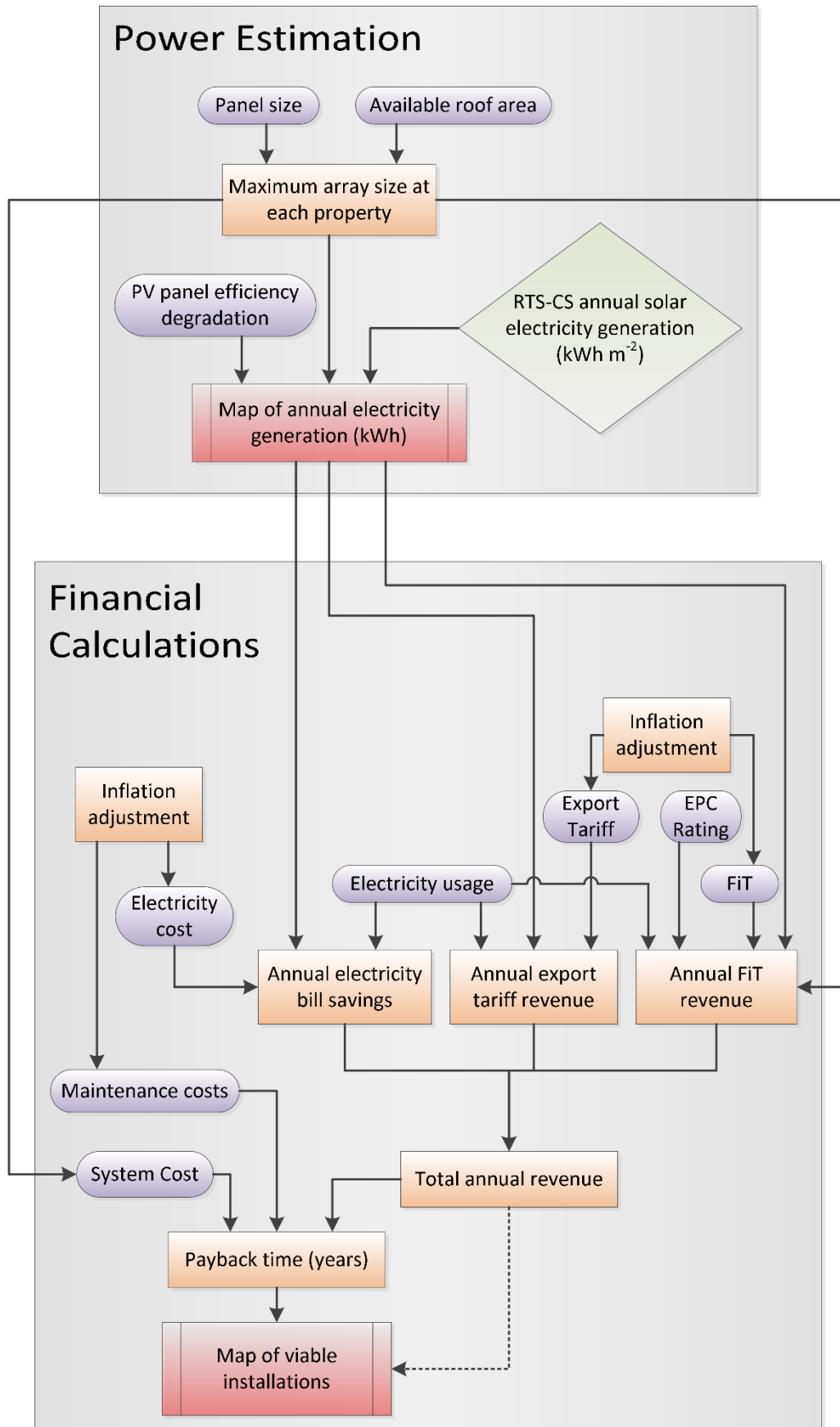


Figure 6-9 Process chart for solar PV viability assessment using the same key as Figure 6-3



For installations across complex roofs where specific panels have to be located in areas prone to occasional shade, an array of micro-inverters may be more efficient than a single inverter. This is because the shaded parts of an installation with micro-inverters do not negatively impact the total power output of the installation to the same degree as they would for an installation with a solitary inverter. The unshaded regions feed current to a separate inverter. However, devising bespoke inverter arrangements is beyond the scope of this research into city-scale microgeneration viability which has the key aim of providing a first estimate of viability for stakeholders to then pursue further, site-specific investigation as necessary.

#### 6.1.2.2.2 Financial Viability

The CAPEX costs for solar PV comprise of the costs of the panels, roof mountings, inverter, wiring and labour. Two solar PV installation companies based in the study area have provided the quotes in Table 6-3 that incorporate all of these costs into a £/kWp installed figure.

Company	Size of Array (kWp)	Installed Cost (£/kWp)
GMI Energy <sup>b</sup>	1	1,600
Leeds Solar <sup>a</sup>	2.5	1,400
Leeds Solar <sup>a</sup>	2.7	1,407
Leeds Solar <sup>a</sup>	3.78	1,230
Leeds Solar <sup>a</sup>	4	1,200
Leeds Solar <sup>a</sup>	4.86	1,049
Leeds Solar <sup>a</sup>	5	1,040
GMI Energy <sup>b</sup>	50	950
GMI Energy <sup>b</sup>	250	800

Table 6-2 Quotes for total cost of solar PV systems. <sup>a</sup>(Platt, 2016b) <sup>b</sup>(Roberts, 2016).

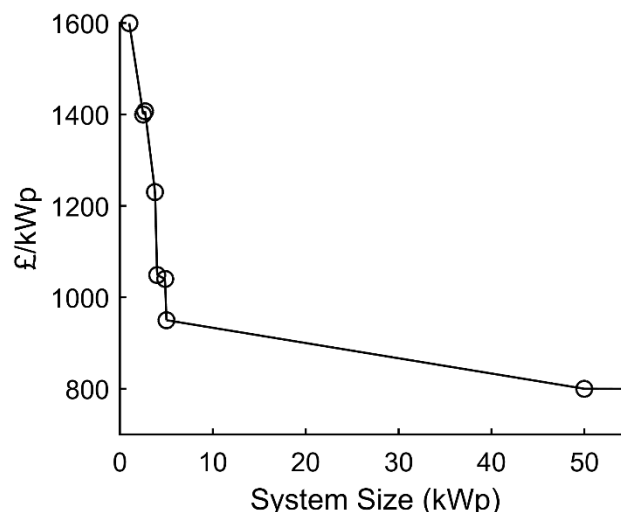


Figure 6-10 Interpolated PV array costs from Table 6-2 to 55 kWp

Figure 6-10 shows an interpolation of the PV panel costs where the line continues from the £950 / kWp at 50 kWp through the remaining system sizes shown in Table 6-3. It is from this line that panel costs are calculated for the wide range of system sizes that occur in a city-

scale study. In addition to the CAPEX costs, solar PV is also subject to an OPEX cost. An annual maintenance cost of £15 for every kWp of solar panels installed has been selected that is consistent with Dufton (2012) and is later adjusted for RPI inflation.

Annual revenue is calculated by summing income from the FiT and export tariff for the electricity generated with savings made on electricity bills. For the baseline scenario, FiT rates that were accurate as of 1<sup>st</sup> January 2016 have been adopted. Table 6-3 shows the categorisations of solar PV systems by kWp size and subcategories of higher, medium and lower rates.

<b>System Size (kWp)</b>	<b>Higher (p/kWh)</b>	<b>Middle (p/kWh)</b>	<b>Lower (p/kWh)</b>
<=4	12.03	10.83	5.73
>4, <=50	10.90	9.81	5.73
>50, <=150	9.29	8.36	5.73
>150, <=250	8.89	8.00	5.73
>250	5.73	5.73	5.73

**Table 6-3 Summary of FiT rates applicable for 1<sup>st</sup> January 2016 (ofgem, 2015)**

The lower rate is applied to properties that do not have an environmental performance certificate (EPC) rating of A to D. The medium rate is applicable to properties with an EPC rating of A to D but where the owner has 25 (or greater) FiT-registered installations. The higher rate is for buildings with an EPC rating of A to D where the owner has fewer than 25 FiT-registered installations. Two assumptions have been made with respect to selection of the appropriate rate. First, this study will not link installations to owners and so will not consider the middle rate. The second is an approximation that all properties will have, or could easily attain, an EPC rating of A to D. This is based on the current EPC ratings data for the city of Leeds from the Department for Communities and Local Government which shows that over 78% of properties already have an EPC rating of A to D (DCLG, 2015). FiT rates for solar microgeneration have undergone even greater change than those for wind over the past six years and Figure 1-1 showed the impact that the first major alterations had on the industry. At the time of writing, the solar FiT rates were to be significantly reduced from those quoted in Table 6-3, the full extent of which are discussed in the scenario testing section but by way of example, the rate for installations under 4 kW is reduced by 76% to 4.39 p/kWh. Fortunately, the export tariff is less complex to incorporate as it is fixed at 4.85 p/kWh for all sizes of solar PV installation and there were no plans to change it at the time of writing.

Electricity bill savings are modelled using the same approach as described for wind whereby the proportion of electricity generated that is used on site is estimated first. The assumed 50% usage figure found in the original FiT to define the export tariff (and applied in Adam et al. (2015)) was estimated at a time when PV system sizes were smaller on average. Falling prices have meant that larger systems are more affordable and so whilst in 2011 the average system size was 2.75 kWp it is now 4 kWp (Energy Saving Trust, 2016). It is reasonable to suggest that consumption of electricity during times of peak production has not grown at the same rate and for this reason, a figure of 25% for residential usage of electricity generated from solar PV has been adopted. Owing to the increased likelihood of a large (> 200m<sup>2</sup>) property being a place of work and so having a higher electricity consumption during times of peak solar PV electricity generation, a higher usage of 40% of electricity generated by solar PV has been assumed in the baseline scenario. For a more complete understanding, the sensitivity of the model to on-site usage will be investigated by varying the percentage and testing the impact on payback time.

Adjustments for inflation have been made to increase the FiT, cost of electricity and export tariff using the same five-year average RPI rate described in section 6.1.2.1.3. All of the revenues and costs are then brought together to calculate ROI (using equation (6-4)) and payback time.

### 6.1.3 Scenario Testing

The baseline model has been adapted to investigate potential future conditions for microgeneration investment as summarised in Table 6-4. Demonstrating the model's adaptability, three scenarios have been developed that are unique configurations of the five variables defined in Table 6-5. The paragraphs that then follow discuss the reasoning behind the design of the scenarios.

ID	Description	Variables				
		FiT Rates	Installation Cost	Electricity Cost	Generated Electricity Usage	Technology Efficiency
1	New FiT	Low	Baseline			
2	Optimistic	Low	Low	High	High	Solar only: PR to 0.85
3	Pessimistic	Low	High	Low	Low	Baseline

Table 6-4 Three scenario Conditions

Variable	Condition			
	High	Baseline		Low
FIT Rates	NA	Applicable prior to 15/01/2016		Applicable: 15/01/2016 to 31/03/2016
		Wind: £0.137 / kWh	Solar: see Table 6-3	Wind: £0.085 / kWh Solar (< 10 kW): £0.044 / kWh (10-50 kW): £0.046 / kWh (>50, <=250 kW): £0.027/kWh
Installation Cost	Solar: Interpolated values of Figure 6-10 + 20% Wind: Quoted values +16%	See Figure 6-10 interpolated values		Solar: Interpolated values of Figure 6-10 - 20% Wind: Quoted values -16%
Electricity Cost	£0.162 / kWh	£0.150 / kWh		£0.147 / kWh
Generated Electricity Usage	Solar: Large properties 50%, small properties 30% Wind: WindEn 25% Kingspan KW15 35%	Solar: Large properties 40%, small properties 25% Wind: WindEn 20% Kingspan KW15 30%		Solar: Large properties 30%, small properties 20% Wind: WindEn 15% Kingspan KW15 25%

Table 6-5 Variable definitions for scenario testing

Scenario 1 is designed to investigate how the FiT rates that are applicable from 15/01/2016 to 31/03/2016 will impact microgeneration viability so all other variables are unchanged from the baseline. The rates that immediately follow (applicable from 01/04/2016 to 30/06/2016) are only £0.001 / kWh lower and so the results of this scenario are highly indicative for that time period also. A new feature added to the FiT system in 2016 is the deployment cap which will reduce FiT rates for all microgeneration technologies if the number of installations deployed in the preceding quarter is deemed too high by Ofgem. Due to the high complexity of forecasting the number of installations, it has been assumed that deployment rates will remain below the threshold. The first monthly report from Ofgem to

assess deployment against the cap found that solar PV (< 10 kW) had reached only 15.7% of its 48.4 MW cap limit for the quarter in the first month (Ofgem, 2016). Solar PV of 10-50 kW had reached 12.3% and there were no wind turbines of less than 50 kW installed in the month (Ofgem, 2016). This scale of deployment serves to vindicate the assumption made.

As in scenario 1, scenario 2 also incorporates the upcoming FiT rates but is otherwise an optimistic perspective on microgeneration financial viability as installation costs are lower, electricity bills are higher and technology efficiency increases. Communications with two solar PV installation companies in the study area have revealed that solar PV prices have fallen significantly in recent years (Platt, 2016b; Roberts, 2016). For example, the price per kWp of a 2.5 kWp array now stands at £1,400 having been £1,920 just 18 months ago (Adam et al., 2015). The trend is repeated when looking across the country using statistics from DECC that show the cost of solar panels also decreased before that, from 2013 to 2015, around the time that data was collected for Gooding et al. (2013). In a nationwide average, a 4-10 kWp installation cost £1,620 per kWp in April 2013 and went on to cost £1,512 per kWp in February 2015 (DECC, 2015f). Whilst the cost reduction stated by the installers in the study area amounted to a 27% fall in prices, both sources stated that the fall in price was strongly related to currency exchange rates and changes in their business strategy: reducing profit margins to counteract the negative effects of the changes in the FiT. For these reasons, the optimistic scenario uses a slightly more conservative 20% fall in installation costs. Personal communications with the installers of the two wind turbines have revealed no such change in installation cost (Bjerknäs, 2016; Kerr, 2016) although a lower-rated version of the Kingspan KW15, the 6 kW Kingspan KW6, has fallen in price by 16% over the last two years. Therefore, the optimistic scenario applies this scale of price reduction to the cost of the Kingspan KW15 and WindEn 45 turbines.

There are various reasons to test the impact of higher electricity bills. The clearest justification is that they have risen above inflation for the past 5 years with the exception of 2015 which was a slight reduction (Doward, 2013; DECC, 2015e). International influences on electricity prices, such as political instability in oil producing countries and volatile international relationships with natural gas suppliers such as Russia, are factors to be aware of that justify a scenario featuring higher electricity costs. Inflation adjusted electricity prices described by DECC (2015e) for the last five years have been used to define the scale of a potential increase. A linear interpolation was applied to the data and then expanded to extrapolate the increase in electricity price for the next year which was found to be an 8% increase. Therefore, the increased electricity cost is defined as £0.1621 per kWh.

Scenario 2 also has an assumption of high technology efficiency which is incorporated into the model by increasing the PR from 0.8 to 0.85. There are numerous recent studies that have looked at the performance of solar PV installations and reported PR in excess of 0.8 (Reich et al., 2012; Leloux et al., 2012) and it is also important to note that the efficiency of solar panels reaching the mass market has gradually increased with time.

The optimistic scenario also incorporates a higher usage on site of the electricity generated from the wind or solar installation. Such an increase could occur if current behaviours change and more owners start to coincide their electricity consumption with the peak production times of their installations through the use of timers. For example, a solar PV installation generates the most electricity during the day when an owner is typically away and electricity demand at the property is low. If the owner set a timer for electrical equipment such as dishwashers, immersion water heaters and washing machines their demand for electricity from the grid would fall and their usage of the electricity their installation has generated would increase. There is also the possibility that batteries for domestic storage of microgenerated electricity could become more mainstream than at present. For these reasons, higher usages have been investigated that are of the same scale, but the opposite sign, to the pessimistic scenario usage rates.

In contrast to scenario 2, scenario 3 constitutes a set of conditions less favourable for microgeneration investment. Here, technology costs increase, electricity bills decrease, electricity usage is reduced and there is no improvement to solar PV efficiency. The difference in technology costs between those reported in Adam et al. (2015) and those reported in Table 6-2 are largely due to substantial changes in currency exchange rates to favour imports from China (Roberts, 2016; Platt, 2016b). As these rates could easily change to be less favourable and the fact that many global events could negatively impact the cost of PV panels (such as Britain leaving the EU, an economic crisis in China), investigating the possibility of an increase in the cost of solar PV panels is important. As a counterbalance to the 20% fall in technology price used in the optimistic scenario, a 20% rise in the cost of the technology is projected in the pessimistic scenario. Electricity bills have become a focus of recent UK government policy. Whether the shifts towards electricity production by nuclear energy that is more expensive than wind and solar in the long term are truly in line with aiming for lower electricity bills is a debatable topic but it is important to include the possibility of lower electricity bills in the scenario testing. This is further warranted by recent cuts to electricity prices from major energy providers. The electricity cost reduction

incorporated is an extension of the 2.24% decrease observed between 2014 and 2015 (DECC, 2015e) which results in an average domestic electricity cost of £0.147 per kWh.

## **6.2 Results and Analysis**

This section introduces the outputs of the city-scale microgeneration viability model, first under the baseline scenario and then for each of the adaptations described in section 6.1.3.

The processing time for the solar financial viability calculations was approximately 36 minutes for the 80,365 rooftops assessed across the study area whilst the wind turbine viability codes executed far more rapidly. This performance was achieved using an Intel® Xeon® 3.1GHz processor and 8 GB of RAM which is in line with the research objective of producing a methodology that can be executed without the need for high power computing.

### **6.2.1 Baseline Scenario**

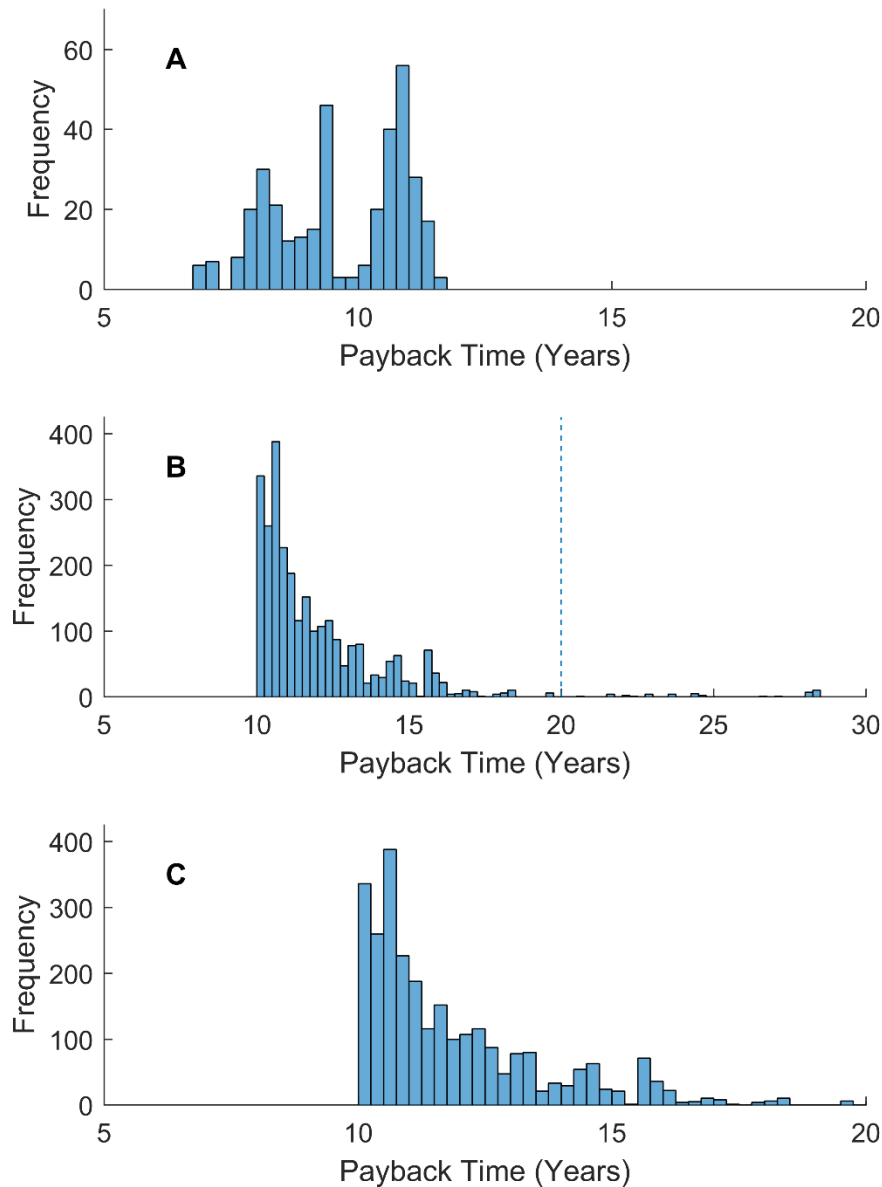
Table 6-1 (page 138) summarised the costs and revenues used in the baseline scenario which were representative of conditions prior to January 15<sup>th</sup> 2016. The performance of the two selected wind turbines are described in terms of payback times and annual ROI before the results for solar installations across the study area are presented. For both wind and solar technologies, the sensitivity of the model to the proportion of generated electricity that is used on site is discussed. There is a final sub-section to discuss the cumulative potential of both technologies to meet electricity demand in the study area.

#### **6.2.1.1 Wind**

Figure 6-11 shows histograms for both the WindEn 45kW (A) and Kingspan KW15 (B and C) turbines in which the 1,833 locations identified as suitable for a WindEn 45kW turbine all pay back within the 20 year lifespan of the FiT. Payback times for the Kingspan KW15 are less impressive although 5,659 sites of the 5,701 (99%) sites suitable for the Kingspan KW15 also break even within 20 years.

The results are presented on twenty-year timescales to align with the lifespan of the FiT. However, it is important to consider what constitutes a viable installation to investors in microgeneration and 20 years is unlikely to be attractive to many. Unfortunately this aspect has not received widespread attention in the literature, especially for investment in small to medium wind turbines. Two studies that have explored this area for solar PV have very different conclusions as to what is an acceptable payback time. Claudy et al. (2011) state that property owners would be willing to pay for an installation that could break even in 9 years

whereas Willis et al. (2011) found that figure to be 3-5 years although their study centred on more aged demographics. Whilst the payback times for solar and wind rarely reached as short as five years, there was a sizeable resource of solar and wind installations that could payback within 9 years, as shown by the baseline results for wind (Figure 6-11).

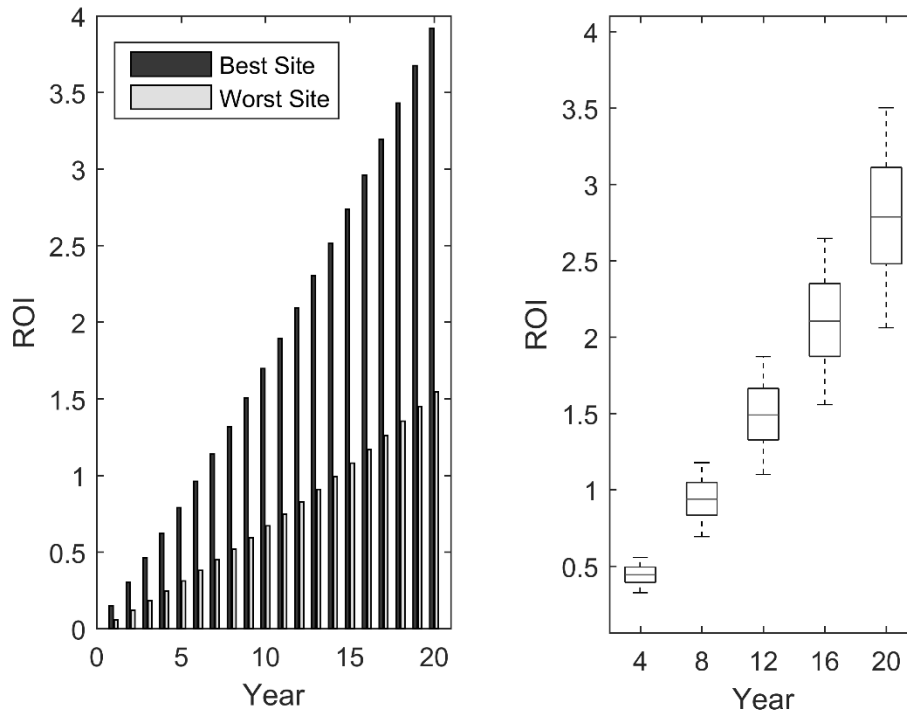


**Figure 6-11 Payback times for selected turbines under the baseline scenario. A: WindEn 45kW, B: Kingspan KW15. C: Kingspan KW15 for all locations where payback is less than 20 years. The dotted line in B denotes 20 years, the lifespan of the FIT**

Figure 6-12 (left) shows the annual ROI for the WindEn 45 KW turbine at the best and worst sites in the study area and both demonstrate a steady growth pattern. The worst site, which still reaches a ROI of approximately 1.5 in year 20, had an long term average wind speed of  $3.94 \text{ ms}^{-1}$  whilst the best site had an long term average wind speed of  $7.72 \text{ ms}^{-1}$  and an ROI of just less than 4 after 20 years. Figure 6-12 (right) shows that ROI has a greater spread as time progresses and that the 5<sup>th</sup> percentile at year 12 is more than ROI = 1. Owing to the



nature of the distributions, there were no outliers and so no turbines had failed to pay back by year 12.



**Figure 6-12 Annual ROI for most and least optimal sites (left) and distribution of ROI across all sites for year 4, 8, 12, 16 and 20 (right).**

Figure 6-13 shows the less attractive ROI figures for the Kingspan KW15. Again, the growths of ROI are shown to be steady and consistent across the twenty year period (Figure 6-13, left) and the best site produces an impressive ROI, this time of almost 3. However, the worst site fails to reach ROI = 1 and so does not pay back within twenty years. Across the results as a whole, however, Figure 6-13 (right) shows that the 5<sup>th</sup> to 95<sup>th</sup> percentile range is almost at ROI = 1 after 16 years so the vast majority of turbines had paid back by this time.

Referring back to Figure 6-4 on page 132, the Kingspan KW15 has a smaller rotor diameter that meant that it was suitable for a great number of sites that the WindEn 45 kW was too large for. This meant that the turbine could be placed in more urbanised areas that have lower long-term mean wind speeds. It is unsurprising therefore, that the box and whisker plots (Figure 6-13 right) should contain more outliers below the 5<sup>th</sup> percentile than were observed in Figure 6-12.

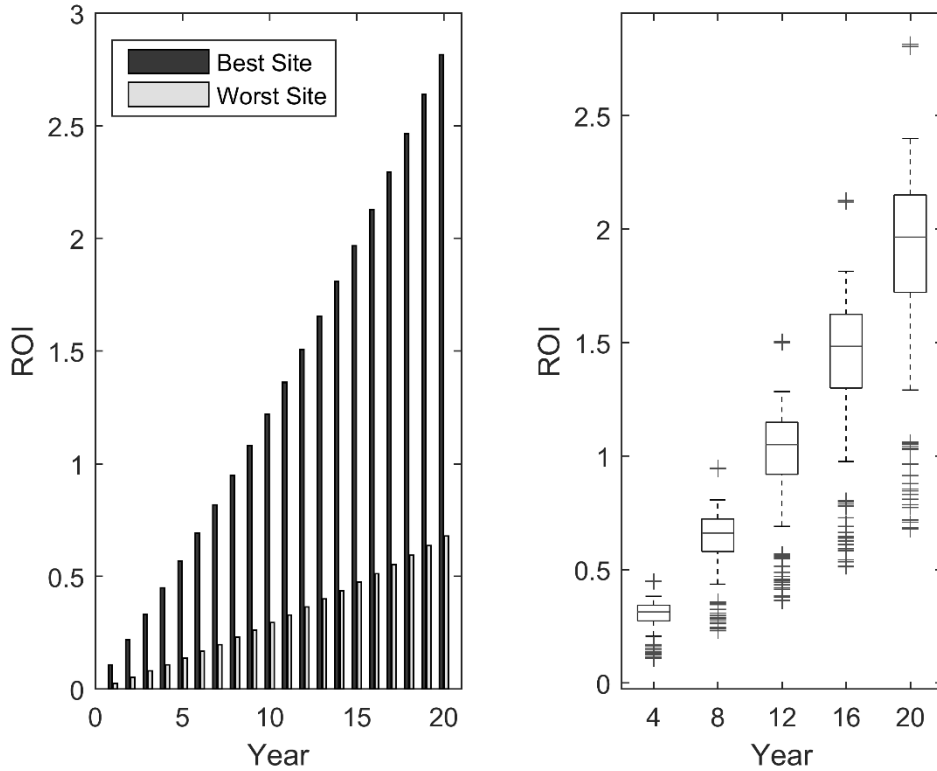


Figure 6-13 Annual ROI for Kingspan KW15 at most and least optimal sites (left) and distribution of ROI across all sites for year 4, 8, 12, 16 and 20 (right). In the boxplots, the bottom and top whiskers denote the 5<sup>th</sup> and 95<sup>th</sup> percentiles, the bottom and top edges of the rectangles represent the 25<sup>th</sup> and 75<sup>th</sup> percentiles and the central line is the median. The plus signs are outliers.

**6.2.1.2 Solar**

Across the study area, 69,176 locations were found where a solar PV installation would pay back within 20 years under the baseline scenario. The payback times for all such systems are shown in Figure 6-14 where the longest payback times are for the smallest systems reflecting their lower annual power generation.

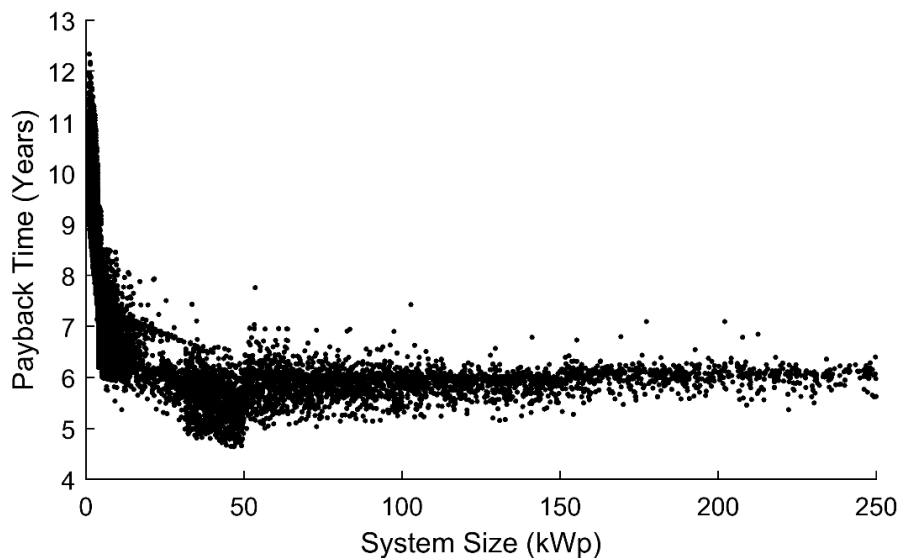
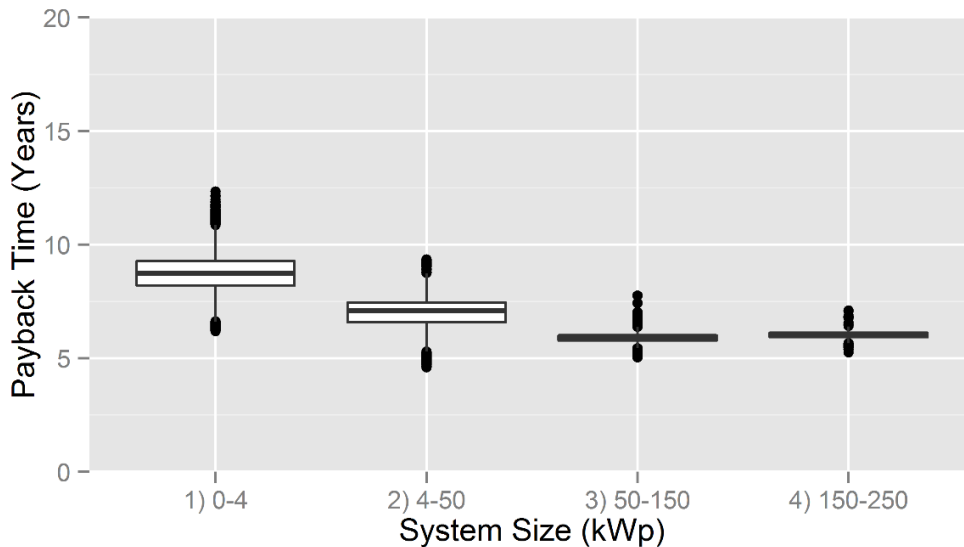


Figure 6-14 Payback times and system sizes for all viable installations

The shortest payback times occur just before system size reaches 50 kWp and the FiT rate changes from 10.9 p/kWh to 9.29 p/kWh. At this point payback times then plateau until the FiT rate drops again at 150 kWp resulting in a small rise in payback time. Payback time and ROI are strongly influenced by the FiT so Figure 6-15 shows the payback times for all installations categorised by size using the baseline scenario FiT bandings. There is a trend of decreasing payback time until the largest system size banding which is marginally greater than the 50 – 150 kWp banding.



**Figure 6-15 Payback time and system size in the baseline scenario FiT bandings. The boxes, whiskers and outlier dots represent the data in the same way as used in the rest of the thesis**

The broadest interquartile range (0-4 kWp) is constrained to 1.06 years showing that variability amongst this grouping caused by system sizes, shading and roof geometries is low. The interquartile ranges are particularly constrained for the two largest FiT bandings which was observed in the highly consistent payback times in Figure 6-14. At this point the greater CAPEX and OPEX are offsetting the additional revenue from increased annual power generation.

The 20 year ROI values (Figure 6-16) for all installations show similar patterns to the payback times described in Figure 6-14 but with slightly more pronounced impacts from FiT band changes at 50 kWp and 150 kWp.

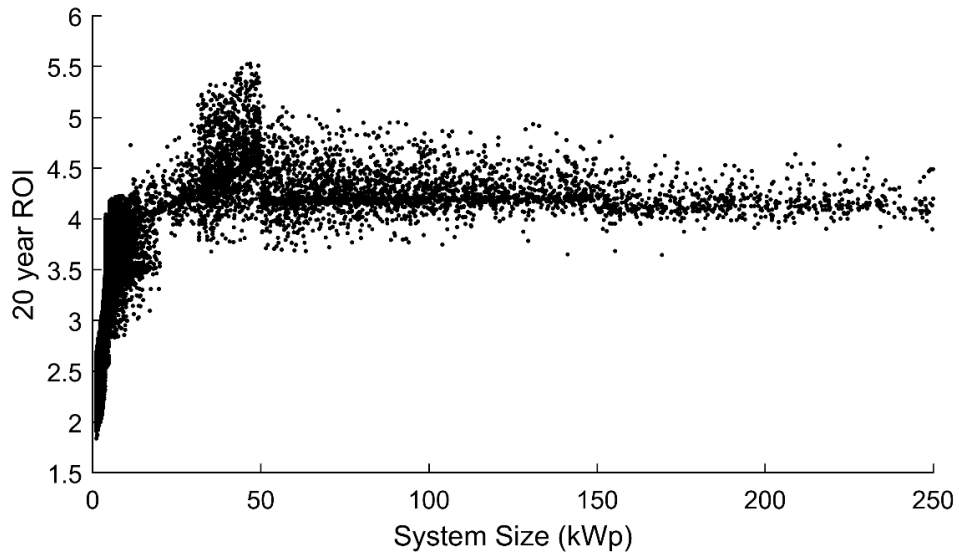


Figure 6-16 20 year ROI for all sizes of solar PV installation

The effect of changes to the percentage of electricity generated and used on site has been investigated with respect to payback time (Figure 6-17). The legend shows two numbers for each grouping in which the first number is the usage for smaller properties and the second is a large property usage.

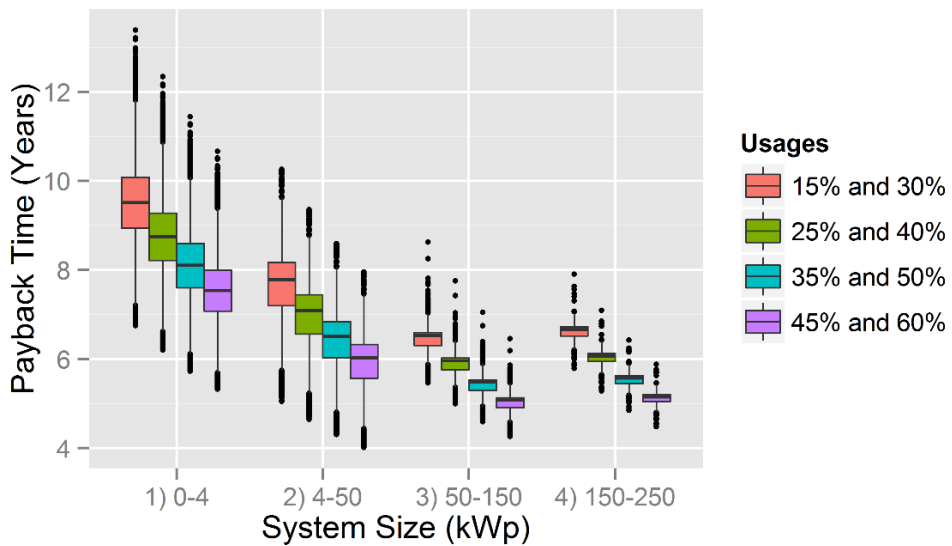


Figure 6-17 Sensitivity of payback time to percentage of generated electricity used on site

There is a clear trend for payback time to decrease as usage increases across all system sizes which is to be expected given the increase in electricity bill savings that are made. From the baseline conditions of 25% and 40%, a rise of ten percent in usage of electricity generated on site is found to decrease the median payback period by 0.65 of a year for systems sized 0-4 kWp. Whilst for the same system size category, a decrease of ten percent led to an increase in the median payback time of 0.76 of a year. These were the largest changes in payback time observed across all system size categories. The trend shows that owners of microgeneration systems can reduce the payback time of their installations by altering their

behaviours and consuming more electricity at peak solar PV production times (i.e. during the day). The median payback times of the larger systems reach approximately 5 years when the usage is increased by 20% from the baseline conditions. These levels are by no means unobtainable, in fact, the 45% for residential is still 5% below that used in other studies and a modern commercial property that has a large daytime workforce could quite conceivably use more than 50% of the solar PV electricity generated. Storage of electricity generated on site using batteries offers a route with which to significantly increase usage and decrease demand from the grid. An historical barrier to this has been the high cost of battery systems and their rapid efficiency degradation. However, the automotive and energy storage company Tesla has brought products to market (of 3.3 and 7 kWh capacities) specifically for this purpose with ten year warranties that could improve the prospects for on-site storage from microgeneration sources. Real-world testing and uptake is at a nascent stage and there are fundamental physical issues with Lithium-ion and lead acid battery technologies that have not been addressed for the considerable time that batteries have existed. In fact, there are studies to show that payback times for the batteries themselves could be ten to 17 years (Doyle and Barnes, 2016), which is greater than the nine years identified as desirable by Claudy et al. (2011). A key positive message remains, however, which is that the technologies to store electricity are being developed by companies with significant finances at their disposal and that the cost of batteries is continuing to fall (see Figure 6-18).

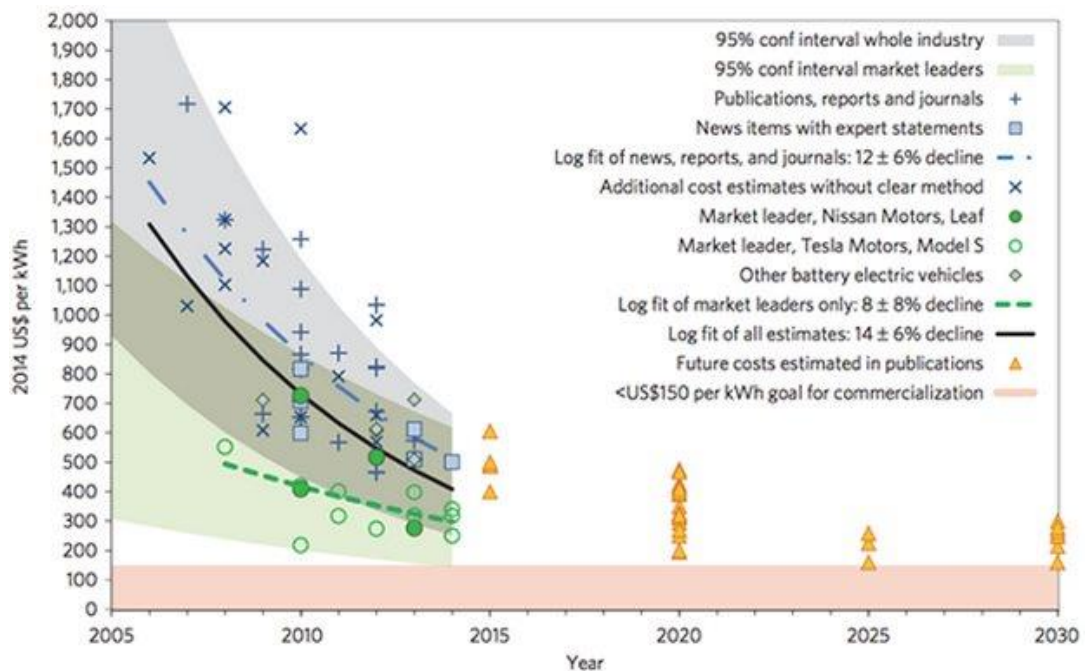


Figure 6-18 Past and predicted costs of batteries (Mathiesen, 2015)

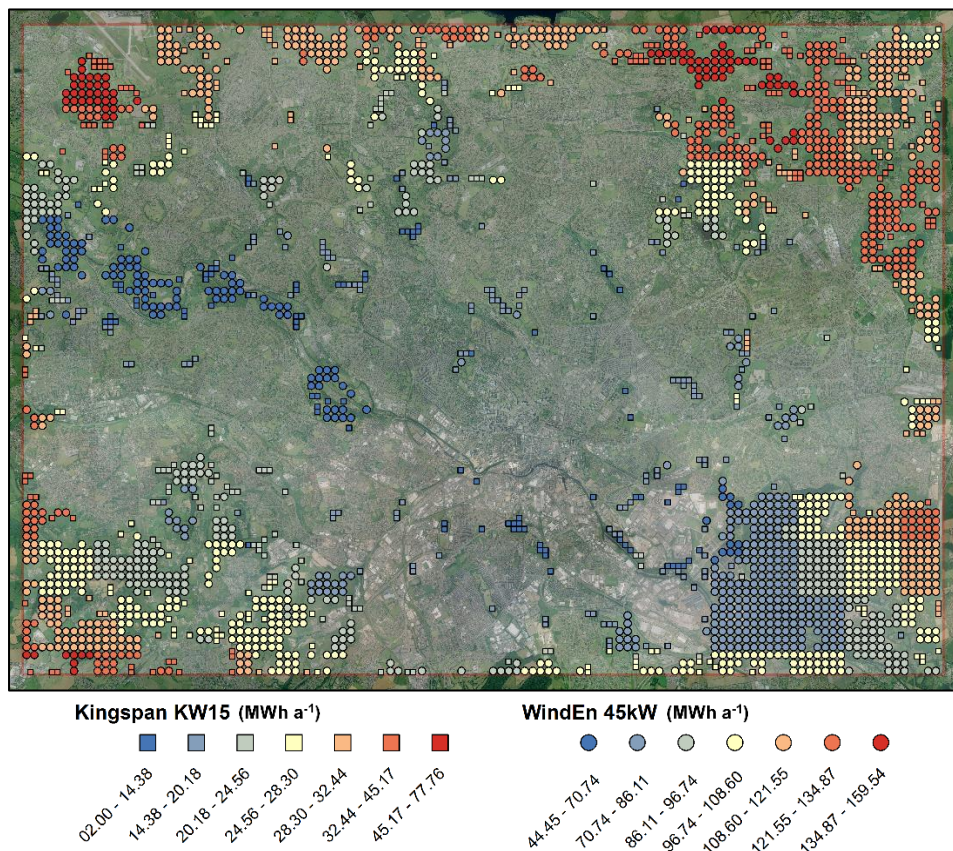
The shortened payback times that result from increased usage of electricity generated on site are not only encouraging for investors but may also signal that solar PV viability can

eventually become independent of the government incentives that have recently been greatly reduced in recent years.

**6.2.1.3 Cumulative Potential**

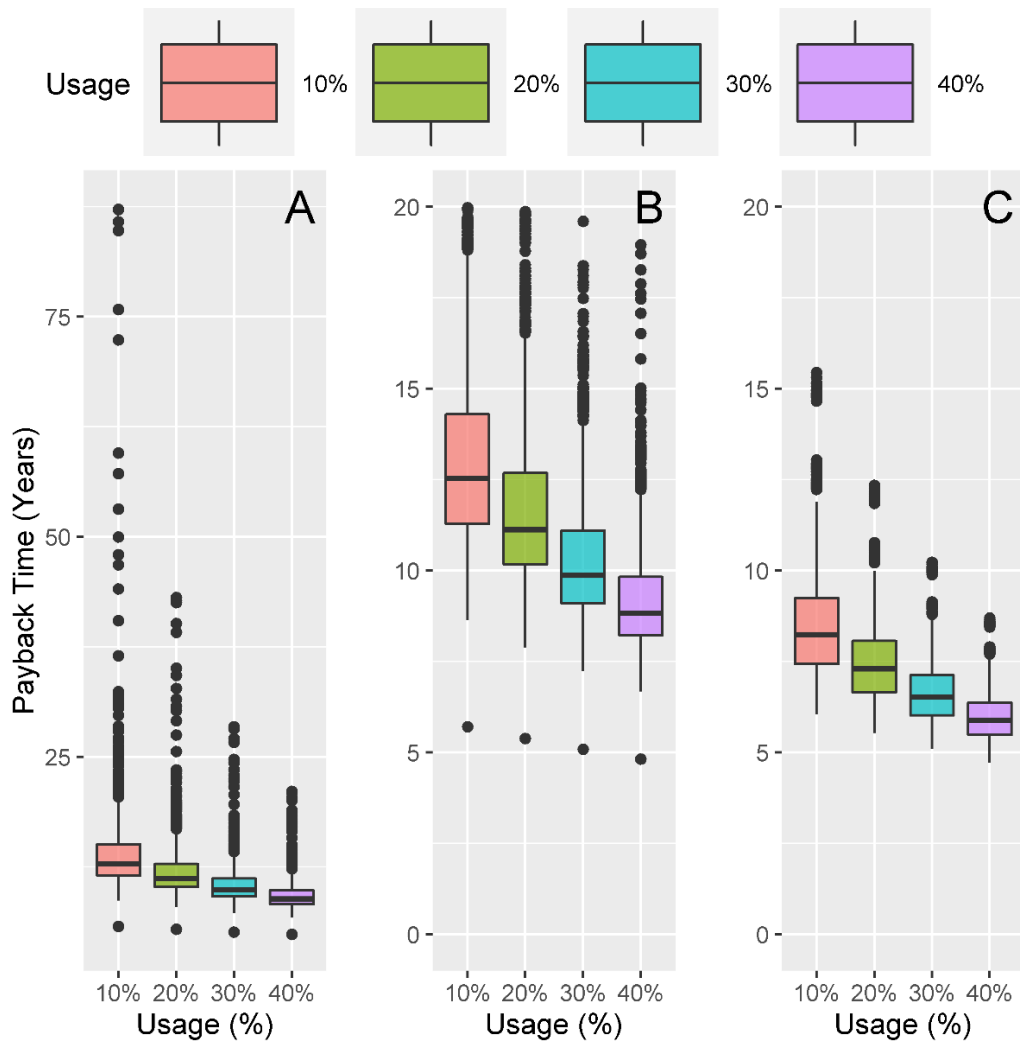
**6.2.1.3.1 Wind**

The results presented in section 6.2.1.1 showed the potential for both turbines at every possible site but in order to explore the cumulative potential of wind turbines in the study area, a decision has to be made where both turbines are viable to select the turbine that is most cost effective for the space the turbine requires. It was found that the annual production of a Kingspan KW15 for a site with a long term mean wind speed of  $5.77 \text{ m s}^{-1}$  was  $36.7 \text{ MWh a}^{-1}$  in comparison to the  $131.5 \text{ MWh a}^{-1}$  of electricity produced by the WindEn 45kW which equates to the Kingspan KW15 producing only 28% of the electricity a WindEn 45kW turbine would at the same site. For this reason, it was decided that for locations where both turbines could be installed, the WindEn 45kW would take precedence. Figure 6-19 shows the potential sites once this criterion is incorporated along with the annual electricity production for the first year of operation.



**Figure 6-19 Annual electricity production (MWh a<sup>-1</sup>) of both selected turbines at all spatially suitable sites for the first year of operation**

The wind turbine locations featured in Figure 6-19 have been used to investigate the sensitivity of payback times predicted by the baseline model to the percentage of generated electricity that is used on site. The usage parameter was altered to range from 10% to 40% (in increments of 10%) for each turbine. Increasing the usage of electricity generated on site clearly reduces payback times, more so for the worst performing turbines than sites that are more favourable.

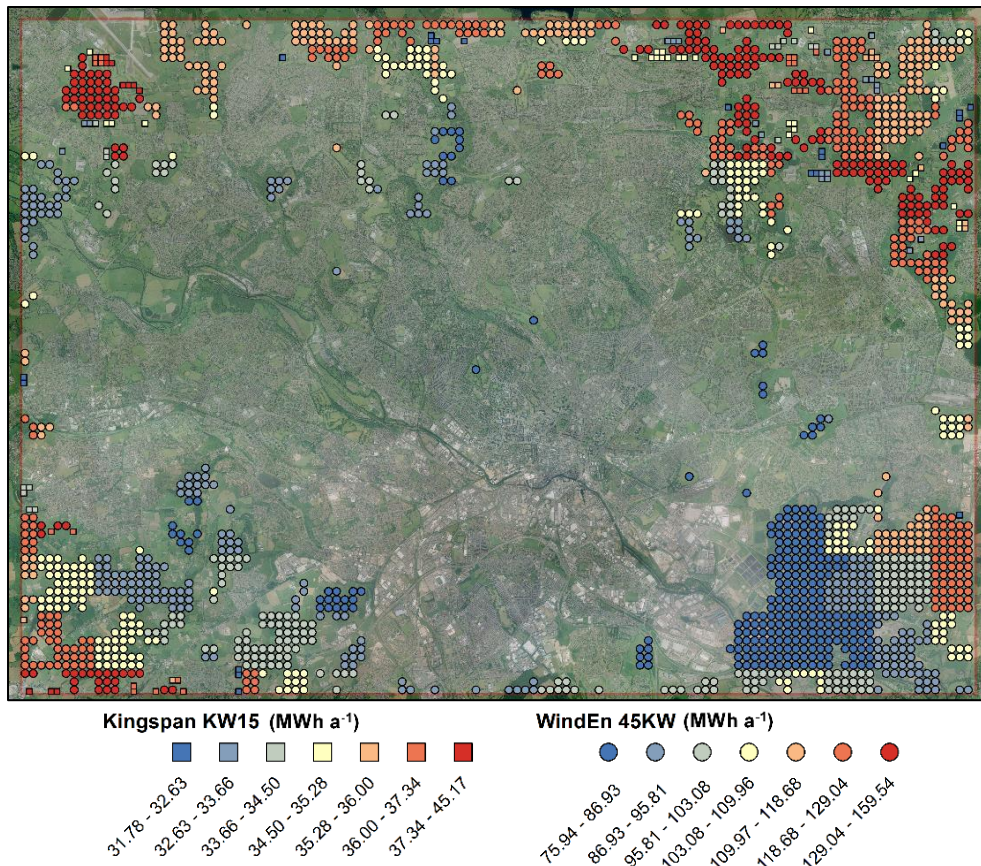


**Figure 6-20 Payback Times for Kingspan KW15 across all time (A) and for less than 20 years only (B) and WindEn 45KW (C) turbines with different usage rates**

Figure 6-19 and Figure 6-20 only showed sites and payback times for the turbines that are spatially suitable. They did not focus on only financially viable turbines which explains why there are Kingspan KW 15 turbines that generate under  $4 \text{ MWh a}^{-1}$  and WindEn 45kW with less than  $70 \text{ MWh a}^{-1}$  which are very poor performances for turbines of these sizes. For the purposes of the city-scale assessment of cumulative potential to generate electricity, financial viability is defined using the nine year payback time quoted in Claudy et al. (2011). For a Kingspan KW15 to pay back inside this time, it was found that the turbine must produce



in excess of 31.78 MWh a<sup>-1</sup> whilst this figure was 75.94 MWh a<sup>-1</sup> for the WindEn 45kW. When these criteria are applied, the distribution of viable sites is as shown in Figure 6-21 which again features the first year electricity generation although this is with reconfigured colour scales.



**Figure 6-21 Geospatial distribution of turbines that meet the 9 year payback criterion and their annual electricity production (MWh a<sup>-1</sup>)**

There is a decrease in the total number of turbines shown in Figure 6-19 (2,407) to the total number in Figure 6-21 (1,761) of 26.9%. Table 6-6 details the aggregated statistics for the turbines shown in Figure 6-21 which contains 121 Kingspan KW15 and 1,640 WindEn 45KW sites. Even after the degradation factor is accounted for, the eight and 20 year production figures are very substantial theoretically viable power output estimations. To place the figures into an appropriate context, electricity demand from all source for the city of Leeds in 2010 was 3,622.2 GWh (DECC, 2010), so the first year generation equates to 4.97% of total electricity demand. The DECC (2010) statistics for 2010 show that domestic demand, at 1,336.3 GWh, was far lower than that of commercial and industrial customers (2,285.9 GWh) meaning that first year outputs from the two turbines could meet 13% of domestic demand. As the average domestic consumption in Leeds was 3,938 kWh in 2010 (DECC, 2010), the electricity generated is equivalent to powering 45,723 domestic properties.



Turbine	Number of Viable Sites	Cumulative Production		
		First year (GWh a <sup>-1</sup> )	8 Years (GWh)	20 Years (GWh)
<b>Kingspan KW15</b>	121	4.22	33.05	79.73
<b>WindEn 45KW</b>	1,640	175.84	1,377.56	3,323.45
<b>Combined</b>	1,761	180.06	1,410.61	3,403.18

Table 6-6 Production from all financially viable turbines (paying back within 9 years) across the study area

The potential for wind turbines described in this study is far greater than described in Drew et al. (2013) who focused only on much smaller roof mounted turbines (typically less than 6 kW) in the city of London. They found that only 6% of the 1 km<sup>2</sup> neighbourhoods they divided the capitol in to would be suitable for a roof-mounted turbine if 4.5 ms<sup>-1</sup> was selected as a threshold wind speed. Unfortunately, Drew et al. (2013) did not explicitly state the potential for the technologies in terms of kWh for a specific year. Whilst it is likely that the spacing criteria used in this research would eliminate many locations across London, it would be very interesting to evaluate the accuracy of boundary layer and log-profile methods for cities as large as London and to then investigate the potential for small to medium wind energy. One study that has quantified the maximum potential for wind energy at the city-scale is by McIntyre et al. (2011) who found that 10% of the electricity demand of the city of Guelph, Ontario could be met by an array of 10 kW wind turbines. The 0.1% of demand that the Kingspan KW15 could meet that is presented here is for one key reason. The wind turbines in the McIntyre et al. (2011) study were positioned at set intervals across the city regardless of topography, building layout or turbine interaction. They were not subject to the minimum distance from residence criteria that this study has used. It is also likely that, given that Leeds has a population approximately double that of Guelph and large industrial and commercial sectors, electricity demand is far higher for the UK city.

#### 6.2.1.3.2 Solar

In contrast to wind, there are no discernible geospatial trends at the city scale in relation to the viability of solar PV installations. Instead, viability is defined by the localised factors (roof geometry, positioning and shading) and given the number of potential sites that pay back in under nine years was 51,674 a city-scale map would not be informative. Table 6-7 gives the total electricity generated from solar PV installations that pay back within the nine year desired time frame defined by Claudy et al. (2011).

Building Size Band	Number of Viable Sites	Cumulative Production		
		First year (GWh a <sup>-1</sup> )	8 Years (GWh)	20 Years (GWh)
Small	45,718	169.44	1,344.68	3,315.82
Large	5,956	833.16	6,611.85	16,304.03
<b>Total</b>	51,674	1,002.60	7,956.53	19,619.85

Table 6-7 Total theoretically viable production from Solar PV sites that pay back within 9 years

As in the cumulative analysis for wind (section 6.2.1.3.1), the figures presented in Table 6-7 can be given more meaning by comparing the first year production to the electricity demand of the city within the study area, which was 3,622.2 GWh in 2010 (DECC, 2010). Production for the first year was 27.68% of total electricity demand. When compared only to domestic electricity demand, generation from the identified viable sites would meet 75.03% of demand or, put another way, would be the equivalent of the demand of 254,595 domestic properties.

#### 6.2.1.3.3 Combined

The total electricity that could be generated from financially viable installations of the selected wind and solar PV technologies under the baseline scenario are shown in Table 6-8.

Technology	No. of viable sites	First year (GWh a <sup>-1</sup> )	8 Years (GWh)	20 Years (GWh)
Solar	51,674	1,002.60	7,956.53	19,619.85
Wind	1,761	180.06	1,410.61	3,403.18
<b>Combined</b>	53,435	1,182.66	9,367.14	23,023.03

Table 6-8 Total electricity generation under the baseline scenario from wind and solar PV installations that pay back in under 9 years across the study area

The first year figure shown in Table 6-8 is 32.65% of total electricity demand in 2010 for the city of Leeds (based on DECC (2010)). When compared only to domestic electricity demand, generation from the identified viable sites would meet 88.5% of demand or the equivalent of powering 300,319 domestic properties if those properties consumed the same as the average for the city of Leeds provided by DECC (2010).

## 6.2.2 Scenarios

The influence of various factors in microgeneration investment have been explored using three scenarios which are presented here alongside the baseline results for comparison.

### 6.2.2.1 Wind

The payback times for both selected turbines are shown in Figure 6-22 with the WindEn 45 kW producing more impressive results across all scenarios despite its CAPEX cost being approximately 2.3 times greater than the Kingspan KW15. This emphasises the benefits of

the WindEn 45 kW turbine's far more productive power curve and taller mast height that expose such turbines to greater long term average wind speeds.

The pessimistic scenario presented possible investment conditions that have a strongly negative effect on payback times. The entire interquartile ranges for both turbines in Figure 6-22 are significantly in excess of those for all other scenarios. The median payback time under the baseline scenario for the Kingspan KW15 (Figure 6-22A) was 9.9 years and 7.3 years for the WindEn 45 kW (Figure 6-22B). Therefore the majority of Kingspan KW15 turbine payback times fall outside the 9 years payback time identified by Claudy et al. (2011) but the distribution shows that a sizeable proportion of the sites in the study (220 in total) do meet this criterion. Unfortunately, the same cannot be said of the Kingspan KW15 under the new FiT scenario for which the 5<sup>th</sup> percentile is approximately equal to ten years which suggests that the new FiT rate is likely to have a significant impact on the attractiveness of investing in a Kingspan KW15 if those scenario conditions materialise in the real world.

It is interesting to note that the baseline scenario gives the shortest median payback times for both wind turbines despite the alterations to key financial variables in the optimistic scenario. There is a caveat that for the Kingspan KW15 turbine the medians of the two scenarios are very similar and that the IQRs are smaller in the optimistic scenario which follows the pattern shown in Figure 6-20 whereby increased usage on site leads to a reduction in IQR. However, the payback time of the 5<sup>th</sup> and 25<sup>th</sup> percentile is less in the baseline scenario than the optimistic and given that it is these most optimal sites that would be invested in first, the statistics further emphasize the negative impacts of the FiT change on potential wind energy investments even if all other conditions became more favourable.

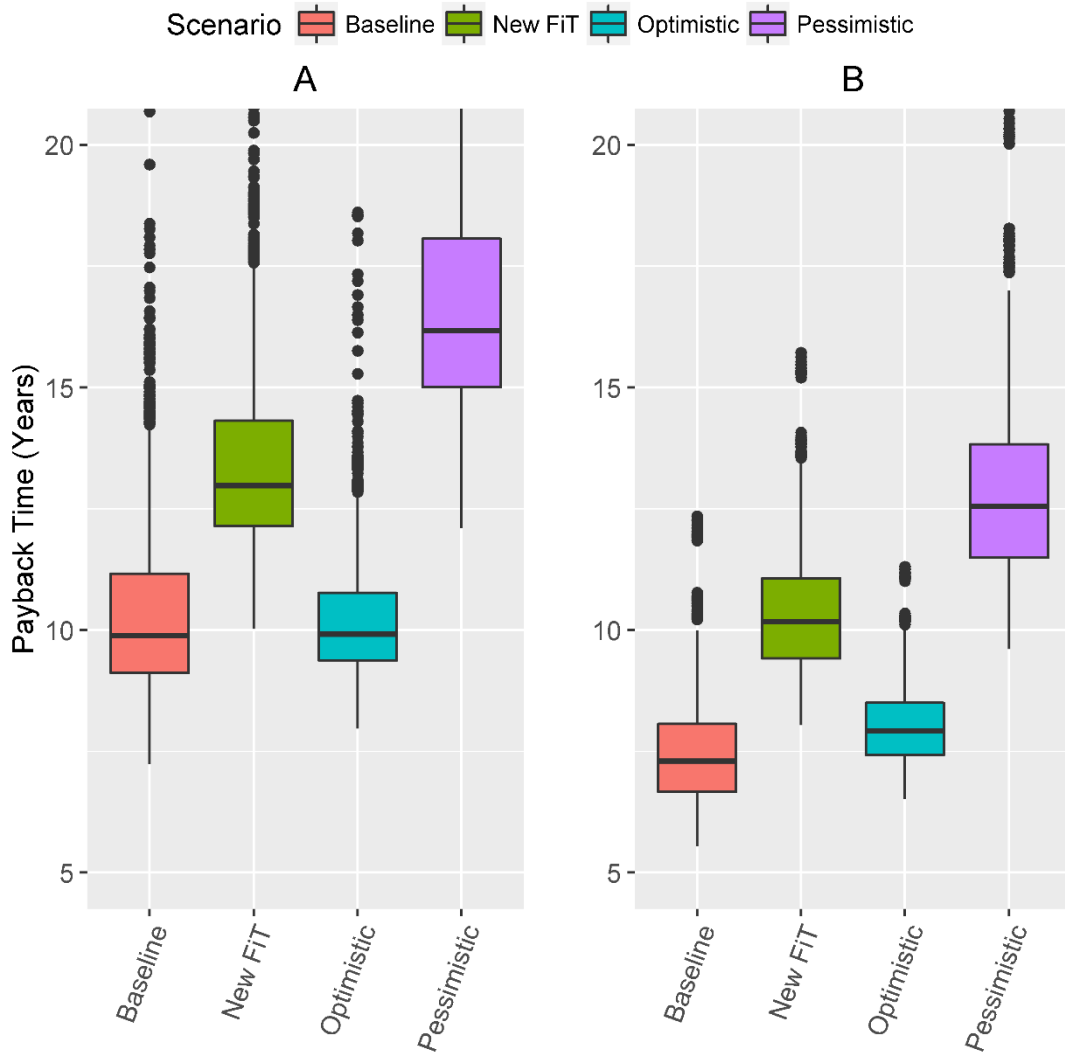
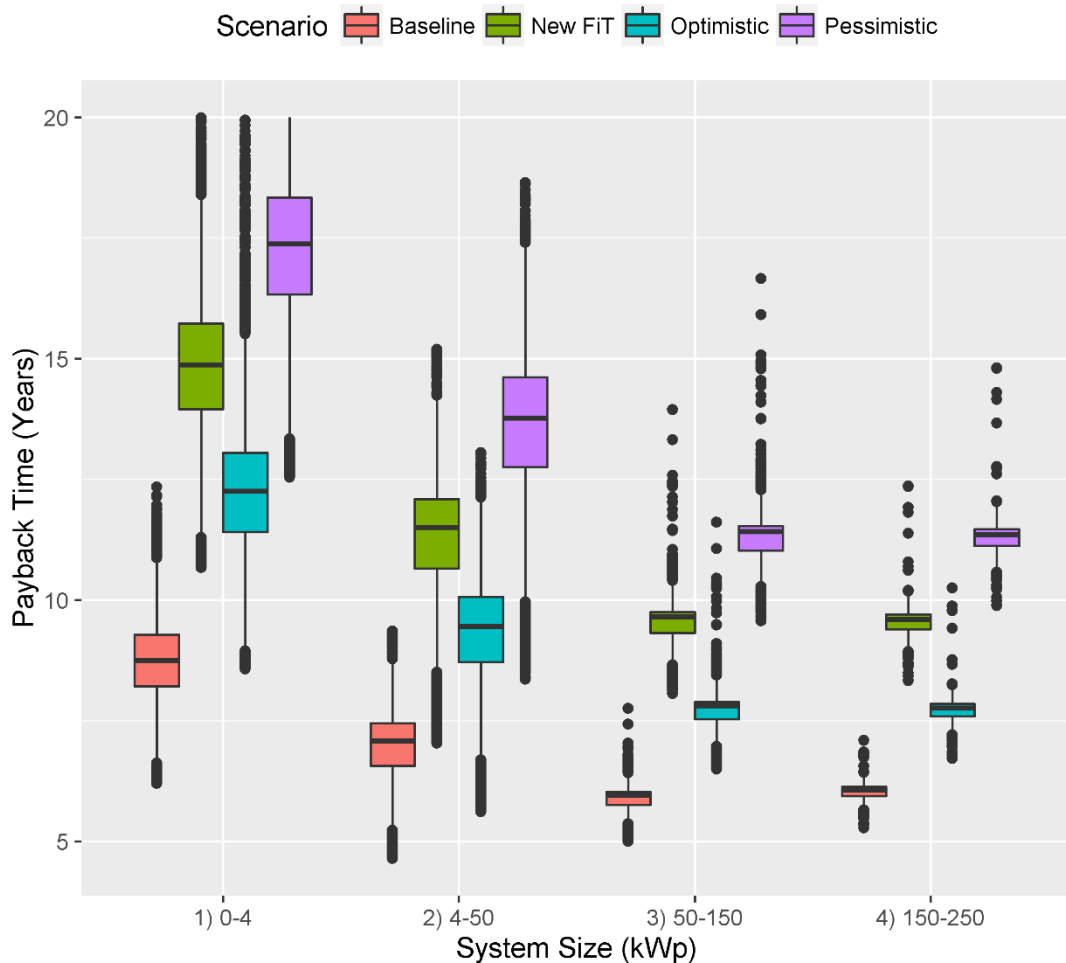


Figure 6-22 Payback times for the Kingspan KW15 (A) and the WindEn 45 kW (B) turbines under all scenarios

The optimistic scenario has incorporated a variety of factors that are, by design, slightly unlikely to occur individually and very unlikely to occur in unison. It is difficult to justify suggesting more favourable investment conditions that have at least a sensible probability of occurring so this analysis suggests that the changes to the FiT will lead to longer payback times that are less attractive to investors no matter what happens to wider influential factors.

#### 6.2.2.2 Solar

Figure 6-23 shows the payback times for solar installations under the baseline conditions and the three scenarios using the system size bins from the baseline FiT. There is a clear trend that repeats across all of the bins for the baseline scenario to provide a shorter payback time than all other scenarios. The interquartile and 5<sup>th</sup> to 95<sup>th</sup> percentile ranges decrease with increasing system size which could be for a wide range of reasons such as the higher likelihood of shading on smaller installations.



**Figure 6-23 Payback times under the baseline and scenario conditions**

The shortest payback time outputs under the new FIT scenario bear similarity to estimations from an installation company based in the study area. They projected 10 year payback periods for 2 kWp arrays and 9 year payback periods for 3 and 4 kWp arrays that have optimal azimuth and slope and are unshaded (Platt, 2016a). Their estimations have shorter payback times which could be because they assume that 50% of electricity generated by such installations will be used on site when 25% has been used in the new FIT scenario.

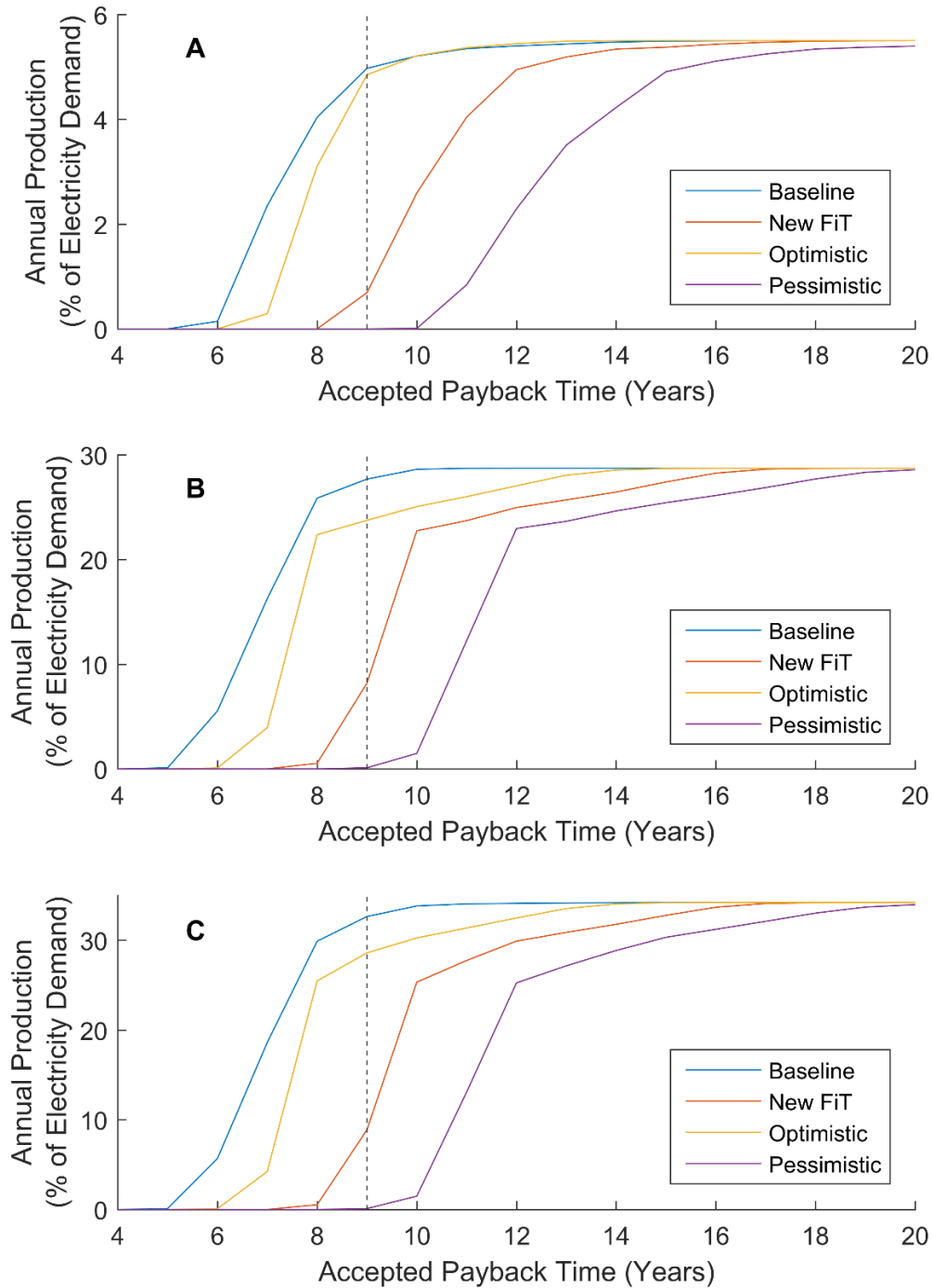
The second best performer is the optimistic scenario although there is still a considerable increase in payback time across the distributions from the baseline. This is concerning because the values used in this scenario are very much a best possible case in terms of solar PV viability. Therefore, it is clear that the FIT changes have damaging consequences for payback time that will not be counteracted by other factors as was found to be the case for the baseline solar, baseline wind and wind scenario analyses.

### **6.2.2.3 Cumulative Potential**

Analysing the impact of the scenarios on the annual production of electricity is an effective way to investigate broad themes across the entire study area caused by the alteration of key

variables in the viability calculations. Figure 6-24A shows the percentage electricity demand in the study area that could be met by the wind turbines that are spatially suitable (shown in Figure 6-19). The dotted line in Figure 6-24A shows that the baseline annual production from the two turbine types is 4.97% of demand when accepted payback time is set to nine years as discussed in section 6.2.1.3.1. There is then a trend for the increase in annual production to slow after this point. This suggests that a falling number of less optimal sites are then starting to be included in the annual production. The accepted payback time at which the percentage of demand rises above zero is largest for the pessimistic scenario at approximately 10 years which is double that of the baseline scenario. The pessimistic scenario curve has a smaller gradient than optimistic which suggests that the number of sites contributing to the annual production of the study area grows less rapidly under the pessimistic scenario.

It is interesting to note that the optimistic scenario curve slightly exceeds the baseline curve when accepted payback time is 11 to 14 years in Figure 6-24A. At this point there are few optimal sites where long-term mean wind speed is relatively large remaining to add to the annual production in the study area. Here then, the optimistic conditions (lower installation cost, higher grid electricity prices and higher usage on site) lead to sites with poor long-term mean wind speeds being incorporated into the total annual production figure at a faster rate than under the baseline scenario. The optimistic scenario plateaus at approximately at 5.5% when 13 years is the acceptable payback period which the baseline scenario requires a further two years to reach. The new FiT is not at this level until 18 years is the acceptable payback period and the pessimistic scenario does not reach this production before the maximum acceptable payback time shown (20 years). The plateau effect is caused by there being no further sites to add to the total annual production figure for the study area that are sub-optimal but could still pay back.



**Figure 6-24** First year production (as a percentage of electricity demand in the study area) from wind turbines (A), solar panels (B) and both technologies (C) in each scenario as “acceptable” payback time increases

The dotted line in Figure 6-24B shows that under the baseline scenario and an acceptable payback period of 9 years, 27.68% of the electricity demand in the study area could be met by solar PV which has been discussed in section 6.2.1.3.2. Whilst there is a similar trend in the order of the curves, their shapes are more angular from one accepted payback time to the next, particularly when first exceeding zero. This is caused by large numbers of sites being added with each increment and then a sudden reversal in this trend, suggesting that optimal

sites have payback times that are similar when aggregated to years to payback, rather than if payback was sub-divided from years (whether decimally or to calendar month).

The baseline and new FiT curves are broadly similar in shape across all of the line charts in Figure 6-24 but do differ from each other in that the new FiT scenario contributes nothing to the study area's annual production figure unless the accepted payback time is eight years or more. These two scenarios were the most similar and therefore, most reflective of conditions in the immediate aftermath of the FiT change. The grey dashed line in Figure 6-24C shows that there is then a large difference in the percentage of the study area's electricity demand that could be met by wind and solar technologies when the 9 year acceptable payback period presented by Claudy et al. (2011) is applied. At this accepted payback time, the new FiT scenario models first-year wind and solar microgeneration of electricity that would meet 8.88% of the study area's electricity demand whilst the baseline scenario would meet 32.65%, meaning 23.77% of demand would have to be met by other, more polluting technologies. However, if events led to the conditions defined in the pessimistic scenario, which is entirely possible, and 9 years was an accepted payback time, all but 0.1% of electricity demand met by solar PV and wind microgeneration would be lost.

### **6.3 Conclusions**

This chapter has presented work that directly addresses the research objective to apply the outputs of improved solar and wind resource appraisal methodologies to inform investment decision making. Chapter 4 showed that the use of the RTS-CS method for solar insolation is a significant improvement in terms of accuracy in modelling solar insolation at the city scale than the more commonly used ArcGIS method. Wind resource, meanwhile, has been modelled using a simplified version of an accurate model that is rapidly executable. The outputs from these methodologies have been used to investigate payback periods and ROI for microgeneration across a study area incorporating the city of Leeds, UK. The research has shown that wind and solar PV microgeneration at sites that pay back within nine years could theoretically meet 88.5% of annual domestic electricity demand in the city of Leeds, or would be the equivalent of providing electricity to 300,319 homes. Therefore, despite the substantial changes to the FiT since its inception in 2008, it is important to state that under the baseline conditions described in this research, solar PV and wind microgeneration is viable at a very large number of locations.

A key finding is that because payback time falls when more of the electricity generated by solar PV or wind is used on site, the solar and wind microgeneration industries could consider



moving towards solutions such as battery storage to promote usage over exporting to the grid. This could also have the additional benefit of mitigating grid integration issues such as those experienced in Germany over recent years where the variable input from the large numbers of solar PV arrays installed has caused serious problems. However, it must be noted that solar and wind systems were not being widely installed with battery storage at the time of writing and that the full costs and revenues of domestic battery storage are perhaps interesting avenues to research in the future.

The method has also explored solar and wind viability at the city scale across a breadth of very different but still plausible future scenarios and has the flexibility to be adapted and refined to investigate specific conditions. The results have shown that the solar and wind microgeneration industries are at a particularly interesting period in time. The growth of both industries over the last ten years has been highly impressive which has been driven by supportive investment conditions. For most of that time period the FiT has been a strong driver of investment. But, the FiT rates applicable from 01/04/2016 to 30/06/2016 for an array up to 4kWp in size quoted in Table 6-5 represent a decrease of around 90% compared to those that were applicable in 2012. Now that the FiT has been substantially reduced, the export tariff and electricity bill savings have become key sources of revenue and the importance of technology costs has increased. Even after incorporating optimistic investment conditions through manipulation of the costs and revenues, however, the changes to the FiT still mostly lead to longer payback times that are likely to damage the growth of the UK solar PV and small to medium wind industries. In more stark terms, when the costs and revenues are defined from a pessimistic but still realistic perspective and 9 years is defined as an acceptable payback period, all but 0.1% of the percentage of the study area's electricity demand that could be met by solar and wind microgeneration is lost. This suggests that the FiT has not "done its job" and is very much still required to drive investment in solar PV and wind microgeneration.

## **Chapter 7 Final Discussion and Conclusions**

### **7.1 Research Summary**

The research described in this thesis has focused on predicting the viability of wind and solar microgeneration at the city scale without the use of high power computing. This has required the creation of methodologies to interpret digital representations of urban surfaces and examine the implications of that information for wind and solar resources.

The first study of solar PV viability (section 3.1) applied widely used processes for roof geometry and solar insolation modelling to a comparative socio-economic study of conditions for microgeneration investment in large UK cities. It became clear that this methodology was incapable of modelling roof shapes for typical domestic properties which led to the work in section 3.2 that increased the accuracy of roof geometry modelling from low resolution DSM data. The accuracy of the solar insolation model then became the focus of section Chapter 4 which was addressed by developing a process to apply a DSM derived shading model to a radiative transfer model. Whilst the accuracy of an existing methodology to predict long term average wind speed was found to be satisfactory, its complexity and computational requirements were areas that section 5.2 improved on, leading to a model that could be rapidly deployed as part of a city-scale wind and solar financial viability methodology which was introduced in Chapter 6. The model developed in Chapter 6 then became a vehicle for the investigation of the wider policy and financial contexts associated with microgeneration investment in the UK.

### **7.2 Results and Implications**

The results of all the research undertaken have shown great potential for solar PV and wind microgeneration of electricity at the city scale in the UK, often with compelling business cases for investment despite the increasingly less favourable policy context. Section 3.1 described a methodology combining physical properties of study area surfaces derived from LiDAR with trends in socio-economic demographics to explore how cities may differ in the uptake of PV. Across all seven cities in the analysis, there was significant potential for solar PV microgeneration to meet a sizeable percentage of electricity demand. This was despite a sizeable reduction to the FiT that had actually accelerated the installation of solar PV systems briefly but then greatly slowed investment. Limited to seven cities, but with a large variation in their latitudes, the results did not show a north-south divide in physical resource as might be expected and the most northerly city, Dundee, actually provided the greatest physical resource relative to its population. This was because Dundee's building stock is characterised

by a large proportion of industrial properties with big roofs that face due South because of building alignment to the North bank of the Tay Firth. Building stock was again found to impact the scale of solar PV viability as cities with greater proportions of houses and bungalows to flats were found to perform better. As the study incorporated electricity demand per person, a reduction in roof space ownership per person had a negative effect. It is partly for this reason that Glasgow, where tenement flats are common, performed poorly. Smaller arrays (from buildings of  $< 200 \text{ m}^2$ ) were found to have shorter payback periods than large arrays and suggested a skew in the FiT mechanism (in its 2011 guise) to aid investors in small PV installations.

The accuracy of roof shape modelling for properties smaller than  $200 \text{ m}^2$  in chapter 3.1 was a concern that section 3.2 sought to address. A methodology to model roof shapes using building footprint and low-resolution DSM data was presented that was computationally efficient and suited to application at the city scale. Against a validation dataset of 536 buildings, the method identified the correct roof shape in 87% of cases. The MAE in roof slope modelling was  $\pm 3.76^\circ$  when validated against survey measurements of 182 buildings. Roof slope was defined with greater accuracy than by the application of regression techniques to areas of roofs defined by building footprint data alone. In the example provided, the mean error of roof slope calculation from the current method was  $3.06^\circ$  whereas using more simplistic method consisting of interpolation on areas of the DSM identified by building footprints led to a mean error of  $9.85^\circ$ .

With the geometrical inputs to a solar viability methodology modelled more accurately, attention turned to the accuracy of the insolation model used in chapter 3.1 which has been strongly criticised in the literature. Chapter 4 developed a way to incorporate DSM-derived shading information into a radiative transfer model of global solar insolation to give the RTS model. When validated using annual power output data for the year 2013 at 17 sites across four cities, the RTS model outperformed the methodology incorporated into the esri ArcMap solar radiation toolset. RTS modelled global solar radiation with +2.62% and -3.68% mean percentage error under assumed performance ratios of 0.8 and 0.75 respectively. Esri ArcMap incurred -15.97% and -20.78% mean percentage errors under the 0.8 and 0.75 PRs whilst the results for PVGIS were +10.23% and +3.34% mean percentage error for each PR.

The adaptations of the RTS method for application on a city scale created the RTS-CS model meaning that, unlike PVGIS, the method could be used to inform large numbers of investment decisions and provide greater accuracy than previously possible using the esri ArcMap methodology whilst remaining executable on standard desktop computers.

Chapter 5 introduced a simplified model for long term average wind speed prediction that was ideally suited to city scale applications. It produced only a small increase (1.75%) in MAPE when compared to a more complex and computationally intensive methodology. The key to the improved computational performance was the combination of height-independent variables ( $\lambda_p$  and  $\sigma_h$ ) with empirically determined coefficients to predict the aerodynamic parameters  $d$ ,  $h_{m-eff}$  and  $z_0$  from DEM and building footprint data.

When these aerodynamic parameters were applied to the logarithmic wind profile equation and validated against 12 sites from four major UK cities, there was an error in wind speed estimation of 17.88% MAPE which compares to 16.13% MAPE under the more complex existing methodology. These results are set in sharp contrast by the error in long term average wind speed when aerodynamic parameters derived under the still widely cited Macdonald model were used. This led to long term average wind speed estimations with 38.76% MAPE showing that the Macdonald model should be used with great caution if applied to wind resource assessment in cities because it is not suitable for arrays of buildings with heterogeneous height profiles.

Chapter 6 brought together the advancements made in both city-scale solar and wind resource and introduced a financial model to calculate installation viability which directly addressed the main research objective of the thesis. A viable cumulative capacity was introduced which suggests that 32.65% of the annual electricity demand for the city of Leeds (UK) (1.183 TWh) could be met from wind and solar PV microgeneration. The chapter also explored solar and wind viability at the city scale across a breadth of different future scenarios demonstrating the utility of the method and opening a discussion on the latest contexts surrounding the solar and wind microgeneration industries. In similarity to chapter 3.1, the FiT was undergoing another significant reduction, this time falling to just 10% of the value of the rates that were applicable five years earlier. This has greatly increased the importance of other factors such as installation cost and the proportion of generated electricity that is used on site in solar PV and small wind viability. However, the scenarios showed that the changes to the FiT lead to longer payback times even when those other conditions are changed to be more favourable for microgeneration investment. Despite this, in all but the pessimistic scenario there remained a large number of locations where solar or wind microgeneration is viable across a UK city and that microgeneration can play a big role in providing low carbon electricity in the future.

### 7.3 Limitations and Further work

Although the research presented in this thesis has focused on improving the physical modelling of solar and wind resources from the work described in Chapter 3, the socio-economic aspects of that study are important in understanding the drivers behind people's ability and desire to install low carbon technologies. This work could be taken further to try to gain insight into how government and local authority policy could be better focused on encouraging certain demographics to invest and perhaps how to best support such individuals following investment. Also, the performance of solar installations could be looked into in greater detail and the accuracy of annual yield forecasting could be improved with respect to the behaviours of buildings' inhabitants. Whilst this thesis has focused on modelling geometry and insolation with greater accuracy, further work could investigate how the generated electricity is used. There are city-scale datasets of demographics that could classify houses as occupied during the day or not which is likely to have a significant influence on how much electricity is being used on site. Then behaviours of electricity consumption could be attached to certain properties. Alternatively, the city-scale methodologies presented here could be inputs to a tool where users define their own electricity usage patterns to produce a more tailored estimation of the revenues they are likely to reap.

A limitation in Chapter 3 was access to data that could validate the model of physical resource. At the time the research was carried out, there was no access to any insolation measurements in any of the study areas and only a very limited number of installations that could provide an annual power output to compare the model to, though they were not in any of the study areas. During the time that followed the writing of that chapter, criticisms of the esri ArcGIS insolation model that underpinned the work surfaced which were described in section 4.1. Therefore, it is fortunate that the study was predominantly comparative between the cities tested and that the maximum physical capacities were not held as absolute values for solar power generation that had any likelihood of ever being achieved.

It should be noted that the development of the neighbouring buildings approach to modelling small property roof geometries at the city scale was strongly influenced by the building stock that characterises typical UK cities and that it was not influenced by cities from any other country. It would be interesting to test the method described in section 3.2 to other settings and refine it for the building stocks that characterise cities in different countries around the world but it is possible that it just is not appropriate where large

suburban estates of very similar houses have not been built in bursts of development. It would also be interesting to investigate how the model performs against higher resolution DSM datasets if they were to become available for entire cities. Whilst the expansion of open access data to incorporate such data is less likely given the decision by referendum for the UK to leave the EU (Ambasna-Jones, 2016), there might come a time when the level of modelling and processing described in this work is not required and direct interpolation of, for example, 0.25 m horizontal resolution data performs adequately.

The solar insolation model described in Chapter 4 was altered for deployment on a city scale and although the execution time was entirely satisfactory when compared to how long the esri ArcMap process takes to run there are opportunities to further streamline the process. For example, a contour fit or lookup table could be built from the underlying radiance files whose outputs are true for large areas (3.2 km by 5.6 km) of land. The sensitivity of the model to slope and tilt (Figure 4-8 in section 4.5) showed that there are ranges of slope and orientation that give very similar annual insolation outputs. This means there could be scope for assigning annual insolation outputs to entire bands of slope and orientation which could greatly reduce the computational requirements for city-scale deployment.

Although developed from findings in the literature which featured sizeable validation datasets, the use of a PR to convert insolation estimation into a solar PV power output could be further justified by comparison to pyranometer data within the Leeds study area. Some of the more recent literature has suggested that PR should not be less than 0.8 (Pearsall and Gottschalg, 2012; Ayompe et al., 2011) which could lead to an interesting study because the EU JRC ESRA databases that are widely used in academia and industry performed best under that condition.

In order to avoid the use of wind turbines with misleading power curves, Chapter 5 featured only wind turbines with MCS approval. However, the MCS does not independently test the turbines and so there is the possibility that the results for the selected turbines were not carried out exactly as prescribed. More importantly, the conditions that the turbines are subjected to in the testing required by the MCS is far removed from those in the real world. The lack of performance testing for the smaller 15 kW turbine in turbulent conditions is a particular limitation. It is possible for this turbine to be installed in areas that are surrounded by development and, given its lower mast height, it is more likely to be exposed to flows made more turbulent by near-by buildings and vegetation. For greater accuracy in city-scale wind turbine viability assessment, it would be an improvement if the areas where turbines could be installed were given some form of turbulence intensity attribute and if a

proportional reduction to power output could perhaps be incorporated. The work of Emejeamara and Tomlin (2016) to map turbulence intensity across UK cities may make this a practicable improvement in the future.

Wind turbines are not a completely mature technology and there is scope to improve the modelling of the impact that inverter efficiency and control gear improvements could have in the future. It would also be interesting to test the extent to which a wind turbine can be optimised to a location given its long term mean wind speed or turbulence intensity and what role the different parts of the turbine play in that optimisation.

The incorporation of inverter performance and the degradation in performance of an installation could be better justified if studies were available that were relevant to wind and solar microgeneration. There has been anecdotal evidence to suggest that inverters degrade to such an extent on solar PV installations that it is cost-effective to replace them after 10 years but no studies could be found to sufficiently support this.

Chapter 6 presented a range of unique but plausible scenarios in an attempt to set bounds on how future events could impact microgeneration investment. There could be a lot of further work in examining any one of the conditions included in the scenarios to the finest detail, such as how electricity bills may change in future years. The chapter also mentioned domestic electricity storage which could play a bigger role in the future though is very much at a nascent stage in its development at the time of writing. The scale of the theoretical potential for solar PV presented in the chapter immediately inspires a series of questions about what might stop it from being anything more than theoretical. How would the grid cope with this scale of variable input? What would be the rare Earth material requirements, and the true lifecycle costs to produce such a number of PV panels and turbines? What capacity could the UK solar and wind industries actually deliver given current logistical barriers? How might attitudes and cultures change if even a tenth of this deployment was suddenly installed? Whilst many of these are very big questions there are also aspects for further work that are smaller in scope such as how could the information on wind and solar PV viability presented in Chapter 6 could be presented to both potential investors and those that are largely unaware of the technologies. There is an opportunity to develop tools from this data to engage and inspire members of the public in the study area and beyond.

Although not mentioned in this research, there may be another group of actors that could play a role in increasing the rate of solar PV and wind microgeneration deployment. At present, legal and infrastructure barriers are highly restrictive to community groups wishing

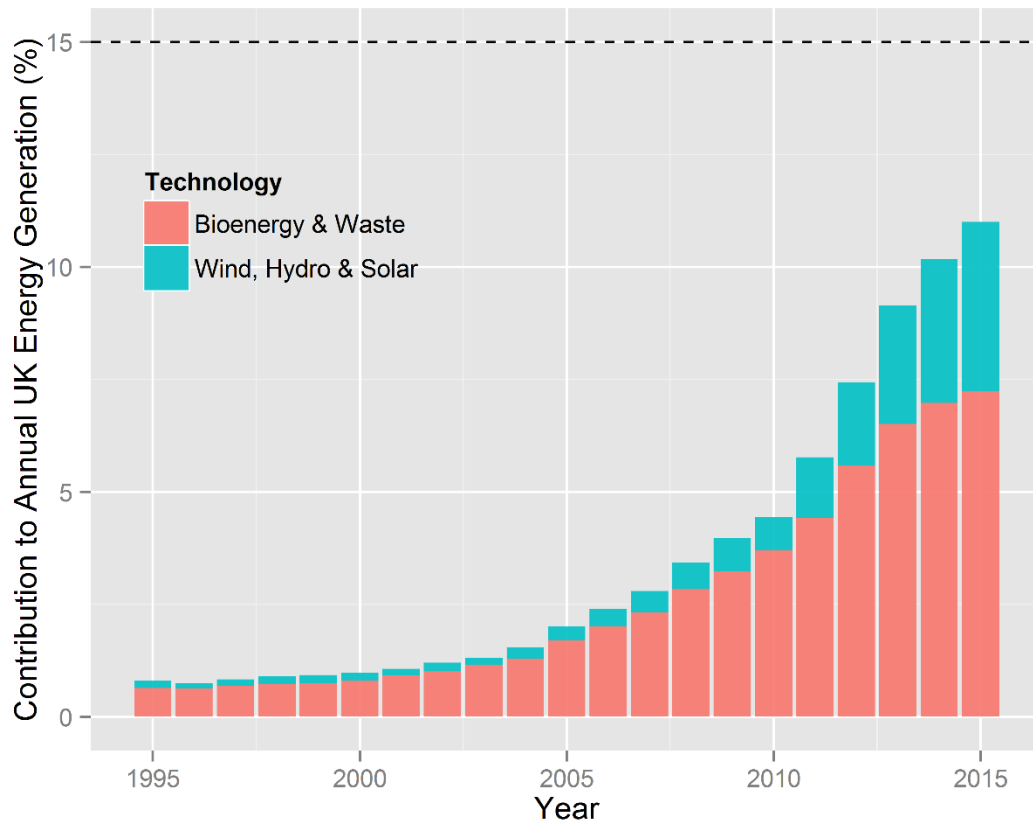
to generate their own electricity from a shared resource such as a wind turbine with a private line. There is a fundamental advantage to small groups of people coming together to invest in renewable electricity generation as the biggest barrier to many individuals' investment in low carbon electricity generation is the CAPEX requirement. There are many interesting research avenues that could be investigated such as where in the UK could be best suited to this approach and how the finances could be best evaluated.

Whilst this research has focused purely on where a technology is spatially suitable and where the resource is richest, it has not incorporated the broad range of factors that influence the decision-making processes of a large private land owner or a local authority. It would be interesting to study historical investments in renewable technologies and identify common barriers and how they could be overcome.

#### **7.4 UK Solar PV and Wind Microgeneration in Perspective**

The government's strategy to reduce greenhouse gas emissions is firmly rooted in meeting specific targets such as the commitment that by 2020, 15% of energy generation will come from renewable sources. Figure 7-1 uses DECC statistics to show that the contribution to meeting annual UK energy demand from wind, hydro and solar sources has grown substantially since the Energy Act of 2008. A big part of this contribution has come from FIT eligible wind and solar PV which, as of June 2016, contributed 585.8 and 4,308.6 MWp of installed capacity respectively (DECC, 2016b).



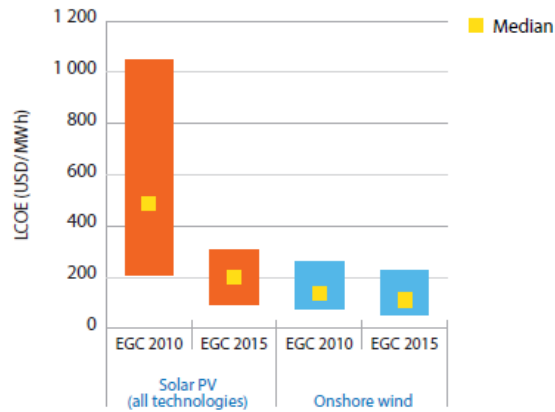


**Figure 7-1 Percentage contribution of renewables to annual UK energy generation using data from (DECC, 2016a). Dotted line represents the 15% of energy generation from renewables target by 2020**

Figure 7-1 illustrates that the contribution of wind, hydro and solar has not been dwarfed by bioenergy and waste despite that source benefitting from recent adaptations to huge power stations (such as Drax) to process biomass. The figure also shows that it is by no means guaranteed that the 15% target will be reached by 2020. The resilience shown by the solar PV industry to keep growing at the rapid pace it has despite the increasingly apathetic, or even hostile, policy context should not be taken for granted. The massive drop in cumulative wind and solar capacity under the pessimistic future scenario presented in section 6.2.2.3 showed that if circumstances beyond the Government's control were to conspire against the technologies, deployment could fall dramatically. This is of particular concern as the current emphasis of UK energy policy appears to be most in favour of cultivating the contribution of nuclear and shale gas sources at the expense of wind and solar PV sources. This is confusing because nuclear and shale gas are amongst the most expensive sources of energy for electricity generation (Harrabin, 2016b) and must lead directly to higher electricity bills which directly contradicts a central aim of the current government's energy policies.

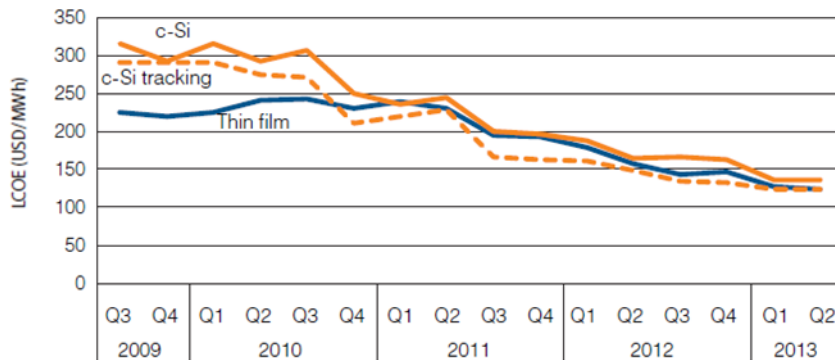
This research has focused on wind and solar PV deployment viability in UK cities but the models presented are highly sensitive to global factors, such as the price of the technologies. Around the world, conditions for investment in solar and small to medium wind energy are

becoming more favourable at a rapid pace because of falling CAPEX requirements. Figure 7-2 shows that the levelised cost of electricity (LCOE) (where inflation has been accounted for) for both technologies in developed country markets has decreased over the last five years; especially so for solar PV.



**Figure 7-2 LCOE (\$/MWh) of solar PV and onshore wind technologies in developed country markets for 2010 and 2015 (IEA-PVPS, 2015)**

The LCOE for the most popular solar PV technology types are shown in Figure 7-3. Over the course of the than four years shown, the LCOE from crystallised silicon cell solar PV panels has fallen by over 50%.



**Figure 7-3 LCOE (\$/MWh) for solar PV technology types**

The research has shown that in many circumstances, electricity bill savings are a key source of revenue to support a decision to invest in solar PV or wind microgeneration. Certain types of investor, such as large industrial or commercial properties, are able to use large proportions of the electricity generated on site, thus avoiding all government incentives because their actual contribution to the grid is likely to be metered. Effectively, an investment decision is being made without the need for the central government’s financial incentive. Given the current trends in solar PV prices, the circumstances where financial incentives are not required could broaden considerably and it is not impossible that one day this could extend to domestic properties.

It is clear that solar and wind microgeneration have the potential to make a small but not insignificant contribution towards meeting long-term greenhouse gas emission reduction targets in the UK and around the world. Not only do such installations make a direct contribution to the grid, their increased prevalence serves as evidence of a greater consciousness of a global issue that is difficult to humanly appreciate because, for example, we cannot see greenhouse gas concentration levels or sense global temperature variation. The increasingly common sight of a roof-top PV or sub-50 kWp wind turbine installation at the periphery of an urban area is a visual cue that suggests society as a whole is becoming more aware of the true value of energy and specifically its costs to the planet.

## References

- Adam, K. et al. 2015. Methodologies for city-scale assessment of renewable energy generation potential to inform strategic energy infrastructure investment. *Cities*.
- AECOM. 2011. Low Carbon and Renewable Energy Capacity in Yorkshire and Humber. AECOM.
- Ali-Oettinger, S. 2013. *Fall in market share for top ten PV inverter suppliers*. [Online]. [Accessed 16/01/2015]. Available from: [http://www.pv-magazine.com/news/details/beitrag/fall-in-market-share-for-top-ten-pv-inverter-suppliers\\_100011132/#axzz2VnZEgoeQ](http://www.pv-magazine.com/news/details/beitrag/fall-in-market-share-for-top-ten-pv-inverter-suppliers_100011132/#axzz2VnZEgoeQ).
- Allman, L. et al. 2004. The progress of English and Welsh local authorities in addressing climate change. *Local Environment*. **9**(3), pp.271-283.
- Ambasna-Jones. 2016. *What does Brexit mean for open data in the UK?* [Online]. [Accessed 31/07/2016]. Available from: <https://www.theguardian.com/media-network/2016/jul/21/what-does-brexit-mean-open-data-uk>.
- Anesco. 2012. *PV Panel Prices*,
- Ayompe, L.M. et al. 2011. Measured performance of a 1.72 kW rooftop grid connected photovoltaic system in Ireland. *Energy Conversion and Management*. **52**(2), pp.816-825.
- Bale, C.S.E. et al. 2012. Strategic energy planning within local authorities in the UK: A study of the city of Leeds. *Energy Policy*. **48**(0), pp.242-251.
- Barker. 2013. *Doing Solar Business in the UK*. [Online]. [Accessed 04/08/2015]. Available from: <https://www.gov.uk/government/speeches/doing-solar-business-in-the-uk>
- Bergamasco, L. and Asinari, P. 2011a. Scalable methodology for the photovoltaic solar energy potential assessment based on available roof surface area: Application to Piedmont Region (Italy). *Solar Energy*. **85**(5), pp.1041-1055.
- Bergamasco, L. and Asinari, P. 2011b. Scalable methodology for the photovoltaic solar energy potential assessment based on available roof surface area: Further improvements by ortho-image analysis and application to Turin (Italy). *Solar Energy*. **85**(11), pp.2741-2756.
- Bergman, N. and Eyre, N. 2011. What role for microgeneration in a shift to a low carbon domestic energy sector in the UK? *Energy Efficiency*. **4**(3), pp.335-353.
- Best, M. et al. 2008. *Small-scale wind energy Technical Report*. UK Met Office.
- BetterGeneration. 2015. *WindEn 45 Wind Turbine*. [Online]. [Accessed 28/12/2015]. Available from: <http://www.bettergeneration.co.uk/wind-turbine-reviews/winden-45-wind-turbine.html>.
- Bjerknäs, J. 2016. *WindEn 45kW turbine Price Enquiry*, 11/01/2016.
- Boland, R.P. and Urrutia, J. 2001. Finding the Largest Axis-Aligned Rectangle in a Polygon in. In: *In Proc. 13th Canad. Conf. Comput. Geom*: Citeseer.
- Borrmann, D. et al. 2011. The 3D Hough Transform for Plane Detection in Point Clouds: A Review and a New Accumulator Design. *3D Research*. **2**, pp.1-13.
- Bottema, M. 1996. Roughness parameters over regular rough surfaces: Experimental requirements and model validation. *Journal of Wind Engineering and Industrial Aerodynamics*. **64**(2-3), pp.249-265.
- Bottema, M. 1997. Urban roughness modelling in relation to pollutant dispersion. *Atmospheric Environment*. **31**(18), pp.3059-3075.
- Bou-Zeid, E. et al. 2007. On the parameterization of surface roughness at regional scales. *Journal of the Atmospheric Sciences*. **64**(1), pp.216-227.
- Brenner, C. 2000. Towards Fully Automatic Generation of City Models. *International Archives of Photogrammetry, Remote Sensing and Spatial Information Sciences*. **33**, pp.85-92.

- Brenner, C. and Haala, N. 1999. Rapid Acquisition of Virtual Reality City Models from Multiple Data Sources. *International Archives of Photogrammetry, Remote Sensing and Spatial Information Sciences*. **32**, pp.323-330.
- Brenner, C. and Haala, N. 2000. Rapid Acquisition of Virtual Reality City Models from Multiple Data Sources. *International Archives of Photogrammetry, Remote Sensing and Spatial Information Sciences*. (35), pp.469 - 496.
- Bristol City Council. 2012. *Solar map - is my house suitable?* [Online]. Available from: <http://www.bristol.gov.uk/page/environment/solar-energy#jump-link-0>.
- Brito, M.C. et al. 2012a. Photovoltaic potential in a Lisbon suburb using LiDAR data. *Solar Energy*. **86**(1), pp.283-288.
- Brito, M.C. et al. 2012b. Photovoltaic potential in a Lisbon suburb using LiDAR data. *Solar Energy*. **86**(1), pp.283-288.
- Britter, R.E. and Hanna, S.R. 2003. Flow and dispersion in urban areas. *Annual Review of Fluid Mechanics*. **35**, pp.469-496.
- Bull, J. 2012. Loads of green washing-can behavioural economics increase willingness-to-pay for efficient washing machines in the UK? *Energy Policy*. **50**, pp.242-252.
- Bureau of Economic Geology. 2009. Measuring Shoreline Change Along Bays and Oceans Using Historical Aerial Photography and Airborne Topographic Lidar Surveys. *Coast Studies*.
- Burton, T. 2001. *Wind Energy Handbook*. John Wiley & Sons.
- Bush, R. et al. 2014. The carbon payback of micro-generation: An integrated hybrid input-output approach. *Applied Energy*. **119**(0), pp.85-98.
- BWEA. 2012. *NOABL Database*. [Online]. [Accessed 29/07/2013]. Available from: [www.bwea.com/noabl](http://www.bwea.com/noabl)
- Caird, S. et al. 2008. Improving the energy performance of UK households: Results from surveys of consumer adoption and use of low- and zero-carbon technologies. *Energy Efficiency*. **1**(2), pp.149-166.
- Candelise, C. et al. 2010. Conditions for photovoltaics deployment in the UK: The role of policy and technical developments. *Proceedings of the Institution of Mechanical Engineers, Part A: Journal of Power and Energy*. **224**(2), pp.153-166.
- Castro, I.P. et al. 2006. Turbulence over urban-type roughness: Deductions from wind-tunnel measurements. *Boundary-Layer Meteorology*. **118**(1), pp.109-131.
- CCC. 2015. *About Us*. [Online]. [Accessed 04/08/2015]. Available from: <https://www.theccc.org.uk/about/>.
- CCL Components. 2009. *Technical Data: WINDY BOY 5000A / 6000A*. [Online]. [Accessed 30/12/2015]. Available from: <http://www.cclcomponents.com/product.asp?ID=1646>.
- Chen, H.H. et al. 2014. Strategic policy to select suitable intermediaries for innovation to promote PV solar energy industry in China. *Applied Energy*. **115**, pp.429-437.
- Cheng, H. and Castro, I.P. 2002a. Near-wall flow development after a step change in surface roughness. *Boundary-Layer Meteorology*. **105**(3), pp.411-432.
- Cheng, H. and Castro, I.P. 2002b. Near wall flow over urban-like roughness. *Boundary-Layer Meteorology*. **104**(2), pp.229-259.
- Cheng, H. et al. 2007. Flow over cube arrays of different packing densities. *Journal of Wind Engineering and Industrial Aerodynamics*. **95**(8), pp.715-740.
- Cheng, L. et al. 2013. Integration of LiDAR Data and Optical Multi-view Images for 3D Reconstruction of Building Roofs. *Optics and Lasers in Engineering*. **51**, pp.493-502.
- Cherrington, R. et al. 2013. The feed-in tariff in the UK: A case study focus on domestic photovoltaic systems. *Renewable Energy*. **50**(0), pp.421-426.

- Clark, P. and Ward, A. 2016. *Green campaigners furious as climate change ministry scrapped*. [Online]. [Accessed 23/07/2016]. Available from: <https://next.ft.com/content/4d544cb2-49e2-11e6-8d68-72e9211e86ab>.
- Claudy, M.C. et al. 2011. The diffusion of microgeneration technologies – assessing the influence of perceived product characteristics on home owners' willingness to pay. *Energy Policy*. **39**(3), pp.1459-1469.
- Climate Change Act. 2008. *Climate Change Act*. [Online]. Available from: <http://www.legislation.gov.uk/ukpga/2008/27/contents>.
- Crago, R.D. et al. 2012. Equations for the Drag Force and Aerodynamic Roughness Length of Urban Areas with Random Building Heights. *Boundary-Layer Meteorology*. **145**(3), pp.423-437.
- Crook, R. 2012. Solar Energy (Sustainable Energy Processes PEME5431/3431): Photovoltaics [Powerpoint Slides]. Available on request.
- Daniels, K. et al. 1997. Finding the largest area axis-parallel rectangle in a polygon. *Computational Geometry*. **7**(1–2), pp.125-148.
- DCLG. 2015. *Live tables on Energy Performance of Buildings Certificates*. [Online]. [Accessed 21/01/2016]. Available from: [https://www.gov.uk/government/uploads/system/uploads/attachment\\_data/file/472494/LA1 - Domestic EPCs.xls](https://www.gov.uk/government/uploads/system/uploads/attachment_data/file/472494/LA1_-_Domestic_EPCs.xls)
- DECC. 2010. *Sub-National Electricity Consumption Data*. [Online]. [Accessed 24/07/2016]. Available from: [http://webarchive.nationalarchives.gov.uk/20121217150421/http://decc.gov.uk/en/content/cms/statistics/energy\\_stats/regional/electricity/electricity.aspx](http://webarchive.nationalarchives.gov.uk/20121217150421/http://decc.gov.uk/en/content/cms/statistics/energy_stats/regional/electricity/electricity.aspx).
- DECC. 2011. *The Carbon Plan: Delivering our Low Carbon Future*. [Online]. [Accessed 04/08/2015]. Available from: [https://www.gov.uk/government/uploads/system/uploads/attachment\\_data/file/47613/3702-the-carbon-plan-delivering-our-low-carbon-future.pdf](https://www.gov.uk/government/uploads/system/uploads/attachment_data/file/47613/3702-the-carbon-plan-delivering-our-low-carbon-future.pdf).
- DECC. 2012. *Current tariff table and Older tariff tables*. [Online]. [Accessed 30/09/2012]. Available from: [http://www.decc.gov.uk/en/content/cms/meeting\\_energy/renewable\\_ener/feedin\\_tariff/feedin\\_tariff.aspx](http://www.decc.gov.uk/en/content/cms/meeting_energy/renewable_ener/feedin_tariff/feedin_tariff.aspx).
- DECC. 2013a. *Feed-in Tariffs: Get Money for Generating Your own Electricity*. [Online]. [Accessed 04/08/2015]. Available from: <https://www.gov.uk/feed-in-tariffs/overview>.
- DECC. 2013b. *Increasing the use of Low-carbon Technologies*. [Online]. [Accessed 26/07/2013]. Available from: <https://www.gov.uk/government/policies/increasing-the-use-of-low-carbon-technologies>
- DECC. 2014a. *Community Energy Strategy: Full Report*. London: Department of Energy and Climate Change.
- DECC. 2014b. *UK Solar PV Strategy Part 2: Delivering a Brighter Future*. London: DECC,.
- DECC. 2015a. *Average annual domestic electricity bills for selected towns and cities in the UK and average unit costs*. [Online]. [Accessed 02/01/2016]. Available from: [https://www.gov.uk/government/uploads/system/uploads/attachment\\_data/file/487643/table\\_223.xls](https://www.gov.uk/government/uploads/system/uploads/attachment_data/file/487643/table_223.xls).
- DECC. 2015b. *Controlling the cost of renewable energy*. [Online]. [Accessed 10/08/2015]. Available from: <https://www.gov.uk/government/news/controlling-the-cost-of-renewable-energy>.
- DECC. 2015c. *Green Deal Finance Company funding to end*. [Online]. [Accessed 10/08/2015]. Available from: <https://www.gov.uk/government/news/green-deal-finance-company-funding-to-end>.

- DECC. 2015d. Monthly feed-in tariff commissioned installations by month. *Department of Energy and Climate Change*. (05/07/2015), pp.<https://www.gov.uk/government/statistics/monthly-small-scale-renewable-deployment>.
- DECC. 2015e. *Quarterly Energy Prices December 2015*. [Online]. [Accessed 05/03/2016]. Available from: [https://www.gov.uk/government/uploads/system/uploads/attachment\\_data/file/487856/QEP\\_final\\_Dec\\_15.pdf](https://www.gov.uk/government/uploads/system/uploads/attachment_data/file/487856/QEP_final_Dec_15.pdf).
- DECC. 2015f. *Solar PV Cost Data*. [Online]. [Accessed 05/03/2016]. Available from: [https://www.gov.uk/government/uploads/system/uploads/attachment\\_data/file/428743/Cost\\_data\\_summary\\_2014\\_15.xlsx](https://www.gov.uk/government/uploads/system/uploads/attachment_data/file/428743/Cost_data_summary_2014_15.xlsx).
- DECC. 2016a. *Energy Trends: Total Energy*. [Online]. [Accessed 31/03/2016]. Available from: <https://www.gov.uk/government/statistics/total-energy-section-1-energy-trends>.
- DECC. 2016b. *Monthly Feed-in Tariff Commissioned Installations by Month*. [Online]. [Accessed 10/08/2015]. Available from: <https://www.gov.uk/government/statistics/monthly-small-scale-renewable-deployment>.
- Defra. 2011. Local Authority Data 08-09.
- Department of Environment. 2008. *PPS 18: Renewable Energy*. [Online]. [Accessed 29/12/2015]. Available from: [http://www.planningni.gov.uk/index/policy/planning\\_statements\\_and\\_supplementary\\_planning\\_guidance/pps18-draft-renewable-energy.pdf](http://www.planningni.gov.uk/index/policy/planning_statements_and_supplementary_planning_guidance/pps18-draft-renewable-energy.pdf).
- Department of Trade and Industry. 1996. *THE ASSESSMENT AND RATING OF NOISE FROM WIND FARMS*. [Online]. [Accessed 29/12/2015]. Available from: [https://www.gov.uk/government/uploads/system/uploads/attachment\\_data/file/49869/ETSU\\_Full\\_copy\\_Searchable.pdf](https://www.gov.uk/government/uploads/system/uploads/attachment_data/file/49869/ETSU_Full_copy_Searchable.pdf).
- Doward, J. 2013. Energy bills rise by 37% in three years. *The Guardian*.
- Doyle, C. and Barnes, C. 2016. *TESLA POWERWALL PAYBACK TIME*. [Online]. [Accessed 23/07/2016]. Available from: <https://www.choice.com.au/home-improvement/energy-saving/solar/articles/tesla-powerwall-payback-time>.
- Drew, D.R. et al. 2013. Estimating the potential yield of small wind turbines in urban areas: A case study for Greater London, UK. *Journal of Wind Engineering and Industrial Aerodynamics*. **115**, pp.104-111.
- Dufton. 2012. *Solar PV Cost Update*. [Online]. [Accessed 21/01/2016]. Available from: <https://www.gov.uk/government/statistics/pv-cost-update>.
- EDINA. 2013. *Privacy and Cookies Policy*. [Online]. [Accessed 19/05]. Available from: <http://edina.ac.uk/privacyandcookies.html>.
- Ellison, G. 2004. Renewable Energy Survey 2004: Draft Summary Report of Findings. *ORC International, London*.
- Emejamara, F.C. and Tomlin, A.S. 2016. A method for mapping the turbulence intensity and excess energy available to building mounted wind turbines over a UK City. *Wind Energy*. **19**(8), pp.1423-1438.
- Energy Act. 2008. *Energy Act*. [Online].
- Energy Saving Trust. 2015a. *Feed-in Tariffs*. [Online]. [Accessed 02/01/2016]. Available from: <http://www.energysavingtrust.org.uk/domestic/feed-tariffs>
- Energy Saving Trust. 2015b. *Measuring the electricity you export*. [Online]. [Accessed 27/03/2016]. Available from: <http://www.energysavingtrust.org.uk/domestic/sites/default/files/reports/Measuring%20the%20electricity%20you%20export.pdf>.



- Energy Saving Trust. 2016. *Generate cheap, green electricity from sunlight*. [Online]. [Accessed 27/03/2016]. Available from: <http://www.energysavingtrust.org.uk/domestic/solar-panels>.
- Environment Agency. 2016. *POPULAR DATASETS*. [Online]. [Accessed 26/06/2016]. Available from: <https://data.gov.uk/publisher/environment-agency>.
- ESRI. 2014. *ArcGIS Help 10.1: Area Solar Radiation (Spatial Analyst)*. [Online]. [Accessed 08/05/2014]. Available from: [http://resources.arcgis.com/en/help/main/10.1/index.html#/Area\\_Solar\\_Radiation/009z000000t5000000/](http://resources.arcgis.com/en/help/main/10.1/index.html#/Area_Solar_Radiation/009z000000t5000000/).
- EU-JRC. 2012. *PV Estimation Utility, European Union Joint Research Council*. [Online]. [Accessed 23.04.2014]. Available from: <http://re.jrc.ec.europa.eu/pvgis/apps4/pvest.php>.
- Faiers, A. and Neame, C. 2006. Consumer attitudes towards domestic solar power systems. *Energy Policy*. **34**(14), pp.1797-1806.
- Fischer, P. and Höffgen, K.-U. 1994. Computing a maximum axis-aligned rectangle in a convex polygon. *Information Processing Letters*. **51**(4), pp.189-193.
- Fischler, M.A. and Bolles, R.C. 1981. Random Sample Consensus: a paradigm for model fitting with application to image analysis and automated cartography. *Communications of the ACM*. **24**(6), pp.381-395.
- Friends of the Earth. 2016. [Online]. [Accessed 23/07/2016]. Available from: [https://www.foe.co.uk/resource/press\\_releases/our-reaction-scraping-decc-andrea-leadsoms-appointment-new-head-defra](https://www.foe.co.uk/resource/press_releases/our-reaction-scraping-decc-andrea-leadsoms-appointment-new-head-defra).
- Fu, P. 2000. *A Geometric Solar Radiation Model with Applications in Landscape Ecology*. thesis, University of Kansas.
- Fu, P. and Rich, P.M. 1999. Design and implementation of the Solar Analyst: an ArcView extension for modeling solar radiation at landscape scales. In: *Proceedings of the 19th annual ESRI user conference, San Diego, USA*.
- Fu, P. and Rich, P.M. 2000. The Solar Analyst 1.0 Manual. *Helios Environmental Modeling Institute*
- Garratt, J.R. 1990. The Internal Boundary-Layer - a Review. *Boundary-Layer Meteorology*. **50**(1-4), pp.171-203.
- Gipe, P. 2004. *Wind Power*. James and James Ltd.
- Gipe, P. 2013. *Questionable Turbines and Siting Give Architects, LEED, Green Builders, and Wind Bad Name*. [Online]. [Accessed 26/07/2013]. Available from: [http://www.wind-works.org/cms/index.php?id=64&tx\\_ttnews%5Btt\\_news%5D=2535&cHash=05835e46d90b73bb0b734dee3800a9b6](http://www.wind-works.org/cms/index.php?id=64&tx_ttnews%5Btt_news%5D=2535&cHash=05835e46d90b73bb0b734dee3800a9b6).
- Goe, M. and Gaustad, G. 2014. Strengthening the case for recycling photovoltaics: An energy payback analysis. *Applied Energy*. **120**, pp.41-48.
- Gooding, J. et al. 2013. Solar City Indicator: A methodology to predict city level PV installed capacity by combining physical capacity and socio-economic factors. *Solar Energy*. **95**, pp.325-335.
- Gouldson, A. et al. 2012. *The Economics of Low Carbon Cities: A Mini-Stern Review for the Leeds City Region*. Leeds, UK;: Centre for Low Carbon Futures.
- Gouldson, A., Kerr, N., Topi, C., Dawkins, E., . 2011. *The Economics of Low Carbon Cities: A Mini-Stern Review for the Leeds City Region*. [Online]. [Accessed 21/05]. Available from: [http://www.lowcarbonfutures.org/sites/default/files/2449\\_mainreport\\_LCC\\_WEB\\_1325868558.pdf](http://www.lowcarbonfutures.org/sites/default/files/2449_mainreport_LCC_WEB_1325868558.pdf).
- Grimmond, C.S.B. and Oke, T.R. 1999a. Aerodynamic properties of urban areas derived from analysis of surface form. *Journal of Applied Meteorology*. **38**(9), pp.1262-1292.



- Grimmond, C.S.B. and Oke, T.R. 1999b. Aerodynamic properties of urban areas derived, from analysis of surface form. *Journal of Applied Meteorology*. **38**(9), pp.1262-1292.
- Gueymard, C.A. 2008. From Global Horizontal to Global Tilted Irradiance: How Accurate are Solar Energy Engineering Predictions in Practice? In: *American Solar Energy Society, San Diego, CA, USA*.
- Gueymard, C.A. 2012. Clear-sky irradiance predictions for solar resource mapping and large-scale applications: Improved validation methodology and detailed performance analysis of 18 broadband radiative models. *Solar Energy*. **86**(8), pp.2145-2169.
- Hagishima, A. et al. 2009. Aerodynamic parameters of regular arrays of rectangular blocks with various geometries. *Boundary-Layer Meteorology*. **132**(2), pp.315-337.
- Haitao, L. et al. 2007. Fusion of High-Resolution Aerial Imagery and LIDAR Data for Object-oriented Urban Land-cover Classification Based on SVM. *International Archives of Photogrammetry, Remote Sensing and Spatial Information Sciences*. **36**, pp.179-184.
- Harrabin, R. 2015. AA joins protest at government's green changes. [Online]. [Accessed 10/08/2015]. Available from: <http://www.bbc.co.uk/news/science-environment-33724781>.
- Harrabin, R. 2016a. *Government Axes Climate Department*. [Online]. [Accessed 23/07/2016]. Available from: [http://www.bbc.co.uk/news/science-environment-36788162?utm\\_source=Daily+Carbon+Briefing&utm\\_campaign=ad8ef1d2bf-cb\\_daily&utm\\_medium=email&utm\\_term=0\\_876aab4fd7-ad8ef1d2bf-303426797](http://www.bbc.co.uk/news/science-environment-36788162?utm_source=Daily+Carbon+Briefing&utm_campaign=ad8ef1d2bf-cb_daily&utm_medium=email&utm_term=0_876aab4fd7-ad8ef1d2bf-303426797).
- Harrabin, R. 2016b. *Renewables subsidy cuts could increase energy bills*. [Online]. [Accessed 05/03/2016]. Available from: <http://www.bbc.co.uk/news/business-35706645>.
- Harvey, F. 2013. Zero-carbon home 'dithering' is threatening UK housing industry. *The Guardian*.
- Heath, M.A. and Walshe, J.D. 2007. Estimating the Potential Yield of Small Building-mounted Wind Turbines. *Wind Energy*. **10**, pp.271-287.
- Henn, A. et al. 2013. Model driven reconstruction of roofs from sparse LIDAR point clouds. *Isprs Journal of Photogrammetry and Remote Sensing*. **76**(0), pp.17-29.
- Hofierka, J. 2002. The solar radiation model for open source GIS: implementation and applications. In: *Open Source GIS-GRASS Users Conference, Trento, Italy*.
- Hofierka, J., Suri, M., Huld, T. 2007. *r.sun – Solar irradiance and Irradiation Model*. [Online]. [Accessed 10/02/2015].
- Hong, T. et al. 2014. A GIS (geographic information system)-based optimization model for estimating the electricity generation of the rooftop PV (photovoltaic) system. *Energy*. **65**, pp.190-199.
- Hough, P.V.C. 1962. *Method and Means for Recognizing Complex Patterns*.
- Huang, H. et al. 2011. 3D building roof reconstruction from point clouds via generative models. In: *19th ACM SIGSPATIAL International Conference on Advances in Geographic Information Systems, ACM SIGSPATIAL GIS 2011, Chicago, IL*. pp.16-24.
- Huang, H. et al. 2013. A generative statistical approach to automatic 3D building roof reconstruction from laser scanning data. *Isprs Journal of Photogrammetry and Remote Sensing*. **79**, pp.29-43.
- Hurvich, C.M. and Tsai, C.L. 1989. Regression and time series model selection in small samples. *Biometrika*. **76**(2), pp.297-307.
- IEA-PVPS. 2015. *Annual Reports*. [Online]. [Accessed 20/12/2015]. Available from: <http://www.iea-pvps.org/index.php?id=6>.
- Izquierdo, S. et al. 2008. A method for estimating the geographical distribution of the available roof surface area for large-scale photovoltaic energy-potential evaluations. *Solar Energy*. **82**(10), pp.929-939.

- Jacques, D.A. et al. 2014. Methodology for the assessment of PV capacity over a city region using low-resolution LiDAR data and application to the City of Leeds (UK). *Applied Energy*. **124**(0), pp.28-34.
- Jager, W. 2006. Stimulating the diffusion of photovoltaic systems: A behavioural perspective. *Energy Policy*. **34**(14), pp.1935-1943.
- Jakubiec, J.A. and Reinhart, C.F. 2013. A method for predicting city-wide electricity gains from photovoltaic panels based on LiDAR and GIS data combined with hourly Daysim simulations. *Solar Energy*. **93**, pp.127-143.
- Jasinski, M.F. et al. 2005. Bulk surface momentum parameters for satellite-derived vegetation fields. *Agricultural and Forest Meteorology*. **133**(1-4), pp.55-68.
- JBA. 2012. *West Midlands Regional Renewable and Low Carbon Energy Planning Study*.
- Jiang, D. et al. 2008. Systematic influence of different building spacing, height and layout on mean wind and turbulent characteristics within and over urban building arrays. *Wind and Structures, An International Journal*. **11**(4), pp.275-289.
- Jiang, D., Jiang, WM, Liu, HN, Sun, JN 2008. Systematic influence of different building spacing, height and layout on mean wind and turbulent characteristics within and over urban building arrays. *Wind and Structures*. **11**, pp.275-289.
- Jordan, D.C. and Kurtz, S.R. 2013. Photovoltaic Degradation Rates—an Analytical Review. *Progress in Photovoltaics: Research and Applications*. **21**(1), pp.12-29.
- JRC European Commission. 2014. *Photovoltaic Geographical Information System - Interactive Maps*. [Online]. [Accessed 07/05/2014]. Available from: <http://re.jrc.ec.europa.eu/pvgis/apps4/pvest.php#>.
- Kada, M. 2007. *Scale-dependent simplification of 3D building models based on cell decomposition and primitive instancing*. 8th International Conference on Spatial Information Theory, COSIT 2007. Melbourne. 4736 LNCS. pp.222-237. [Conference Paper]. [Accessed 19 September 2007 through 23 September 2007]. Available from: <https://www.scopus.com/inward/record.uri?eid=2-s2.0-38049086327&partnerID=40&md5=9f5322100edf11f0bf8c8ace043830be>.
- Kada, M. and McKinley, L. 2009. 3D Building Reconstruction from LIDAR Based on a Cell Decomposition Approach. *International Archives of Photogrammetry, Remote Sensing and Spatial Information Sciences*. **38**, pp.47-52.
- Kalmikov, A., Dupont, G., Dykes K., Chan, C. 2010. Wind Power Resource Assessment in Complex Urban Environments: MIT Campus Case-study Using CFD Analysis. In: *AWEA 2010 WINDPOWER Conference*.
- Kanda, M. et al. 2013. A New Aerodynamic Parametrization for Real Urban Surfaces. *Boundary-Layer Meteorology*. **148**(2), pp.357-377.
- Kanters, J. et al. 2014. The Solar Map as a Knowledge Base for Solar Energy Use. *Energy Procedia*. **48**(0), pp.1597-1606.
- Kasten, F. 1996. The linke turbidity factor based on improved values of the integral Rayleigh optical thickness. *Solar Energy*. **56**(3), pp.239-244.
- Kasten, F.Y., A.T. 1989. Revised Optical Air Mass Tables and Approximation Formula. *Applied Optics*. **28**, pp.4735-4738.
- Keirstead, J. 2007. The UK domestic photovoltaics industry and the role of central government. *Energy Policy*. **35**(4), pp.2268-2280.
- Kelleher, J. and Ringwood, J.V. 2009. A computational tool for evaluating the economics of solar and wind microgeneration of electricity. *Energy*. **34**(4), pp.401-409.
- Kelly, S. and Pollitt, M. 2011. *The local dimension of energy*. Cambridge.
- Kerr, G. 2016. *Re: Kingspan KW15*, 05/02/2016.
- Kingspan. 2015. *High Performance Small Wind Turbines*. [Online]. [Accessed 27/03/2016]. Available from: <http://www.kingspanwind.com/media/1068/ks-wind-brochure-12pp-may15-lr.pdf>.

- Knauer, C. et al. 2012. Largest inscribed rectangles in convex polygons. *Journal of Discrete Algorithms*. **13**(0), pp.78-85.
- Kodysh, J.B. et al. 2013. Methodology for estimating solar potential on multiple building rooftops for photovoltaic systems. *Sustainable Cities and Society*. **8**(0), pp.31-41.
- Kucuksari, S. et al. 2014. An Integrated GIS, optimization and simulation framework for optimal PV size and location in campus area environments. *Applied Energy*. **113**, pp.1601-1613.
- Lafarge, F. et al. 2010. Structural Approach for Building Reconstruction from a Single DSM. *Pattern Analysis and Machine Intelligence, IEEE Transactions on*. **32**(1), pp.135-147.
- Lafarge, F. and Mallet, C. 2012. Creating large-scale city models from 3D-point clouds: A robust approach with hybrid representation. *International Journal of Computer Vision*. **99**(1), pp.69-85.
- Landmap. 2014a. *Landmap - Spatial Discovery*. [Online]. [Accessed 19/05]. Available from: <http://landmap.ac.uk/>.
- Landmap. 2014b. *Landmap: Spatial Discovery*. [Online]. Available from: <http://www.landmap.ac.uk/>.
- Largent, R. et al. 2003. *Solar Cells: Resources for the Secondary Science Teacher*. Key Centre for Photovoltaic Engineering, University of New South Wales, Faculty of Engineering.
- Leeds Solar. 2012. *Leeds Solar PV Price Guide* [Online]. [Accessed 14/12/2012]. Available from: <http://www.leeds-solar.co.uk/price-guide>.
- Leloux, J. et al. 2012. Review of the performance of residential PV systems in France. *Renewable and Sustainable Energy Reviews*. **16**(2), pp.1369-1376.
- Li-COR. 2012. *EddyPro 3.0 Help and User's Guide*. [Online]. [Accessed 13/12/2012]. Available from: [http://envsupport.licor.com/help/EddyPro3/Content/Topics/Displacement\\_Height.htm](http://envsupport.licor.com/help/EddyPro3/Content/Topics/Displacement_Height.htm)
- Li, Z. et al. 2014. Domestic integration of micro-renewable electricity generation in Ireland - The current status and economic reality. *Renewable Energy*. **64**, pp.244-254.
- Lim, H.C. et al. 2009. Flow around a cube in a turbulent boundary layer: LES and experiment. *Journal of Wind Engineering and Industrial Aerodynamics*. **97**(2), pp.96-109.
- Lodha, K.S. et al. 2006. Aerial LiDAR Data Classification using Support Vector Machines. In: *3rd International Symposium on 3D Data Processing, Visualization and Transmission, Chapel Hill, NC, USA*. pp.567-574.
- Lukac, N. et al. 2013. Rating of roofs' surfaces regarding their solar potential and suitability for PV systems, based on LiDAR data. *Applied Energy*. **102**, pp.803-812.
- Maas, H.G. and Vosselman, G. 1999. Two algorithms for extracting building models from raw laser altimetry data. *Isprs Journal of Photogrammetry and Remote Sensing*. **54**(2-3), pp.153-163.
- Macalister, T. and Vaughan, A. 2015. *Green energy sector attacks chancellor's changes to climate change levy*. [Online]. [Accessed 10/08/2015]. Available from: <http://www.theguardian.com/business/2015/jul/09/green-energy-sector-attacks-budget-climate-change-levy>.
- Macdonald, R.W. 2000. Modelling the mean velocity profile in the urban canopy layer. *Boundary-Layer Meteorology*. **97**(1), pp.25-45.
- Macdonald, R.W. et al. 1998. An improved method for the estimation of surface roughness of obstacle arrays. *Atmospheric Environment*. **32**(11), pp.1857-1864.
- Markvart, T. 2003. Introduction. *Practical Handbook of Photovoltaics*. Amsterdam: Elsevier Science, pp.1-2.
- MasterMap, O. 2008. Topography Layer [GML geospatial data], Coverage: West Yorkshire. *EDINA Digimap Ordnance Survey Service*.
- MasterMap, O. 2011. *[Shape geospatial data]*. Digimap.

- Mathiesen, K. 2015. *Will Tesla's home battery really transform our energy infrastructure?* [Online]. [Accessed 23/07/2016]. Available from: <https://www.theguardian.com/environment/2015/may/01/will-teslas-home-battery-really-transform-our-energy-infrastructure>.
- MATLAB. 2012. *version 7.14.0.739 (R2012a)*. The MathWorks, Inc.
- MATLAB and Statistics Toolbox Release R2014b*. 2014. Natick, Massachusetts, United States of America: The MathWorks Inc.
- McGlone, J.C. et al. 2004. *Manual of Photogrammetry*. 5th ed. ASPRS.
- McIntyre, J.H. et al. 2011. Local wind-energy potential for the city of Guelph, Ontario (Canada). *Renewable Energy*. **36**(5), pp.1437-1446.
- Met Office. 2009. *Virtual Met Mast<sup>TM</sup>*. [Online]. [Accessed 22/05/2012].
- Met Office. 2012a. *[City] Climate*. [Online]. [Accessed 23/07/2016]. Available from: <http://www.metoffice.gov.uk/public/weather/climate/gcr5qn5iy>.
- Met Office. 2012b. *Virtual Met Mast<sup>TM</sup>: Verification Report*. [Online]. [Accessed 22/05/2012]. Available from: [http://www.metoffice.gov.uk/media/pdf/s/q/VMM\\_verification\\_report\\_September11.pdf](http://www.metoffice.gov.uk/media/pdf/s/q/VMM_verification_report_September11.pdf).
- Met Office. 2016. *UK Climate*. [Online]. [Accessed 28/05/2016]. Available from: <http://www.metoffice.gov.uk/public/weather/climate>.
- Millward-Hopkins, J.T. et al. 2011. Estimating Aerodynamic Parameters of Urban-Like Surfaces with Heterogeneous Building Heights. *Boundary-Layer Meteorology*. **141**(3), pp.443-465.
- Millward-Hopkins, J.T. et al. 2013a. Aerodynamic Parameters of a UK City Derived from Morphological Data. *Boundary-Layer Meteorology*. **146**(3), pp.447-468.
- Millward-Hopkins, J.T. et al. 2013b. Assessing the potential of urban wind energy in a major UK city using an analytical model. *Renewable Energy*. **60**(0), pp.701-710.
- Millward-Hopkins, J.T. et al. 2013c. Mapping the wind resource over UK cities. *Renewable Energy*. **55**(0), pp.202-211.
- Molano, R. et al. 2012. Finding the largest area rectangle of arbitrary orientation in a closed contour. *Applied Mathematics and Computation*. **218**(19), pp.9866-9874.
- Muhammad-Sukki, F. et al. 2013. Revised feed-in tariff for solar photovoltaic in the United Kingdom: A cloudy future ahead? *Energy Policy*. **52**(0), pp.832-838.
- NewEnCo. 2004. *SYSTEM TO CONNECT 20 – 50KW WIND TURBINE TO LOW VOLTAGE POWER MAINS*. [Online]. [Accessed 30/12/2015]. Available from: <http://www.newenco.co.uk/EEI-Wind-Inverters?gclid=CKHUxpD5g8oCFQYTwwodL1IOPQ>.
- Nguyen, V. et al. 2005. A comparison of line extraction algorithms using 2D laser rangefinder for indoor mobile robotics. In: *International conference on intelligent robots and systems, Edmonton, Canada*. p.6.
- Office for National Statistics. 2010. *Survey of Personal Incomes 2007-2008, Office of National Statistics*. [Online]. [Accessed 30/10/2011]. Available from: [http://www.hmrc.gov.uk/stats/income\\_distribution/table3-14-feb2010.pdf.>](http://www.hmrc.gov.uk/stats/income_distribution/table3-14-feb2010.pdf.>).
- ofgem. 2015. *Feed-in Tariff Scheme: Tariff Table 1 January 2016 PV Only*. [Online]. [Accessed 21/01/2016]. Available from: <https://www.ofgem.gov.uk/publications-and-updates/feed-tariff-scheme-tariff-table-1-january-2016-pv-only>.
- Ofgem. 2016. *Feed-in Tariff (FIT) Deployment Caps that have been reached in Tariff Period 1 (08 February – 31 March 2016)*. [Online]. [Accessed 05/03/2016]. Available from: [https://www.ofgem.gov.uk/system/files/docs/2016/02/fit\\_deployment\\_caps\\_that\\_have\\_been\\_reached\\_in\\_tariff\\_period\\_1\\_1.pdf](https://www.ofgem.gov.uk/system/files/docs/2016/02/fit_deployment_caps_that_have_been_reached_in_tariff_period_1_1.pdf).

- ONS. 2015. *Consumer Price Indices - RPI seasonally adjusted RPIY: 1987 to 2015*. [Online]. [Accessed 16/01/2015]. Available from: <http://www.ons.gov.uk/ons/datasets-and-tables/data-selector.html?table-id=2.7&dataset=mm23>.
- Ortner, M. et al. 2007. Building outline extraction from digital elevation models using marked point processes. *International Journal of Computer Vision*. **72**(2), pp.107-132.
- Oude Elberink, S. 2009. Target Graph Matching for Building Reconstruction. *International Archives of Photogrammetry, Remote Sensing and Spatial Information Sciences*. **38**, pp.49-54.
- Oude Elberink, S. and Vosselman, G. 2011. Quality analysis on 3D building models reconstructed from airborne laser scanning data. *ISPRS Journal of Photogrammetry and Remote Sensing*. **66**(2), pp.157-165.
- Overby, J. et al. 2004. Automatic 3D building reconstruction from airborne laser scanning and cadastral data using Hough transform. *International Archives of Photogrammetry, Remote Sensing and Spatial Information Sciences*. **35**(PART B3), pp.296-301.
- Peacock, A.D. et al. 2008. Micro wind turbines in the UK domestic sector. *Energy and Buildings*. **40**(7), pp.1324-1333.
- Pearsall, N. and Gottschalg, R. 2012. Performance monitoring. *Earth and Planetary Sciences*. pp.775-786.
- Platt, C. 2016a. *Payback times for PV*, 07/03/2016.
- Platt, C. 2016b. *Re: Solar PV panel quotes*, 22/01/2016.
- Poullis, C. and You, S. 2009. Photorealistic large-scale Urban city model reconstruction. *IEEE Transactions on Visualization and Computer Graphics*. **15**(4), pp.654-669.
- Ratti, C. et al. 2002. Analysis of 3-D urban databases with respect to pollution dispersion for a number of European and American cities. *Water Soil Air Poll Focus*. **2**, pp.459-469.
- Raupach, M. 1992. Drag and drag partition on rough surfaces. *Boundary-Layer Meteorology*. **60**(4), pp.375-395.
- Raupach, M.R. 1994. Simplified expressions for vegetation roughness length and zero-plane displacement as functions of canopy height and area index. *Boundary-Layer Meteorology*. **71**(1-2), pp.211-216.
- Reich, N. 2012. Performance ratio revisited: is PR > 90% realistic? *Progress in Photovoltaics: Research and Applications*. **20**(6), pp.717-716.
- Reich, N.H. et al. 2012. Performance ratio revisited: is PR > 90% realistic? *Progress in Photovoltaics: Research and Applications*. **20**(6), pp.717-726.
- Remund J., W.L., Lefevre M., Ranchin T., Page J., . 2003. Worldwide Linke turbidity information. In: *ISES Solar World Congress, Göteborg, Sweden*.
- Rich, P.M. et al. 1994. Using Viewshed Models to Calculate Intercepted Solar Radiation: Applications in Ecology. *American Society for Photogrammetry and Remote Sensing Technical Papers*. pp.524-529.
- Rich, P.M. and Fu, P. 2000. Topoclimatic Habitat Models. In: *Fourth International Conference on Integrating GIS and Environmental Modeling*.
- Roberts, P. 2016. *Solar panel pricing*, 22/01/2016.
- Rodrigo, J.S. 2010. *Sate-of-the-Art Wind Resource Assessment*. [Online]. [Accessed 29/07/2013]. Available from: [www.waudit-itn.eu/download.php?id=103&parent=79](http://www.waudit-itn.eu/download.php?id=103&parent=79)
- Römer, C. and Plümer, L. 2010. Identifying architectural style in 3D city models with Support Vector Machines. *Photogrammetrie, Fernerkundung, Geoinformation*. **2010**(5), pp.371-384.
- Rooney, G.G. 2001. Comparison of upwind land use and roughness length measured in the urban boundary layer. *Boundary-Layer Meteorology*. **100**(3), pp.469-486.



- Rottensteiner, F. and Briese, C. 2003. Automatic Generation of Building Models from LIDAR Data and the Integration of Aerial Images. *International Archives of Photogrammetry, Remote Sensing and Spatial Information Sciences*. **34**, pp.174-180.
- Rottensteiner, F. et al. 2005. Automated delineation of roof planes in lidar data. *The International Archives of the Photogrammetry, Remote Sensing and Spatial Information Sciences*. **36**(3 W19), pp.221-226.
- Rudd, A. 2015. *Changes to onshore wind subsidies protect investment and get the best deal for bill payers*. [Online]. [Accessed 10/08/2015]. Available from: <https://www.gov.uk/government/news/changes-to-onshore-wind-subsidies-protect-investment-and-get-the-best-deal-for-bill-payers>.
- San Francisco Department of the Environment. 2007. *San Francisco Solar Map*. [Online]. [Accessed 02/05/2012]. Available from: <http://sf.solarmap.org/>
- Sauter, R. and Watson, J. 2007. Strategies for the deployment of micro-generation: Implications for social acceptance. *Energy Policy*. **35**(5), pp.2770-2779.
- Scharmer, K. and Grief, J. 2000. *The European Solar Radiation Atlas: Fundamentals and Maps*. [Online]. [Accessed 19/06/2016]. Available from: <http://catalog.mines-paristech.fr/Files/ESRA11res.pdf>.
- Schindler, K. and Bauer, J. 2003. Towards Feature-Based Building Reconstruction From Images. In: *WSCG 2003, Plzen, Czech Republic*.
- Scott, C.E. et al. 2014. The direct and indirect radiative effects of biogenic secondary organic aerosol. *Atmospheric Chemistry and Physics*. **14**(1), pp.447-470.
- Scottish Government. 2014. *Onshore Wind Turbines*. [Online]. [Accessed 06/02/2016]. Available from: <http://www.gov.scot/Resource/0045/00451413.pdf>.
- SCROL. 2011. *SCROL Analyser*. [Online]. [Accessed 30/10/2011]. Available from: <http://www.scrol.gov.uk/scrol/common/home.jsp>.
- Seguro, J. and Lambert, T. 2000. Modern estimation of the parameters of the Weibull wind speed distribution for wind energy analysis. *Journal of Wind Engineering and Industrial Aerodynamics*. **85**(1), pp.75-84.
- Semikron. 2012a. *P-N Junction*. [Online]. [Accessed 17/07/2016]. Available from: <http://www.powerguru.org/p-n-junction/>.
- Semikron. 2012b. *Semiconductor Doping*. [Online]. [Accessed 17/07/2016]. Available from: <http://www.powerguru.org/semiconductor-doping/>
- SEPA. 2011. Waste Data Digest 11: Data Tables, Scottish Environmental Protection Agency.
- [*Shape Geospatial Data*]. 2011. Ordnance Survey (GB).
- SMA. 2015a. *Sunny Boy 1.5/2.5 Data Sheet*. [Online]. [Accessed 16/01/2016]. Available from: [http://www.sma-uk.com/fileadmin/content/global/Products/Documents/Wechselrichter\\_ohne\\_Trafo/Data\\_Sheet\\_SB\\_1.5\\_2.5.pdf](http://www.sma-uk.com/fileadmin/content/global/Products/Documents/Wechselrichter_ohne_Trafo/Data_Sheet_SB_1.5_2.5.pdf).
- SMA. 2015b. *SUNNY BOY 3000TL / 3600TL / 4000TL / 5000TL: Data sheet*. [Online]. [Accessed 20/01/2016]. Available from: <http://files.sma.de/dl/15330/SB5000TL-21-DEN1551-V20web.pdf>.
- SMA. 2015c. *Sunny Boy 6000TL Data Sheet*. [Online]. [Accessed 16/01/2015]. Available from: <http://files.sma.de/dl/15330/SB6000TL-21-DEN1420W.pdf>.
- SMA. 2015d. *Sunny Tripower 5000TL - 12000TL*. [Online]. [Accessed 16/01/2016]. Available from: <http://files.sma.de/dl/18915/SPortalWebcon-BA-en-13.pdf>.
- SMA. 2015e. *SUNNY TRIPOWER 20000TL / 25000TL*. [Online]. [Accessed 16/01/2016]. Available from: <http://files.sma.de/dl/24336/STP25000TL-30-DEN1540-V22web.pdf>.

- Small-scale wind energy technical report*. 2008. [Online]. [Accessed 10/11/2014]. Available from: <http://www.carbontrust.com/media/85174/small-scale-wind-energy-technical-report.pdf>.
- Smith, C.J. et al. 2016. An all-sky radiative transfer method to predict optimal tilt and azimuth angle of a solar collector. *Solar Energy*. **123**, pp.88-101.
- Smith, L. 2015. *Briefing Paper: Planning for onshore wind*. [Online]. [Accessed 29/12/2015]. Available from: [www.parliament.uk/briefing-papers/sn04370.pdf](http://www.parliament.uk/briefing-papers/sn04370.pdf).
- Solar Century. 2012. *Your Estimate: System Cost*. [Online]. [Accessed 05/11/2012]. Available from: <http://www.solarcentury.co.uk/estimate/?postcode=ls2@-email=hollyaed%40hotmail.com>.
- Solar Essence. 2012. *PV Price & Feed-in Tariff Calculator*. [Online]. [Accessed 14/12/2012]. Available from: <http://www.solaressence.co.uk/domestic-pv/pv-price-&-payback-calculator.html?gclid=CLbst52VmrQCFczHtAodCAQAHQ>.
- Sproul, A. 2003. *Solar Cells: Resource for the Secondary Science Teacher*. [Online]. Available from: [http://www2.pv.unsw.edu.au/nsite-files/pdfs/UNSW\\_Understanding\\_the\\_p-n\\_Junction.pdf](http://www2.pv.unsw.edu.au/nsite-files/pdfs/UNSW_Understanding_the_p-n_Junction.pdf).
- Staffell, I. and Green, R. 2014. How does wind farm performance decline with age? *Renewable Energy*. **66**, pp.775-786.
- Stamnes, K. et al. 2000. DISORT, a general purpose Fortran program for discrete-ordinate-method radiative transfer in scattering and emitting layered media: Documentation of methodology. *Dept. of Physics and Engineering Physics, Stevens Institute of Technology, Hoboken, NJ, USA*.
- Stankovic, S. et al. 2009. *Urban Wind Energy*. Earthscan.
- Stern, N. and Treasury, G.B. 2007. *The Economics of Climate Change: The Stern Review*. Cambridge University Press.
- Sun, Y.-w. et al. 2013. GIS-based approach for potential analysis of solar PV generation at the regional scale: A case study of Fujian Province. *Energy Policy*. **58**(0), pp.248-259.
- Sunderland, K.M. et al. 2013. Estimating the wind resource in an urban area: A case study of micro-wind generation potential in Dublin, Ireland. *Journal of Wind Engineering and Industrial Aerodynamics*. **118**(0), pp.44-53.
- Šúri, M. and Hofierka, J. 2004. A new GIS-based solar radiation model and its application to photovoltaic assessments. *Transactions in GIS*. **8**(2), pp.175-190.
- Šúri, M. et al. 2007. Potential of solar electricity generation in the European Union member states and candidate countries. *Solar Energy*. **81**(10), pp.1295-1305.
- Suveg, I. and Vosselman, G. 2004. Reconstruction of 3D Building Models from Aerial Images and Maps. *ISPRS Journal of Photogrammetry and Remote Sensing*. **58**, pp.202-224.
- Tarsha-Kurdi, F. et al. 2008. EXTENDED RANSAC ALGORITHM FOR AUTOMATIC DETECTION OF BUILDING ROOF PLANES FROM LIDAR DATA. *The photogrammetric journal of Finland*. **21**(1), pp.97-109.
- Tarsha-Kurdi, F. et al. 2007. Model-driven and data-driven approaches using LIDAR data: Analysis and comparison. In: *Munich*. pp.87-92.
- Taylor, J., Leloux, J., Everard, A. M., Briggs, J. Buckley, A. . 2015. Monitoring thousands of distributed PV systems in the UK: Energy production and performance. In: *PVSAT 11, Leeds, UK*.
- The European Wind Energy Association. 2013. *Wind Energy – The Facts (Volume 2). Costs and Prices*. [Online]. [Accessed 02/01/2016]. Available from: [http://www.ewea.org/fileadmin/ewea\\_documents/documents/publications/WETF/Facts\\_Volume\\_2.pdf](http://www.ewea.org/fileadmin/ewea_documents/documents/publications/WETF/Facts_Volume_2.pdf).
- The GeoInformation Group. 2008. *Cities Revealed*. [Online].
- Truss, E. 2014. *Subsidies for solar farms to be cut to help safeguard farmland*. [Online]. [Accessed 10/08/2015]. Available from:

- <https://www.gov.uk/government/news/subsidies-for-solar-farms-to-be-cut-to-help-safeguard-farmland>.
- Turner. 2014. *Critical Values of  $r$* . [Online]. Available from: <http://turner.faculty.swau.edu/mathematics/math241de/materials/rctable/rc.php>.
- Vallet, B. et al. 2011. Building footprint database improvement for 3D reconstruction: A split and merge approach and its evaluation. *ISPRS Journal of Photogrammetry and Remote Sensing*. **66**(5), pp.732-742.
- Van Hoesen, J. and Letendre, S. 2010. Evaluating potential renewable energy resources in Poultney, Vermont: A GIS-based approach to supporting rural community energy planning. *Renewable Energy*. **35**(9), pp.2114-2122.
- Vaughan, A. 2016a. *Abolition of Decc 'major setback for UK's climate change efforts'*. [Online]. [Accessed 23/07/2016]. Available from: <https://www.theguardian.com/environment/2016/jul/15/decc-abolition-major-setback-for-uk-climate-change-efforts>.
- Vaughan, A. 2016b. *Solar power sets new British record by beating coal for a day*. [Online]. Available from: <http://www.theguardian.com/environment/2016/apr/13/solar-power-sets-new-british-record-by-beating-coal-for-a-day>.
- von Kármán, T. 1930. 'Mechanische Ähnlichkeit und Turbulenz. *Nachrichten von der Gesellschaft der Wissenschaften zu Göttingen, Fachgruppe 1 (Mathematik)*. (5), pp.58-76.
- Vosselman, G. and Dijkman, E. 2001. 3D BUILDING MODEL RECONSTRUCTION FROM POINT CLOUDS AND GROUND PLANS. *International Archives of Photogrammetry, Remote Sensing and Spatial Information Sciences*. **34**, pp.37-43.
- Weekes, S. 2014. *Small-scale Wind Energy: Methods for Wind Resource Assessment*. thesis, The University of Leeds.
- Weekes, S. and Tomlin, A. 2013. Evaluation of a semi-empirical model for predicting the wind energy resource relevant to small-scale wind turbines. *Renewable Energy*. **50**, pp.280-288.
- Wiginton, L.K. et al. 2010. Quantifying rooftop solar photovoltaic potential for regional renewable energy policy. *Computers, Environment and Urban Systems*. **34**(4), pp.345-357.
- Willis, K. et al. 2011. Renewable energy adoption in an ageing population: Heterogeneity in preferences for micro-generation technology adoption. *Energy Policy*. **39**(10), pp.6021-6029.
- WindEn. 2015. *Overview: WindEn 45*. [Online]. [Accessed 02/01/2016]. Available from: <http://www.winden.se/en/products/overview/browse/1/article/kundtraeff-i-soederaakra.html>.
- Xie, Z.T. et al. 2008. Large-Eddy simulation of flows over random urban-like obstacles. *Boundary-Layer Meteorology*. **129**(1), pp.1-23.
- Zaki, S. et al. 2011a. Aerodynamic Parameters of Urban Building Arrays with Random Geometries. *Boundary-Layer Meteorology*. **138**(1), pp.99-120.
- Zaki, S.A. et al. 2011b. Aerodynamic Parameters of Urban Building Arrays with Random Geometries. *Boundary-Layer Meteorology*. **138**(1), pp.99-120.